

DOCTOR OF PHILOSOPHY

Development of innovative composite coatings containing sustainably sourced particles for industrial applications

Merrill, Richard James

Award date:
2019

Awarding institution:
Coventry University

[Link to publication](#)

General rights

Copyright and moral rights for the publications made accessible in the public portal are retained by the authors and/or other copyright owners and it is a condition of accessing publications that users recognise and abide by the legal requirements associated with these rights.

- Users may download and print one copy of this thesis for personal non-commercial research or study
- This thesis cannot be reproduced or quoted extensively from without first obtaining permission from the copyright holder(s)
- You may not further distribute the material or use it for any profit-making activity or commercial gain
- You may freely distribute the URL identifying the publication in the public portal

Take down policy

If you believe that this document breaches copyright please contact us providing details, and we will remove access to the work immediately and investigate your claim.

Development of innovative composite coatings containing sustainably sourced particles for industrial applications

Richard James Merrill

*A thesis submitted in partial fulfilment of the University's requirements for the
Degree of Doctor of Philosophy*

January 2019



Some materials have been removed from this thesis due to Third Party Copyright or confidentiality issues. Pages where material has been removed are clearly marked in the electronic version. The unabridged version of the thesis can be viewed at the Lanchester Library, Coventry University



Certificate of Ethical Approval

Applicant:

Richard Merrill

Project Title:

Development of innovative composite coatings containing sustainably sourced particles for industrial applications

This is to certify that the above named applicant has completed the Coventry University Ethical Approval process and their project has been confirmed and approved as Low Risk

Date of approval:

16 July 2018

Project Reference Number:

P74093



Certificate of Ethical Approval

Applicant:

Richard Merrill

Project Title:

Development of innovative composite coatings containing sustainably sourced particles for industrial applications

This is to certify that the above named applicant has completed the Coventry University Ethical Approval process and their project has been confirmed and approved as Low Risk

Date of approval:

05 April 2016

Project Reference Number:

P42034

Certificate of Ethical Approval

Applicant:

Richard Merrill

Project Title:

Nickel and copper electrodeposited composite coatings incorporating naturally occurring antibacterial particles

This is to certify that the above named applicant has completed the Coventry University Ethical Approval process and their project has been confirmed and approved as Low Risk

Date of approval:

11 August 2016

Project Reference Number:

P43246

Abstract

Composite coatings are of great academic and industrial importance to the UK and the wider world. They can offer many improvements over single-phase materials in microhardness, wear resistance, thermal resistance, hydrophobic behaviour and corrosion resistance, however, electrodeposited composite coatings are not without their drawbacks. Composites are difficult to recycle, and the particles used in them can be expensive and require energy intensive production methods to produce them, which can make them unsustainable in the long term. The Aim of this research was to produce copper and nickel composite coatings from a more sustainable source of filler particles (turmeric), and then characterise their properties. The coatings were deposited from various electrolytes including acid copper, Watts nickel and a low nickel ion concentration electrolyte (LICE).

The hardness, hydrophobic behaviour, surface roughness, and corrosion rate of the coatings were then characterised. To understand these properties the surface texture, grain structure, and composition of the coatings was analysed. The results showed the incorporation of turmeric into the copper coating reduced the grain size of the deposit and increased the microhardness, water contact angle and electrochemical corrosion resistance of the coating, however, there was a reduction in corrosion resistance when the coatings were tested using the salt spray standard method ASTM B 117 – 03. An additional unexpected finding was that the size of turmeric particles in the electrolyte had a greater influence on the coating's properties than the concentration of turmeric in the electrolyte, and that there was an optimal size of turmeric particles (of circa 250 nm) for reducing the grain size of the copper deposit. This result correlates with the findings obtained from copper nano-diamond deposits in this research, which also showed an optimal particle size of 250 nm for reducing the grain size of the deposit. The incorporation of turmeric into the nickel deposit also reduced the grain size and increased the microhardness corrosion resistance and the water contact angle of the coating. At 5.0 g/l of turmeric in the nickel electrolyte both the resistance to electrochemical and salt spray corrosion was also increased. This research demonstrates that turmeric particles could be used as a sustainable filler particle for nickel and copper composite coatings.

Acknowledgements

Foremost, I would like to express my sincere gratitude to my director of study Prof. Andrew Copley for his support throughout my Ph.D. research, for his motivation, enthusiasm, and patience. His guidance helped me throughout my studies and my thesis writing. I could not have hoped for a better supervisor and mentor.

Besides my director of study, I would like to thank the rest of my supervisory team: Dr John E. Graves, and Dr Jamie Beddows for their encouragement and insightful comments.

I thank my colleague Dr Liang Wu for his help, insight, and expertise in many areas of this research.

Last but not the least, I would like to thank Elena Fuentes from IK4-TEKNIKER for performing the glow discharge optical emission spectrometry. Without her assistance this analysis would not have been possible.

Table of Contents

1. Introduction	5
1.1. Surface coatings	5
1.2. Composite materials	6
1.3. Research aim	7
1.4. Reference list	7
2. Literature Review	8
2.1. Overview	8
2.2. Composite coatings	9
2.2.1. Methods of producing Composite Coatings	9
2.2.2. Electrodeposited composite coatings	10
2.2.3. Spices	15
2.3. Electrodeposition of composites	16
2.3.1. Basics of electrodeposition	16
2.3.2. Electrodeposition of nickel and copper	17
2.3.2.1. Nickel	17
2.3.2.2. Copper	18
2.3.3. Mechanism of composite electrodeposition	19
2.4. Factors affecting the electrocodeposition	23
2.4.1. Current density	23
2.4.2. Electrolyte composition	26
2.4.3. Agitation	28
2.4.3.1. Ultrasound	29
2.5. Conclusions	31
2.6. Reference list	32
3. Methods	45
3.1. Overview	45
3.2. Spice particle size and deagglomeration	46
3.3. Electrodeposition of coatings	47
3.3.1. Preparation of electrodes	48
3.3.2. Preparation of electrolytes	49
3.3.2.1. Copper electrolyte preparation	49
3.3.2.2. Watts nickel electrolyte	49

3.3.2.3. Low ion concentration nickel electrolyte (LICE) preparation	50
3.3.3. Electrodeposition current density analysis	50
3.3.4. Current efficiency of electrodeposition methods	51
3.3.5. Electrodeposition of coatings	52
3.4. Coating properties.....	55
3.4.1. Vicker's Hardness.....	55
3.4.2. Water contact angle.....	57
3.4.3. White light interferometry (WLI)	57
3.4.4. Corrosion rate	58
3.4.4.1. Tafel method.....	59
3.4.4.2. Salt spray corrosion analysis	60
3.5. Microstructure analysis	61
3.5.1. Scanning electron microscope (SEM).....	62
3.5.2. Electron back scatter detection (EBSD).....	62
3.5.3. Focused ion beam (FIB-SEM)	63
3.5.4. Glow-discharge optical emission spectrometry.....	64
3.6. Statistical analysis.....	65
3.7. Reference list.....	67
4. Turmeric preparation	69
4.1. Overview	69
4.2. Turmeric particle morphology.....	70
4.3. Turmeric deagglomeration experiment.....	72
4.3.1. Effects of stirring on deagglomeration	72
4.3.2. Effects of ultrasound on deagglomeration	75
4.4. Variation mean Z-average size	82
4.4.1. Variation at different concentrations	82
4.4.2. Effect of ultrasound power on Z- average size.....	85
4.5. Turmeric preparation discussion	87
4.6. Conclusions	89
4.7. Reference list.....	89
5. Copper results	91
5.1. Overview	91
5.2. Electrodeposition	91
5.2.1. Hull cell test	91
5.2.2. Copper coating surface finish	92

5.3. Microstructure	94
5.3.1. Particle content.....	94
5.3.2. Surface morphology.....	97
5.3.3. Grain structure	100
5.3.4. Grain size.....	103
5.4. Copper coating properties.....	107
5.4.1. Hardness	107
5.4.2. Surface roughness.....	109
5.4.3. Hydrophobic behaviour	111
5.4.4. Corrosion rate	114
5.4.4.1. Electrochemical corrosion tests	114
5.4.4.2. Salt spray analysis	116
5.5. Copper results discussion	118
5.6. Conclusions	122
5.7. Reference list.....	123
6. Nickel results	127
6.1. Overview	127
6.2. Electrodeposition	128
6.2.1. Watts nickel deposition	128
6.2.2. Hull cell test	130
6.2.3. Lower ion concentration electrolyte (LICE) nickel	131
6.3. Microstructure	133
6.3.1. Particle content.....	133
6.3.2. Surface morphology.....	138
6.3.3. Grain structure	142
6.3.4. Grain Size	145
6.4. Nickel coating properties.....	146
6.4.1. Hardness	146
6.4.2. Surface roughness.....	148
6.4.3. Hydrophobic behaviour	150
6.4.4. Corrosion rate	154
6.4.4.1. Electrochemical corrosion tests	154
6.4.4.2. Salt spray.....	155
6.5. Nickel results discussion.....	158
6.6. Conclusions	161

6.7. Reference list	162
7. Conclusions	168
7.1. Research conclusions	168
7.2. Future Recommendation	170
7.3. Reference list	171
Appendix A Spice selection	172
A.1. Overview	172
A.2. Methods	172
A.2.1. Spice preparation	172
A.2.2. The solubility of the spices	173
A.2.3. Ultrasonic equipment used for dispersion	174
A.2.4. Spice particle dispersion and suspension	176
A.3. Results	177
A.3.2. Spice grinding	177
A.3.3. Spice solubility test	183
A.3.4. Spice particle dispersion and suspension	184
A.4. Discussion	186
A.5. Conclusions	188
A.6. Reference list	188

1. Introduction

1.1. Surface coatings

Material selection is a vital part of any engineering project, where the aim is to meet the desired performance characteristics while minimizing cost. The successful selection of materials can be the difference between a successful project and a failure [1,2]. When selecting a material for an engineering project there are a number of important aspects to consider, the materials mechanical properties (such as strength, elongation, hardness and fatigue limit), cost, ability to be manufactured, and wear and corrosion rates [3]. In some circumstances a material may possess some of the required properties (e.g. strength, fatigue limit or cost), but lack other desired properties (e.g. wear resistance, corrosion resistance or hardness), in these cases a surface coating may be utilised.

A surface coating can be used to change or enhance the surface properties of a material, while leaving the underlying bulk materials properties unchanged. Surface coatings can be used to impart wear resistance, corrosion resistance, heat resistance, electrical resistance, anti-microbial activity, or even increase the hardness and fatigue strength of a material. They are essential for many industries including automotive, aerospace, construction, energy, healthcare, mining, transport, textiles, and even food and drink [4]. In June 2014 a report by the Surface Engineering and Advanced Coatings (SEAC) special interest group stated that the surface engineering and advanced coatings industry was worth £11 billion per annum to the UK economy, and effected products worth £140 billion [4].

Two metals commonly utilised as surface coatings due to their unique properties are nickel and copper. Nickel is hard, ductile, ferromagnetic up to 360 °C, highly resistant to corrosion in both water and air and resists most acids (except for oxidizing acids such as nitric). Nickel has many uses but is often used as a protective coating, having many important applications including tubing in desalination plants, coinage, aircraft turbine components, and marine petroleum and chemical processing equipment [5]. Nickel is also used as a solderable surface in the electronics industry and as a diffusion barrier layer for bearings in internal combustion engines [6].

Copper has been used by humans for thousands of years. It is a soft metal that is ductile, highly electrical and thermally conductive, has strong antibacterial properties and is non-magnetic. Copper coatings are often used for heat exchangers, printed circuit boards, antibacterial surfaces and decorative finishes [7-9].

1.2. Composite materials

For certain applications single metals surface coatings may be insufficient for the required task, in these cases a composite coating may be used. Composite materials are defined as artificial combinations of two or more components (fillers and matrix) that remain chemically separate when combined (Figure 1.1.). Composites can be defined by either their geometry (such as laminated, fibrous, and particulate), or by their matrix material (such as polymer–matrix, cement–matrix, metal–matrix, carbon–matrix, and ceramic–matrix) [10].

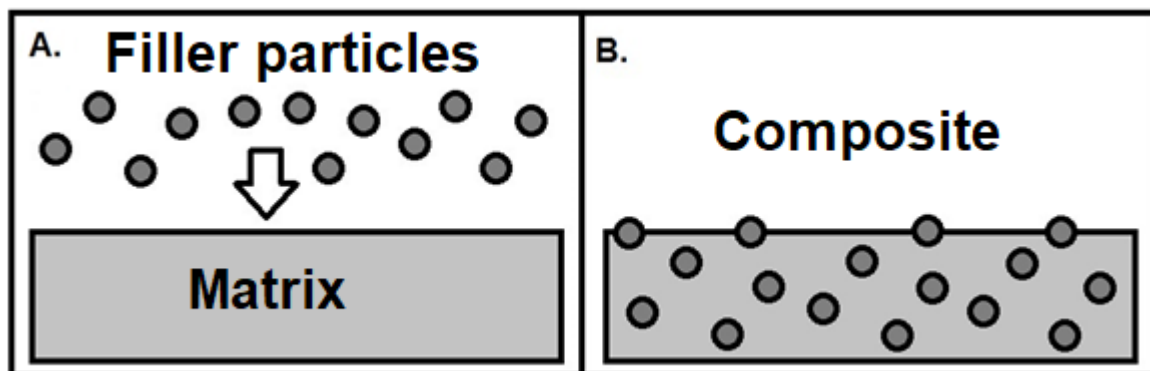


Figure 1.1. diagram of composite material. A) Two separate materials a filler and matrix. B) the two materials combined to produce a composite material.

The incorporation of inert particles into a metal matrix (creating a composite) can enhance the properties of the material or impart completely new properties onto the metal. As such the use of a composite coating can give superior performance when compared to their single material counterparts. As such composite coatings are widely utilised throughout many industries including aerospace, transportation, oil, gas and marine industries [11].

However composite materials (as coatings and bulk materials) are not without drawbacks. The filler particles used can be expensive and/or require energy intensive

production methods to produce them. Due to the inherent heterogeneous nature of the matrix with filler material, composite materials can be extremely difficult to recycle (both for matrix and filler materials) compared to their single material counterparts [12]. These problems can make composite coatings expensive and unsustainable.

1.3. Research aim

The main aim of this current research project was to produce a more sustainable and less expensive composite coating from nickel and copper matrices. This would be achieved by using a more sustainable naturally occurring source of filler particles. The properties of the composite coatings would then be characterise to assess the possible industrial applications.

1.4. Reference list

- [1] M.F. Ashby, K. Johnson, Materials and Design: The Art and Science of Material Selection in Product Design, Butterworth-Heinemann, 2013.
- [2] H. Holleck, Material selection for hard coatings, Journal of Vacuum Science & Technology A: Vacuum, Surfaces, and Films. 4 (1986) 2661-2669.
- [3] Senadheera. Jayakody, Basic Facts to Consider for Material Selection in Engineering, 2019 (2019).
- [4] SEAC Special interest group, Time for strategic change: UK Surface Engineering and Advanced Coatings Industry, A report by the SEAC Special interest group. (2014) 1-44.
- [5] AZoM, Nickel (Ni) - Properties, Applications, 2018 (2001).
- [6] J. Sudagar, J. Lian, W. Sha, Electroless nickel, alloy, composite and nano coatings—A critical review, Journal of Alloys and Compounds. 571 (2013) 183-204.
- [7] M. Antonijevic, M. Petrovic, Copper corrosion inhibitors. A review, International Journal of Electrochemical Science. 3 (2008) 1-28.
- [8] R. Dalton, G. Diaz, R. Price, A. Zunkel, The cuprex metal extraction process: recovering copper from sulfide ores, JOM. 43 (1991) 51-56.

[9] H. Chiba, T. Ogushi, H. Nakajima, T. Ikeda, Heat transfer capacity of lotus-type porous copper heat sink, JSME International Journal Series B Fluids and Thermal Engineering. 47 (2004) 516-521.

[10] D. Gay 1942-, D. Gay 1942- author, Composite Materials: Design and Applications, Third edition. ed, 2015.

[11] Grand view research, Composite Coatings Market Report Composite Coatings Market Analysis, Market Size, End-Use Industry Analysis, Regional Outlook, Competitive Strategies And Forecasts, 2016 To 2025, 2019 (2016).

[12] Y. Yang, R. Boom, B. Irion, D. van Heerden, P. Kuiper, H. de Wit, Recycling of composite materials, Chemical Engineering and Processing: Process Intensification. 51 (2012) 53-68.

2. Literature Review

2.1. Overview

This Chapter reviews literature from the past and present to address the serious issue of the sustainability of composite coatings, and to identify how this problem might be addressed. The Chapter is split into three sections:

- composite coatings: this section looks at the methods used to produce composite coatings, composite electrodeposits, and the use of spices as a potential sustainable filler particle.
- Electrodeposition of composites: this section briefly looks at the basics of electrodeposition, electrodepositing of nickel and copper, and the mechanisms of composite electrodeposition.
- The factors effecting electrocodeposits: this section looks at how current density, bath composition, agitation, and ultrasound can affect the characteristics of a composite coating.

2.2. Composite coatings

2.2.1. Methods of producing Composite Coatings

The production method is an important consideration when developing a composite coating, as the method of production can influence the grain structure and particle content of the composite, influencing the physical characteristics of the material. Due to the industrial and academic importance of composite coatings, several synthetic routes have been developed to produce them [1].

- Laser cladding (LC): LC of composite coatings was developed to incorporate hard reinforcing particles, examples of which are WC, TiC, and SiC [2-4]. A laser beam is used as a heat source to bond the metals and particles together. The laser melts the coating metal in the form of a powder or wire onto a substrate containing the required particles. Laser cladding gives good metallurgical bonds with minimal dilution of the particles, which is hard to achieve with other hard-facing techniques [1,5].
- Laser melt injection (LMI): In LMI the surface of the substrate is melted up to a depth of 1 mm, the solid particles are then delivered to the surface by inert gas [1]. Laser melt injection has several drawbacks; the particles are not sufficiently wetted by the melted alloy, which is required to push the particles into the surface [6]. The density difference between the particles and the matrix, and the chemical reactions at the surface of the particles can cause problems. However, this can be overcome if the particles are formed in situ during cooling [7].
- Brazing: Samples can be deformed by mechanical stresses due to rapid cooling of the melted areas and non-uniform temperatures when lasers are used (as in LC and LMI). Brazing heats the whole sample in a high vacuum or inert gas atmosphere. This reduces the mechanical stresses placed on the coating and avoids the problem of deformation [1].

- **Electrodeposition:** Electrodeposition or electro-co-deposition as it is often called, uses an electrochemical reaction to deposit a material onto an electrically conductive substrate. Particles are dispersed into an electrolyte and codeposited into the growing matrix. A wide variety of parameters can be adjusted, allowing the grain structure of the matrix and particle content to be fine-tuned. Electrodeposition is also easily scalable and relatively inexpensive when compared to other methods [1,8].

Laser cladding, laser melt injection and brazing all use high temperatures. High temperature and mechanical stresses can damage or destroy some particles. The low temperature, low cost and easy scalability of electrodeposition make it a more suitable technique for producing composite coatings containing naturally occurring filler particles.

2.2.2. Electrodeposited composite coatings

Composite electrodeposition can be traced back to the United States of America in the 1920's, where copper graphite coatings were developed for the automotive industry [9,10]. Electrodeposited composite coatings saw substantial development throughout the following years, and still receive a great deal of interest today. The properties of composite coatings depend strongly on the nature (type, size and composition) of the particles incorporated [11-14]. Table 2.1 shows some examples of filler particles used in electrodeposited coatings, and the effect these particles have on the properties of the material.

Table 2.1. List of filler particles and their effect of nickel and copper deposits.

Matrix	Filler particle	Particle size/ concentration	Particles effect on the deposit	ref
Ni	Titania	12 nm 33-200 g/l	The concentration of particles in the deposit increased with electrolyte concentration. Reduction in grain size. Increase the hardness and corrosion resistance.	[15]

Ni	SiC	300 nm 0.56-56.2 g/l 700 nm 0.28-57.1 g/l 5000 nm 1.04-104 g/l	Decreased the wear resistance Optimal properties were observed for deposits contained between 4-5 vol % of 300 and 700 nm particles.	[16]
Ni	TiO ₂	21 nm 20-100 g/l	Increasing TiO ₂ concentration increased the concentration of particles in the deposit. Change in grain structure.	[17]
Ni	hBN and WS ₂		lower coefficient of friction. No stick slip motion under lubrication conditions. Under non-lubrication conditions it prevented coating failure.	[18]
Ni	ZrO ₂	10-30 nm 10 g/l	Increased in wear resistance and hardness.	[19]
Cu	WC	3000-5000 nm 100 g/l	A smooth crystalline deposit. Increased hardness. Increase in wear resistance.	[20]
Cu	SiO ₂	30-40 nm 3.0 g/l	increased hardness. Reduction in electrical conductivity and the deposition rate.	[21]
Cu	Graphite	5000 nm 5-20 g/l	Change in preferential crystal orientation of the deposit. Increase in corrosion resistance.	[22]
Cu	CeO ₂	5-40 g/l 30-40 nm	Increased in tribological properties (friction, wear, and lubrication). Increase in hardness.	[23]

The literature has shown that different types of particles have different effects on different metal matrices (Table 2.1). The incorporation of carbon nanotubes into nanocrystalline nickel has been shown to increase the hardness from 572 HV to 645 HV,

and the tensile strength from 1162 to 1475 MPa. The reinforcing and lubrication effects of the carbon nanotubes enhances the wear resistance of the nano-crystalline nickel [24]. The incorporation of carbon nanotubes into a copper matrix has also been shown to reduce the coefficient of friction and lower the wear rate when compared to pure copper; however, this is due not only to the reinforcing and lubrication effect of the carbon nanotubes but also the formation of a carbonaceous film on the contact surface [25]. Graphene incorporated into nickel has been shown to increase the hardness from 265 HV to 510 HV, and reduce the corrosion rate from 10.45×10^{-3} mm/year to 4.26×10^{-3} mm/year [26]. Graphene incorporated into a copper matrix increases the elastic modulus and the hardness of the material to 255 HV (approximately double that of pure copper) without adversely affecting the electrical conductivity of the material [27].

The size of the particles incorporated into the matrix has also been shown to affect the properties of the composite. Microparticles of SiC incorporated into a copper matrix increases the hardness from 118 to 159 HV and reduces the weight loss due to abrasion by 88% compared to pure copper, when nanoparticles of SiC are incorporated the hardness increases from 118 to 190 HV, however, the weight loss due to abrasion is only reduced by 58% [28]. Microparticles of SiC incorporated into a nickel matrix reduces the coefficient of friction when compared to pure nickel, the coefficient of friction is further reduced if the microparticles are replaced with nanoparticles [29]. The greater enhancement seen in some properties when nanoparticles are incorporated could be due to several factors:

- Nanoparticles have greater surface area than the equivalent mass of microparticles. The greater surface area of the nanoparticle would offer greater reinforcement of the matrix and disruption to grain growth (resulting in a smaller grain size).
- The smaller size of the nanoparticle could result in a greater number of particles being incorporated into the matrix. This would offer greater reinforcement and grain growth disruption. However, this is difficult to assess as most studies evaluate the mass of particles in the matrix not the number (which could be quite different).

The concentration of particles used in the electrolyte when producing a composite can also impact the properties of the material. The literature has shown that incorporating

CeO₂ particles into a nickel deposit by electrodeposition increases the hardness and wear resistance of the coating; however, the extent of this increase depends on the concentration of CeO₂ used in the electrolyte. The hardness of the nickel coating can be increased from 283 HV to approximately 400 HV, and the wear height loss decreased from 42 µm to approximately 25 µm when 10.0 g/l of CeO₂ is added to the electrolyte; whereas, if 30.0 g/l is added to the electrolyte, the hardness can be increased to approximately 446 HV, and the wear height loss decreased to approximately 18 µm [30]. The incorporation of graphene into a nickel matrix by electrodeposition increases the hardness and wear resistance of the deposit. Again, the extent of this increase depends on the concentration of graphene used in the electrolyte. The hardness of the nickel deposit can be increased from 428 HV to 493 HV, and the wear rate decreased from 10.17x10⁻⁴ mm³/Nm to 8.56x10⁻⁴ mm³/Nm by increasing the graphene concentration from 100 mg/L to 500 mg/L [31]. Although the particle content of the deposits was not analysed in these studies it is a major consideration, as increasing the particle content of the deposit can increase the reinforcing effect and grain growth disruption. Increasing the concentration of the particles in the electrolyte generally results in an increase in the particle content of the composite. This increases the hardness and wear resistance of the deposit; whereas, increasing the electrolyte particle concentration too high can result in a reduction in the particle content in the deposit reducing hardness and wear resistance. In some cases this has been attributed to an increase in particle agglomeration in the electrolyte [16,17,23,32,33].

The reinforcing, hardness and lubrication properties of the particles in the composite is not the only factor leading to the enhancement of the properties of the composite; it is also the modifying effects the particles have on the grain structure of the matrix. Research has shown that incorporating particles into a matrix can both change the preferred crystal orientation and grain size [34-38]. When graphite was incorporated into a copper deposit, it was shown to change the preferred crystal orientation from [200] to [220] and reduce the grain size from 134 nm to 61 nm [22].

All crystals are anisotropic due to the difference in overlap between atomic orbitals of atoms in different orientation plains (Figure 2.2.). Differences in orbital overlap lead to differences in bond strength, and different properties [39-45].

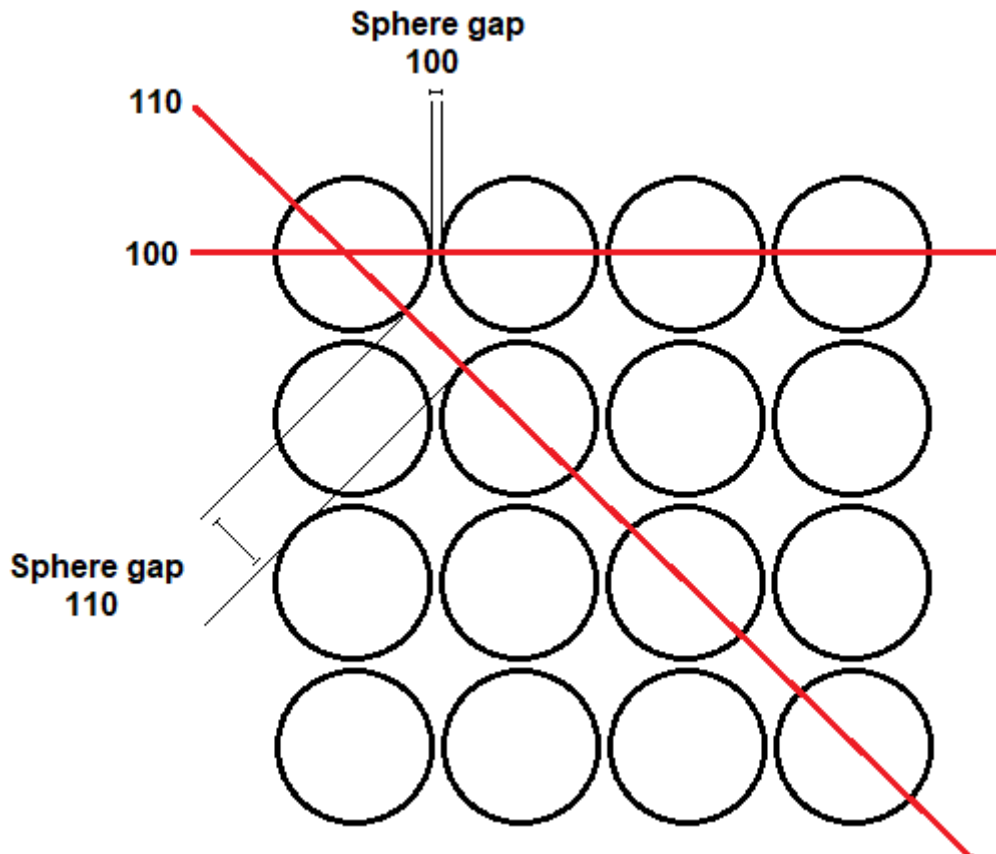


Figure 2.2. Diagram of a metallic cubic crystal lattice. The gap between spheres (representing metallic atoms) in the 100-crystal orientation plain is significantly smaller than that of the gap between spheres in the 110-crystal orientation plain.

As the grain size in a metal is reduced the number of grain boundaries is increased (Figure 2.3.). When sufficient force is applied to a metal, dislocations are forced to pile up at grain boundaries, either because a barrier to crossing over exists, or a source must be activated in the next grain boundary. A specific concentration for a given grain is required to initiate slip into its neighbouring grain boundary. This concentration is most likely achieved through a dislocation build-up. Stress is higher as the number of dislocations increases; the more substantial the grain size the quicker the stress is reached. However, this is only true at low temperatures where creep due to plastic deformation is irrelevant, and below a certain grain size, simulations have shown a reverse Hall–Petch effect, where a reduction in grain size leads to a softening of the material [46-48].

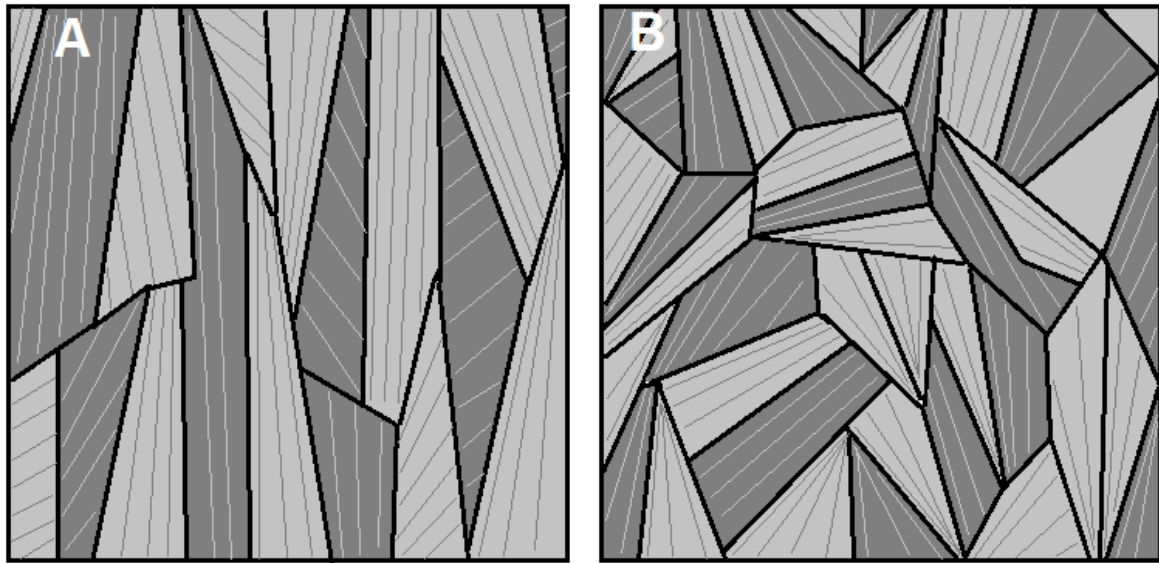


Figure 2.3. Diagram showing the increase in the number of grain boundary with decreasing grain size. (A) Metal with larger grains and fewer grain boundaries (represented by black lines). (B) Metal with smaller grains and more grain boundaries.

2.2.3. Spices

Herbs and spices have been used throughout history, as aides to flavour, as preservatives, as medicines and even as currency [49]. Documents have suggested that hunter gatherers may have wrapped meat in bush leaves, accidentally discovering it enhanced the flavour. Over the centuries medical uses were discovered for spices and herbs. According to myth, Shen Nung wrote “The Classic Herbal” around 2700 BCE, which contains details of hundreds of medicinal plants and spices [50]. Egyptian papyri from 1555 BCE classify fennel, cumin, coriander, juniper, thyme and garlic as health promoting spices [50]. Every major civilization from ancient China and Mesopotamia to Greece and Rome has used spices and herbs for medical purposes [50]. Spices have also been used for financial transactions; ancient Greeks held black pepper in such high regard it could be used to paid taxes and ransoms [51].

In recent years a great deal of interest in the antibacterial nature of spices has been shown. Studies have found that even when *V. parahaemolyticus* (a type of bacteria found in some seafood) is incubated in ideal growth conditions (nutrient rich medium at 30 °C) basil, cloves, garlic, horseradish, marjoram, oregano, rosemary, and thyme inhibited the bacteria’s growth [52]. Additional studies have also shown that carom

seed, ginger, Japanese pepper, sage, spearmint, and turmeric have a strong inhibitory effect on *V. parahaemolyticus* [53,54]. Basil, cloves, and marjoram have also been shown to inhibit the growth of other bacteria, such as *E. Coli* and other Gram-negative bacteria [53-55].

Despite the many uses of spices and herbs throughout the centuries and their many unique properties, research into the use of spices and herbs as filler particles in composite materials has not yet been conducted. Natural spices and herbs are inexpensive, do not require energy intensive production methods to produce and have relatively low toxicity [56-58]. The use of spices and herbs as filler particles may be a route to producing less expensive and more sustainable composite coatings.

2.3. Electrodeposition of composites

2.3.1. Basics of electrodeposition

IUPAC defines electrodeposition (sometimes referred to as electroplating or just plating) as the deposition of dissolved or suspended material by an electric field onto an electrode [59]. When electrodepositing a metal onto a cathode (an electrically conductive substrate which is given a negative charge), the cathode and an anode (given a positive charge) are immersed into an electrolyte containing a salt of the desired deposition metal. Positively charged metal ions are attracted to the negatively charged cathode, where they are reduced and deposited onto the cathode. If a soluble anode is used, the metal ions from the electrolyte can be replenished as the metal anode is oxidised. By this method, coatings of the desired metal can be produced onto the substrate (Figure 2.4.) [60-62]. The coatings can be enhanced by varying the microstructure of the deposit which can be achieved by changing certain parameters, including pH, ion concentration, bath temperature, and current density [63-70]. Additives such as brighteners and surfactants can change the microstructure of the deposit enhancing the coatings properties [71-79]. However, varying these parameters can impart unwanted side effects onto the coating, such as intrinsic stress which can lead to microcracks [80,81].

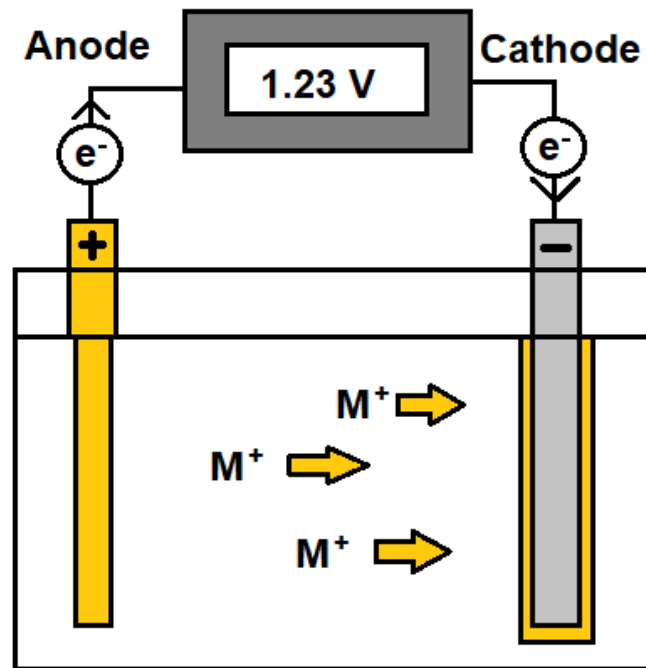


Figure 2.4. Diagram of a basic electrolytic cell with a soluble anode. Oxidation of the metals occurs at the anode, reduction of the metals ions occurs at the cathode. The anode is eroded in this process as a coating of the metal is produced over the cathode.

2.3.2. Electrodeposition of nickel and copper

2.3.2.1. Nickel

Watts nickel and nickel sulphamate are the two most commonly used nickel electrodeposition baths; however, the nickel Watts bath is the most widely used for industrial applications.

The nickel Watts bath was developed by Oliver Patterson Watts in 1915 and consisted of 240 g/L of nickel sulphate, 20 g/L of nickel chloride and 20 g/L of boric acid with an electrodeposition temperature of 70 °C [82,83]. Depending on the application, the concentration of the components in the bath can be varied. A typical nickel Watts electrolyte will have a nickel sulphate concentration of between 150 and 400 g/L, nickel chloride between 20 and 80 g/L and boric acid between 15 and 50 g/L, with an electrodeposition temperature of between 45 and 65 °C and pH of between 2 and 4.5 [84,85]. However, modified nickel Watts baths do exist for low nickel ion concentration

electrolytes [26,36,86]. Nickel sulphate is the primary source of Ni^{2+} in the Watts bath, nickel chloride provides a source of Cl^- to assist in the anode dissolving, and boric acid is used as a buffer to maintain pH [84]. Varying the parameters of the bath to reduce grain size can often lead to an increase in internal stress (which can be overcome by incorporating inert particles into the matrix to form a composite) [87-89].

Nickel sulphamate baths (where nickel sulphamate is used as a substitute for nickel sulphate) have been used in industries since 1949 and produce deposits that have different properties to those produced from a Watts bath. Nickel produced from a sulphamate bath is more ductile with lower internal stresses than that produced from a Watts bath [90,91]. Nickel sulphamate baths typically have nickel sulphamate concentrations of between 300 and 450 g/L, nickel chloride of between 0 and 30 g/L, and 30 g/L of boric acid, with an operating temperature of between 40 and 60 °C and a pH of between 3.5 and 4.5 [92].

2.3.2.2. Copper

Copper cyanide, non-cyanide alkaline copper, and acid copper are the three most commonly used copper electrolytes.

Copper cyanide baths have been one of the most widely used industrial electrolytes over the last century and produce high-quality deposits [93]. The temperature varies with solution composition but typically lies between 54 and 82 °C, the higher the temperature the higher the permissible current density and cathode efficiency (within this range) [94]. pH is rarely measured but is near 14 in high efficiency electrolytes. Copper-cyanide concentrations range between 15 and 75 g/L, sodium cyanide between 28 and 100 g/L. The efficiency of the electrolytes can be further increased by adding potassium-cyanide, which increases the stability of the solution and helps the anode dissolve. Copper-cyanide is insoluble in water, however the presence of cyanide alkaline such as sodium-cyanide or potassium-cyanide forms a copper complex ion ($\text{Cu}(\text{CN})_3^{2-}$), which then disassociates into copper ions (Cu^+). Although potassium-cyanide solutions are more efficient sodium cyanide is more commonly used due to the cost of potassium cyanide [95]. However, cyanide is extremely

hazardous to both worker health and the environment due to high toxicity, requiring the development of less hazardous alternatives.

Non-cyanide alkaline copper baths have found increasing interest since the mid-1980s due to the environmental issue of cyanide baths [96]. In typical non-cyanide alkaline copper, the copper ions (Cu^{2+}) are provided from a metal salt such as copper chloride, and complexing agents such as fluoborate, pyrophosphate, EDTA, citrate, ammonia, ethylenediamine, glycerol, and tartrate replace the cyanide ions [93,97,98]. However, disadvantages do exist, such as a high operating cost, greater sensitivity to impurities and difficulty to control chemically [96].

The composition of an acid copper electrolyte can vary greatly depending on the application. A typical copper acid bath contains copper sulphate of between 5 and 240 g/L, between 0 and 60 mg/L of chloride ions (often from HCl) and has an operating pH of between 0.5 and 3. Copper sulphate is used as the source of Cu^{2+} . The reduction of Cu^{2+} to $\text{Cu}_{(s)}$ takes place via a 2-step mechanism.



The presence of Cl^- stabilise Cu^+ and speeds up step 1 however, the presence of too much Cl^- can make Cu^+ too stable and slow down step 2 [99]. Sulphuric acid is added to change the pH of the electrolyte and help the dissociation of CuSO_4 to Cu^{2+} increasing the conductivity of the solution [21,100-106].

2.3.3. Mechanism of composite electrodeposition

Composite electrodeposition can be traced back to the late 1920s and saw substantial development throughout the 1960s and 1970s [10]. Many models have been developed to account for the mechanism of the co-deposition of inert particles into a metal matrix [107-113].

A two-step model was proposed in 1972; it stated that particles approach the cathode surface (after the formation of an ionic cloud around them) and become loosely adsorbed, the ionic cloud is lost, and the particles are then strongly adsorbed [10,108]. Not all particles that reach the cathode will be absorbed, and for those that are a certain residential time is required [10,114]. This model allowed the quantitative analysis of the effect of current density and bath particle concentration on the particle incorporation rate, however, excludes hydrodynamic effects and particle characteristics [108,115]. To correct for the adsorption and hydrodynamics effects a third order polynomial equation can be included. This correction may only be valid within a narrow range of experimental conditions (2.3.) [116]:

$$\alpha = \frac{nFdV_o}{MJ_o^{B/A}} \cdot \frac{C}{\left(\frac{1}{k} + C\right)} \cdot J_c^{\left(\frac{B}{A}-1\right)} \cdot h \cdot f(\omega, C) \quad (2.3.)$$

where α volume of particles suspending in the deposit, n is the valence of the deposited metal, F is Faraday's constant, d is the density of the electrodeposited metal, V_o is the constant for particle deposition, M is the molecular weight of the deposited metal, J_o is the exchange current density, B is the constant in the Tafel equation for particle deposition, A is the constant in the Tafel equation for metal deposition, C is the volume percentage of particles in suspension in the electrolyte, k is the coefficient of adsorption, J_c is the current density, h is a constant, $f(\omega, C)$ is a function that can be determined by experimental curves [117].

In 1987 a five-step model was developed that incorporated some of the features of previous models Figure 2.5. [110].

- Formation of an ionic cloud around the particle, caused by ion absorption.
- Transport of particle by convection and diffusion to the cathode (Figure 2.6.).
- Weak absorption of the particle with its ionic cloud onto the cathode.
- The loss of the ionic cloud and strong absorption of the particle onto the cathode.
- The entrapment of the particle into the growing metal matrix.

The model requires empirical factors that are system specific and require experimental analysis to determine [10].

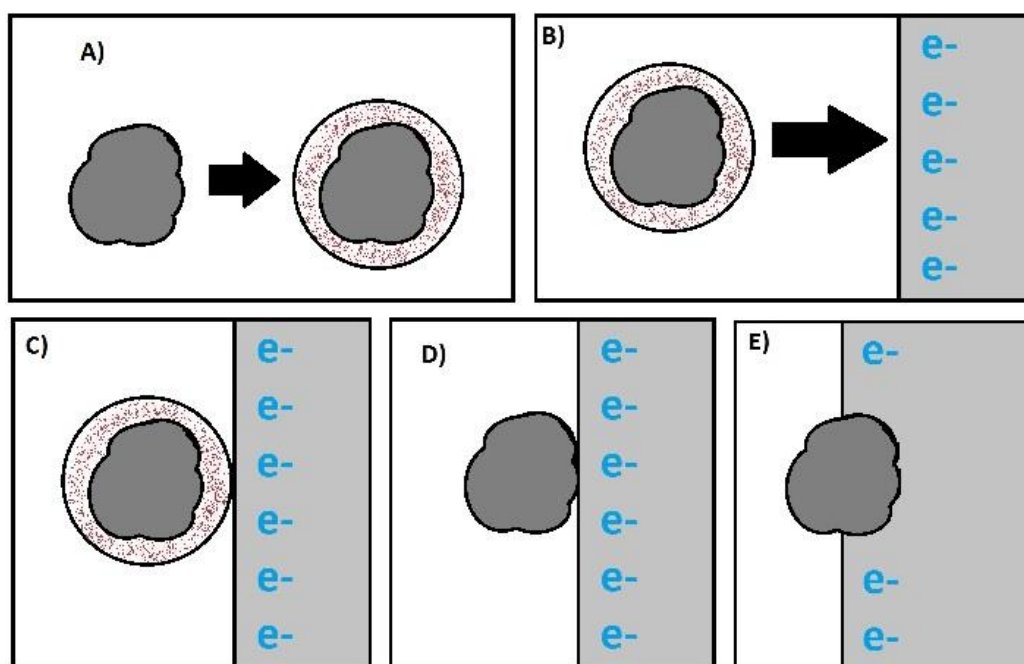


Figure 2.5. Diagram of the five-step model. (A) An ionic cloud is formed around the particle. (B) The particle migrates towards the cathode. (C) The particle is weakly absorbed. (D) The ionic cloud is lost, and the particle is strongly absorbed. (E) The particle is entrapped in the growing metal matrix.

In 1992 a model based on trajectory analysis using the deposition of spherical particles on to a rotating cylinder electrode was developed. The trajectory of the particle can be determined using a motion equation (taking all forces acting on the particle into account). Assuming the particle attachment is proportional, the co-deposition rate can be determined [10,111,118]. Also in 1992, it was shown that a model accounting for diffusion and gravitational forces could describe the kinetics of a nano-size particle incorporated into a metal deposit [10,113,118].

In 1993 it was suggested that the reduction of metal ions has three current densities (although experimental validation never took place) [10,112,118].

- At low current densities only proton reduction takes place.

- At intermediate current densities proton reduction reaches its rate limiting value and metal ion reduction starts.
- At high current densities protons and metal ions reach their rate limiting value.

Cathode

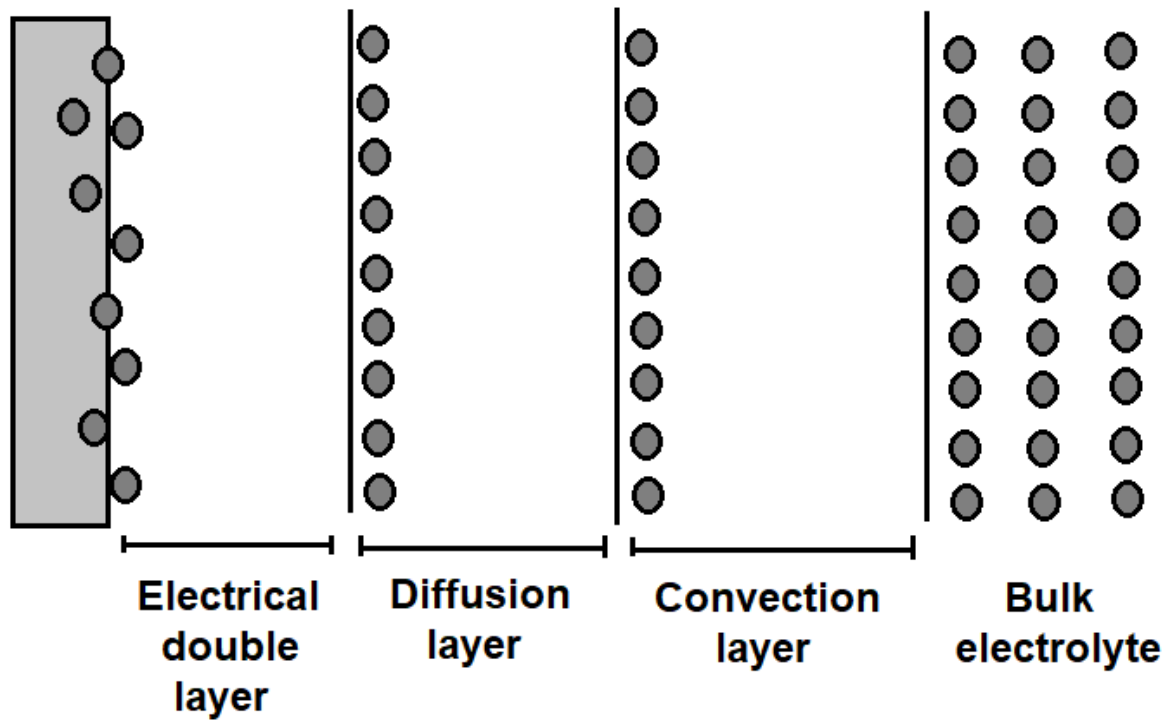


Figure 2.6. Diagram of particle migration through the electrolyte.

For a complete understanding of the co-deposition of particles into a metal matrix much more work is still needed, and an agreement between the theoretical and experimental findings [10]. The literature has shown that the size of the particle in the electrolyte can have an impact on the particle content of the coating [30,31]. However, in the models proposed no account is taken of the particle size only its volume in the electrolyte. The literature has also shown that deposits produced from pulse current and pulse reverse current have increased particle content compared to their direct current counterparts, the models proposed take no account of the current type just current density [8,119-121].

2.4. Factors affecting the electrocodeposition

2.4.1. Current density

Many parameters can affect the process and properties of an electrodeposited composite, bath composition, additives, particles, electrodes, agitation, and current density; of these current density is one of the most studied [10,118]. Current density is defined as the amount of current (measured in amperes) over a specific cross-sectional unit area (measured in cm^2) [119].

When depositing metals, generally an optimal range of current density exists well within the normal operating parameters, which is often chosen when incorporating particles into that metal matrix [10]. Many studies have shown a small increase in current density leads to an increase in particle incorporation. However, the behaviour is system dependent, and a few studies have shown an increase in current density decreases or has little effect on particle incorporation [118,122-128].

The particles in the electrolyte can affect current density. A study showed when producing Ag- Al_2O_3 coatings, adding Al_2O_3 to the electrolyte at low overpotentials reduced the current density, while at high overpotentials adding particles increased it. The authors suggested at low overpotentials the particles adsorbed onto the cathode, suppressing silver deposition, while at high overpotentials, the particles reduced the thickness of the diffusion layer [118,129].

Current density can affect the smoothness of a composite coating. A study showed when depositing alumina particles into a nickel matrix; a smooth coating was produced at current densities lower than 1 A/dm^{-2} ; over 1 A/dm^{-2} the coating became rough, and progressively more so with increasing current density. This was attributed to the incorporation of alumina particles into the matrix, the alumina particles electrical insulating properties prevented nickel from depositing directly over the top, as such the nickel deposited around the particles. At high current densities the nickel ions deposit faster than they can be diffused across the surface of the deposit, resulting in a rougher coating Figure 2.7. [130].

The maximum current that can flow through the electrolyte is limited by the mass transfer of ions between electrodes. This maximum current is known as the limiting current. As current is applied to the electrolyte ions flow from the anode to the cathode, the applied current can be increased until the ion flow between the electrodes is at a maximum. Any increase in applied current after this will result in the discharge of extraneous ions (hydrogen). [131]. However, the limiting current can be increased by increasing the mass transfer in the system (by increasing electrolyte temperature, agitation and ion concentration).

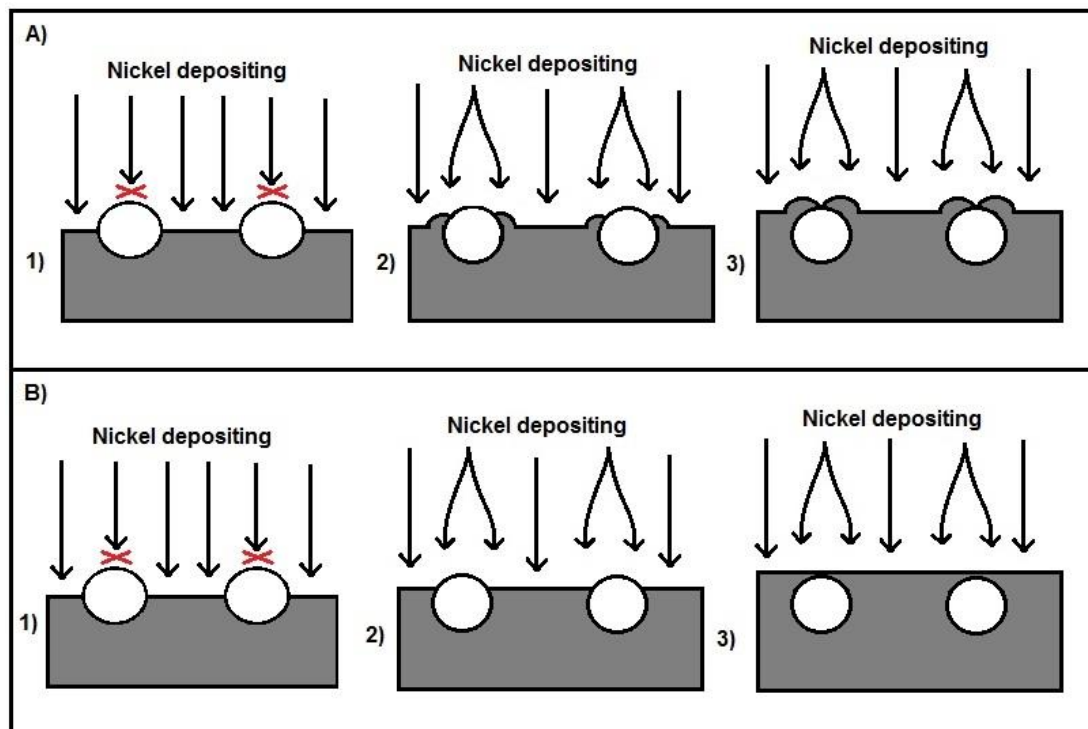


Figure 2.7. Diagram of nickel depositing around alumina particles. (A) Deposition of nickel at current densities over 1 A/dm^2 . (1) Nickel cannot deposit directly over alumina particles. (2) Nickel deposits to the edges of alumina particles. (3) Nickel deposits faster than it can diffuse across the surface of the coating. (B) Deposition of nickel at current densities of 1 A/dm^2 or lower. (1) Nickel cannot deposit directly over alumina particles. (2) Nickel deposits to the edges of alumina particles. (3) Nickel diffuses across the surface of the coating as fast or faster than it is deposited.

More recent studies have focused on pulse current. Pulsed current utilizes a series of pulses of certain amplitude for a specified duration. Each pulse consists of an on time

(current applied) and off time (no current applied). Pulse current has two key advantages over direct current.

- High current density areas of the electrolyte become depleted of ions compared to low current density areas when using direct current. The off time during pulse plating allows the replenishment of depleted areas.
- The formation of a charged double layer on the cathode during electrodeposition obstructs ions from reaching the cathode at certain points. An off time allows the layer to partially discharge the double layer.

Pulsed electrodeposition has three parameters on time T_{on} , off time T_{off} and peak current density I_p . The duty cycle γ is the percentage of the total time of a cycle [132].

$$\gamma = \frac{T_{on}}{T_{on} + T_{off}} = T_{on} f \quad (2.4.)$$

$$f = \frac{1}{T_{on} + T_{off}} = \frac{1}{T} \quad (2.5.)$$

Pulsed current composite electrodeposits have been shown to have increased hardness, increased particle content and more uniform particle distribution when compared to the same metal electrodeposited by direct current. This is due to the off time allowing more particles to reach the double layer, and therefore a more homogeneous distribution of particles in front of the cathode is achieved. This results in a greater and more uniform particle distribution in the deposit, increasing its physical properties such as hardness. Adjusting the on and off time by changing parameter such as duty cycle and pulse frequency allows the microstructure of the deposit to be fine-tuned [118,120,133,134].

Pulsed reverse current is similar to pulsed current; however, a stripping time is introduced where the polarity of the cathode an anode is reversed [132]. Like pulsed current pulsed reverse current replenishes the diffusion layer, however, whilst pulsed current only does so during the off time, pulsed reverse current does so continuously (as ions and particles are continuously moved to and from the electrodes). The

uniformity and smoothness of the coating is improved; this is caused by the selective dissolving of protrusions from the surface of the deposit, achieved by the stripping time. The reverse pulsed also allows negatively charged particles to be incorporated into the deposit [132]. However, some disadvantages to pulsed and pulsed reverse current do exist. The cost of pulse plating rectifiers are much greater than direct current units and the additional parameters require additional considerations [132].

2.4.2. Electrolyte composition

The solvent used to prepare the electrolyte is a major factor affecting the electrodeposition process [10]. Three main types of solvents are used in electrodeposition: aqueous, ionic liquid (IL) and deep eutectic solvent (DES). Aqueous electrolytes are the simplest and most commonly used, they consist of a salt dissolved in water. Aqueous electrolytes are relatively inexpensive and are employed for a wide variety of deposits. However, conventional aqueous electrolytes are not always suitable. They cannot be used to deposit metals with very negative redox potentials due to their narrow electrochemical windows and have a low range of operating temperatures [4].

An IL is defined as a salt composed of anions and cations in its liquid state below 100°C. They typically consist of a large organic cation with an inorganic or organic anion. The cations and anions in IL's do not form a well-organised lattice resulting in a low melting temperature. Their physiochemical properties are highly tuneable, due to the large variety of cations and anions that can be combined. IL's possess unusual properties, a wide electrochemical stability window, high thermal stability, and low vapour pressure. Many studies have shown the ability to obtain a uniform deposit using IL electrolytes. IL's can be expensive, therefore aqueous solvents are preferable when the conditions allow [121,135-137].

Deep eutectic solvents (DES) are similar to ILs (similar conductivities, polarities, viscosities, densities, surface tensions, refractive indexes and chemical inertness). Some of their constituents have no charge, and they are usually formed from a quaternary ammonium salt with hydrogen bond donors. Many DES's are inexpensive (when compared to IL's) non-toxic non-flammable and biodegradable [138].

The electrolyte pH can play a fundamental role in determining the structure and properties of an electrodeposit [74,139]. The literature has shown when depositing SiC particles into a nickel matrix, a coating particle content of approximately 16.2 % wt was achieved at a pH of 3.5. Whereas, at pH 4.0 there was a significant increase in particle content to approximately 21.2 % wt [140]. Also, when depositing alumina particles into a nickel matrix, it has been shown that a particle content of 4 % wt can be achieved by using an alkaline bath, and only 1.5 % wt is achieved when using an acidic bath [141]. Additives (complexing agents, surfactants and brighteners) have a significant effect on the microstructure, and properties of an electrodeposit. When depositing Al_2O_3 particles into a nickel matrix the addition of the surfactant hexadecylpyridinium bromide (HPB) was found to increase the particle content of the coating and promoted the uniform distribution of particles throughout the deposit. This increase in the particle content increased the wear resistance of the composite [142]. The structure of a surfactant allows greater spatial separation between the particles, this can help prevent the agglomeration of particles and improve both the amount and the distribution of the particles in the coating [143]. The charge on a surfactant can also improve the incorporation of particles in the deposit. When incorporating Si_3N_4 into a copper matrix adding just 0.01g/L of dodecyl sodium sulphate (an anionic surfactant) to the electrolyte increases the particle incorporation from around 0.6% of the coating by weight to around 3.0% [144].

Some surfactants can also act as brightening agents. A brightening additive's main function is to increase the levelling capabilities of the electrolyte, and thus the brightness of the deposit. Brightening additives can be commonly referred to as carriers, brighteners and wetting agents. Carriers interfere with the nucleation and growth of newly forming deposits, refining the grain structure and producing a brighter finish. However, for coatings that require a mirror bright finish, brighteners are required. Brighteners increase the electrolyte's levelling ability by inducing preferential deposition at scratches and defects. Some brighteners achieve this by being attracted to the cathode at points of high electropotential, temporarily packing the area stopping further deposits. As the deposit levels, the high potential points disappear, and the brightener migrates away [8]. Wetting agents are tensioactive, depositing on the surface of the growing coating reducing surface tension and facilitating the detachment of gas bubbles (such as $\text{H}_{2(\text{g})}$). However, the use of additives is not without drawbacks,

they can introduce carbonaceous materials or sulfur into the electrodeposit. Sulfur acts as a solid solution strengthener and causes intergranular embrittlement [87,145].

2.4.3. Agitation

Agitation is an important part of the composite electrodeposition process, and in the absence of surfactants even more so; it assists transport and dispersion of particles in the electrolyte [8,146]. The most common forms of agitation are mechanical stirring bar, parallel plate channel flow, overhead stirrer, reciprocating plate plunger, cathode movement, eductors, bubblers/ air pumps and pumped recycle loop of the electrolyte. Rotating disc and rotating cylinder electrodes also exist, although these are most commonly used in analytical electrochemistry (Figure 2.8.) [8].

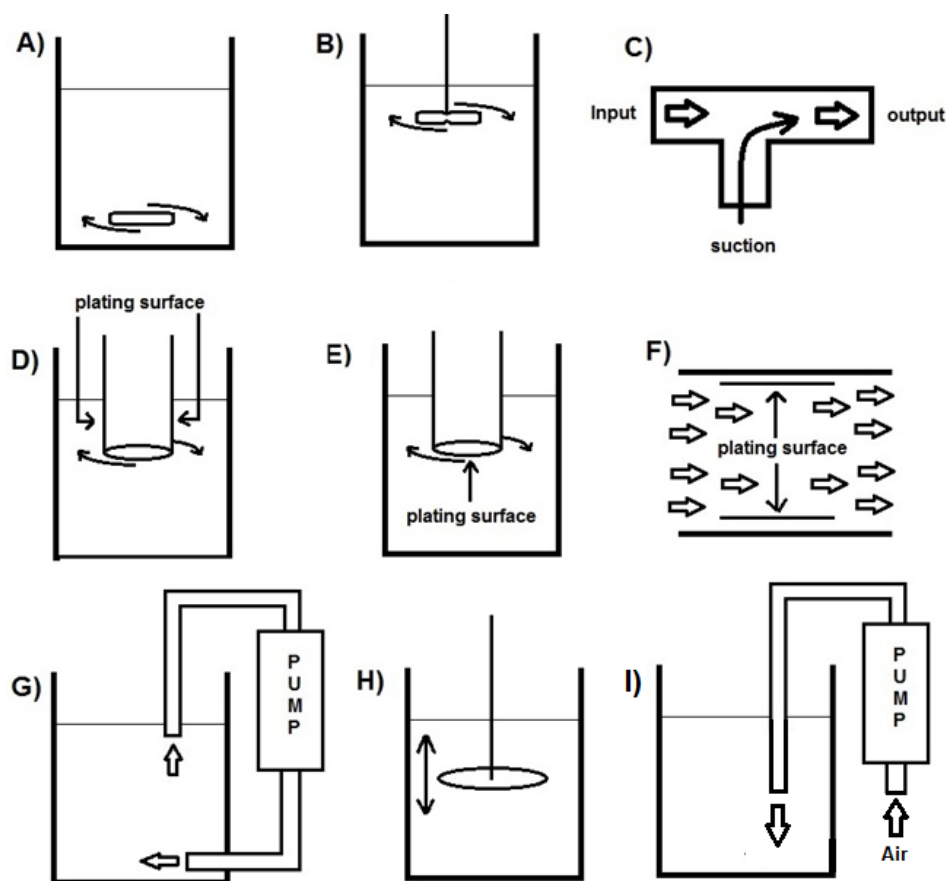


Figure 2.8. Diagram of agitation methods. (A) mechanical stirring bar. (B) overhead stirrer. (C) eductor. (D) rotating cylinder electrode. (E) rotating disc electrode. (F) parallel plate channel flow. (G) pumped recycle loop of the electrolyte. (H) reciprocating plate plunger. (I) Air bubbler/pump.

The application of different agitation methods to an electrolyte can bring about three different flow regimes (Figure 2.9.). Rotating disc electrodes have smooth laminar flow at commonly used rotation speeds whilst rotating cylinder electrodes and mechanical stirring bars have severe turbulence even at low speeds [8,60,115].

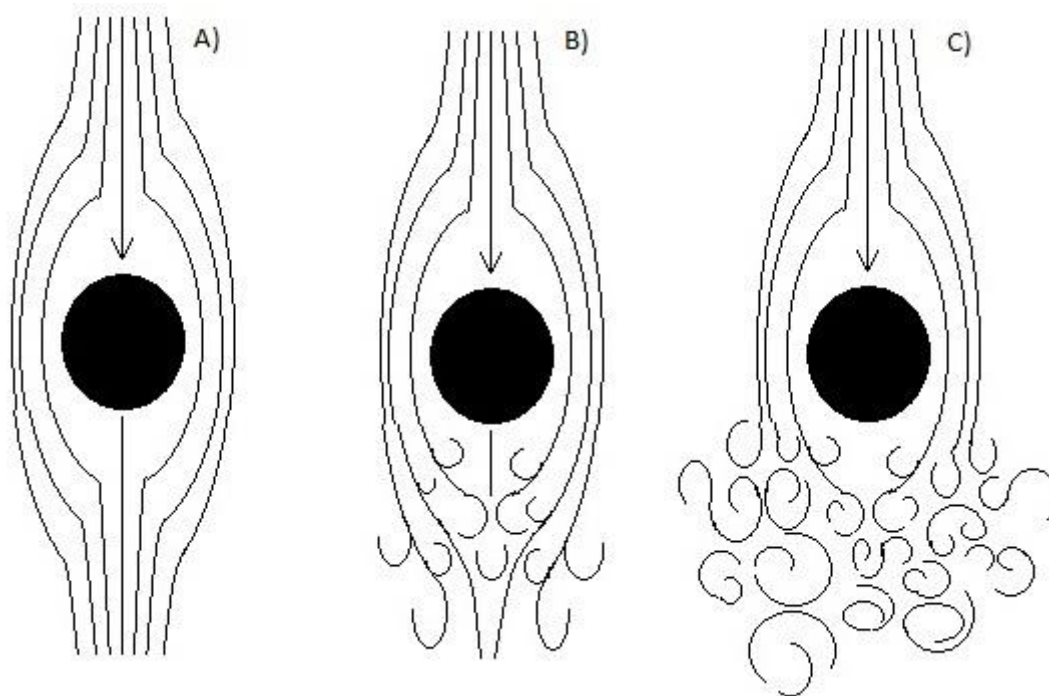


Figure 2.9. Diagram of three types of flow around a generic rod electrode. A) Laminar flow. B) Transitional flow (between laminar and turbulent). C) Turbulent flow.

When depositing micro-sized particles; the particle content of the deposit tends to decrease with increasing flow rate in turbulent flow regions, increase with increasing flow rate in transitional flow regions, and in laminar flow regions no significant change from increasing flow rate is seen [8].

2.4.3.1. Ultrasound

Ultrasound as also proven to be an efficient method of particle dispersion and deagglomeration [147].

The application of ultrasound to a liquid medium (such as an aqueous electrolyte) can cause acoustic cavitation, cavitation fields, micro-jetting (acoustic streaming, and high-

speed particle collisions), which break the weak van der Waals forces dispersing and deagglomerating the particles [147,148]. An ultrasonic wave is propagated through a liquid medium by a series of compression and rarefaction cycles. During the rarefaction cycle (if power is sufficient) the expansion force caused by the ultrasound, will exceed that of the intermolecular forces between the molecules in the liquid, and a cavity is formed. As the cavity grows it becomes unstable and collapses, creating a hotspot where temperatures of around 5000 K and pressures around 1000 atm can be reached [147]. Mass transfer between the electrodes is improved by the many cavitation phenomena (acoustic streaming, micro-jetting and shock waves) of high power ultrasound [147,149,150]. Ultrasound has been shown to increase the hardness, wear resistance, fatigue strength, corrosion resistance, and reduce the surface roughness of the electrodeposit [151-158]. Ultrasound enhances the hardness and tribological properties of composite coatings by refining the grain size and incorporating finer more dispersed particles into the deposit (without the need for additives), providing a hindrance to dislocation movement which can increase wear resistance [159-161].

The effects of ultrasound both before and during electrodeposition also has many benefits for composite electrodeposition, not only enhancing dispersion and deagglomeration of the particles but also to improve the incorporation of finely and uniformly distributed particles into the deposit [147]. When incorporating TiO₂ particles into a zinc matrix, it has been demonstrated that a higher particle content can be achieved when applying ultrasound from a 38 kHz bath at a power 53 mW/cm³ during electrodeposition compared to silent conditions, however, drawbacks do exist [162]. For example, ultrasound can cause random bubble structures on the surface of the substrate when used during electrodeposition leading to fringe patterning and pitting [163].

Other important factors are frequency and power; lower frequency ultrasound (when compared to higher frequencies) has been shown to give a higher and better dispersed particle content [164,165]. Mechanical effects are more dominant at lower frequencies and chemical effects at higher frequencies. Generally speaking, the formation and intensity of cavitation phenomena progressively increase as frequency decreases [166,167]. Increasing power (at both high and low frequency) generally increases

particle content until a maximum is reached, at which point any further increase reduces or has no effect on particle content [160,168,169].

The ultrasonic systems used to apply ultrasound to the electrolyte, are an important consideration.

- Ultrasonic horns are generally low frequency achieving huge ultrasonic cavitation due to the large vibrational amplitude produced at the emitter surface (which is directly in contact with the liquid). Most of the cavitation phenomena occur near the surface of the emitter, in a cone shaped cloud. The violent cavitation phenomena that can be achieved with horns, can reduce particle content, due to the force of the particles colliding with the surface of the electrode causing particles to break away [160,170-174].

Ultrasonic baths which generally operate at 40 kHz achieve lower vibrational amplitude by transducers that are not directly in contact with the electrolyte, the sound travels through the liquid in the bath and the vessel walls of the container holding the electrolyte, resulting in less efficient transmission. The position of the beaker in the bath also affects the intensity of the ultrasound. However, ultrasonic baths are lower cost with more evenly distributed cavitation phenomena throughout the walls and the electrolyte [163].

2.5. Conclusions

- Many methods of producing composite coatings have been developed, Laser cladding, laser melt injection, brazing, and electrodeposition. Laser cladding, laser melt injection and brazing all require high temperature which could destroy spice particles.
- Electrodeposition is a convenient method to produce composite coatings. Many parameters including current density, agitation, and additives can be adjusted to fine tune the properties of the coating; it is relatively inexpensive and easy to scale up.
- Spices have been used for centuries for medicines, aides to flavour, and even currency; however, no research into their properties as filler particles have been

conducted. Spices are inexpensive to produce and have low toxicity. Composite coatings containing spices as filler particles may offer a more sustainable alternative to the more common filler particles used.

- Many factors can influence the properties of an electrodeposited composite coating including, current density, bath agitation, type size and concentration of particle.

2.6. Reference list

[1] P. Baumli, A. Al-Azzawi, Methods of composite coating: a review, *Materials Science & Engineering*. 40 (2015) 26-32.

[2] Y.T. Pei, J.H. Ouyang, T.C. Lei, Y. Zhou, Microstructure of laser- clad SiC-(Ni alloy) composite coating, *Materials Science & Engineering A*. 194 (1995) 219-224.

[3] Y.T. Pei, T.C. Zuo, Gradient microstructure in laser clad TiC- reinforced Ni- alloy composite coating, *Materials Science & Engineering A*. 241 (1998) 259-263.

[4] F. Liu, Y. Deng, X. Han, W. Hu, C. Zhong, Electrodeposition of metals and alloys from ionic liquids, *Journal of Alloys and Compounds*. 654 (2016) 163-170.

[5] Q. Ming, L.C. Lim, Z.D. Chen, Laser cladding of nickel- based hardfacing alloys, *Surface and Coatings Technology*. 106 (1998) 174-182.

[6] G. Kaptay, Interfacial Phenomena during Melt Processing of Ceramic Particle-Reinforced Metal Matrix Composites. Part I. Introduction (incorporation) of solid particles into melts, *Materials Science Forum*. 215-216 (1996) 459-466.

[7] O. Verezub, Z. Kálazi, G. Buza, N.V. Verezub, G. Kaptay, In- situ synthesis of a carbide reinforced steel matrix surface nanocomposite by laser melt injection technology and subsequent heat treatment, *Surface and Coatings Technology*. 203 (2009) 3049-3057.

[8] F. C. Walsh, C. Ponce de Leon., A review of the electrodeposition of metal matrix composite coatings by inclusion of particles in a metal layer: an established and diversifying technology, *Transactions of the Institute of Metal Finishing*. 92 (2014) 83-98.

[9] J-P. Celis, J. R. Roos, C. Buelens, A Mathematical Model for the Electrolytic Codeposition of Particles with a Metallic Matrix, *Journal of the Electrochemical Society*. 134 (1987) 1402-1408.

[10] F.C. Walsh, C.T.J. Low, A review of developments in the electrodeposition of tin, *Surface and Coatings Technology*. 288 (2016) 79-94.

- [11] X. Chen, F. Cheng, S. Li, L.P. Zhou, D. Li, Electrodeposited nickel composites containing carbon nanotubes, *Surface and Coatings Technology*. 155 (2002) 274-278.
- [12] L. Shi, C. Sun, P. Gao, F. Zhou, W. Liu, Electrodeposition and characterization of Ni–Co–carbon nanotubes composite coatings, *Surface and Coatings Technology*. 200 (2006) 4870-4875.
- [13] B. An, L. Li, H. Li, Electrodeposition in the Ni-plating bath containing multi-walled carbon nanotubes, *Materials Chemistry and Physics*. 110 (2008) 481-485.
- [14] X. Chen, J. Peng, X. Li, F. Deng, J. Wang, W. Li, Tribological behavior of carbon nanotubes—reinforced nickel matrix composite coatings, *Journal of Materials Science Letters*. 20 (2001) 2057-2060.
- [15] J. Li, Y. Sun, X. Sun, J. Qiao, Mechanical and corrosion-resistance performance of electrodeposited titania–nickel nanocomposite coatings, *Surface and Coatings Technology*. 192 (2005) 331-335.
- [16] I. Garcia, J. Fransaer, J. Celis, Electrodeposition and sliding wear resistance of nickel composite coatings containing micron and submicron SiC particles, *Surface and Coatings Technology*. 148 (2001) 171-178.
- [17] S. Spanou, E. Pavlatou, N. Spyrellis, Ni/nano-TiO₂ composite electrodeposits: Textural and structural modifications, *Electrochimica Acta*. 54 (2009) 2547-2555.
- [18] I. Tudela, A.J. Cobley, Y. Zhang, Tribological performance of novel nickel-based composite coatings with lubricant particles, *Friction*. 7 (2019) 169-180.
- [19] W. Wang, F. Hou, H. Wang, H. Guo, Fabrication and characterization of Ni–ZrO₂ composite nano-coatings by pulse electrodeposition, *Scripta Materialia*. 53 (2005) 613-618.
- [20] V. Medelienė, A. Kosenko, Structural and functional properties of electrodeposited copper metal matrix composite coating with inclusions of WC, *Materials Science*. 14 (2008) 29-33.
- [21] H. Li, Y. Wan, H. Liang, X. Li, Y. Huang, F. He, Composite electroplating of Cu–SiO₂ nano particles on carbon fiber reinforced epoxy composites, *Applied Surface Science*. 256 (2009) 1614-1616.
- [22] H. Zhao, L. Liu, Y. Wu, W. Hu, Investigation on wear and corrosion behavior of Cu–graphite composites prepared by electroforming, *Composites Science and Technology*. 67 (2007) 1210-1217.
- [23] V. Mangam, S. Bhattacharya, K. Das, S. Das, Friction and wear behavior of Cu–CeO₂ nanocomposite coatings synthesized by pulsed electrodeposition, *Surface and Coatings Technology*. 205 (2010) 801-805.

- [24] P. Dai, W. Xu, Q. Huang, Mechanical properties and microstructure of nanocrystalline nickel-carbon nanotube composites produced by electrodeposition, *Materials Science and Engineering: A*. 483 (2008) 172-174.
- [25] K. Rajkumar, S. Aravindan, Tribological studies on microwave sintered copper-carbon nanotube composites, *Wear*. 270 (2011) 613-621.
- [26] A. Gajewska-Midziątek, Composite coatings with nickel matrix and graphene as dispersed phase, *Polish Journal of Chemical Technology*. 20 (2018) 54-59.
- [27] C.L.P. Pavithra, B.V. Sarada, K.V. Rajulapati, T.N. Rao, G. Sundararajan, A new electrochemical approach for the synthesis of copper-graphene nanocomposite foils with high hardness, *Scientific reports*. 4 (2014) 4049.
- [28] M. Lekka, D. Koumoulis, N. Kouloumbi, P. Bonora, Mechanical and anticorrosive properties of copper matrix micro-and nano-composite coatings, *Electrochimica Acta*. 54 (2009) 2540-2546.
- [29] P. Gyftou, M. Stroumbouli, E. Pavlatou, P. Asimidis, N. Spyrellis, Tribological study of Ni matrix composite coatings containing nano and micro SiC particles, *Electrochimica Acta*. 50 (2005) 4544-4550.
- [30] N. Qu, D. Zhu, K. Chan, Fabrication of Ni-CeO₂ nanocomposite by electrodeposition, *Scripta Materialia*. 54 (2006) 1421-1425.
- [31] H. Algul, M. Tokur, S. Ozcan, M. Uysal, T. Cetinkaya, H. Akbulut, A. Alp, The effect of graphene content and sliding speed on the wear mechanism of nickel-graphene nanocomposites, *Applied Surface Science*. 359 (2015) 340-348.
- [32] D. Iacovetta, J. Tam, U. Erb, Synthesis, structure, and properties of superhydrophobic nickel-PTFE nanocomposite coatings made by electrodeposition, *Surface and Coatings Technology*. 279 (2015) 134.
- [33] G. Wu, N. Li, D. Zhou, K. Mitsuo, Electrodeposited Co-Ni-Al₂O₃ composite coatings, *Surface and Coatings Technology*. 176 (2004) 157-164.
- [34] Q. Zhang, Y. Liu, Y. Liu, Y. Ren, Y. Wu, Z. Gao, X. Wu, P. Han, Enhanced tensile ductility and strength of electrodeposited ultrafine-grained nickel with a desired bimodal microstructure, *Materials Science and Engineering: A*. 701 (2017) 196-202.
- [35] Y. Yang, Y. Wang, Y. Ren, C. He, J. Deng, J. Nan, J. Chen, L. Zuo, Single-walled carbon nanotube-reinforced copper composite coatings prepared by electrodeposition under ultrasonic field, *Materials Letters*. 62 (2008) 47-50.
- [36] G. Burkat, T. Fujimura, V.Y. Dolmatov, E. Orlova, M. Veretennikova, Preparation of composite electrochemical nickel-diamond and iron-diamond coatings in the presence of detonation synthesis nanodiamonds, *Diamond and related materials*. 14 (2005) 1761-1764.

- [37] M. Stroumbouli, P. Gyftou, E. Pavlatou, N. Spyrellis, Codeposition of ultrafine WC particles in Ni matrix composite electrocoatings, *Surface and Coatings Technology*. 195 (2005) 325-332.
- [38] C. Low, R. Wills, F. Walsh, Electrodeposition of composite coatings containing nanoparticles in a metal deposit, *Surface and Coatings Technology*. 201 (2006) 371-383.
- [39] F. Nasirpour, M.R. Sanaeian, A.S. Samardak, E.V. Sukovatitsina, A.V. Ognev, L.A. Chebotkevich, M.-. Hosseini, M. Abdolmaleki, An investigation on the effect of surface morphology and crystalline texture on corrosion behavior, structural and magnetic properties of electrodeposited nanocrystalline nickel films, *Applied Surface Science*. 292 (2014) 795-805.
- [40] A. Lausic, B. Bouwhuis, J. McCrea, G. Palumbo, G. Hibbard, Mechanical anisotropy in electrodeposited nanocrystalline metal/metal composite foams, *Materials Science and Engineering: A*. 552 (2012) 157-163.
- [41] W. Choi, Tuteja. A, Mabry. J, R. Cohen, McKinley. G, A modified Cassie–Baxter relationship to explain contact angle hysteresis and anisotropy on non-wetting textured surfaces, *Journal of Colloid and Interface Science*. 339 (2009) 208-216.
- [42] S.I. Ranganathan, M. Ostoja-Starzewski, Universal elastic anisotropy index, *Physical Review Letters* 101 (2008) 055504.
- [43] J. Shenoy, M. Das, J. Cooper Jr, M. Melloch, J. Palmour, Effect of substrate orientation and crystal anisotropy on the thermally oxidized SiO₂/SiC interface, *Journal of Applied Physics*. 79 (1996) 3042-3045.
- [44] A. Meyer, A. Gleizes, J.J. Girerd, M. Verdaguer, O. Kahn, Crystal structures, magnetic anisotropy properties and orbital interactions in catena-(μ -nitrito)-bis(ethylenediamine) nickel (II) perchlorate and triiodide, *Inorganic Chemistry*. 21 (1982) 1729-1739.
- [45] R. Hall, Single crystal anisotropy and magnetostriction constants of several ferromagnetic materials including alloys of NiFe, SiFe, AlFe, CoNi, and CoFe, *Journal of Applied Physics*. 30 (1959) 816-819.
- [46] E.O. Hall, *Proceedings of the Physical Society London B*. 64 (1951).
- [47] N.J. Petch, *The Journal of the Iron and Steel Institute*. 174 (1953).
- [48] J. Schiøtz, F.D. Di Tolla, K.W. Jacobsen, Softening of nanocrystalline metals at very small grain sizes, *Nature*. 391 (1998) 561.
- [49] L. Tapsell, I. Hemphill, L. Cobiac, M. Fenech, C. Patch, S. Roodenrys, J. Keogh, P. Clifton, P. Williams, V. Fazio, I. Ke, Health benefits of herbs and spices: the past, the present, the future, *The Medical Journal of Australia*. 185 (2006) S1-24.
- [50] McCormick science institute, History of spices, 2016.

- [51] Halal Food, Product and Travel, Black Pepper the Currency Spices in ancient times, 2018.
- [52] M.M. Tajkarimi, S.A. Ibrahim, D.O. Cliver, Antimicrobial herb and spice compounds in food, *Food Control*. 21 (2010) 1199-1218.
- [53] L.R. Beuchat, Sensitivity of *Vibrio parahaemolyticus* to spices and organic acids. *Journal of Food Science*. (1976) 899-902.
- [54] M.S. Yutaka Yano, Antimicrobial effect of spices and herbs on *Vibrio parahaemolyticus*, Hiroshi Oikawa, *International Journal of Food Microbiology*. (2006) 6-11.
- [55] Deans, S.G., Ritchie, G., Antibacterial properties of plant essential oils, *International Journal of Food Microbiology*. 5 (1987) 165-180.
- [56] I.A. Al Mofleh, Spices, herbal xenobiotics and the stomach: friends or foes? *World Journal of Gastroenterology*. 16 (2010) 2710-2719.
- [57] A. Shah, A. Al-Shareef, A. Ageel, S. Qureshi, Toxicity studies in mice of common spices, *Cinnamomum zeylanicum* bark and *Piper longum* fruits, *Plant Foods for Human Nutrition*. 52 (1998) 231-239.
- [58] S. Lee, B. Lee, W. Choi, B. Park, J. Kim, B.C. Campbell, Fumigant toxicity of volatile natural products from Korean spices and medicinal plants towards the rice weevil, *Sitophilus oryzae* (L), *Pest Management Science: formerly Pesticide Science*. 57 (2001) 548-553.
- [59] A.D. McNaught, A. Wilkinson, IUPAC. *Compendium of Chemical Terminology*, 2nd ed., Blackwell Scientific Publications, Oxford, 1997.
- [60] D.R. Gabe, G.D. Wilcox, J. Gonzalez-Garcia, F.C. Walsh, The rotating cylinder electrode: its continued development and application, *Journal of Applied Electrochemistry*. 23 (1998) 759-780.
- [61] F. Touyeras, J.Y. Hihn, X. Bourgoin, B. Jacques, L. Hallez, V. Branger, Effects of ultrasonic irradiation on the properties of coatings obtained by electroless plating and electro plating, *Ultrasonics - Sonochemistry*. 12 (2005) 13-19.
- [62] A.J. Bard, R.W. Murray, *Electrochemistry, Proceedings of the National Academy of Sciences of the United States of America*. 109 (2012) 11484.
- [63] N.P. Wasekar, P. Haridoss, S. Seshadri, G. Sundararajan, Influence of mode of electrodeposition, current density and saccharin on the microstructure and hardness of electrodeposited nanocrystalline nickel coatings, *Surface and Coatings Technology*. 291 (2016) 130-140.
- [64] W. Cheng, W. Ge, Q. Yang, X. Qu, Study on the corrosion properties of nanocrystalline nickel electrodeposited by reverse pulse current, *Applied Surface Science*. 276 (2013) 604-608.

- [65] F. Su, C. Liu, P. Huang, Effect of complexing agents and pH on microstructure and tribological properties of Co–W coatings produced by double pulse electrodeposition, *Applied Surface Science*. 258 (2012) 6550-6557.
- [66] E. Chason, J. Shin, S. Hearne, L. Freund, Kinetic model for dependence of thin film stress on growth rate, temperature, and microstructure, *Journal of Applied Physics*. 111 (2012) 083520.
- [67] Y. Zheng, S. Zhang, X. Lü, Q. Wang, Y. Zuo, L. Liu, Low-temperature Electrodeposition of Aluminium from Lewis Acidic 1-Allyl-3-methylimidazolium Chloroaluminate Ionic Liquids, *Chin. Chemical Engineering Journal*. 20 (2012) 130-139.
- [68] N.A. Badarulzaman, A.A. Mohamad, S. Puwadaria, Z.A. Ahmad, The evaluation of nickel deposit obtained via Watts electrolyte at ambient temperature, *Journal of coatings technology and research*. 7 (2010) 815-820.
- [69] J. Zheng, G. Lu, L. Qiao, L. Jiang, M. Jiang, Copper electrodeposition from non-cyanide alkaline baths containing methylene diphosphonic acid as a complexing agent, *Wuli Huaxue Xuebao/ Acta Physico - Chimica Sinica*. 27 (2011) 143-148.
- [70] M.A.M. Ibrahim, R.S. Bakdash, New non- cyanide acidic copper electroplating bath based on glutamate complexing agent, *Surface and Coatings Technology*. 282 (2015) 139.
- [71] I. Mladenović, J. Lamovec, V. Jović, V. Radojević, Synergetic effect of additives on the hardness and adhesion of thin electrodeposited copper films, *Serbian Journal of Electrical Engineering*. 14 (2017) 1-11.
- [72] I. Matsui, Y. Takigawa, T. Uesugi, K. Higashi, Effect of additives on tensile properties of bulk nanocrystalline Ni–W alloys electrodeposited from a sulfamate bath, *Materials Letters*. 99 (2013) 65-67.
- [73] T. Oishi, M. Yaguchi, K. Koyama, M. Tanaka, J.-. Lee, Effect of additives on monovalent copper electrodeposition in ammoniacal alkaline solutions, *Hydrometallurgy*. 133 (2013) 58-63.
- [74] R. Fukui, Y. Katayama, T. Miura, The effect of organic additives in electrodeposition of Co from an amide-type ionic liquid. *Electrochimica Acta*. 56 (2011) 1190-1196.
- [75] M. Pasquale, L. Gassa, A. Arvia, Copper electrodeposition from an acidic plating bath containing accelerating and inhibiting organic additives, *Electrochimica. Acta*. 53 (2008) 5891-5904.
- [76] A. Fahami, B. Nasiri-Tabrizi, M. Rostami, R. Ebrahimi-Kahrizsangi, Influence of surfactants on the Characteristics of Nickel Matrix Nanocomposite Coatings, *ISRN Electrochemistry*. (2013) 1-8.

- [77] A. Wang, B. Chen, L. Fang, J. Yu, L. Wang, Influence of branched quaternary ammonium surfactant molecules as levelers for copper electroplating from acidic sulfate bath, *Electrochimica Acta*. 108 (2013) 698-706.
- [78] M.A. Malik, M.A. Hashim, F. Nabi, S.A. Al-Thabaiti, Z. Khan, Anti-corrosion ability of surfactants: a review, *International Journal of Electrochemical Science*. 6 (2011) 1927-1948.
- [79] R. Vittal, H. Gomathi, K. Kim, Beneficial role of surfactants in electrochemistry and in the modification of electrodes, *Journal of Colloid and Interface Science*. 119 (2006) 55-68.
- [80] A. Engwall, Z. Rao, E. Chason, Origins of residual stress in thin films: Interaction between microstructure and growth kinetics, *Materials & Design*. 110 (2016) 616-623.
- [81] E. Chason, A. Engwall, F. Pei, M. Lafouresse, U. Bertocci, G. Stafford, J.A. Murphy, C. Lenihan, D.N. Buckley, Understanding residual stress in electrodeposited Cu thin films, *Journal of the Electrochemical Society*. 160 (2013) D3285-D3289.
- [82] O.P. Watts, Rapid nickel plating, *Transactions of the American Electrochemical Society*. 29 (1916) 395-403.
- [83] D. Gabe, Watts of Watts nickel fame, Loughborough University Institutional Repository. (2007).
- [84] J.K. Dennis, T.E. Such, *Nickel and Chromium Plating*, Elsevier, 1993.
- [85] G.A. Di Bari, Electrodeposition of nickel, *Modern electroplating*. 5 (2000) 79-114.
- [86] C.P. Kumar, T. Venkatesha, R. Shabadi, Preparation and corrosion behavior of Ni and Ni-graphene composite coatings, *Materials Research Bulletin*. 48 (2013) 1477-1483.
- [87] A. El-Sherik, U. Erb, J. Page, Microstructural evolution in pulse plated nickel electrodeposits, *Surface and Coatings Technology*. 88 (1997) 70-78.
- [88] Y. Li, H. Jiang, L. Pang, B. Wang, X. Liang, Novel application of nanocrystalline nickel electrodeposit: Making good diamond tools easily, efficiently and economically, *Surface and Coatings technology*. 201 (2007) 5925-5930.
- [89] Y. Xuetao, W. Yu, S. Dongbai, Y. Hongying, Influence of pulse parameters on the microstructure and microhardness of nickel electrodeposits, *Surface and Coatings Technology*. 202 (2008) 1895-1903.
- [90] E. Marquis, A. Talin, J. Kelly, S. Goods, J. Michael, Effects of current density on the structure of Ni and Ni-Mn electrodeposits, *Journal of Applied Electrochemistry*. 36 (2006) 669-676.
- [91] D. Baudrand, Nickel sulfamate plating, its mystique and practicality, *Metal Finishing*. 94 (1996) 15-18.

- [92] Nickel institute, Nickel plating handbook, Nickel institute, Brussels, 2014.
- [93] J. Ballesteros, E. Chainet, P. Ozil, Y. Meas, G. Trejo, Electrodeposition of copper from non-cyanide alkaline solution containing tartrate, *International Journal of Electrochemical Science*. 6 (2011) 2632-2651.
- [94] N. Mandich, Cyanide copper plating reinvents itself: Understanding the influence of bath parameters helps achieve the most from a copper cyanide bath, *Metal Finishing*. 103 (2005) 30-36.
- [95] I.K. Hong, J.W. Park, S.B. Lee, Balancing of plating solution in CuCN electroplating process, *Journal of Industrial and Engineering Chemistry*. 20 (2014) 3068-3074.
- [96] M. Schlesinger, M. Paunovic, *Modern Electroplating*, John Wiley & Sons, 2011.
- [97] D.D.S. J.W. Dini, M. Schlesinger, M. Paunovic (Eds.), *Modern Electroplating*, (2010).
- [98] J. Ballesteros, E. Chaînet, P. Ozil, G. Trejo, Y. Meas, Initial stages of the electrocrystallization of copper from non-cyanide alkaline bath containing glycine, *Journal of Electroanalytical Chemistry*. 645 (2010) 94-102.
- [99] P. Sebastián, E. Torralba, E. Vallés, A. Molina, E. Gómez, Advances in Copper Electrodeposition in Chloride Excess. A Theoretical and Experimental Approach, *Electrochimica. Acta*. 164 (2015) 187-195.
- [100] V. Medeliene, M. Kurtinaitienė, G. Bikulčius, V. Stankevič, A study of copper coatings electrodeposited in electrolyte with a metallic powder of chromium, *Surface and Coatings Technology*. 200 (2006) 6123-6129.
- [101] Z. Wang, X. Cai, C. Yang, L. Zhou, C. Hu, An electrodeposition approach to obtaining carbon nanotubes embedded copper powders for the synthesis of copper matrix composites, *Journal of Alloys and Compounds*. 735 (2018) 1357-1362.
- [102] M. Eslami, H. Saghafian, F. Golestani-fard, A. Robin, Effect of electrodeposition conditions on the properties of Cu–Si₃N₄ composite coatings, *Applied Surface Science*. 300 (2014) 129-140.
- [103] V. Stankovic, M. Gojo, Electrodeposited composite coatings of copper with inert, semiconductive and conductive particles, *Surface and Coatings Technology*. 81 (1996) 225-232.
- [104] J. Zhu, L. Liu, G. Hu, B. Shen, W. Hu, W. Ding, Study on composite electroforming of Cu/SiCp composites, *Materials Letters*. 58 (2004) 1634-1637.
- [105] H.S. Maharana, A. Basu, Surface-mechanical and oxidation behavior of electro-co-deposited Cu-Y₂O₃ composite coating, *Surface and Coatings Technology*. 304 (2016) 348-358.

- [106] J.P. Healy, D. Pletcher, M. Goodenough, The chemistry of the additives in an acid copper electroplating bath: part I. Polyethylene glycol and chloride ion, *Journal of The Electrochemical Society*. 338 (1992) 155-165.
- [107] F.C. Walsh, C.T.J. Low, R.G.A. Willis, Electrodeposition of composite coatings containing nanoparticles in a metal deposit, *Surface and Coatings Technology*. 201 (2006) 371-383.
- [108] N. Guglielmi, Kinetics of the Deposition of Inert Particles from Electrolytic Baths, *Journal of The Electrochemical Society*. 119 (1972) 1009.
- [109] S. Wang, W. Wei, Kinetics of electroplating process of nano-sized ceramic particle/Ni composite, *Materials Chemistry and Physics*. 78 (2003) 574-580.
- [110] J.P. Celis, J.R. Roos, C.: Buelens, A Mathematical Model for the Electrolytic Codeposition of Particles with a Metallic Matrix, *Journal of The Electrochemical Society*. 134 (1987) 1402-1408.
- [111] J. Fransaer, J.:R. Celis J., Analysis of the Electrolytic Codeposition of Non-Brownian Particles with Metals, *Journal of The Electrochemical Society*. 139 (1992) 413-425.
- [112] B. Hwang, C. Hwang, Mechanism of Codeposition of Silicon Carbide with Electrolytic Cobalt, *Journal of The Electrochemical Society*. 140 (1993) 979-984.
- [113] P.M. Vereecken, I. Shao, P.C. Searson, Particle Codeposition in Nanocomposite Films, *Journal of The Electrochemical Society*. 147 (2000) 2572-2575.
- [114] R. Bazzard, P. Boden, *Transaction of the Institute of Metal Finishing*. 50 (1972) 207-210.
- [115] C.T.J. Low, R.G.A. Wills, F.C. Walsh, Electrodeposition of composite coatings containing nanoparticles in a metal deposit, *Surface and Coatings Technology*. 201 (2006) 371-383.
- [116] P. Berçota, E. Peña-Muñozb, J. Pagettia, Electrolytic composite Ni–PTFE coatings: an adaptation of Guglielmi's model for the phenomena of incorporation, *Surface and Coatings Technology*. 157 (2002) 282-289.
- [117] P. Bercot, E. Pena-Munoz, J. Pagetti, Electrolytic composite Ni–PTFE coatings: an adaptation of Guglielmi's model for the phenomena of incorporation, *Surface and Coatings Technology*. 157 (2002) 282-289.
- [118] R. Morana, The influence of particle type and process conditions on electrodeposited composite coatings, *Loughborough University* (2006).
- [119] V.S. Bagotsky, *Fundamentals of Electrochemistry*, 2nd ed, Hoboken: Wiley, Hoboken, 2005.

- [120] H. Sheua, P. Huang, L. Tsaic, K. Hou, Effects of plating parameters on the Ni–P–Al₂O₃ composite coatings prepared by pulse and direct current plating, *Surface and Coatings Technology*. 235 (2013) 535.
- [121] A.P. Abbott, K.J. McKenzie, Application of ionic liquids to the electrodeposition of metals, *The Journal of Physical Chemistry*. 8 (2006) 4265-4279.
- [122] J.P. CELIS, J.R. ROOS, *Electrolytic and Electroless Composite Coatings*, 1982. 5 (Coatings and Corrosion) 1.
- [123] A.M.J. KARIAPPER, J. FOSTER, Further Studies on the Mechanism of Formation of Electrodeposited Composite Coatings, *Transactions of the Institute of Metal Finishing*. 52 (1974) 87.
- [124] J.P. CELIS, J.R. ROOS, " Kinetics of the Deposition of Alumina Particles from Copper Sulfate Plating Baths, *Journal of the Electrochemical Society*. 124 (1977) 1508.
- [125] G.N.K. RAMESH BAPU, M. MOHAMMED YASUF, Electrodeposition of Nickel-Vanadium Pentoxide Composite and its Corrosion Behaviour, *Materials Chemistry and Physics*. 36 (1993) 134.
- [126] E.V. SAKSIN, A.A. SHEVYREV, A.V. SHKURANKOV, J.R. ROOS, A.V. ROMANYUK, Properties and Structure of Metal-Fluoroplastic Composite Coatings, *Russian Journal of Applied Chemistry*. 68 (1995) 1596.
- [127] R. NARAYAN, B.H. NARAYANA, Electrodeposited Chromium-Graphite Composite Coatings, *Journal of the Electrochemical Society*. 128 (1981) 1704.
- [128] A. HOVESTAD, R.J.C.H.L. HEESSEN, L.J.J. JANSSEN, Electrochemical Deposition of Zinc-Polystyrene Composites in the Presence of Surfactants, *Journal of Applied Electrochemistry*. 29 (1999) 331.
- [129] Y. Suzuki, M. Wajima, O. Asai, Cathodic Polarization Behavior of Ag-Al₂O₃ Electrode in Silver Thiocyanate Solution Containing Al₂O₃ Particles, *Journal of the Electrochemical Society*. 133 (1986) 259-262.
- [130] S.W. BANOVIC, K. BARMAK, A.R. MARDER, Characterization of Single and Discretely-Stepped Electro-Composite Coatings of Nickel-Alumina, *Journal of Materials Science*. 34 (1999) 3203.
- [131] V.R. Kumar, T. Sarakonsri, Introduction to Electrochemical Cells, in *High Energy Density Lithium Batteries: Materials, Engineering, Applications*, (2010).
- [132] M.S. Chandrasekar, M. Pushpavanam, Pulse and pulse reverse plating—Conceptual, advantages and applications, *Electrochimica Acta*. 53 (2008) 3313-3322.
- [133] F. Jiang, Y. Zhang, Effect of pulse current parameters on microstructure of tungstencoating electroplated from Na₂WO₄–WO₃–NaPO₃, *Applied Surface Science*. 331 (2015) 278-284.

- [134] C. Kerr, D. Barker, F. Walsh, J. Archer, The Electrodeposition of Composite Coatings Based on Metal Matrix-Included Particle Deposits, *Transactions of the Institute of Metal Finishing*. 78 (2000) 171.
- [135] F. Endres, D. MacFarlane, A. Abbott, Electrodeposition of Metals, in: F. Endres, D. MacFarlane, A. Abbott (Eds.), *Electrodeposition from Ionic Liquid*, Wiley-VCH Verlag GmbH & Co, 2008.
- [136] W. Simka, D. Puszczuk, G. Nawrat, Electrodeposition of metals from nonaqueous, *Electrochimica Acta*. 54 (2009) 5307-5319.
- [137] A.P. Abbott, G. Frisch, K.S. Ryder, Electroplating Using Ionic Liquids, *Annual Review of Materials Research*. 43 (2013) 358.
- [138] J.C. Malaquias, M. Steichen, M. Thomassey, P.J. Dale, Electrodeposition of Cu–In alloys from a choline chloride based deep eutectic solvent for photovoltaic applications, *Electrochimica Acta*. 103 (2013) 15-22.
- [139] E. Gómez, E. Pellicer, E. Vallés, Influence of the bath composition and the pH on the induced cobalt–molybdenum electrodeposition, *Journal of Electroanalytical Chemistry*. 556 (2003) 137-145.
- [140] S.K. Kim, H.J. Yoo, Formation of bilayer Ni–SiC composite coatings by electrodeposition, *Surface and coatings Technology*. 108 (1998) 564-569.
- [141] A. Bund, D. Thiemig, Influence of bath composition and pH on the electrocodeposition of alumina nanoparticles and nickel, *Surface and Coatings Technology*. 201 (2007) 7092-7099.
- [142] L. Chen, L. Wang, Z. Zeng, J. Zhang, Effect of surfactant on the electrodeposition and wear resistance of Ni–Al₂O₃ composite coatings, *Materials Science and Engineering: A*. 434 (2006) 319-325.
- [143] Y. Reyes-Vidal, R. Suarez-Rojas, C. Ruiz, J. Torres, Ș. Țălu, A. Méndez, G. Trejo, Electrodeposition, characterization, and antibacterial activity of zinc/silver particle composite coatings, *Applied Surface Science*. 342 (2015) 34-41.
- [144] M. Eslami, H. Saghaian, F. Golestani-Fard, A. Robin, Effect of electrodeposition conditions on the properties of Cu–Si₃N₄ composite coatings, *Applied Surface Science*. 300 (2014) 129-140.
- [145] F. Ebrahimi, G. Bourne, M.S. Kelly, T. Matthews, Mechanical properties of nanocrystalline nickel produced by electrodeposition, *Nanostructured materials*. 11 (1999) 343-350.
- [146] M. Eslami, H. Saghaian, F. Golestani-Fard, A. Robin, Effect of electrodeposition conditions on the properties of Cu–Si₃N₄ composite coatings, *Applied Surface Science*. 300 (2014) 129-140.

- [147] I. Tudela, Y. Zhang, M. Pal, I. Kerr, A.J. Cobley, Ultrasound- assisted electrodeposition of composite coatings with particles, *Surface and Coatings Technology*. 259 (2014) 363-373.
- [148] O. Louisnard, J. González-García, *Acoustic cavitation* (Eds.), Springer, New York-Dordrecht-Heidelberg-London, 2011. in: H. Feng, G. Barbosa-Canovas, J. Weiss (Eds.), *Ultrasound Technologies for Food and Bioprocessing*, Springer, New York, Dordrecht, Heidelberg, London, 2011.
- [149] J.L. Hardcastle, J.C. Ball, Q. Hong, F. Marken, R.G. Compton, S.D. Bull, S.G. Davis, Sonoelectrochemical and sonochemical effects of cavitation: correlation with interfacial cavitation induced by 20 kHz ultrasound. *Ultrasonics Sonochemistry*. 7 (2000) 7-14.
- [150] D.J. Walton, S.S. Phull, A. Chyla, J.P. Lorimer, T.J. Mason, L. Burke, M. Murphy, R.G. Compton, J.C. Eklund, S.D. Page, Sonovoltammetry at platinum electrodes: surface phenomena and mass transport processes, *Journal of Applied Electrochemistry*. 25 (1995) 1083-1090.
- [151] P. Prasad, R. Vasudevan, S. Seshadri, Wear characteristics of nickel electrodeposits in ultrasonically agitated bath, *Journal of Materials Science Letters*. 12 (1993) 902-903.
- [152] P.B. Prasad, S. Ahila, R. Vasudevan, S. Seshadri, Fatigue strength of nickel electrodeposits prepared in ultrasonically agitated bath, *Journal of Materials Science Letters*. 13 (1994) 15-16.
- [153] P. Prasad, R. Vasudevan, S. Seshadri, S. Ahila, The effect of ultrasonic vibration on nickel electrodeposition, *Materials Letters*. 17 (1993) 357-359.
- [154] P. Prasad, R. Vasudevan, S. Seshadri, Residual stresses of nickel electrodeposits with ultrasonically agitated bath, *Journal of Materials Science Letters*. 11 (1992) 1424-1425.
- [155] P. Prasad, S. Ahila, R. Vasudevan, S. Seshadri, Corrosion resistance of zinc electrodeposits in an ultrasonically agitated bath, *Journal of Materials Science Letters*. 12 (1993) 1752-1754.
- [156] T. Ohsaka, M. Isaka, K. Hirano, T. Ohishi, Effect of ultrasound sonication on electroplating of iridium, *Ultrasonics Sonochemistry*. 15 (2008) 283-288.
- [157] T. Ohsaka, Y. Goto, K. Sakamoto, M. Isaka, S. Imabayashi, K. Hirano, Effect of intensities of ultrasound sonication on reduction of crack formation and surface roughness in iridium electrodeposits, *Transactions of the Institute of Metal Finishing*. 88 (2010) 204-208.
- [158] T.J. Mason, J. Lorimer, S. Saleem, L. Paniwnyk, Controlling emissions from electroplating by the application of ultrasound, *Environmental Science & Technology*. 35 (2001) 3375-3377.

- [159] Y. Xue, J. Li, W. Ma, M. Duan, M. Lan, Fabrication and wear resistance of Ni-CeO₂ nanocomposite coatings by electrodeposition under ultrasound condition, *International Journal of Surface Science and Engineering*. 4 (2010) 202-213.
- [160] E. García-Lecina, I. García-Urrutia, J. Díez, J. Fornell, E. Pellicer, J. Sort, Codeposition of inorganic fullerene-like WS₂ nanoparticles in an electrodeposited nickel matrix under the influence of ultrasonic agitation, *Electrochimica Acta*. 114 (2013) 859-867.
- [161] D. Dietrich, I. Scharf, D. Nickel, L. Shi, T. Grund, T. Lampke, Ultrasound technique as a tool for high-rate incorporation of Al₂O₃ in NiCo layers, *Journal of Solid State Electrochemistry*. 15 (2011) 1041-1048.
- [162] M.K. Camargo, I. Tudela, U. Schmidt, A.J. Cobley, A. Bund, Ultrasound assisted electrodeposition of Zn and Zn-TiO₂ coatings, *Electrochimica Acta*. 198 (2016) 287-295.
- [163] I. Tudela, Y. Zhang, M. Pal, I. Kerr, T.J. Mason, A.J. Cobley, Ultrasound-assisted electrodeposition of nickel: Effect of ultrasonic power on the characteristics of thin coatings, *Surface and Coatings Technology*. 264 (2015) 49-59.
- [164] P. Indyka, E. Beltowska-Lehman, M. Bieda, J. Morgiel, L. Tarkowski, Microstructure and Deposition Relations in Alumina Particle Strengthened Ni-W Matrix Composites, *Applied Mechanics and Materials*. 186 (2012) 234-238.
- [165] E. Beltowska-Lehman, P. Indyka, A. Bigos, M. Kot, L. Tarkowski, Electrodeposition of nanocrystalline Ni-W coatings strengthened by ultrafine alumina particles, *Surface and Coatings Technology*. 211 (2012) 62-66.
- [166] Mason, T J. and Lorimer, J P., *Applied sonochemistry; the uses of power ultrasound in chemistry and processing*, Scitech Book News. 26 (2002) n/a.
- [167] T.J. Mason, A.J. Cobley, J.E. Graves, D. Morgan, New evidence for the inverse dependence of mechanical and chemical effects on the frequency of ultrasound, *Ultrasonics - Sonochemistry*. 18 (2011) 226-230.
- [168] H. Zheng, M. An, Electrodeposition of Zn-Ni-Al₂O₃ nanocomposite coatings under ultrasound conditions, *Journal of Alloys and Compounds*. 459 (2008) 548-552.
- [169] M. Rezrazi, M. Doche, P. Bercot, J. Hihn, Au-PTFE composite coatings elaborated under ultrasonic stirring, *Surface and Coatings Technology*. 192 (2005) 124-130.
- [170] X.H. Li, Y.J. Xue, D.Y. Zhang, J.S. Li, Effect of ultrasound action modes on the oxidation resistance of Ni-Nd₂O₃ nanocomposite coatings, *Applied Mechanics and Materials*. 120 (2012) 280-283.
- [171] Z.H. Ao, Y.J. Xue, X.H. Li, J.S. Li, Preparation of Ni-Nd₂O₃ nanocomposite coatings by electrodeposition under dual-frequency ultrasound, *Applied Mechanics and Materials*. 591 (2012) 1001-1005.

[172] L. Chang, H. Guo, M. An, Electrodeposition of Ni–Co/Al₂O₃ composite coating by pulse reverse method under ultrasonic condition, *Materials Letters*. 62 (2008) 3313-3315.

[173] H. Zheng, M. An, J. Lu, Surface characterization of the Zn–Ni–Al₂O₃ nanocomposite coating fabricated under ultrasound condition, *Applied Surface Science*. 254 (2008) 1644-1650.

[174] C. Walker, R. Walker, New Explanation for the Hardening Effect of Ultrasound on Electro-deposits, *Nature*. 244 (1973) 141-142.

3. Methods

3.1. Overview

This Chapter contains information on all experimental procedures conducted during the present research project. These experimental procedures have been divided into four subsections:

- Turmeric particle size and deagglomeration: this section includes details on experiments with ultrasound to assess its effects on turmeric particle size and deagglomeration.
- Electrodeposition of coatings: This section includes information on the electrodeposition process. The preparation of both nickel and copper electrolytes, preparation of composite copper and nickel electrolytes, type of electrodes used and their preparation before electrodeposition, and electrodeposition conditions such as current density, agitation, the temperature of electrolyte and electrodeposition time.
- Characterisation: This section includes details of experimental procedures such as hardness indentation, corrosion resistance testing, and hydrophobic properties of the coating.
- Coating analysis: This section contains details of the surface analysis techniques conducted in this project. It includes contact angle testing, White

light interferometry (WLI), scanning electron microscope (SEM), focus ion beam (FIB), and glow-discharge optical emission spectrometry (GDOES).

3.2. Spice particle size and deagglomeration

Although several spices were considered for this research project, an initial set of spice dispersion and survivability experiments suggested that turmeric offered the greatest potential for successful electrocodeposition. The details of the spice dispersion and survivability experiments are included in Appendix A.

Although, a great deal of literature has shown ultrasound can have a deagglomerating effect on particles in solution, ultrasound can also cause the agglomeration of particles [1-5]. Large particle agglomerates in the electrolyte can have an adverse effect on the deposit produced. Large agglomerates can lead to a reduction in the particle content of the deposit, non-uniform distribution of particles in the deposit (leading to non-uniform distribution of properties) and/or weak spots in the deposit [6,7]. The effects of ultrasound and mechanical stirring on the spice particles was examined by dynamic light scattering (DLS) with a Zetasizer nano S (Malvern instruments Ltd, Malvern Ltd), to assess the most efficient method of turmeric particle deagglomeration. The particle size in the form of the Z-average size and polydispersion index was used to assess the deagglomeration. The Z-average size is the intensity weighted mean of the hydrodynamic particle size, which is the size of a hypothetical sphere (most particles in solution do not exist as spheres) which diffuses in the same way as the particle being measured. The polydispersion index is a value that indicates the variation in particle size in solution, the greater the polydispersity the closer the value to 1.0. DLS uses the rate at which the intensity of the scattered light fluctuates, caused by the speed of particle diffusion due to Brownian motion. Smaller particles fluctuate scattered light more rapidly than larger particles [8,9].

Three solutions at five separate concentrations of turmeric (0.5 ± 0.02 g/l, 1.0 ± 0.2 g/l, 2.0 ± 0.2 g/l, 3.0 ± 0.2 g/l and 10.0 ± 0.2 g/l) were made up in separate 150 ml beakers with 100 ml of copper electrolyte mimic (see Appendix A) and 10.0 ml/l of

Tween 20. The solutions were stirred by 35 mm mechanical stirring bar at a speed of 240 rpm for 20 min on an IKA RCT Basic hot plate. After a time of 5, 10, 15, and 20 min three drops of the solutions was added to approximately 2.0 ml of RO water in a 3.0 ml cuvette from a disposable pipette, the particle size was then measured by DLS, at a refraction index of 1.4151 (the refraction index of turmeric). After this the solutions were left to stand, and at 15, 30, and 60 mins, the particle size measured again by the same method. Each measurement was 12 to 18 individual measurements of a minimum of 10 s duration. Three measurements for each sample was recorded and the values of the polydispersity index, Intensity–size distribution graphs and Z-average (which is the mean cluster size based on the scattered laser lights intensity). This process was then repeated with the addition of 1.0 ± 0.01 ml of Tween 20.

To assess the effect of ultrasound the same experiment was run using a 20 kHz ultrasonic horn at a power of 11 W/l and 33 W/l (details of calibration experiments by calorimetry are included in Appendix A). In addition to measuring the particle size after agitation by leaving the solutions to stand for 1 hour after sonication, additional solutions were made and after sonicating for 20 min the solutions stirred for 1 hour and the particle size measured at 15, 30 and 60 mins (to assess if stirring during electrodeposition (after the initial ultrasound) would cause a further reduction in particle size).

3.3. Electrodeposition of coatings

The quality and properties of an electrodeposited composite coating depend on the conditions under which it is produced. As stated in Chapter 2 many parameters can affect the process and properties of an electrodeposited composite such as electrolyte composition, additives, particles size and concentration, electrodes, agitation and current density, and when depositing metals an optimal range of current density generally exists well within the normal operating parameters, which is often chosen when incorporating particles into that metal matrix.

Many papers have been written on the various methods of electrodeposition of both copper, nickel, and their composites. The object of this set of experiments was to adapt and optimise these methods for producing composite coatings by electrocodeposition containing turmeric particles.

3.3.1. Preparation of electrodes

Cleaning dirt and grease from the surface of the electrodes and removing oxidation layers before electrodeposition is essential to ensure good adhesion of the coating to the substrate.

The pure copper and pure nickel anodes were purchased from the online retailer Tifoo Electrodeposition Shop. Both the pure copper and pure nickel anodes were 80 mm x 25 mm x 1 mm.

The cathodes used for corrosion rate testing were produced from 100 mm x 76 mm x 0.3 mm brass hull cell panels supplied by A-Gas Electronic Materials Ltd. The Hull cell sheets were cut into three sections of 76 mm x 25 mm x 0.3 mm with tin snips. Before electrodeposition resist tape was applied to the cathode, leaving a 25 mm² (1.0 mm² plating area for samples used for linear sweep voltammetry) electrodeposition area at the front of each cathode (Figure 3.3.). For Hull cell tests the sheets were used as purchased with no resist tape applied.

For microhardness measurements the cathode needed to be thicker to prevent flexing and bending of the sample during analysis. A thicker substrate was also required for electron back scatter detection (EBSD) to improve the conductivity through the mounted cross section of the sample. For this reason, the cathodes used for hardness testing and coating analysis were produced from 600 mm x 300 mm x 0.9 mm brass sheet supplied by RS components UK. The brass sheet was cut into 76 mm x 25 mm x 0.9 mm sections. Before electrodeposition resist tape was applied to 25 mm² area at the back of the cathode, leaving a 25 mm² electrodeposition area at the front of each cathode (Figure 3.3.).

To ensure good adhesion of the coating to the substrate, the electrodes were degreased, and the oxidation layer removed before electrodeposition. The electrodes were placed in a solution containing 5% Lipsol detergent for 2 min, after which time they were removed and the remaining Lipsol detergent rinsed off with RO water. The electrodes were then placed in a 6.5 M solution of sulphuric acid supplied by Fisher UK Ltd (SG 1.83) for 2 min, the electrodes were then immediately rinsed off again with RO water and placed in the plating solution.

3.3.2. Preparation of electrolytes

3.3.2.1. Copper electrolyte preparation

The electrolyte used for the electrodeposition of copper in this research was adapted from previous methods [14-16]. The copper electrolyte was an aqueous solution of 75.0 ± 1.0 g/l $\text{CuSO}_4 \cdot 6\text{H}_2\text{O}$ supplied by Fisher UK Ltd, 1.6×10^{-2} M of HCl and 3.7 M of concentrated H_2SO_4 (98.5 % SG 1.83) supplied by Fisher UK Ltd, with a pH of between 0.5 – 1.0.

3.3.2.2. Watts nickel electrolyte

The electrodeposition method used for the Watts nickel and Watts nickel composites in this project was adapted from previous papers [13-16]. The Watts nickel electrolyte was an aqueous solution of 50.0 ± 1.0 g/l $\text{NiCl}_2 \cdot 6\text{H}_2\text{O}$ supplied by Alfa Aesar, 250.0 ± 1.0 g/l $\text{NiSO}_4 \cdot 6\text{H}_2\text{O}$ supplied by BDH chemicals Ltd, and 40.0 ± 1.0 g/l H_3BO_3 (>99.5%) Supplied by Sigma Aldrich UK Ltd, with a pH 3.0-3.5.

3.3.2.3. Low ion concentration nickel electrolyte (LICE) preparation

High ion concentration electrolytes can cause hydrophobic particles to aggregate in solution in a process known as salting out [17]. For this reason, a low ion concentration electrolyte (LICE) was produced.

The LICE nickel electrolyte was an aqueous solution of 105.0 ± 1.0 g/l $\text{NiCl}_2 \cdot 6\text{H}_2\text{O}$ supplied by Alfa Aesar, 40.0 ± 1.0 g/L $\text{NiSO}_4 \cdot 6\text{H}_2\text{O}$ supplied by BDH chemicals Ltd, and 40.0 ± 1.0 g/l H_3BO_3 (>99.5%) Supplied by Sigma Aldrich UK Ltd, with a pH 3.0-3.5.

3.3.3. Electrodeposition current density analysis

As stated in Chapter 2 current density is one of the major factors affecting the electrodeposition process. The objective of this stage of the project was to identify the optimal current density for electrodeposition of both copper and nickel using a Hull cell. A Hull cell allows electrodeposition onto a cathode at different current densities at the same time, this is achieved by sloping the cathode so its distance from the anode varies across the length of the cathode (Figure 3.3.). The coating deposition current density then varies across the panel, with the coating at the edge closest to the anode depositing at the highest current density. Visual inspection of the Hull cell after plating can be used to assess the quality of the coatings at different current densities.

The LICE nickel electrolyte was prepared as per section 3.3.2.3. with 250 ml added to a Hull cell. The electrolyte was stirred with a 35 mm mechanical stirring bar at 100 rpm and heated to 50 °C on an IKA RCT Basic hot plate. A pure nickel anode and Hull cell panel were placed into the electrodeposition solution and connected to a Thurlby PL310 (30 V, 1 A) DC rectifier. A current of 2.0 A was applied for 5 min and then the coating assessed for quality of finish. The process was then repeated for copper using a pure copper anode and copper electrolyte.

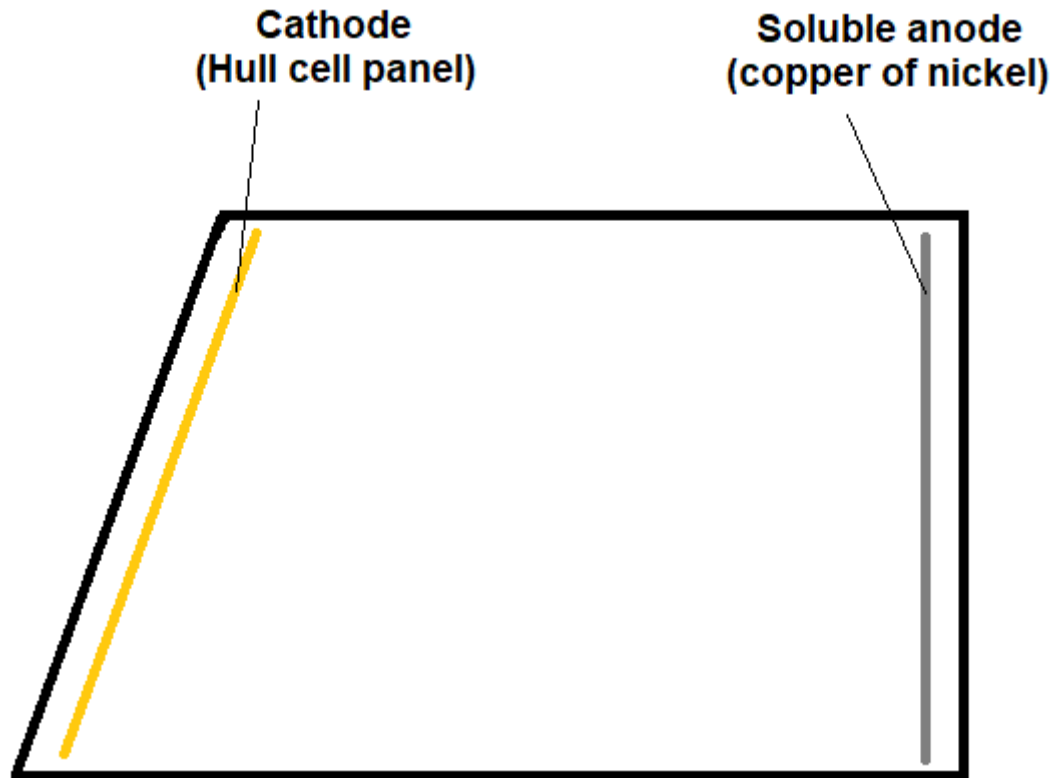


Figure 3.3. Diagram of the top of a Hull cell.

3.3.4. Current efficiency of electrodeposition methods

To accurately predict the time needed to electrodeposit a specific thickness of nickel and copper onto an electrode at a particular current density, the efficiency of the electrodeposition method must be calculated.

The theoretical time needed to deposit a coating of nickel 30 µm thick was calculated by the following equations (3.2. and 3.3.).

$$M = \frac{d s t}{10000} \quad (3.2.)$$

$$t = \frac{M n F}{I Z} \quad (3.3.)$$

Where M is the mass of deposit in g, d is the density of the metal in g cm³, s is the surface area in cm², t is the time in seconds, n is the valence of the metal, F is Faraday's constant and Z is the atomic mass of the metal and I is the current in amps.

The nickel electrodeposition solution was prepared as per Section 3.3. with 200 ml added to a 250 ml beaker. The beaker was setup as per Figure 3.4. and stirred with a 35 mm mechanical stirring bar at 240 rpm and heated to 50 °C on an IKA RCT Basic hot plate. The electrodes (which included a pre-weighed cathode) were placed in the solution to a depth of 30 mm and connected to a Thurlby PL310 (30 V, 1 A) DC rectifier. A current density of 0.04 A/cm² was applied for 36.35 min (which was the theoretical time needed to deposit 30 µm), after which time the cathode was removed, cleaned with RO water, dried and re-weighed. The process was then repeated for the copper from the electrolyte prepared as per Section 3.3. with an electrodeposition time of 34.02 min. The efficiency was then calculated (3.4.).

$$C_{ef} = \frac{M_p}{M} 100 \quad (3.4.)$$

Where C_{ef} is the Faradaic efficiency percentage, M_p is the mass of metal actually deposited onto the cathode after electrodeposition, and M is the mass of the metal deposited onto the cathode based on Faraday's laws of electrolysis.

3.3.5. Electrodeposition of coatings

The equipment set up for the electrodeposition process is shown in Figure 3.4. samples containing turmeric or nano-diamonds (supplied by plasmaChem GmbH) were sonicated for 20 mins with a 20 kHz probe before electrodepositing, then deposited at a current density of 0.04 A/cm².

Table 3.2. shows copper and copper turmeric deposits produced in this research. In order to assess the influence of particle size on the grain structure of the copper deposit, copper deposits containing nano diamonds of a known size were produced. A table of these deposits is shown in Table 3.3. Table 3.4. show the composition of the Watts nickel and Watts nickel turmeric deposits produced in this research. Table 3.5 show the composition of the LICE nickel and LICE nickel turmeric deposits produced in this research.

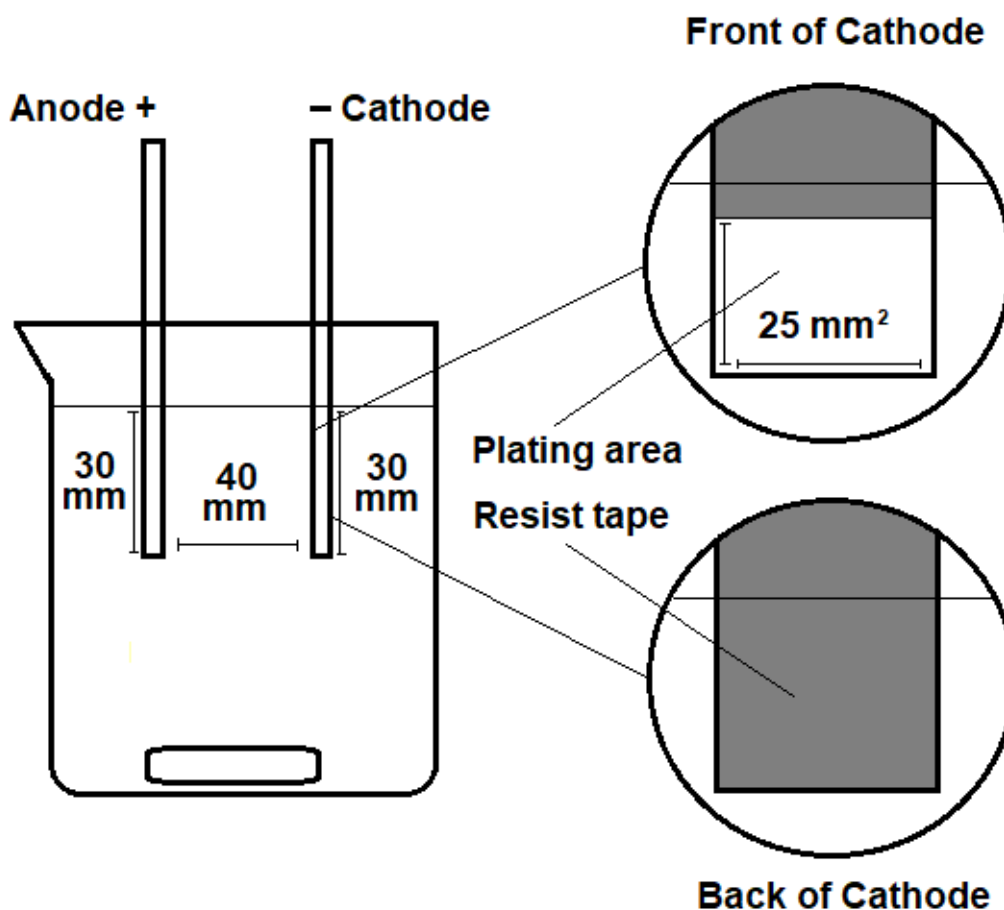


Figure 3.4. Diagram of electrodeposition set up, for all electrodeposition experiments conducted in this present research project.

Table 3.2. Copper and copper turmeric deposits.

Sample	Electrolyte	Tween 20 concentration ml/l	Turmeric concentration g/l	Horn sonication power W/l
Pure copper	Copper	0	0	0
Copper Tween 20	Copper	10.0	0	0
Copper 1.0 g/l turmeric	Copper	10.0	1.0	11
Copper 5.0 g/l turmeric	Copper	10.0	5.0	11
Copper 10.0 g/l turmeric	Copper	10.0	10.0	11
Copper 10.0 g/l turmeric 33 W/l	Copper	10.0	10.0	33

Table 3.3. *Copper nano diamond deposits.*

Sample	Electrolyte	Nano diamond size nm	Concentration of nano diamonds g/l	Horn sonication power W/l
Copper 100 nm 1.0g/l	Copper	100	1.0	11
Copper 100 nm 5.0g/l	Copper	100	5.0	11
Copper 100 nm 10.0g/l	Copper	100	10.0	11
Copper 250 nm 1.0g/l	Copper	250	1.0	11
Copper 250 nm 5.0g/l	Copper	250	5.0	11
Copper 250 nm 10.0g/l	Copper	250	10.0	11
Copper 1000 nm 1.0g/l	Copper	1000	1.0	11
Copper 1000 nm 5.0g/l	Copper	1000	5.0	11
Copper 1000 nm 10.0g/l	Copper	1000	10.0	11

Table 3.4. *Watts nickel and Watts nickel turmeric deposits.*

Sample	Electrolyte	Tween concentration ml/l	Turmeric concentration g/l	Horn sonication power W/l
Pure Watts nickel	Watts	0	0	11
Watts nickel Tween 20	Watts	10.0	0	11
Watts nickel 1.0 g/l turmeric	Watts	10.0	1.0	11
Watts nickel 5.0 g/l turmeric	Watts	10.0	5.0	11
Watts nickel 10.0 g/l turmeric	Watts	10.0	10.0	11

Table 3.5. LICE nickel and LICE nickel turmeric deposits.

Sample	Electrolyte	Tween concentration ml/l	Turmeric concentration g/l	Horn sonication power W/l
Pure LICE nickel	LICE	0	0	11
LICE nickel Tween 20	LICE	10.0	0	11
LICE nickel 1.0 g/l turmeric	LICE	10.0	1.0	11
LICE nickel 5.0 g/l turmeric	LICE	10.0	5.0	11
LICE nickel 10.0 g/l turmeric	LICE	10.0	10.0	11

3.4. Coating properties

To understand how a coating will behave under a certain set of conditions or in a certain environment, it is essential to know the properties of that coating. Characterisation of a coating can also help identify any other future potential applications for that coating.

The object of this set of experiments was to assess the chemical and physical properties of the coatings, in an effort to identify any possible applications. The corrosion rate, hardness, hydrophobic behaviour and surface roughness were tested.

3.4.1. Vicker's Hardness

The mechanical properties (such as hardness) of a material indicate how that material will behave under an applied force. The hardness of a material is a measurement of that materials resistance to permanent shape change from a compressive force applied by an indenter [18].

The value of hardness obtained from a Vicker's microhardness test (HV which has no units), is calculated by applying a load of a known force to the surface of a sample and measuring the area of the indentation (3.5.) [18,19].

$$HV = 0.1891 \frac{F}{d_1 d_2} \quad (3.5.)$$

Where 0.1891 is a conversion factor, F is the force applied in N, and d_1 and d_2 are the dimensions of the indentation in mm (Figure 3.5. B).

Coating samples (3 for each coating) were prepared as per section 3.3. The samples were then placed on the sample holder of a Mitutoyo MVK-H1 hardness testing machine with a Vicker's indenter. A force of between 10 and 300 N (depending on the hardness of the coating) was applied at 7 random positions on the surface of each coating to a depth of up to 10 μm , the indentation was then measured and the Vicker's hardness calculated by the Mitutoyo MVK-H1 hardness testing machine, and the mean obtained.

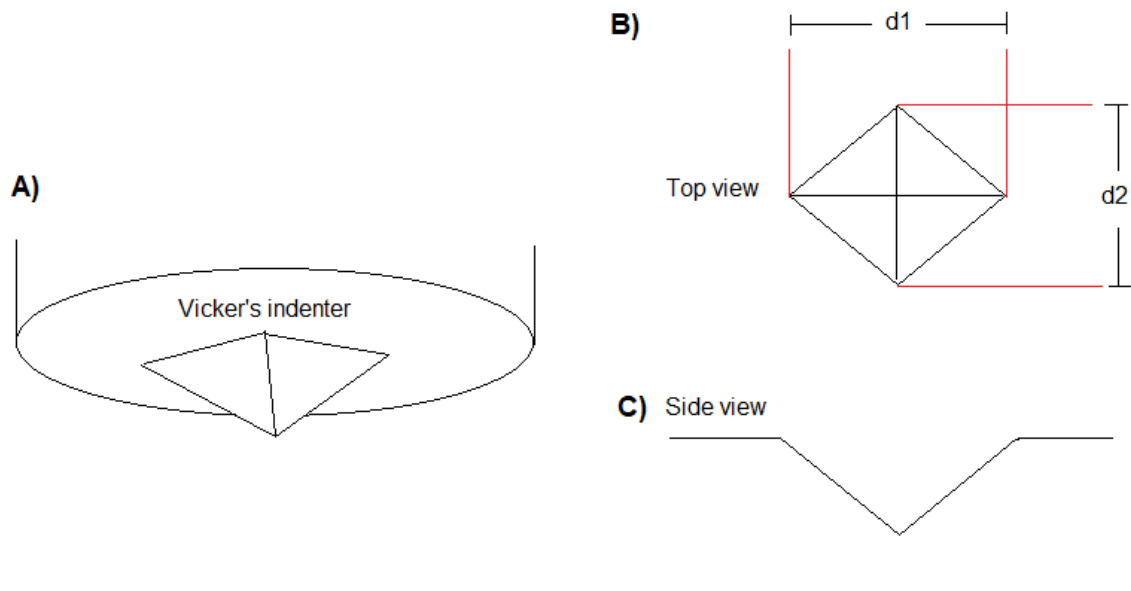


Figure 3.5. Diagram of Vicker's indenter and indentations. (A) square pyramidal Vicker's indenter. (B) top view of indentation produced by Vicker's indenter. (C) side view of indentation produced by Vicker's indenter.

3.4.2. Water contact angle

To identify if the presence of turmeric in the coatings imparted any hydrophobic properties onto the coatings, and if so how the concentration of turmeric affected this, the water contact angle (WCA) was measured with a drop shape analyser.

Coating samples were prepared as per Section 3.3. The coatings were then thoroughly washed with deionised water and dried with an electric hair drier. Immediately after production (within 5 min) the samples were placed on a Kruss DSA 100 drop shape analysis system, and the water contact angle measured using the static sessile drop method. A water droplet of 2 μl was dispensed by a syringe, and the syringe slowly lowered onto the surface of the sample. The syringe was then raised leaving the water droplet on the surface of the sample. Immediately after the droplet was placed on the surface, a camera was used to view the droplets contact with the surface and the contact angle measured. The contact angle measurements were performed at 6 different random locations on the surface of each sample.

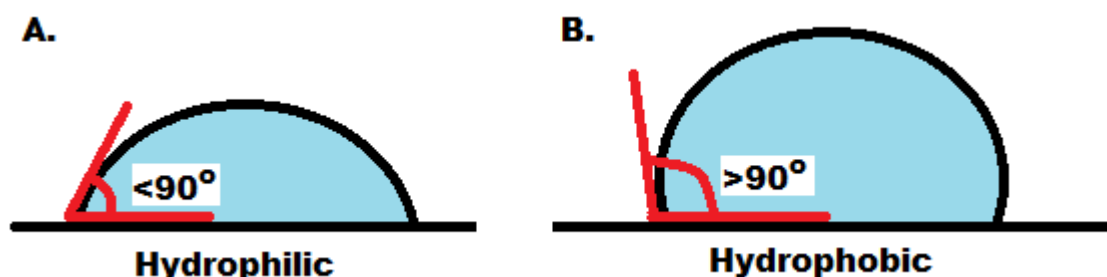


Figure 3.6. Diagram of water contact angle on a flat surface. (A) a WCA of less than 90° denoting a hydrophilic surface. (B) a WCA of greater than 90° denoting a hydrophobic surface.

3.4.3. White light interferometry (WLI)

To assess how the presence of turmeric effected the smoothness of the coatings, WLI was used to obtain topographical information.

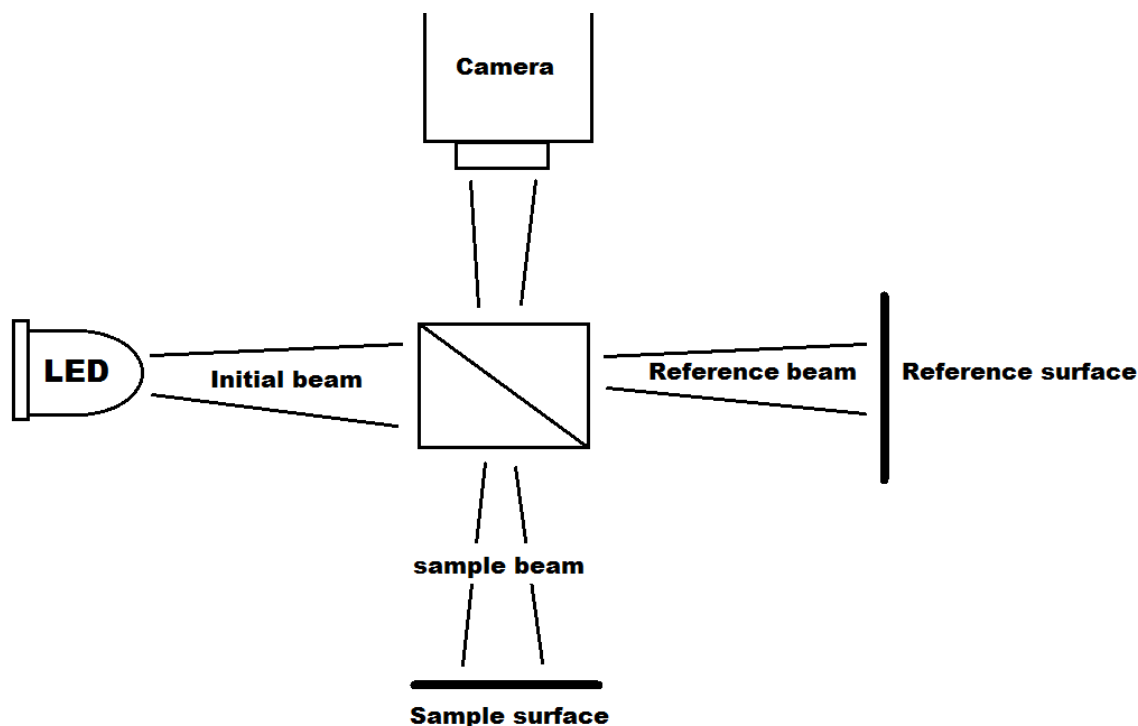


Figure 3.7. *Diagram of a WLI.*

In WLI, a light beam produced by an LED is split into 2 separate beams using a beam splitter; one beam is sent to a reference plane, and the other to the sample. The path length of the reference beam is altered, when the path length of the reference beam is the same as the path length of the sample beam an interference pattern is produced (Figure 3.7.). This interference pattern is used to produce a three-dimensional model of the surface of the sample [20,21].

Coating samples were prepared as per section 3.3. The coatings were then thoroughly washed with deionised water and dried with an electric hair drier. The samples were placed on Bruker contour GT WLI, and the aperture adjusted until an interference pattern was seen. The range of measurement was then set, and the measurement taken from a 2 mm² area at 6 random positions across the surface of the sample.

3.4.4. Corrosion rate

Most metal corrosion happens electrochemically at the interface between the surface of the metal and a solution acting as an electrolyte [22].

The rate at which this corrosion normally occurs is determined by an equilibrium between opposing electrochemical reactions (oxidation and reduction). The metal is oxidized releasing electrons into the metal (changing the potential of the metal to a more negative potential), then solution species (often O₂, H⁺ and Cl⁻) are reduced removing the electrons from the metal (although these reactions can take place between two dissimilar metals that are electrically connected). When these reactions are at equilibrium there is no net current flow [22].

3.4.4.1. Tafel method

The electrochemical potential of a metal is the means by which the equilibrium is controlled. The equilibrium potential of the metal when there is no electrical connection is known as the open circuit potential (OCP). The value of either the anodic or cathodic current at the OCP is known as the corrosion current (I_{corr}) which can be used to calculate the corrosion rate of the metal. However, I_{corr} cannot be measured directly and therefore must be estimated using electrochemical techniques [22]. The Butler Volmer equation (3.6.) predicts how the observed current varies as a function of over potential and the transfer coefficient, this can be used to estimate the corrosion rate.

$$i = i_o \left(\frac{[R]_o}{[R]_{\text{bulk}}} \exp\left(\frac{(1-\alpha)F\eta}{RT}\right) - \frac{[O]_o}{[O]_{\text{bulk}}} \exp\left(\frac{-\alpha F\eta}{RT}\right) \right) \quad (3.6.)$$

where i is the current resulting from the reaction, i_o the exchange current constant, α transfer coefficient, $[R]_o$ the concentration of reactant to be reduced at the surface of the electrode, $[R]_{\text{bulk}}$ the concentration of reactant to be reduced in the bulk solution, $[O]_o$ the concentration of reactant to be oxidised at the surface of the electrode, $[O]_{\text{bulk}}$ the concentration of reactant to be oxidised in the bulk solution, F is the Faraday constant, η is the over potential, R is the gas constant and T is the temperature.

Coating samples were prepared as per section 3.3. The coatings were then thoroughly washed with deionised water and dried with an electric hair drier.

Immediately after sample preparation, the samples were placed in a 0.1 M solution of Na₂SO₄ supplied by fisher scientific (fresh electrolyte was used for each sample). A platinum spade electrode was used as the counter electrode and saturated calomel electrode (SEC) as the reference electrode, which were connected to a VoltaLab PST 050 potentiostat. The OCP was then measured for each sample and a Linear sweep voltammetry conducted. The potential was swept from -200 mV of the OCP to +200 mV of the OCP in steps of 0.1 mV/s at ambient temperature.

A plot of the potential (x axis) against the log of current (y axis) was produced. The large linear regions of the graph were removed, and gradients plotted against the anodic and cathodic current lines. The current at the intersection of the gradients was obtained (I_{corr}) and used to calculate the corrosion rate (CR).

$$CR = \frac{I_{corr} k EW}{d A} \quad (3.7.)$$

Where k is the corrosion rate constant (3272 mm y⁻¹), EW is the equivalent weight (31.7 g for copper and 29 g for nickel), d is the density of the material deposited in cm³ (8.94 g/cm³ for copper 8.91 g/cm³ nickel) and A is the surface area in cm² (1 cm² for copper and Nickel).

3.4.4.2. Salt spray corrosion analysis

The addition of salt (NaCl) to an aqueous solution can increase the conductivity of the solution and accelerate the corrosion rate of a coating. The presence of Na⁺ in the solution acts as a catalyst allowing electrons to be transferred from the metal not only to H⁺ as in the water, but also to Na⁺, this increases the electron transfer and changes the mechanism of corrosion.

These changes can mean that materials corrode more rapidly in a salt environment (such as in or close to a salt water body) than in environment in the absence of salt.

To assess how the coatings would behave in a salt water environment, salt spray analysis was conducted [24].

Coating samples were prepared as per section 3.3. The coatings were then thoroughly washed with deionised water and dried with an electric hair drier.

The method used in this research was adapted from ASTM B 117 – 03, Standard Practice for Operating Salt Spray (Fog) Apparatus. A 5.0 % wt NaCl solution was prepared and 3 of each coating sample was placed in an Ascott cc ip1000 salt spray chamber. The experiment was conducted for a 240-hour period, after which time the samples were removed and washed with deionised water and dried.

The coating samples were weighed before and after salt spray analysis, the difference in mass was calculated and mass loss obtained. The mass lost was then used to calculate the corrosion rate (3.8.).

$$CR = \frac{k W}{A t d} \quad (3.8.)$$

Where k is a corrosion rate constant (3.45×10^6 m/year), W is the mass lost in g, A is area in cm^2 , t is time in hours, and d is the density of the material deposited in g/cm^3 (8.94 g/cm^3 for copper 8.91 g/cm^3 nickel)

3.5. Microstructure analysis

The properties of a composite coating are dependent on factors like grain size, particle content and surface morphology. To assess the surface morphology, particle content, and crystal structure of the coatings, microstructure analysis was conducted. This included scanning electron microscope (SEM), focus ion beam scanning electron microscope (FIB-SEM), and Glow-discharge optical emission spectrometry (GDOES).

3.5.1. Scanning electron microscope (SEM)

The surface features of a coating can affect its properties such as roughness, brightness and WCA. SEM was conducted to examine the surface of the samples under high magnification, in an effort to assess surface features such as nodulation, crystal orientation and surface texture.

Coating samples were prepared as per section 3.3. The coatings were then thoroughly washed with deionised water and dried with an electric hair drier. A 10 mm² sections was cut from the sample and stuck to an aluminium sample holder using carbon tape, and any dust blown off with compressed air. The samples were then examined in Zeiss SEM as per operating instructions.

3.5.2. Electron back scatter detection (EBSD)

The grain structure of an electrodeposited coating is a major factor affecting the coatings properties, such as hardness, WCA and corrosion rate. To assess the grain structure of the deposits EBSD was conducted on the electrodeposited coatings.

Coating samples were prepared for copper, copper turmeric, copper nano diamond, LICE nickel and LICE nickel turmeric as per section 3.3. The coatings were then thoroughly washed with deionised water and dried with an electric hair drier. The samples were then cross sectioned and mounted in a hot mold of PolyFast Struers resin for hot mounts supplied by Struers Ltd. The cross section of the sample was then ground with successively finer grit sanding discs until only small parallel scratch marks could be seen. The final polish was performed with OP-S 0.04 µm solution supplied by Struers Ltd. The samples were then examined in Zeiss SEM as per operating instructions (with a stepping size of 33 nm).

3.5.3. Focused ion beam (FIB-SEM)

Focused Ion Beam - Scanning Electron Microscope (FIB-SEM) is a similar system to SEM, however the electron beam is replaced with a gallium ion (Ga^+) beam. A fine ion beam is used for high-resolution imaging, and heavier beam for cutting into the surface of the sample [28].

The use of the heavier ion beam allows the cross section and grain structure of the coating to be examined [29].

In this research FIB-SEM was used to obtain high resolution images of the cross section of the samples, which was used to obtain information on the particle content and grain size of the coatings.

Coating samples were prepared for copper, copper turmeric, LICE nickel and LICE nickel turmeric as per section 3.3. The coatings were then thoroughly washed with deionised water and dried with an electric hair drier. A 10 mm² sections was cut from the sample and stuck to an aluminium sample holder using silver paint, and any dust blown off with compressed air. The samples were then examined in FEI versa 3D FIB-SEM as per operating instructions.

The line intercept method was used to determine grain size with ImageJ [30-32]. The FIB images were loaded into ImageJ and the scale calibrated using the scale bar on the FIB image. A line of known length was drawn across the image and the number of grains that intercept the line counted, this was repeated for both Y and X-axis. The grain size was then calculated using equation 3.9.

$$Gs = \frac{L}{n} \quad (3.9.)$$

Where Gs is the grain size, L is the length of the line and n is the number of grains that intercept the line.

3.5.4. Glow-discharge optical emission spectrometry

Glow-discharge optical emission spectrometry (GDOES) is an analytical technique that can be used to identify the composition of a metal/alloy or organic polymer.

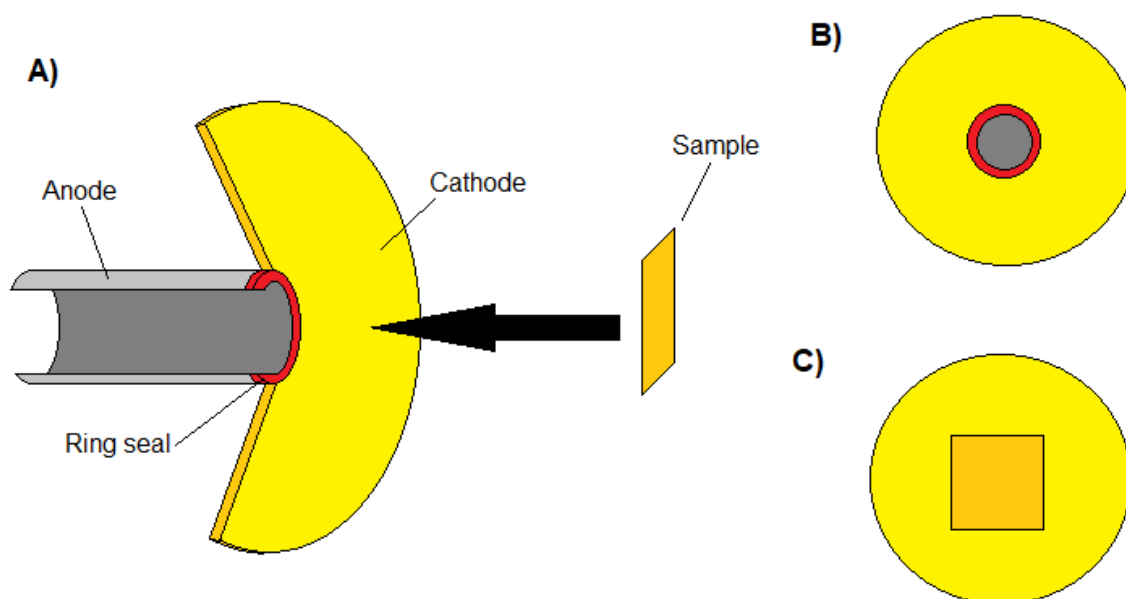


Figure 3.9. Diagram of GDOES inner workings A) Side view of GDOES anode and cathode setup. B) End view of GDOES anode and cathode. C) End view of GDOES anode and cathode with sample in place.

In GDOES the sample is placed onto a cathode becoming the cathode itself (Figure 3.9.). The glow-discharge is filled with argon gas under low pressure, a DC voltage is then applied between the cathode and anode which causes electrons to be released from the surface of the sample. The electrons gain kinetic energy as they are accelerated towards the anode. The electrons collide with argon atoms producing a plasma of argon cations electrons and neutral argon atoms. The argon cations are accelerated towards the samples surface, colliding with it releasing atoms from the sample. The sample atoms diffuse into the plasma where colliding with high energy electrons, exciting the sample atoms to a higher energy state. When the sample atoms relax back to the ground state they release light of a characteristic wavelength. The wavelength is characteristic of that particular atom and the intensity of the light is proportional to its concentration [33,34].

GDOES was used in this research project to quantify the turmeric concentration in the coatings.

Coating samples were prepared as per Section 3.3. The coatings were then thoroughly washed with deionised water and dried with an electric hair drier. The samples were then given to Tekniker IK4 in Spain, where GDOES was conducted on a Horiba GD profiler 2. The result of the GDOES analysis were plotted onto a graph of element percentage (y axis) vs depth of coating (x axis) by Tekniker IK4.

3.6. Statistical analysis

The comparison between the means of two samples is not an accurate method of determining the similarity or difference between those two samples. It is possible for Two samples to have the same mean value but completely different behaviour.

An example of how the mean can be misleading is given in Table 3.6. Sample (A) shows uniform microhardness across the surface of the sample with a mean value of 100 HV. Sample (B) shows very different behaviour with areas of lower and higher microhardness when compared to sample (A) but has the same mean value. Sample (C) shows much closer behaviour to sample (A) however one outlier gives it a greater mean value than both samples (A) and (B).

Table 3.6. Example of hardness taken at five locations across the surface of three samples.

Area of sample	Microhardness sample A HV	Microhardness sample B HV	Microhardness sample C HV
1	101	150	101
2	99	50	99
3	100	225	100
4	101	50	101
5	99	25	130
Mean value	100	100	106

Statistical analysis allows the correct interpretation of data, quantifying the similarity or difference between two sets of data and indicating if the similarity or difference is meaningful (significant) and not just a chance occurrence.

In the research presented here standard deviation (σ) was used to assess the variation in the data and calculate, standard error, T values and F values (3.10). Standard error was used to plot error bars on all graphs (3.11.). A Dixon Q-test was used to assess the validity of outliers in the data (3.12.). In this research F-tests (3.13.) were used to assess if the similarity between two deposits was meaningful (significant), and T-tests (3.14.) were used to assess if the difference between two deposits was meaningful.

$$\sigma = \sqrt{\frac{\sum (x - x^o)^2}{n-1}} \quad (3.10.)$$

$$SE = \frac{\sigma}{\sqrt{n}} \quad (3.11.)$$

$$Q = \frac{gap}{range} \quad (3.12.)$$

$$F = \frac{\sigma_1^2}{\sigma_2^2} \quad (3.13.)$$

$$T = \frac{(x1 - x2)}{\sqrt{\frac{\sigma_1^2}{n1} + \frac{\sigma_2^2}{n2}}} \quad (3.14.)$$

Where x is the sum of the data set, x^o is the mean of the data set and n is the number of data points. σ_1^2 is the standard deviation for highest variation squared, $x1$ the mean for that variance and $n1$ is the number of data points for that variance, σ_2^2 is the standard deviation for lowest variation squared, $x2$ the mean for that variance and $n2$ is the number of data points for that variance.

3.7. Reference list

- [1] T. Mason, Practical sonochemistry user's guide to application in chemistry and chemical engineering, UK: Ellis Horwood. (1991).
- [2] I. Tudela, Y. Zhang, M. Pal, I. Kerr, A.J. Cobley, Ultrasound-assisted electrodeposition of composite coatings with particles, Surface and Coatings Technology. 259 (2014) 363-373.
- [3] K. Sato, J. Li, H. Kamiya, T. Ishigaki, Ultrasonic dispersion of TiO₂ nanoparticles in aqueous suspension, Journal of the American Ceramic Society. 91 (2008) 2481-2487.
- [4] T. Hielscher, Ultrasonic production of nano-size dispersions and emulsions, arXiv preprint arXiv:0708.1831. (2007).
- [5] R. Kachanoski, R. Voroney, E. Gregorich, Ultrasonic dispersion of aggregates: distribution of organic matter in size fractions, Canadian Journal of Soil Science. 68 (1988) 395-403.
- [6] L. Chen, L. Wang, Z. Zeng, J. Zhang, Effect of surfactant on the electrodeposition and wear resistance of Ni–Al₂O₃ composite coatings, Materials Science and Engineering: A. 434 (2006) 319-325.
- [7] H. Gül, F. Kılıç, M. Uysal, S. Aslan, A. Alp, H. Akbulut, Effect of particle concentration on the structure and tribological properties of submicron particle SiC reinforced Ni metal matrix composite (MMC) coatings produced by electrodeposition, Applied Surface Science. 258 (2012) 4260-4267.
- [8] M. Kaszuba, Basic Principles of Dynamic Light Scattering, (2015).
- [9] Malvern Instruments Ltd, Size: What is z-average? 2017.
- [10] W. Basecoat, In the Metal Finishing Field, Metal Finishing. (1995) 87.
- [11] A. Wang, B. Chen, L. Fang, J. Yu, L. Wang, Influence of branched quaternary ammonium surfactant molecules as levelers for copper electroplating from acidic sulfate bath, Electrochimica Acta. 108 (2013) 698-706.
- [12] H. Creutz, R.W. Herr, Electrodeposition of copper. (1978).
- [13] M. Lekka, N. Kouloumbi, M. Gajo, P.L. Bonora, Corrosion and wear resistant electrodeposited composite coatings, Electrochimica Acta. 50 (2005) 4551-4556.
- [14] S. Lajevardi, T. Shahrabi, Effects of pulse electrodeposition parameters on the properties of Ni–TiO₂ nanocomposite coatings, Applied Surface Science. 256 (2010) 6775-6781.

- [15] S. Aruna, C. Bindu, V.E. Selvi, V.W. Grips, K. Rajam, Synthesis and properties of electrodeposited Ni/ceria nanocomposite coatings, *Surface and Coatings Technology*. 200 (2006) 6871-6880.
- [16] C. Low, J. Bello, J. Wharton, R. Wood, K. Stokes, F. Walsh, Electrodeposition and tribological characterisation of nickel nanocomposite coatings reinforced with nanotubular titanates, *Surface and Coatings Technology*. 205 (2010) 1856-1863.
- [17] R. Zangi, B. Berne, Aggregation and dispersion of small hydrophobic particles in aqueous electrolyte solutions, *The Journal of Physical Chemistry B*. 110 (2006) 22736-22741.
- [18] D. François, A. Pineau, A. Zaoui, *Mechanical Behaviour of Materials: Volume II: Fracture Mechanics and Damage*, Springer Science & Business Media, 2012.
- [19] P. Jenei, E.Y. Yoon, J. Gubicza, H.S. Kim, J.L. Lábár, T. Ungár, Microstructure and hardness of copper–carbon nanotube composites consolidated by High Pressure Torsion, *Materials Science & Engineering A*. 528 (2011) 4690-4695.
- [20] P. Hariharan, *Basics of Interferometry*, Elsevier, 2010.
- [21] S.V. Baryshev, A.V. Zinovev, C.E. Tripa, R.A. Erck, I.V. Veryovkin, White light interferometry for quantitative surface characterization in ion sputtering experiments, *Applied Surface Science*. 258 (2012) 6963-6968.
- [22] Gamry Instruments, *Getting Started with Electrochemical Corrosion Measurement*. Application note, Gamry instruments. (2011).
- [23] D. Prasai, J.C. Tuberquia, R.R. Harl, G.K. Jennings, K.I. Bolotin, Graphene: corrosion-inhibiting coating, *ACS nano*. 6 (2012) 1102-1108.
- [24] S. Hassani, K. Roberts, S. Shirazi, J. Shadley, E. Rybicki, C. Joia, Flow loop study of NaCl concentration effect on erosion, corrosion, and erosion-corrosion of carbon steel in CO₂-saturated systems, *Corrosion, The Journal of Science and Engineering*. 68 (2012) 026001-1-026001-9.
- [25] A. Khursheed, *Scanning Electron Microscope Optics and Spectrometers*, World scientific, 2011.
- [26] S. J.W.S. Hearle, J.T. Sparrow, P.M. Cross, *Use of the Scanning Electron Microscope*, 1972.
- [27] J.H. Wittke, *Electron microanalysis core facility*, 2017.
- [28] S. Reyntjens, R. Puers, A review of focused ion beam applications in microsystem technology, *Journal of Micromechanics and Microengineering*. 11 (2001) 287.
- [29] J. Gierak, *Focused ion beam technology and ultimate applications*, *Semiconductor science and technology*. 24 (2009) 043001, 2012.

- [30] M.D. Abràmoff, P.J. Magalhães, S.J. Ram, Image processing with ImageJ, *Biophoton Int.* 11 (2004) 36-42.
- [31] A. Thorvaldsen, The intercept method—2. Determination of spatial grain size, *Acta materialia*. 45 (1997) 595-600.
- [32] H. Engqvist, B. Uhrenius, Determination of the average grain size of cemented carbides, *International Journal of Refractory Metals and Hard Materials*. 21 (2003) 31-35.
- [33] P. Sánchez, B. Fernández, A. Menéndez, J. Orejas, R. Pereiro, A. Sanz-Medel, Quantitative depth profile analysis of metallic coatings by pulsed radiofrequency glow discharge optical emission spectrometry, *Analytica Chimica Acta* 684 (2011) 47-53.
- [34] R.K. Marcus, J.A. Broekaert, *Glow Discharge Plasmas in Analytical Spectroscopy*, Wiley Online Library, 2003.

4. Turmeric preparation

4.1. Overview

The particles deposited in an electrodeposited composite coating are a crucial part of the coatings properties [1-3]. The concentration of particles, the particle size, shape, type and even the charge of the particles in the electrolyte can affect the particle content of the deposit and thus the properties of the composite coating [1]. To ensure properties are uniform throughout the composite coating, the particles must be dispersed evenly throughout the coating [4-6], and to ensure the even dispersion of particles in the coating, a well dispersed electrolyte free from agglomerates is desired [1].

The study in this Chapter aimed to optimise the dispersion and de-agglomeration of turmeric particles in the electrolyte. The study was structured in 3 sections:

- Turmeric morphology pre-dispersion: turmeric powder was viewed under SEM, to assess the size and shape of turmeric particles before dispersion in the electrolyte.

- Deagglomeration: turmeric was dispersed into copper electrolyte mimic by stirring and ultrasound, to assess the most suitable method of dispersion and de-agglomeration.
- Z-average size: the effect of concentration and ultrasound power on the turmeric particle size was assessed using DLS.

4.2. Turmeric particle morphology

Figure 4.1. and Figure 4.2. Shows SEM images of turmeric powder before dispersion in the copper electrolyte mimic.

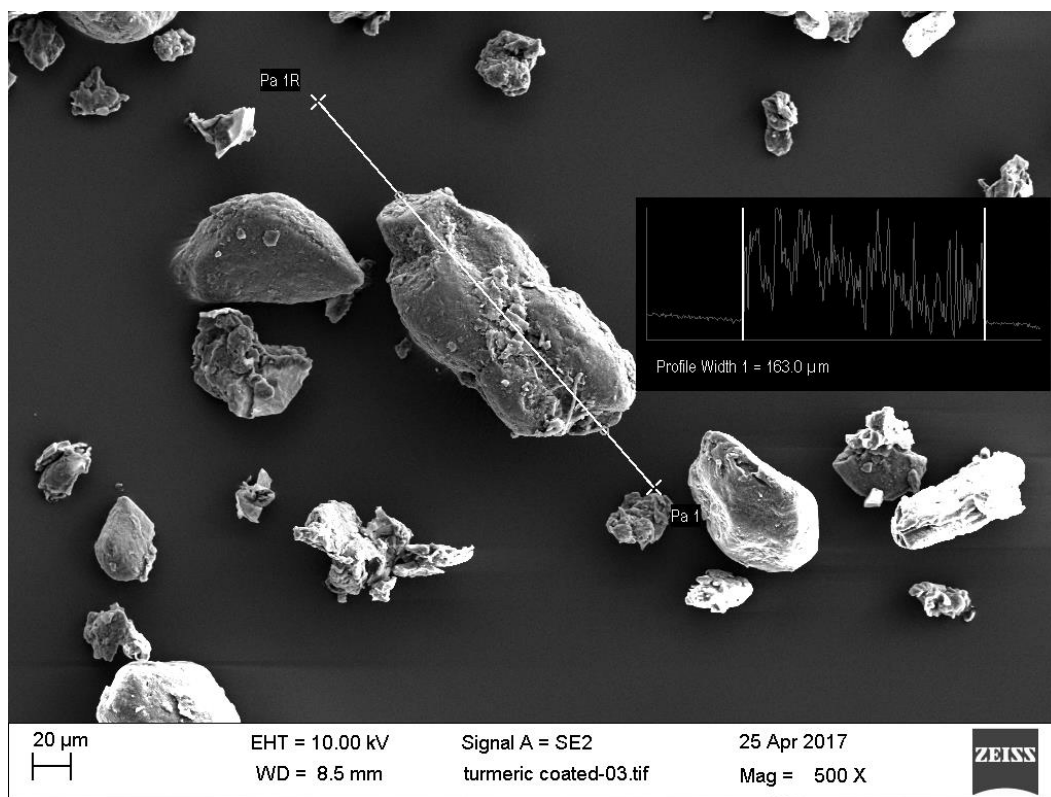


Figure 4.1. SEM image of larger turmeric particles before dispersion in copper electrolyte mimic.

The turmeric particles pre-dispersion exhibited a broad range of morphologies and sizes. Figure 4.1. Shows great variation in the morphology and size of turmeric particles, with larger turmeric particles present having dimensions greater than 160 μm . Figure 4.2. Shows smaller turmeric particles, again with a wide variation in morphologies and sizes, with particles of less than 40 μm present.

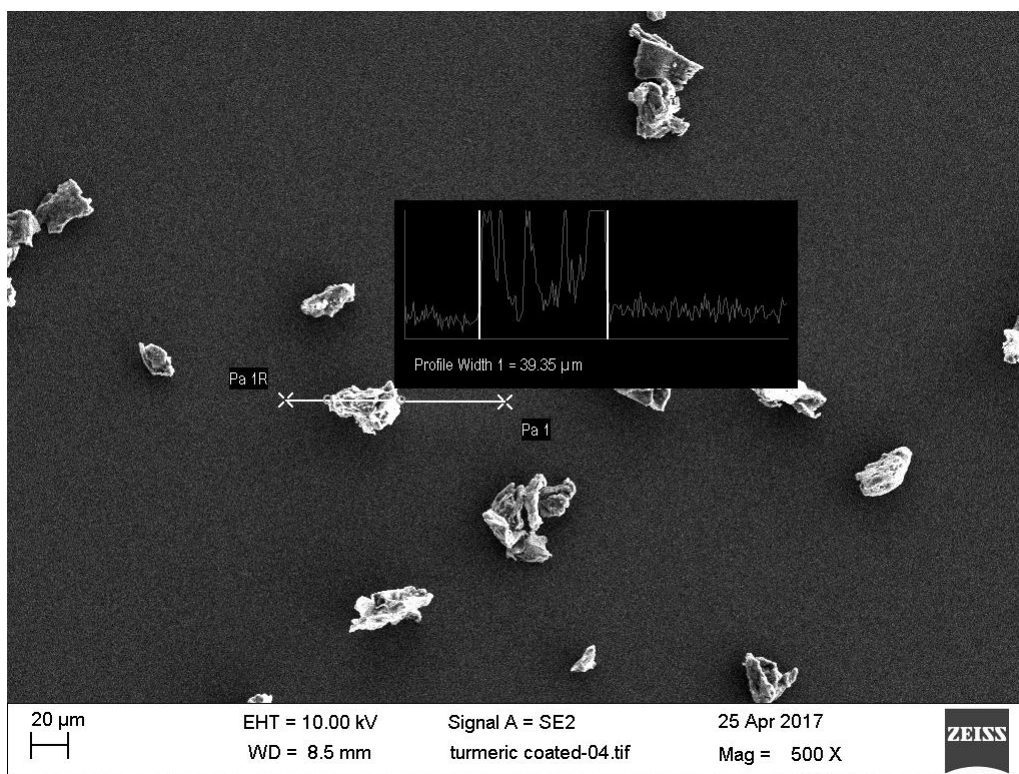


Figure 4.2. SEM image of smaller turmeric particles before dispersion in copper electrolyte mimic.

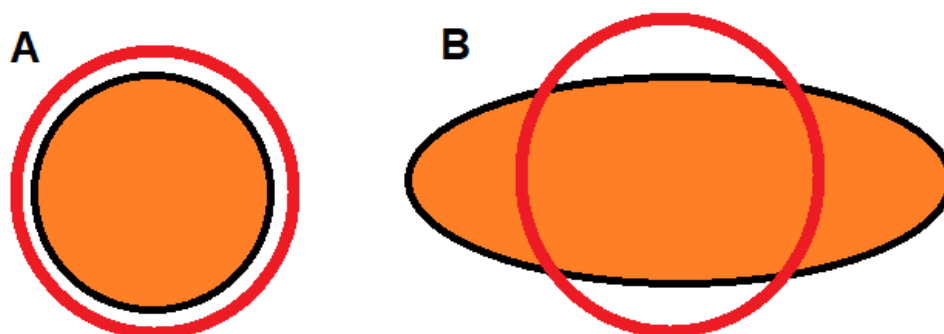


Figure 4.3. Diagram of Z-average size of particles in solution measured by Dynamic light scattering (DLS). (A) Shows a spherical particle with a red circle representing a hydrodynamic sphere. (B) Shows a non-spherical particle with a red circle representing a hydrodynamic sphere.

Dynamic light scattering (DLS) measurements assume that the particles being measured are spherical or near spherical (Figure 4.3.), however, SEM images of the turmeric particles showed this was not the case before dispersion. The diffusion of non-spherical particles in solution may be different to their hydrodynamic sphere calculated by DLS.

4.3. Turmeric deagglomeration experiment

4.3.1. Effects of stirring on deagglomeration

Figure 4.4. Shows the Z-average size of turmeric particles at varying concentrations of turmeric in the electrolyte mimic after 20 min stirring with a 35 mm mechanical stirring bar at 240 rpm.

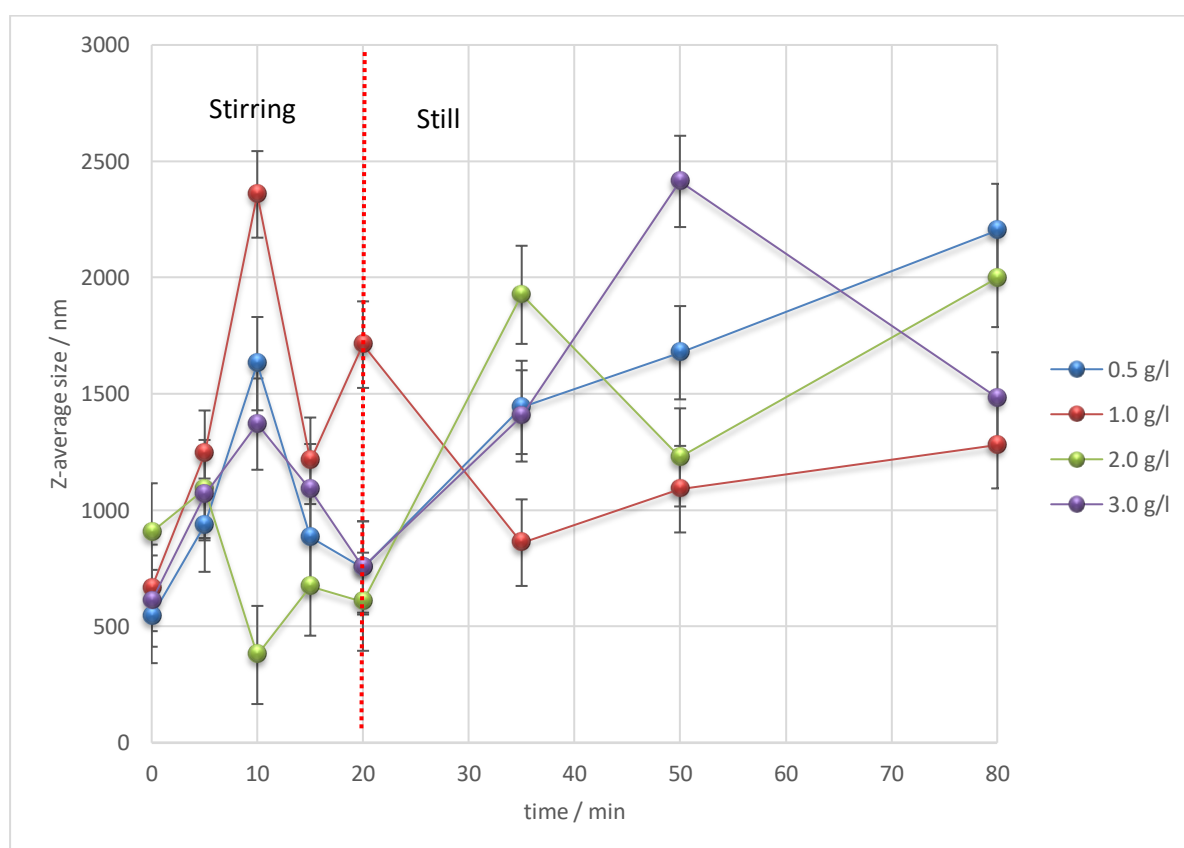


Figure 4.4. The effects of stirring on the Z-average size of turmeric particles at concentrations of 0.5 g/l, 1.0 g/l, 2.0 g/l and 3.0 g/l of turmeric in copper electrolyte mimic. The solutions were stirred for 20 min then left to settle for 1 hour.

After 20 min of stirring the turmeric Z-average size had remained unchanged (within error) for the concentrations of 0.5 g/l, 1.0 g/l, and 2.0 g/l, and increased for the concentration of 3.0 g/l. After stirring was stopped the Z-average increased for all concentrations. At the end of the experiment, the Z-average size for all concentrations was larger than the initial Z-average size. Figure 4.5. Shows the polydispersity index of turmeric particles at varying concentrations of turmeric in the electrolyte mimic after 20 min stirring with a 35 mm mechanical stirring bar at 240 rpm.

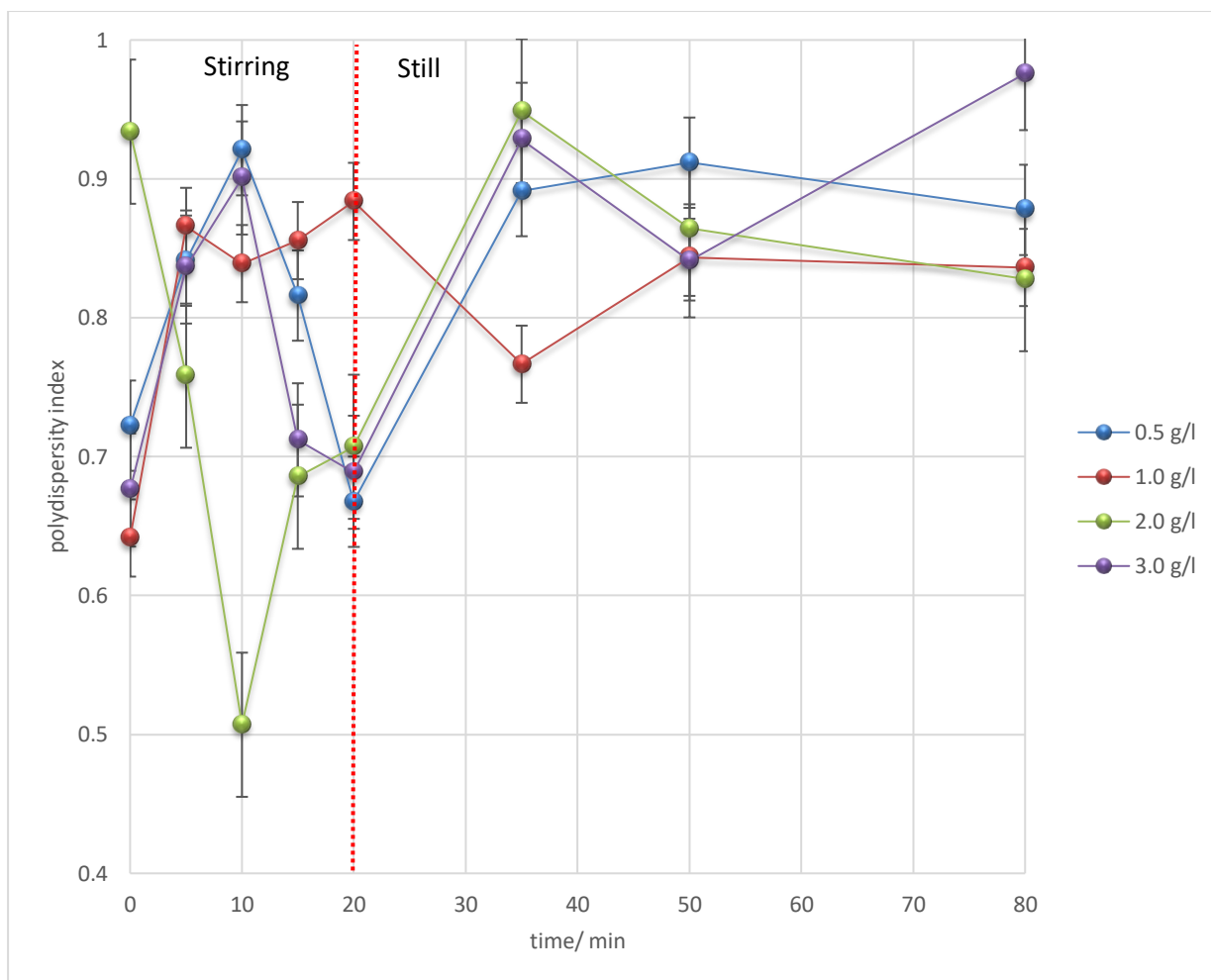


Figure 4.5. The effects of stirring on the polydispersity index of turmeric particles at concentrations of 0.5 g/l, 1.0 g/l, 2.0 g/l and 3.0 g/l in copper electrolyte mimic. The solutions were stirred for 20 min then left to settle for 1 hour.

After 20 min of stirring the turmeric particles polydispersity index had remained unchanged within error for the concentrations of 0.5 g/l and 3.0 g/l, and had decreased for the concentration of 2.0 g/l and increased for 1.0 g/l. After stirring was stopped the polydispersity index increased for the concentrations of 0.5 g/l, 2.0 g/l, and 3.0 g/l, and remained unchanged within error for the concentration of 1.0 g/l. At the end of the experiment, the polydispersity index for all concentrations was above 0.7.

Figure 4.6. Shows how the percentage of turmeric particles in range of detection changes with varying turmeric concentration in the electrolyte mimic after 20 min stirring with a 35 mm mechanical stirring bar at 240 rpm.

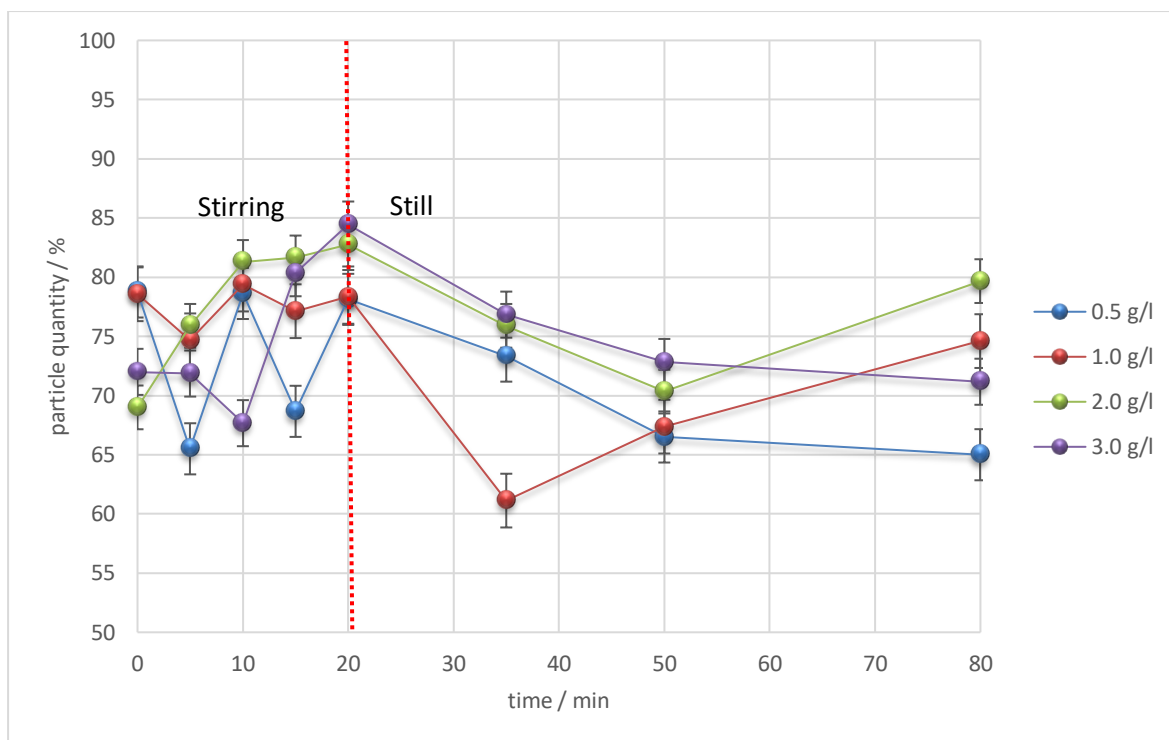


Figure 4.6. The effects of stirring on the percentage of turmeric particles in range of detection at concentrations of 0.5 g/l, 1.0 g/l, 2.0 g/l and 3.0 g/l in copper electrolyte mimic. The solutions were stirred for 20 min then left to settle for 1 hour.

After 20 min of stirring the percentage of turmeric particles with sizes in range of detection (10 nm to 6500 nm) had increased for the concentrations of 2.0 g/l and 3.0 g/l, and had not changed for the concentrations of 0.5 g/l and 1.0 g/l. After stirring was stopped the percentage of turmeric particles with sizes in range of detection initially decreased for all concentrations before increasing for the concentrations of 1.0 g/l and 2.0 g/l. At the end of the experiment, the percentage of turmeric particles with sizes in range of detection had increased for the concentration of 2.0 g/l, decreased for the concentration of 0.5 g/l and remained unchanged for 1.0 g/l and 3.0 g/l within error.

Stirring had little effect on the Z-average size and polydispersion index of the turmeric particles in solution, however a slight improvement in the number of particles with sizes in range of detection was seen. This may indicate that particles above the range of detection (6500 nm) are being broken down to a size close to the Z-average (within error of 200 nm), or there is a progressive break down of particles (of a wide range of sizes) so that the overall Z-average size is not changed (Figure 4.7.).

Once stirring was stopped and the solutions left to settle, the Z-average size and the polydispersity index increased, this would suggest that the turmeric particles were agglomerating in solution.

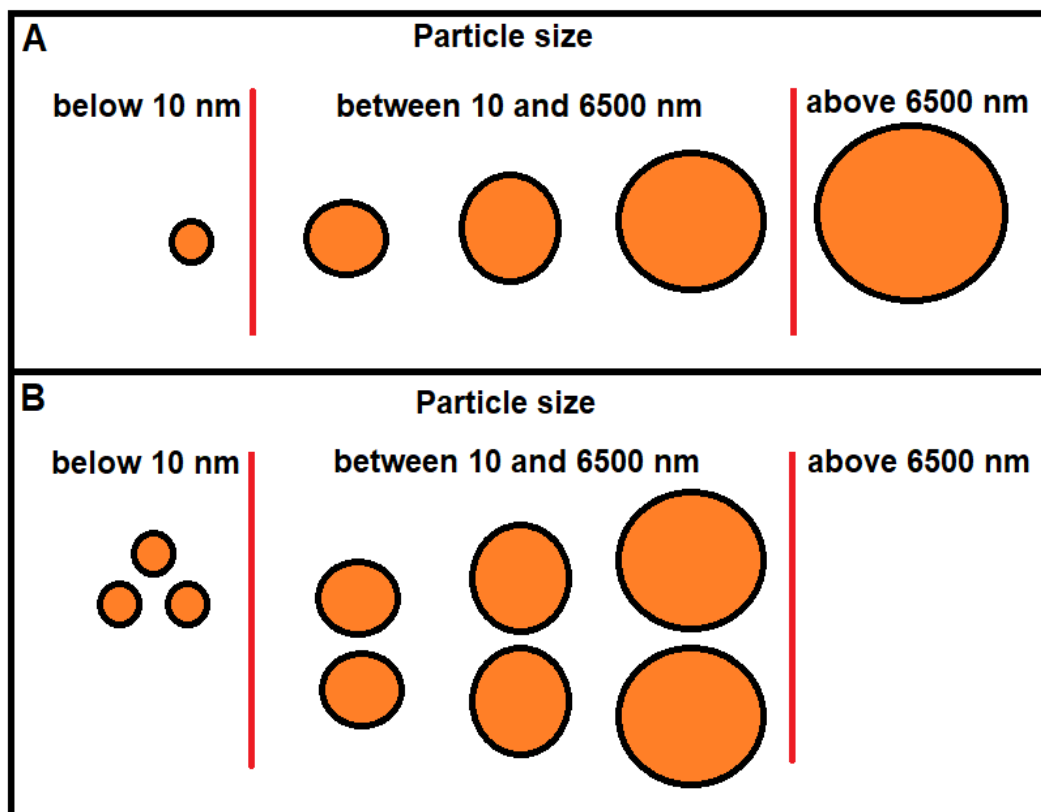


Figure 4.7. Diagram of the progressive break down of turmeric particles in the copper electrolyte mimic. (A) Shows the size distribution of turmeric particles in the electrolyte (B) Shows the particle above 6500 nm has been broken down to a size in range of detection (10 to 6500 nm), however, particles in range of detection have also been broken down, some to a size outside the range of detection (less than 10 nm). The reverse mechanism (e.g. from B to A) would represent the agglomeration of particles in the electrolyte.

4.3.2. Effects of ultrasound on deagglomeration

Figure 4.8 to 4.11. Shows graphs of the change in Z-average size over time with the application of ultrasound from a 20 kHz horn at 11 W/l. Figure 4.12. and Figure 4.13. Show graphs of the change in polydispersity over time with the application of ultrasound from a 20 kHz horn at 11 W/l.

After 20 min of ultrasound with a 20 kHz horn at a power of 11 W/l the turmeric mean Z-average size had significantly decreased for all concentrations. After ultrasound was stopped and the solutions left to settle for 1 hour, no significant change in the mean Z-average was observed for all concentrations.

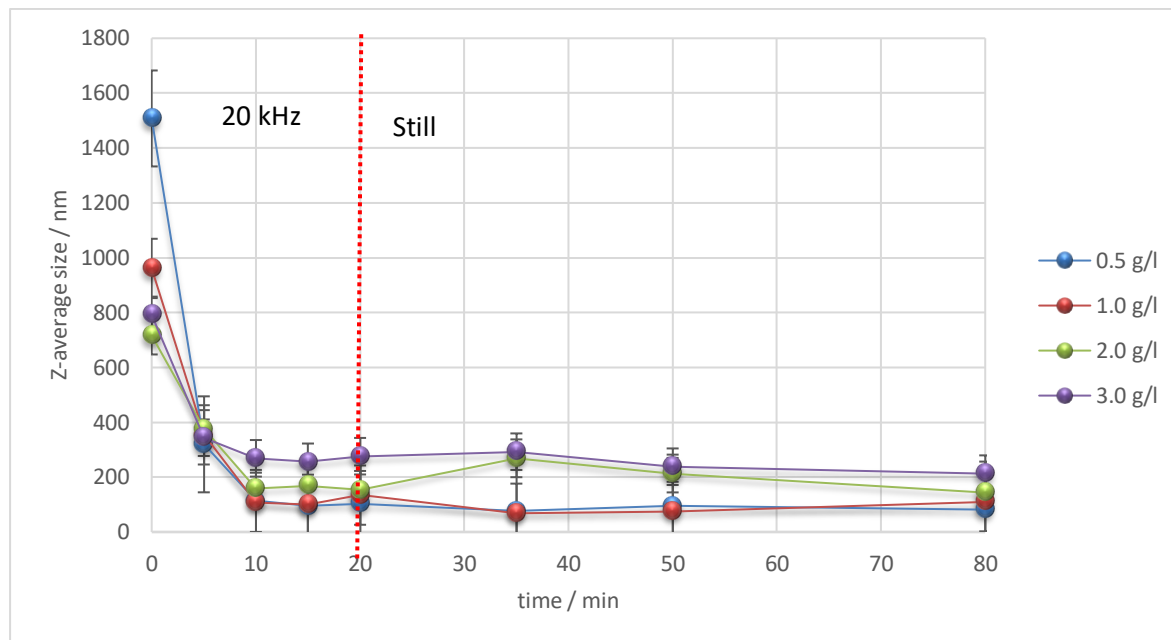


Figure 4.8. The effects of 20 kHz ultrasound at a power of 11 W/l on the Z-average size of turmeric particles in copper electrolyte mimic. The solutions were sonicated for 20 min then left to stand for 1 hour.

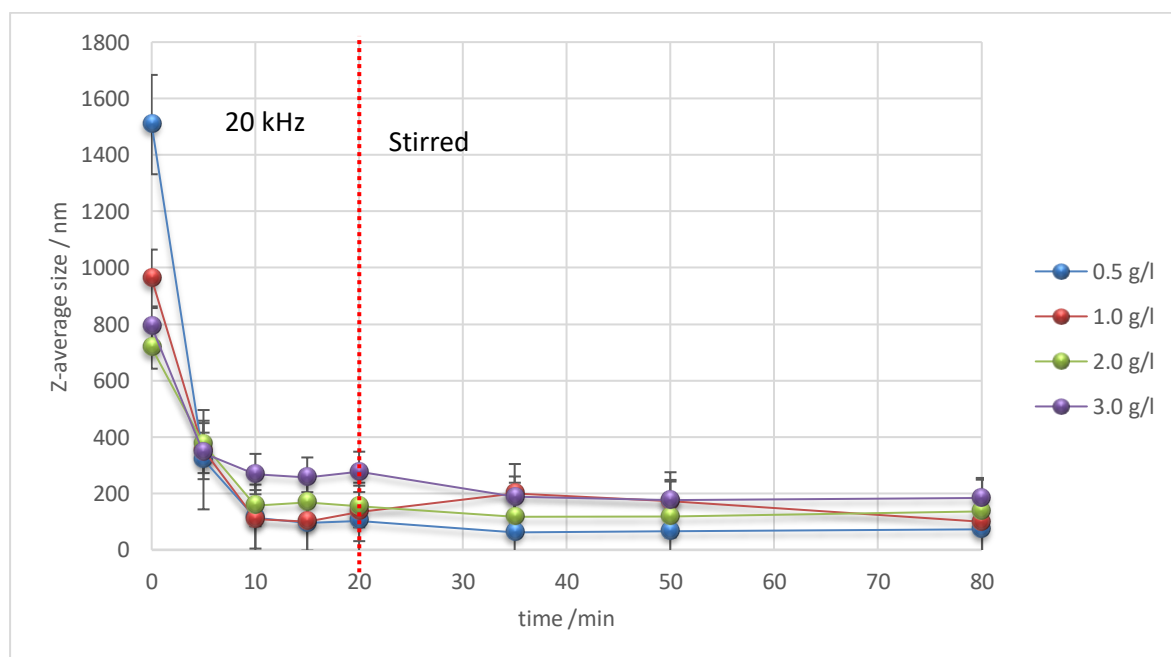


Figure 4.9. The effects of 20 kHz ultrasound at a power of 11 W/l on the Z-average size of turmeric particles in copper electrolyte mimic. The solutions were sonicated for 20 min then stirred for 1 hour.

Stirring the solution for 1 hour after ultrasound again made no significant difference to the observed mean Z-average size of the turmeric particles in solution. Increasing the duration of ultrasound from 20 min to 30 min also showed no significant effect on the turmeric mean Z-average size. Although a small reduction in the mean Z-average size was observed, this was within error of the mean Z-average size after 20 min sonication. Again no significant difference in the mean Z-average size of turmeric particle was observed, if the solutions were left still or stirred for 1 hour after 30 min ultrasound.

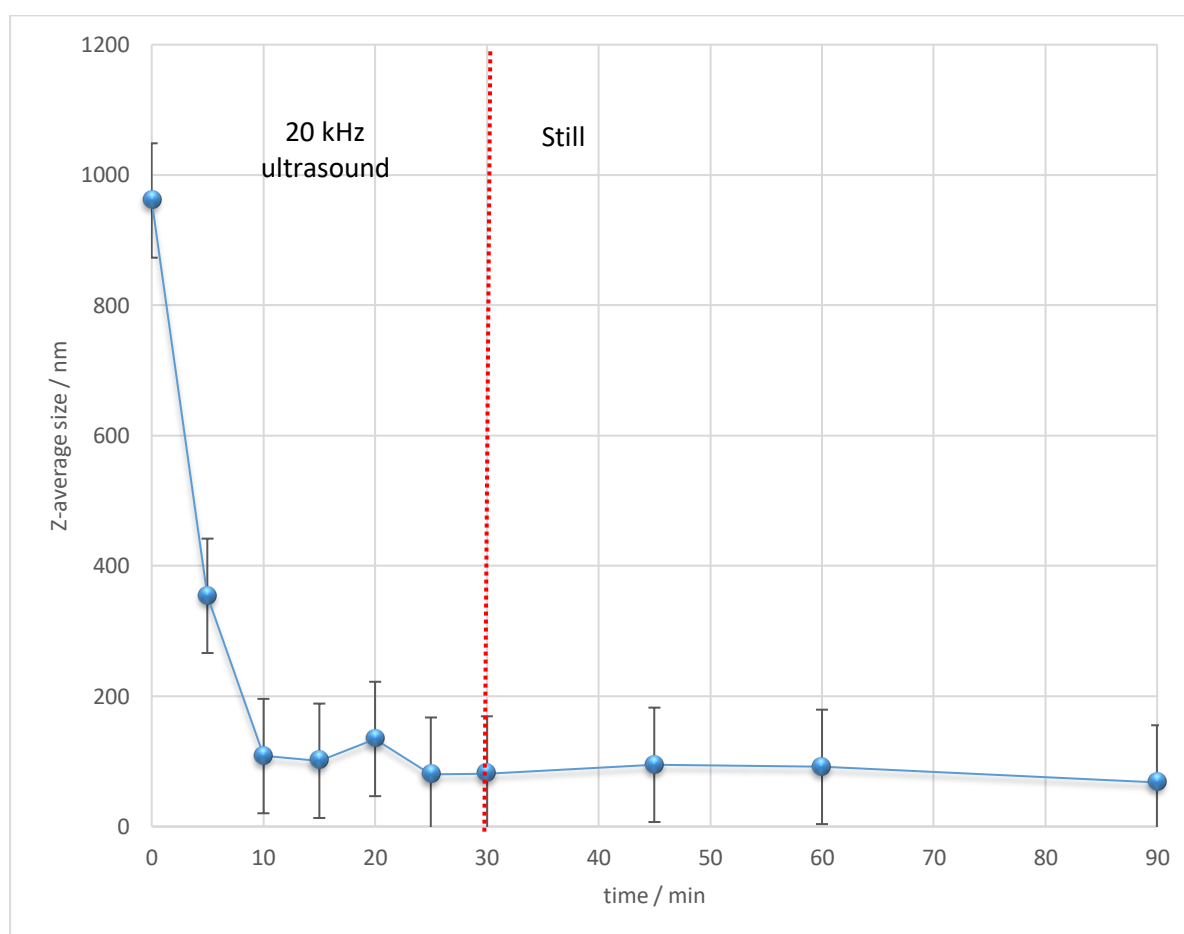


Figure 4.10. The effects of 20 kHz ultrasound at a power of 11 W/l on the Z-average size of turmeric particles, at a concentration of 0.1% in copper electrolyte mimic. The solution was sonicated for 30 min then left to settle for 1 hour.

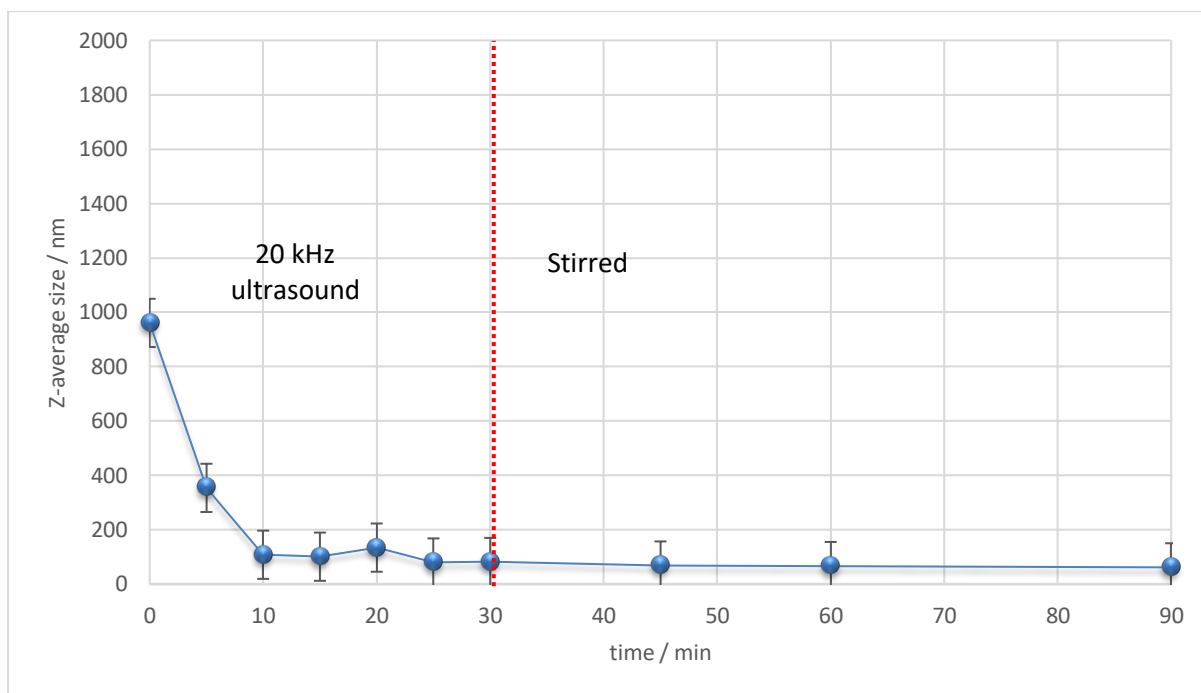


Figure 4.11. The effects of 20 kHz ultrasound at a power of 11 W/l on the Z-average size of turmeric particles, at a concentration of 0.1% in copper electrolyte mimic. The solution was sonicated for 30 min then stirred for 1 hour.

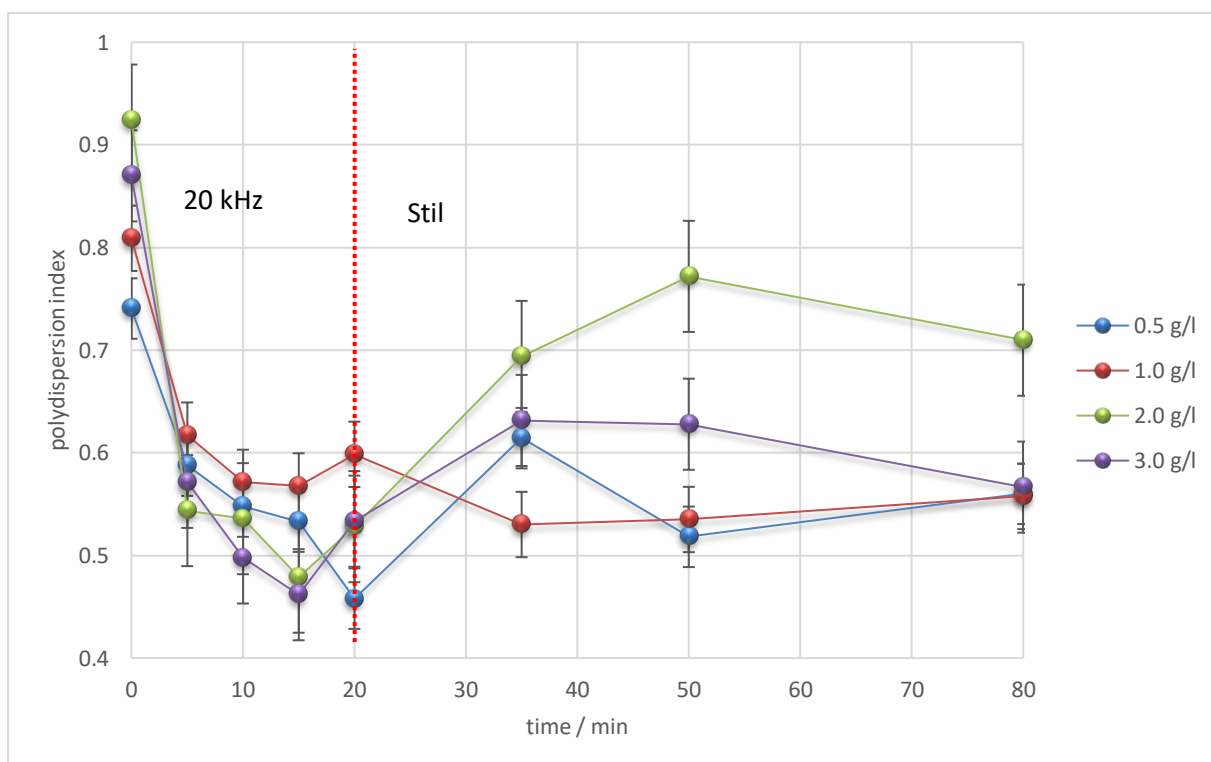


Figure 4.12. The effects of 20 kHz ultrasound at a power of 11 W/l on the polydispersity index of turmeric particles at concentrations of 0.5 g/l, 1.0 g/l, 2.0 g/l and 3.0 g/l in copper electrolyte mimic. The solutions were sonicated for 20 min then left to settle for 1 hour.

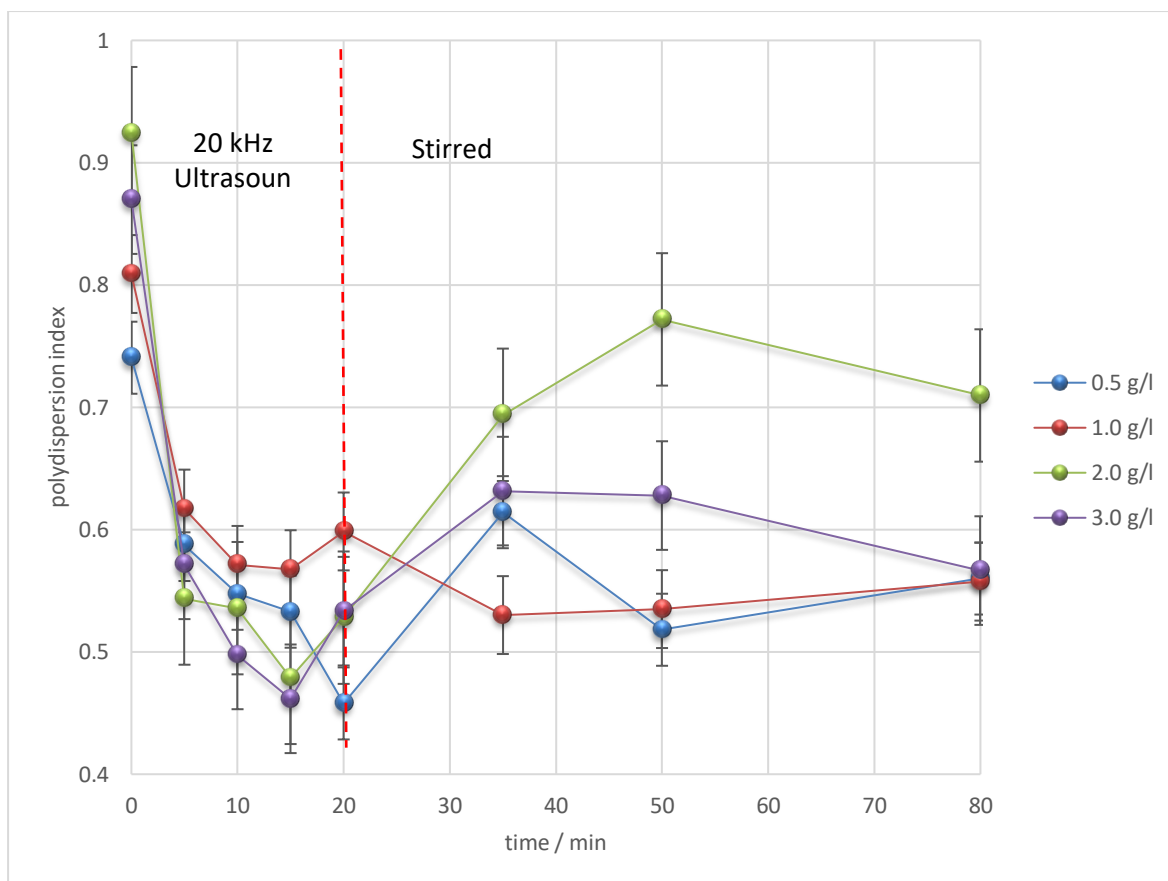


Figure 4.13. The effects of 20 kHz ultrasound at a power of 11 W/l on the polydispersity index of turmeric particles at concentrations of 0.5 g/l, 1.0 g/l, 2.0 g/l and 3.0 g/l in copper electrolyte mimic. The solutions were sonicated for 20 min then stirred for 1 hour.

The application of ultrasound from a 20 kHz horn at a power of 11 W/l had a significant effect on the polydispersity index. After 20 min the polydispersity index had decreased to below 0.7 for all concentrations (below 0.5 for the concentration of 1.0 g/l). After the ultrasound was stopped and the solutions left to stand for 1 hour, the polydispersity index increased for the concentrations of 0.5 g/l, 2.0 g/l and 3.0 g/l (above 0.7 for 3.0 g/l), and remained largely unchanged for the concentration of 1.0 g/l.

Stirring the solutions for 1 hour after ultrasound showed no significant improvement to the polydispersity index when compared to the left to stand solutions (Figure 4.13.). For the concentrations of 0.5 g/l and 2.0 g/l the polydispersity index was seen to increase, but remained largely unchanged (within error) for the concentrations of 1.0 g/l and 3.0 g/l. After the full duration of the experiment all concentrations whether left to stand or stirred for 1 hour after ultrasound showed a reduction in the polydispersity index from their initial values.

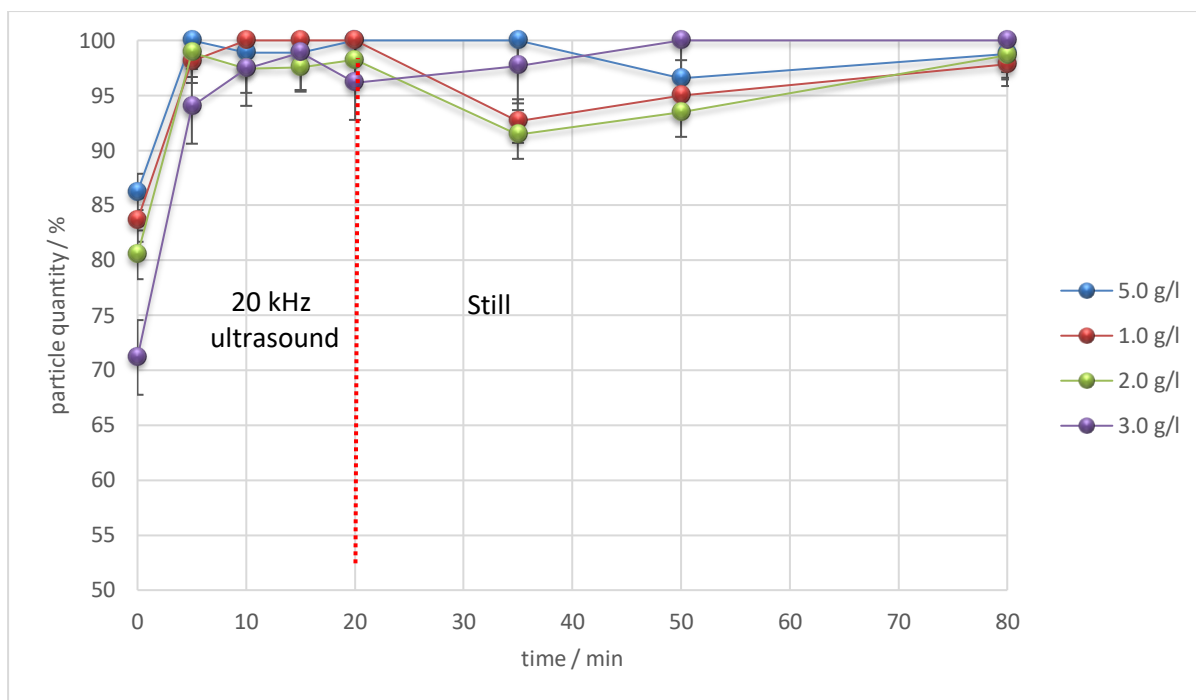


Figure 4.14. The effects of 20 kHz ultrasound at a power of 11 W/l on the percentage of turmeric particles in range of DLS detection at concentrations of 0.5 g/l, 1.0 g/l, 2.0 g/l and 3.0 g/l in copper electrolyte mimic. The solutions were sonicated for 20 min then left to settle for 1 hour.

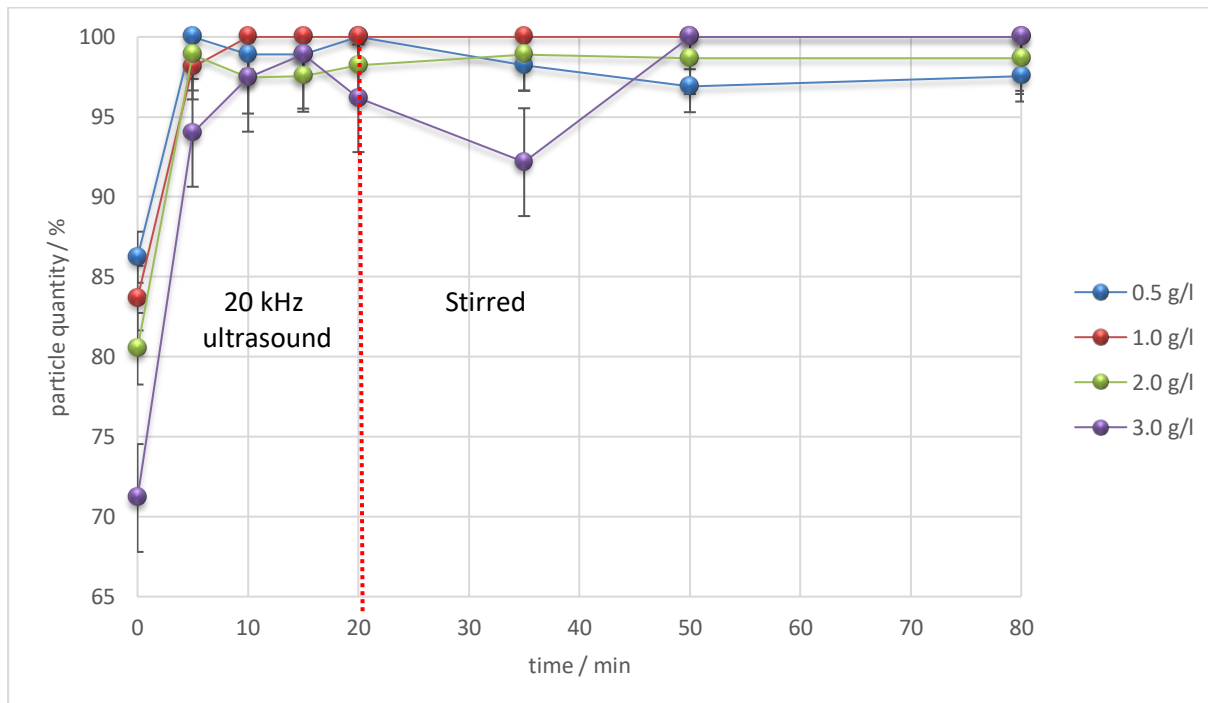


Figure 4.15. The effects of 20 kHz ultrasound at a power of 11 W/l on the percentage of turmeric particles in range of detection at concentrations of 0.5 g/l, 1.0 g/l, 2.0 g/l and 3.0 g/l in copper electrolyte mimic. The solutions were sonicated for 20 min then left to settle for 1 hour.

Figure 4.14. and Figure 4.15. Show the percentage of turmeric particles with a size in range of detection after the application of ultrasound from a 20 kHz horn at a power of 11 W/l. The percentage of turmeric particles with sizes in range of detection (from 10 nm to 6500 nm) after 20 min ultrasound significantly increased for all concentrations. After ultrasound was stopped and the solutions left still for 1 hour, the percentage of turmeric particles with a size in range of detection initially decreased before increasing again for all. Stirring the solutions for 1 hour after ultrasound showed no significant improvement to the percentage of particles with a size in range of detection when compared to the left to stand solutions. For the concentrations of 3.0 g/l there was an initial reduction in the percentage of particles with a size in range of detection before increasing again, all other concentrations remained largely unchanged once stirring was started. After the full duration of the experiment all concentrations whether left to stand or stirred for 1 hour after ultrasound showed a significant increase in the percentage of particles with a size in range of detection.

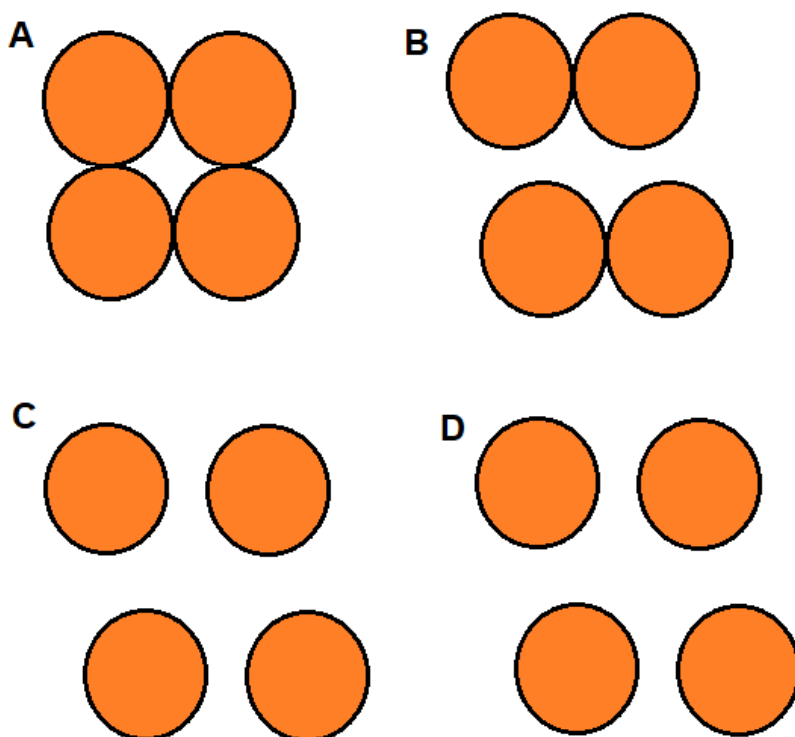


Figure 4.16. Diagram of the deagglomeration of turmeric particles in the copper electrolyte mimic. (A) The turmeric particles before ultrasound. (B) The turmeric particles after 10 min of ultrasound. (C) The turmeric particles after 20 min of ultrasound. (D) The turmeric particles after 30 min of ultrasound.

At all concentrations analysed the mean Z-average size, polydispersion index and number of particles in range of detection was improved after 20 min of ultrasound. However, increasing the ultrasound duration from 20 min to 30 min did not significantly improve the mean Z-average size, polydispersion index or number of particles in range of detection any further. Similar results have also been reported in the literature, where ultrasound progressively reduces particle size overtime up until a certain point is reached, after which ultrasound does not further reduce the size significantly [1,2]. This may be due to the maximum de-agglomeration of the turmeric particles being reached after 20 mins. The turmeric particles are initially agglomerated together in the solution, when ultrasound is applied the agglomerates start to break apart. After 20 min of ultrasound the majority of the agglomerates (that can be broken up at that ultrasound power) are already de-agglomerated. Increasing the duration of ultrasound after this will not significantly reduce the mean Z-average size any further (Figure 4.16.) [3-6].

4.4. Variation mean Z-average size

4.4.1. Variation at different concentrations

Figure 4.17. Shows how the mean Z-average size of turmeric particles changed with increasing turmeric concentration in the copper electrolyte mimic.

Increasing the turmeric concentration in the electrolyte mimic increased the mean Z-average size of the turmeric particles in solution. At a concentration of 1.0 g/l of turmeric, a mean Z-average size of 134 ± 37.0 nm was observed, at 5.0 g/l of turmeric, the mean Z-average size observed was 289 ± 30.0 nm, and at 10.0 g/l of turmeric, a mean Z-average size of 900 ± 184.0 nm was observed.

Figure 4.18. shows the size distribution of turmeric particles in the electrolyte mimic. After 20 min of ultrasound with a 20 kHz horn at a power of 11 w/l, the peak of highest intensity for all concentrations existed above 100 nm. As the concentration of turmeric was increased the peak of highest intensity was also increased and moved closer to the 1000 nm line. The peak below 100 nm decreased in intensity with increasing turmeric concentration, two peaks below 100 nm existed in the 10.0 g/l solution.

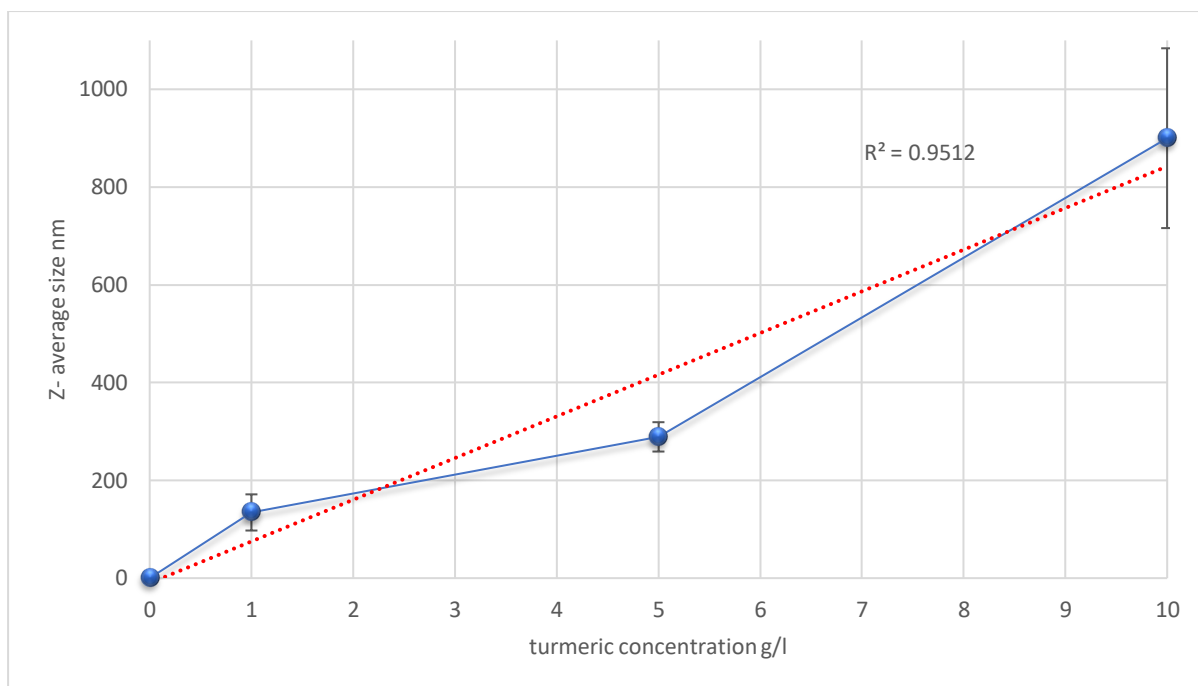


Figure 4.17. The effects of turmeric concentration in the copper electrolyte mimic had on mean Z-average size of turmeric particles in solution, after ultrasound of 20 kHz at a power of 11 W/l.

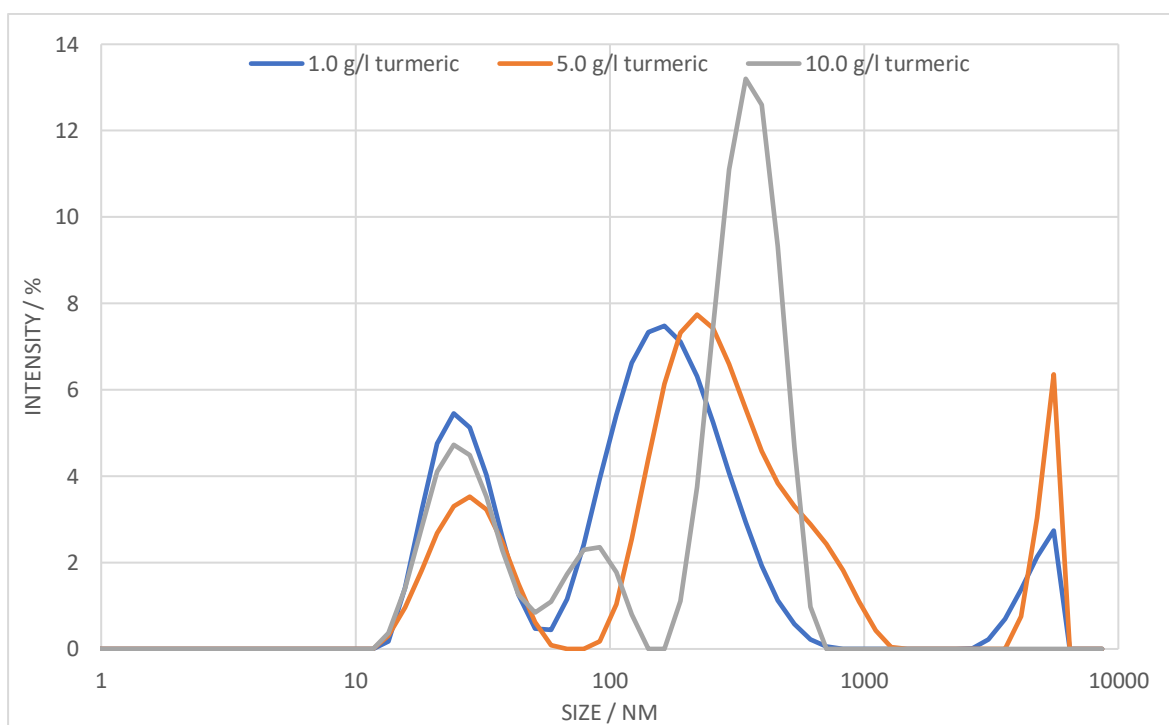


Figure 4.18. The size distribution of turmeric particles measured by signal intensity in a sample with a concentration of 1.0 g/l, 5.0 g/l and 10.0 g/l of turmeric in copper electrolyte mimic, after 20 kHz ultrasound from a horn at a power of 11 w/l for 20 minutes.

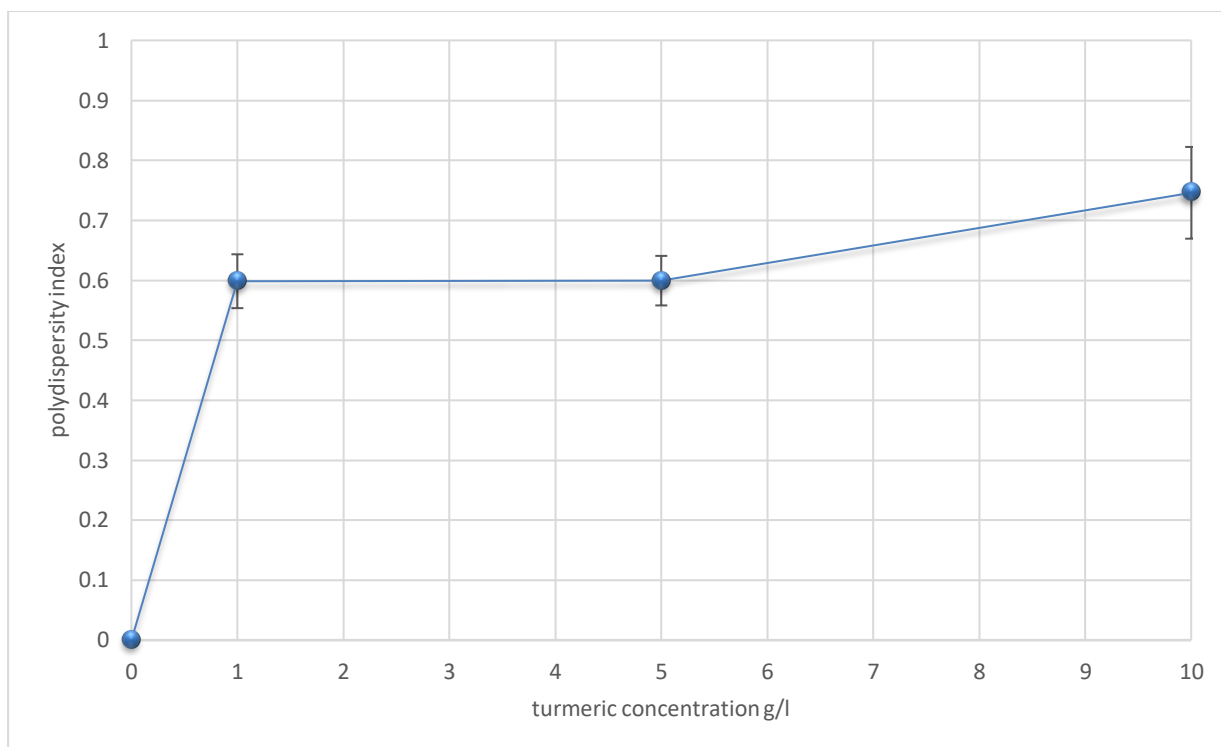


Figure 4.19. The effects of turmeric concentration (in the copper electrolyte mimic) on mean polydispersity index of turmeric particles in solution, after ultrasound of 20 kHz at a power of 11 W/l.

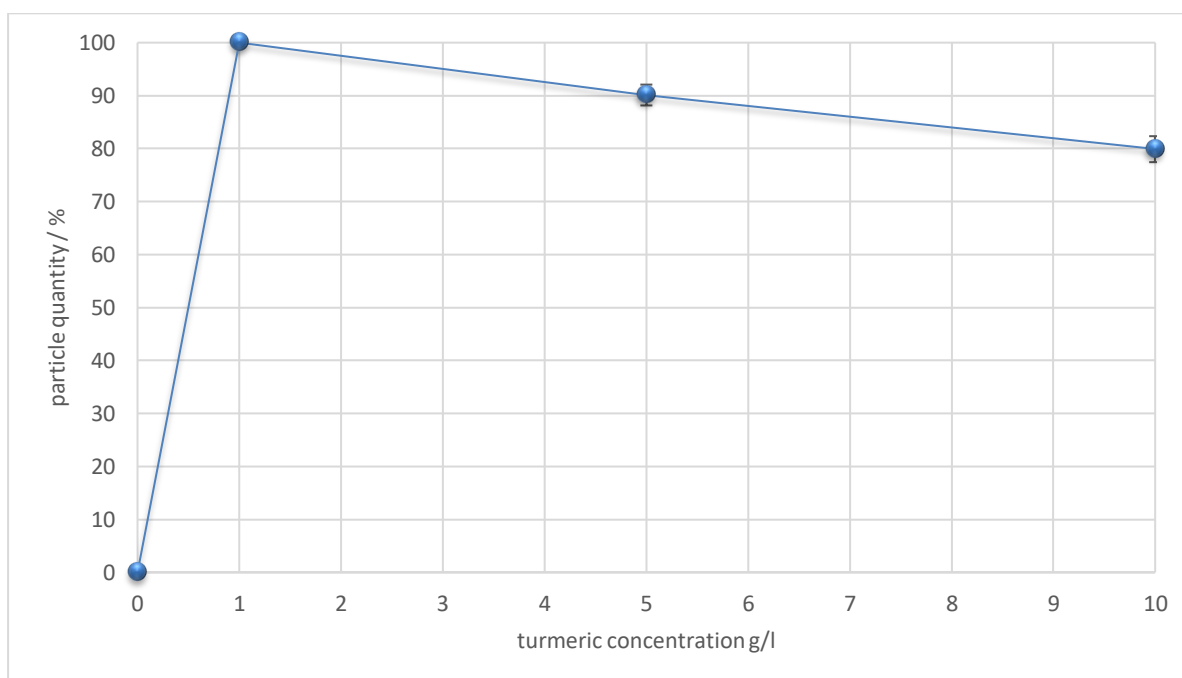


Figure 4.20. The effects of turmeric concentration (in the copper electrolyte mimic) on mean percentage of turmeric particles with a size in range of detection in solution, after ultrasound of 20 kHz at a power of 11 W/l.

Figure 4.19. Shows the change in polydispersity index with increasing turmeric concentration, and Figure 4.20. Shows the change in the percentage of particles in range of detection, with increasing turmeric concentration. Increasing the concentration of turmeric from 1.0 g/l to 5.0 g/l did not affect the polydispersity index, however, increasing the concentration further to 10.0 g/l resulted in an increase in the polydispersity index. A steady decrease in the percentage of particles with sizes inside the range of detection from a concentration of 1.0 g/l to 10 g/l of turmeric was observed.

4.4.2. Effect of ultrasound power on Z- average size.

Figure 4.21. Shows the effect of ultrasound power on the mean Z-average size of turmeric particles in the copper electrolyte mimic. A progressive reduction in the mean Z-average size (and error) of turmeric particles in solution was observed with increasing ultrasound power. At an ultrasound power of 11 W/l a mean Z-average size of 900 ± 184 nm was observed, at 33 W/l a mean Z-average size of 238 ± 30 nm was seen.

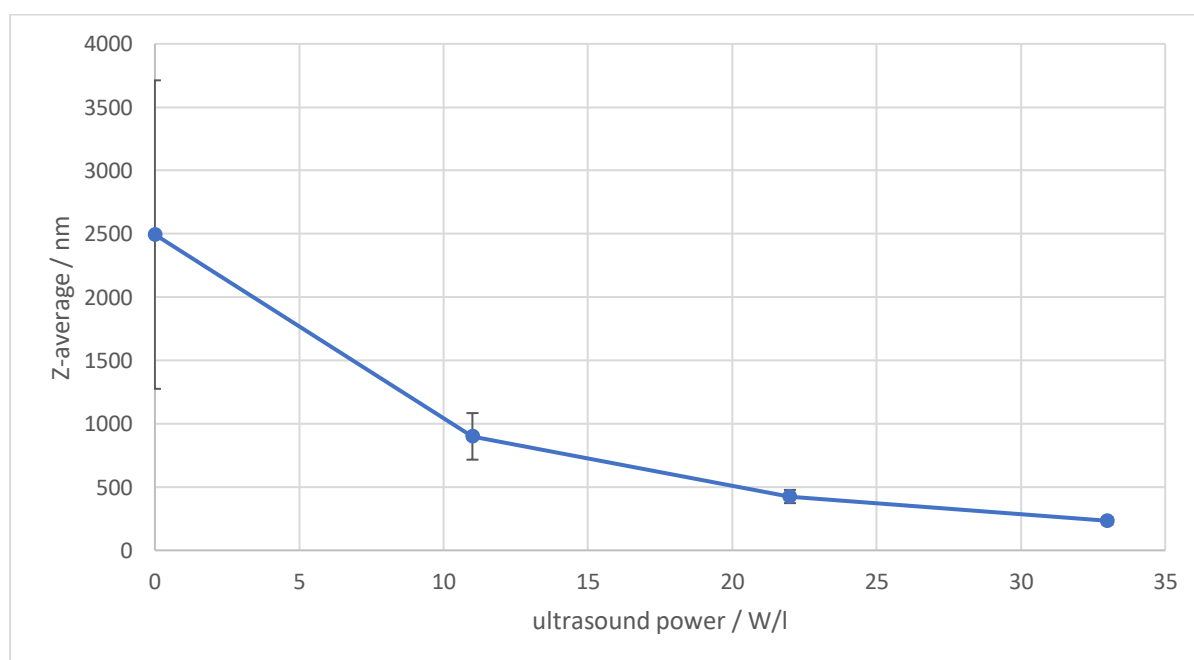


Figure 4.21. Effects of ultrasound power from a 20 kHz horn applied for 20 min on the Z-average size of turmeric particles in a solution of 10.0 g/l of turmeric in the copper electrolyte mimic.

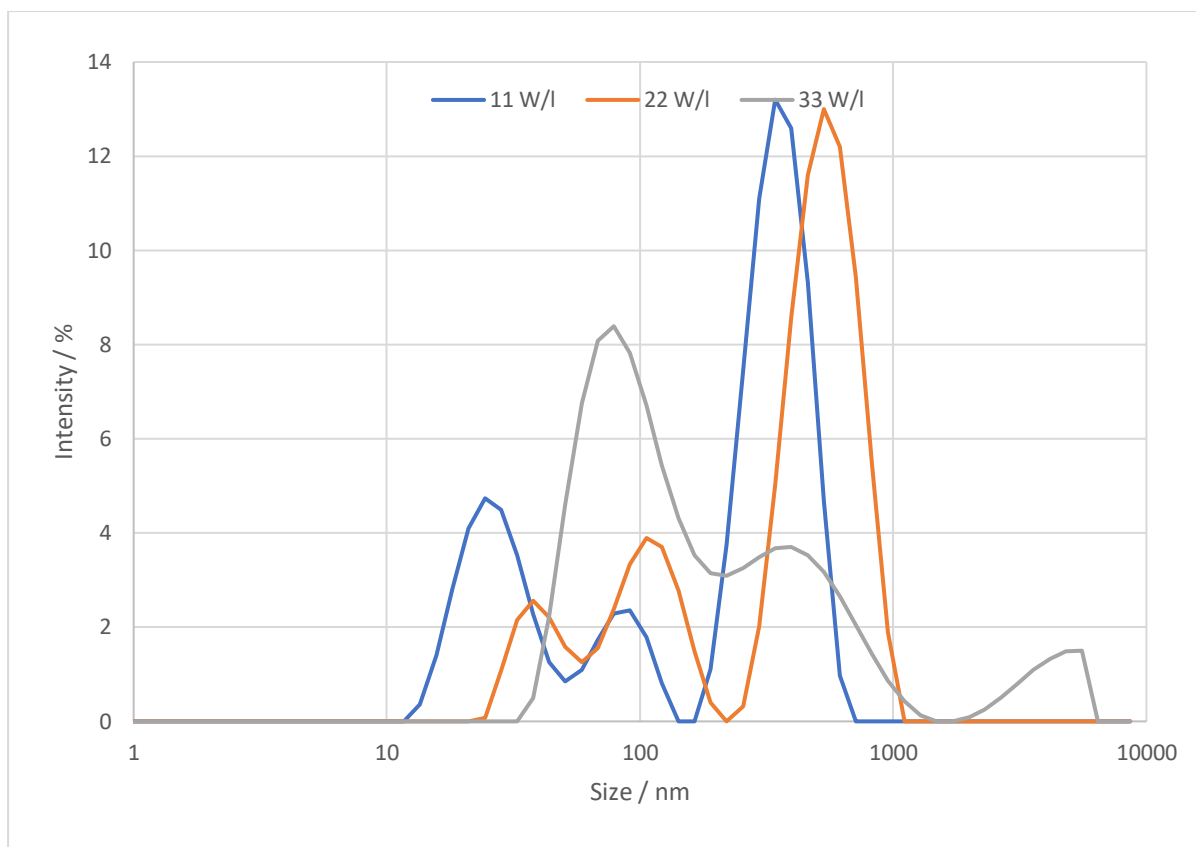


Figure 4.22. The size distribution of turmeric particles measured by signal intensity in a sample with a concentration of 10.0 g/l of turmeric in copper electrolyte mimic, after 20 kHz ultrasound from a horn at a power of 22 W/l for 20 min.

Figure 4.22. Shows how the size distribution of turmeric particles in solution is affected by ultrasound power. At an ultrasound power of 11 W/l the peak of highest intensity in the 10.0 g/l solution existed above 100 nm, with two smaller peaks present below 100 nm. At an ultrasound power of 33 W/l, the peak above 100 nm was reduced in intensity and moved closer to the 100 nm line, only one peak was present below 100 nm which had increased intensity compared to the 10.0 g/l solution sonicated at 11 W/l.

The R^2 value shown in Figure 4.16. was close to 1.0 indicating a strong linear relationship between mean Z-average size of turmeric particle and turmeric concentration in the electrolyte. The polydispersity index and intensity plots show the turmeric particle in the solutions were not monodispersed. The peak between 100 nm and 1000 nm indicated that the majority of turmeric particles in solution existed with a size between 100 nm and 1000 nm. As the concentration of turmeric increased the intensity of the particles between 100 nm and 1000 nm increased and decreased for particles between 10 nm and 100 nm, suggesting an increase in turmeric particles with

a size above 100 nm. Results from the particle dispersion experiments also showed a general trend of increasing turmeric particle size with increasing turmeric concentration. Therefore, the results obtained in this section of research were expected.

Increasing ultrasound power from 11 W/l to 33 W/l, reduced the mean Z-average size and the size distribution of the turmeric particles in solution. Increasing the ultrasound power from 11 W/l to 33 W/l reduced the mean Z-average size from 900 ± 184 nm to 238 ± 30 nm. As the power of the ultrasound was increased, the signal intensity for particles with a Z-average size between 100 and 1000 nm decreased, and the signal intensity for particles with a Z-average size of between 10 and 100 nm increased. The increase in intensity for particles of between 10 and 100 nm can be attributed to larger particles/agglomerates (above 100 nm) being broken down to a size below 100 nm, increasing the percentage of particles in range of detection, decreasing the intensity for particles above 100 nm and reducing the mean Z-average size.

4.5. Turmeric preparation discussion

To ensure the even dispersion of properties throughout the coating it is essential that the particles are evenly disperse throughout the electrolyte, and large agglomerates are avoided. The results show that stirring is ineffective at dispersing and deagglomerating turmeric in the copper electrolyte mimic, and therefore would not be suitable for dispersing the turmeric in the electrolytes before electrodeposition. However, ultrasound from a 20 kHz horn proved very affective.

The stirred solutions showed no significant change in Z-average size or polydispersion index after 20 min. The polydispersion index at the end of the experiment was greater than 0.7. The polydispersity index is a measurement of the variation in the Z-average size of particles in the solution. A polydispersity index of 0.5 or lower is rarely seen and indicates the Z-average size of particles in solution is monodispersed, a polydispersity index of 0.7 or greater indicate a high level of variation in the Z-average size of particles in solution, and the sample may not be suitable for DLS measurements [7-9]. However, the number of particles in range of detection remained the same. This

suggests that agglomeration of turmeric particles was taking place. Agglomeration of turmeric particles at sizes in range of detection would increase the polydispersity index and Z-average size but may not increase the Z-average size of the turmeric particle sufficiently to move them outside of the range of detection. The application of ultrasound at a power of 11 W/l from a 20 kHz horn had a significant effect on the mean Z-average size of the turmeric particles in solution. At all concentrations analysed the mean Z-average size of the turmeric particle was reduced after 20 min of ultrasound. However, increasing the ultrasound duration from 20 min to 30 min did not significantly reduce the mean Z-average size any further. The reduction of the mean Z-average size is likely due to the deagglomeration and physical break down of the turmeric particles due to the acoustic cavitation, acoustic streaming, micro-jetting, cavitation fields, and high-speed particle collisions caused by the ultrasound [10,11]. The polydispersity index was also significantly improved by the application of ultrasound, to 0.6 or below for all concentrations.

The Z-average size of the turmeric particles in solution was dependant on both the concentration of turmeric in solution and the ultrasound power used to disperse it. An increase in turmeric concentration resulted in an increase in the Z-average size of turmeric particles in solution, which is likely due to an increase in agglomeration. When the ultrasound power was increased from 11 W/l to 33 W/l the Z-average size of turmeric particles in solution could be reduced further. The Z-average size of 900 ± 184.0 nm seen in 10.0 g/l solution was reduced to 238 ± 30 nm by increasing the ultrasound power, which was close to that seen for 5.0 g/l solution at 289 ± 30.0 nm. Although the solutions were not monodispersed, this allows the effects of both the size of turmeric particle and their concentration in the electrolyte on the grain structure of the deposits to be compared.

However, the Z-average size measured by DLS is the intensity-weighted mean of the hydrodynamic particle size [8,12]. The Z-average size is known to be the most stable result generated by DLS, as it is not affected by noise [7,8,12,13]. The Z-average size assumes that the particles are spherical (or near spherical) and that the solution is monodispersed. This was not the case for the turmeric solutions, and therefore may not be an accurate representation of the actual turmeric particles size in the copper electrolyte mimic.

4.6. Conclusions

- The SEM images shows that turmeric particles do not have a uniform size or shape before dispersion. As the turmeric particles were not spherical, DLS measurements are less accurate.
- Ultrasound from a 20 kHz horn is an effective method of de-agglomerating turmeric particles in the copper electrolyte mimic.
- After 20 min of ultrasound the maximum de-agglomeration had occurred at that power and increasing duration of ultrasound did not significantly reduce the turmeric particle size any further.
- Once ultrasound was stopped, only a small amount of re-agglomeration took place, which did not have a significant effect on the Z-average size.
- Solutions stirred for 1 hour after ultrasound did not show any significant difference when compared to solutions left to settle after ultrasound.
- Ultrasound from a 20 kHz horn at a power of 11 W/l produced mean Z-average sizes of 134 ± 37.0 nm, 289 ± 30.0 nm, and 900 ± 184.0 nm for solutions with turmeric concentrations of 1.0 g/l, 5.0 g/l and 10.0 g/l respectively. The polydispersity index and intensity distribution plot showed that the solutions were not monodispersed, with the majority of particles having a Z-average size of between 100 and 1000 nm.
- Increasing the ultrasound power from 11 W/l to 33 W/l reduced the Z-average size from 900 ± 184.0 nm to 238 ± 30 nm for the 10.0 g/l solution. The intensity distribution plots show that the solutions were not monodispersed, with the majority of particles having a size between 100 and 1000 nm. With increasing ultrasound power, there was an increase in particles with sizes between 10 and 100 nm.

4.7. Reference list

[1] K. Show, T. Mao, D. Lee, Optimisation of sludge disruption by sonication, Water Research. 41 (2007) 4741-4747.

- [2] J. Jiang, G. Oberdorster, P. Biswas, Characterization of size, surface charge, and agglomeration state of nanoparticle dispersions for toxicological studies.(Report), Journal of Nanoparticle Research: An Interdisciplinary Forum for Nanoscale Science and Technology. 11 (2009) 77.
- [3] S. Chung, J. Leonard, I. Nettleship, J. Lee, Y. Soong, D. Martello, M. Chyu, Characterization of ZnO nanoparticle suspension in water: Effectiveness of ultrasonic dispersion, Powder Technology. 194 (2009) 75-80.
- [4] R. Kachanoski, R. Voroney, E. Gregorich, Ultrasonic dispersion of aggregates: distribution of organic matter in size fractions, Canadian Journal of Soil Science. 68 (1988) 395-403.
- [5] K. Sato, J. Li, H. Kamiya, T. Ishigaki, Ultrasonic dispersion of TiO₂ nanoparticles in aqueous suspension, Journal of the American Ceramic Society. 91 (2008) 2481-2487.
- [6] B. Krause, M. Mende, P. Pötschke, G. Petzold, Dispersability and particle size distribution of CNTs in an aqueous surfactant dispersion as a function of ultrasonic treatment time, Carbon. 48 (2010) 2746-2754.
- [7] Malvern Instruments Worldwide, Dynamic light scattering common terms defined, (2011).
- [8] M. Kaszuba, Basic Principles of Dynamic Light Scattering, (2015).
- [9] International Standard, ISO22412 Particle Size Analysis – Dynamic Light Scattering, International Organisation for Standardisation (ISO), (2008).
- [10] K.A. Kusters, S.E. Pratsinis, S.G. Thoma, D.M. Smith, Energy—size reduction laws for ultrasonic fragmentation, Powder Technology. 80 (1994) 253-263.
- [11] T. Hielscher, Ultrasonic production of nano-size dispersions and emulsions, arXiv preprint arXiv:0708.1831. (2007).
- [12] Malvern Instruments Ltd, Size: What is z-average? 2017.
- [13] International Standard, ISO13321 Methods for Determination of Particle Size Distribution Part 8: Photon Correlation Spectroscopy, International Organisation for Standardisation (ISO), (1996).

5. Copper results

5.1. Overview

In order to understand the effect that the incorporation of turmeric particles has on the properties of the electrodeposited copper coatings, pure copper, copper with Tween 20 and copper with turmeric coatings were produced and characterised. To understand the influence of particle size on the grain structure of the deposit, copper nano-diamond deposits were also produced. This Chapter contains the results and discussion of the properties of the electrodeposited copper coatings, and in an effort to understand these properties the Chapter also contains results and discussion of the microstructure of the copper coatings. This Chapter has been divided into Three sections:

- Electrodeposition: this section contains information on the Hull cell test, and the surface finish of the coatings.
- Microstructure: this section has information on the microstructure of the copper turmeric and copper nano-diamond samples and includes surface morphology, grain structure, grain size, and particle content results.
- Copper coating properties: this section has information on the hardness, hydrophobic behaviour, surface roughness, and both electrochemical and salt spray corrosion resistance.

5.2. Electrodeposition

5.2.1. Hull cell test

Photographic images of Hull cell panels after the electrodeposition of pure copper and copper with 10 ml/l of Tween 20 are shown in Figure 5.1.

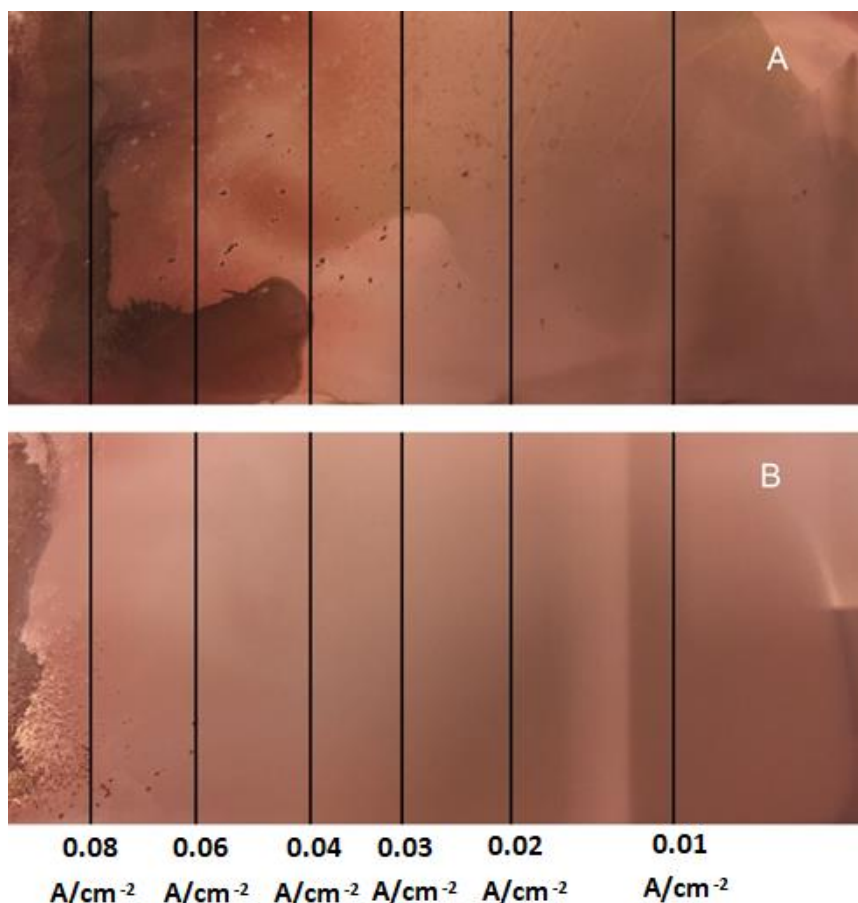


Figure 5.1. Image of Hull cell panels (A) electrodeposited from pure copper electrolyte. (B) electrodeposited from copper electrolyte with 10.0 ml/l of Tween 20.

The pure copper deposit shows no bright areas with a matte finish up to 0.04 A/cm^2 , after which burnt areas were visible. In the copper with 10.0 ml/l of Tween 20 deposit, a bright finish could be seen under 0.01 A/cm^2 , and after 0.01 A/cm^2 the deposit was matte up to 0.08 A/cm^2 , after which burnt areas of the deposit could be seen. Previous studies have shown that the addition of a surfactant to the electrolyte can have many benefits, including widening the operational range of current density [1,2]. To ensure all coatings were produced under similar conditions, all coatings in this research were deposited at 0.04 A/cm^2 .

5.2.2. Copper coating surface finish

Photographic images of the surface finish of copper deposits produced under varying conditions are shown in Figure 5.2.

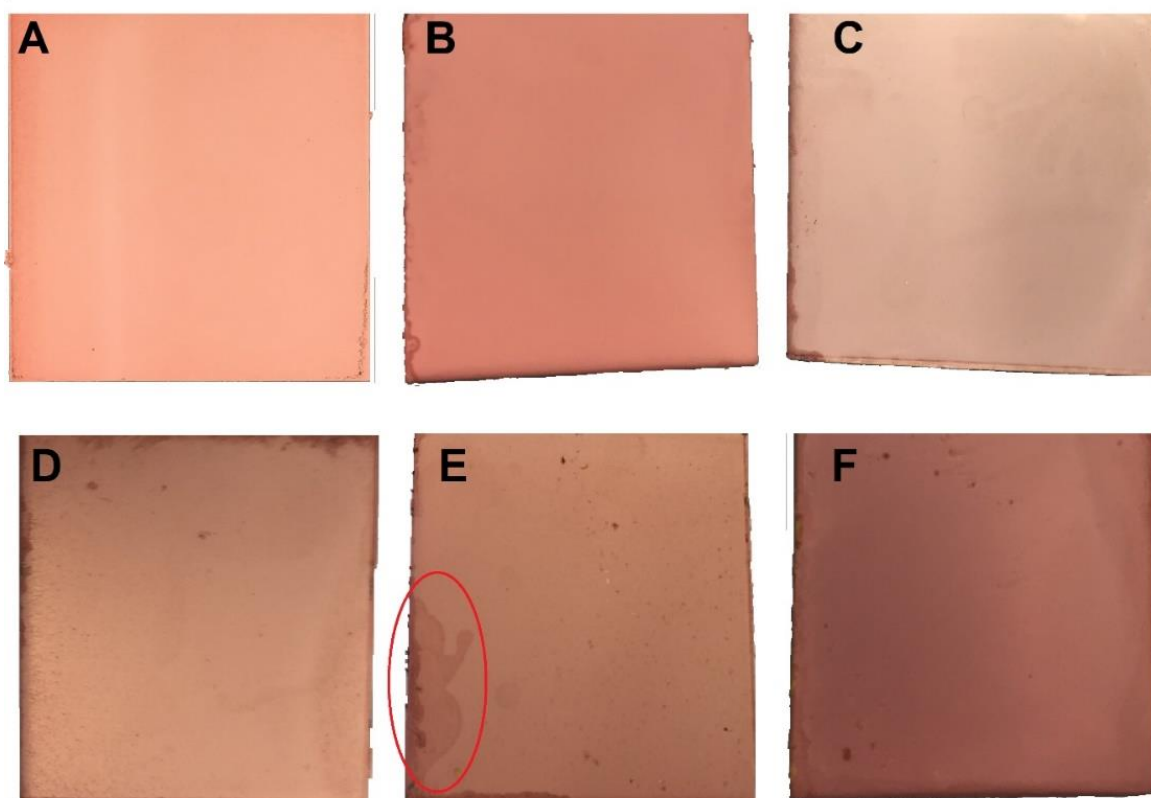


Figure 5.2. Images of the surface of copper coating samples. (A) pure copper (B) copper with Tween 20. (C) copper with Tween 20 and 1.0 g/l of turmeric in the electrolyte. (D) copper with Tween 20 and 5.0 g/l of turmeric in the electrolyte. (E) copper with Tween 20 and 10.0 g/l of turmeric in the electrolyte. (F) copper with Tween 20 and 10.0 g/l of turmeric in the electrolyte sonicated at a power of 33 W/l before electrodeposition. A water stain on sample (E) is marked with a red circle.

Sample (A) showed a smooth uniform salmon pink finish typical of electrodeposited copper. The sample produced from the copper bath with 10 ml/l of Tween 20 (B), showed a smooth uniform rose pink deposit. Sample (C) showed a smooth light pink deposit with a finish similar to that of polychromatic paint, as did all samples incorporating turmeric (samples (C) to (F)). With increasing turmeric concentration in the electrolyte up to 10.0 g/l, the coatings became progressively darker in colour. All samples showed darker areas towards the edges of the coatings. The darker edges can be attributed to a greater thickness of deposit at the edge compared to the centre (edge build up). Edge build up is caused by a non-uniform distribution of current on the cathode, with the current at the edges being higher than at the centre [3,4].

5.3. Microstructure

5.3.1. Particle content

The data showing change in carbon content of the copper turmeric composites with depth obtained by GDOES is presented in Figures 5.3. to 5.6. whilst the mean carbon content is presented in Figure 5.7.

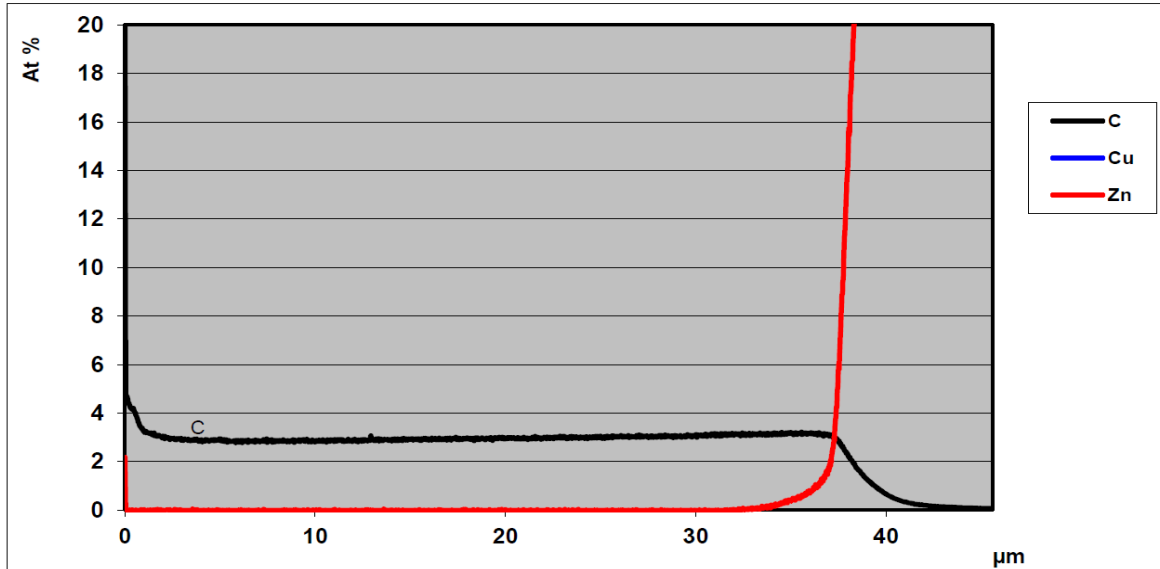


Figure 5.3. Shows the coating composition of copper with 1.0 g/l of turmeric in the electrolyte (sample (C)).

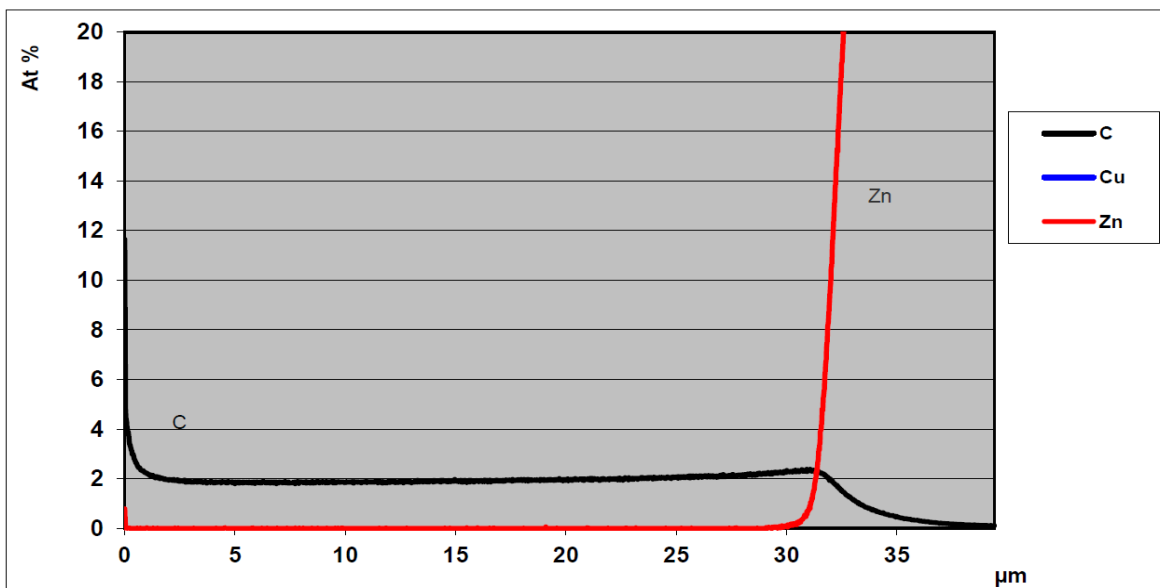


Figure 5.4. Shows the coating composition of copper with 5.0 g/l of turmeric in the electrolyte (sample (D)).

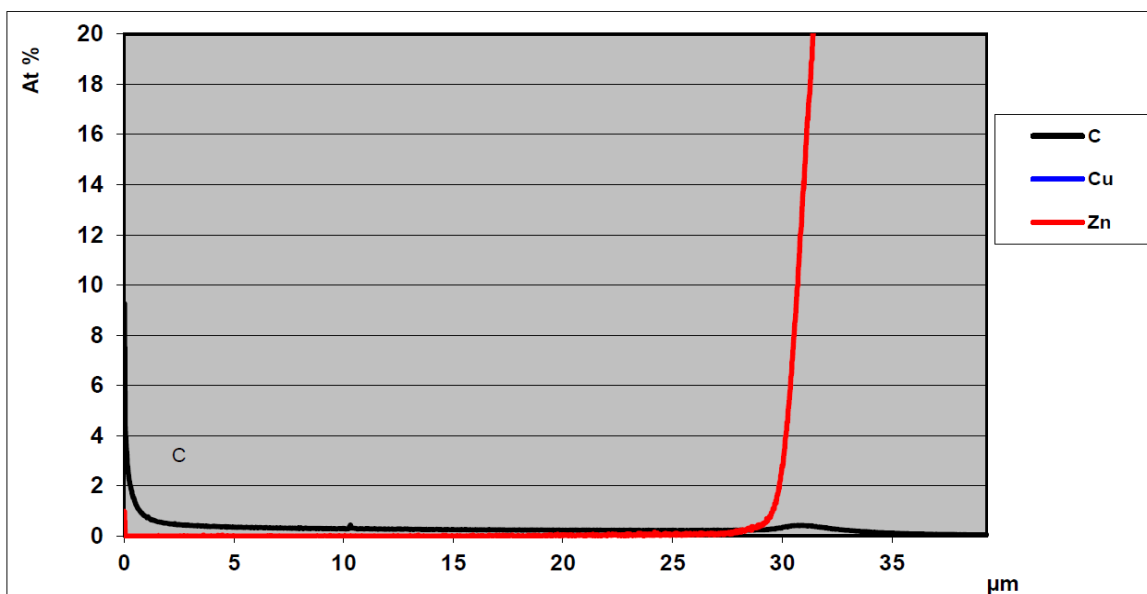


Figure 5.5. Shows the coating composition of copper with 10.0 g/l of turmeric in the electrolyte (sample (E)).

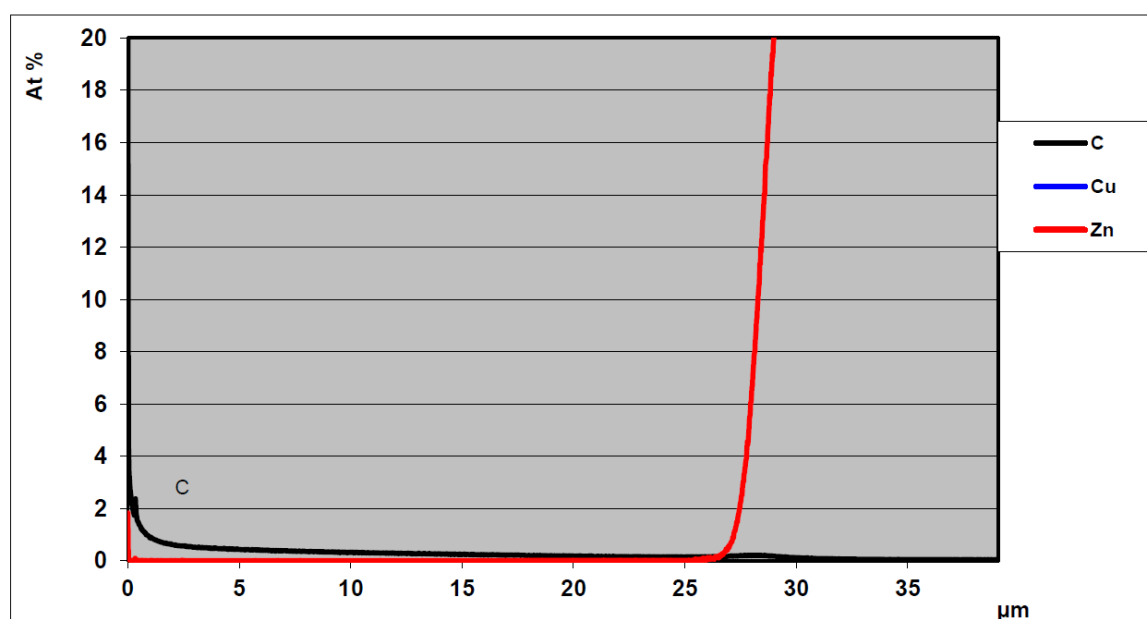


Figure 5.6. Shows the coating composition of copper with 1.0 g/l of turmeric in the electrolyte, sonicated at a power of 33 W/l before electrodeposition (sample (F)).

The large spike in carbon content near the surface of the deposits was likely due to organic contaminants on the surface of the coatings. The carbon content of the coatings reduced from approximately 3.0 % for sample (C) to approximately 0.25 % for samples (E) and (F). A slight increase in carbon content with deposit depth was

observed for samples (C) and (D), with a slight decrease for samples (E) and (F). The thickness of the deposit observed from GDOES data varied from sample to sample.

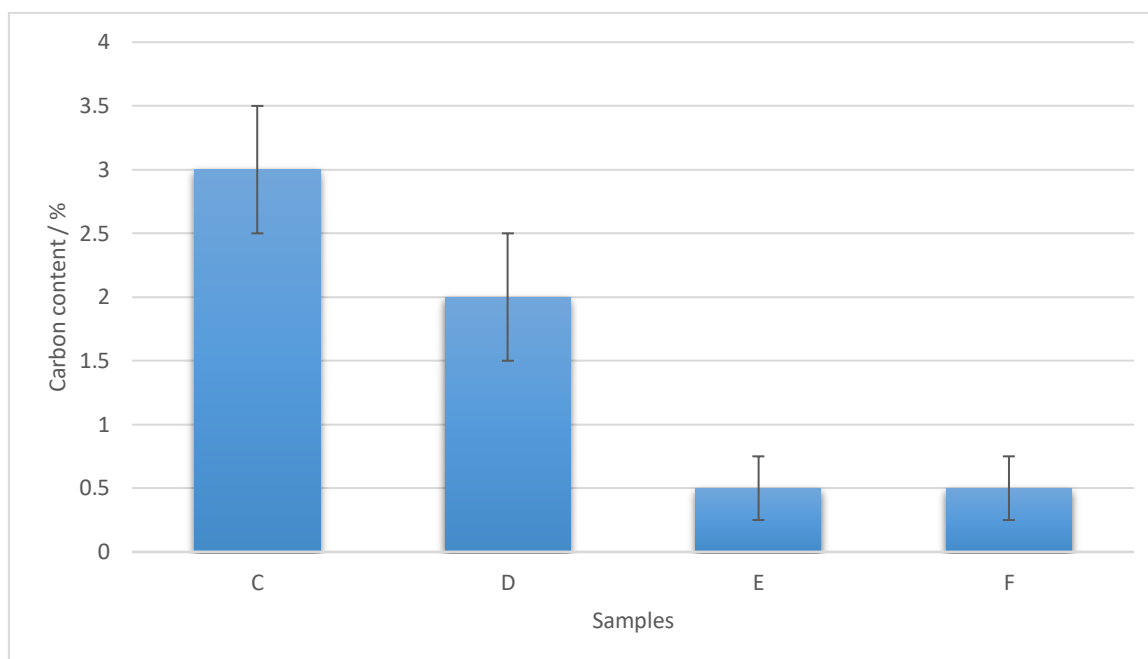


Figure 5.7. Carbon content in copper turmeric deposits obtained by GDOES. (C) copper with Tween 20 and 1.0 g/l of turmeric in the electrolyte. (D). copper with Tween 20 and 5.0 g/l of turmeric in the electrolyte. (E). copper with Tween 20 and 10.0 g/l of turmeric in the electrolyte. (F). copper with Tween 20 and 10.0 g/l of turmeric in the electrolyte sonicated at a power of 33 W/l.

The carbon content of the deposits was likely due to the incorporation of turmeric and/or Tween 20. GDOES data showed there was a reverse correlation between carbon content and turmeric electrolyte concentration, where increasing the bath concentration from 1.0 g/l to 10.0 g/l resulted in reducing the deposits carbon content from 3.0 % to 0.25 %. Although, the literature shows that increasing the particle concentration in an electrolyte generally increases the particle content of the coating until a saturation point is reached (after which it plateaus, or a small reduction is seen), the large extent of reduction in carbon content seen in this research was unexpected [5-7].

The variation in position where GDOES data was obtained across the surface of the deposit is likely responsible for the variation in deposit depth observed. Variation in current density across the surface of the cathode during electrodeposition can lead to variation in the deposit thickness across the surface of the coating. Edge build-up is

common in electrodeposits and can cause the deposit to be thicker at the edges than the centre [3,4].

5.3.2. Surface morphology

SEM images of copper coatings produced with varying concentrations of turmeric in the electrolyte are presented in Figure 5.8. to Figure 5.10.

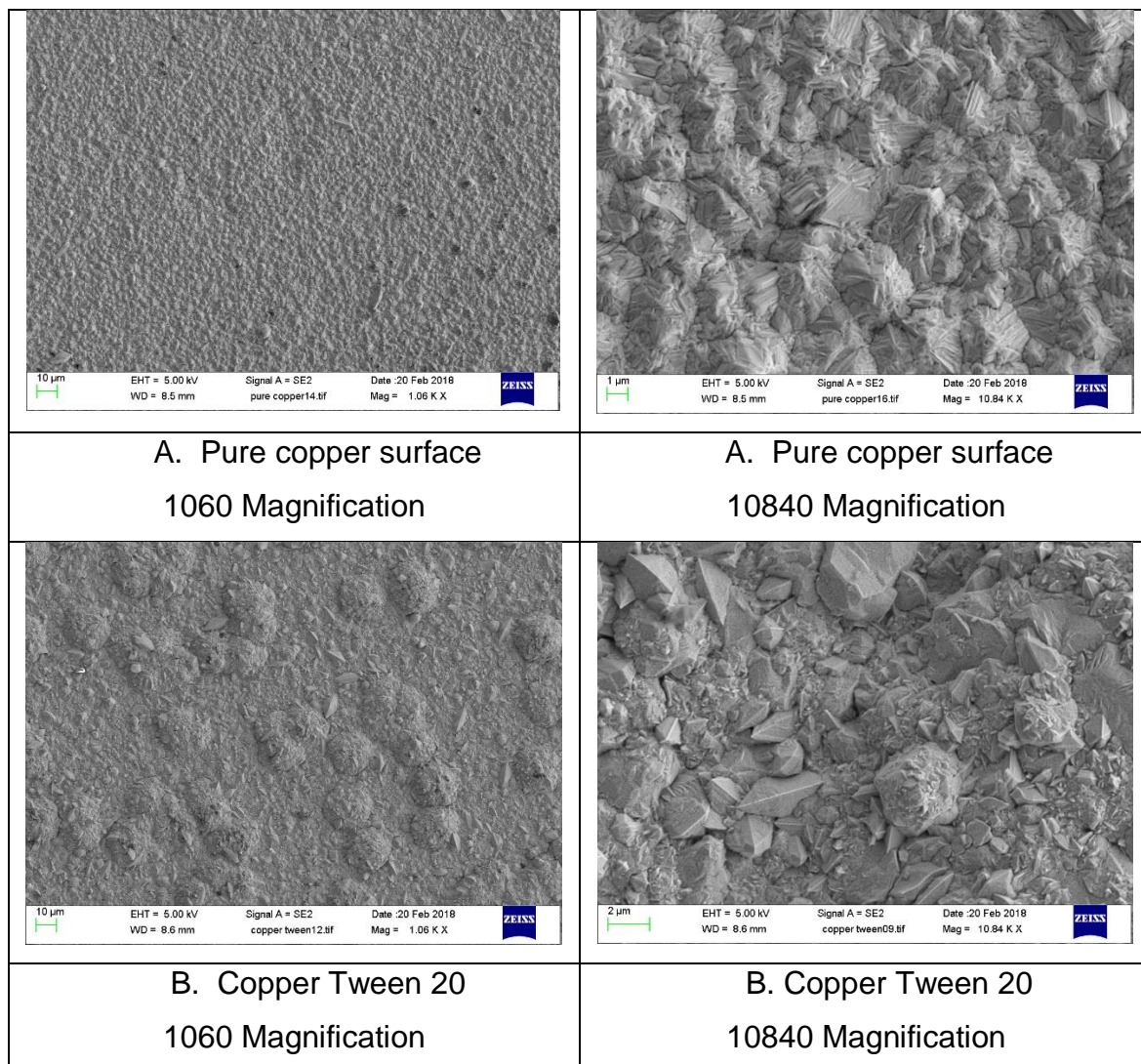


Figure 5.8. SEM Images of surface of copper coating samples.

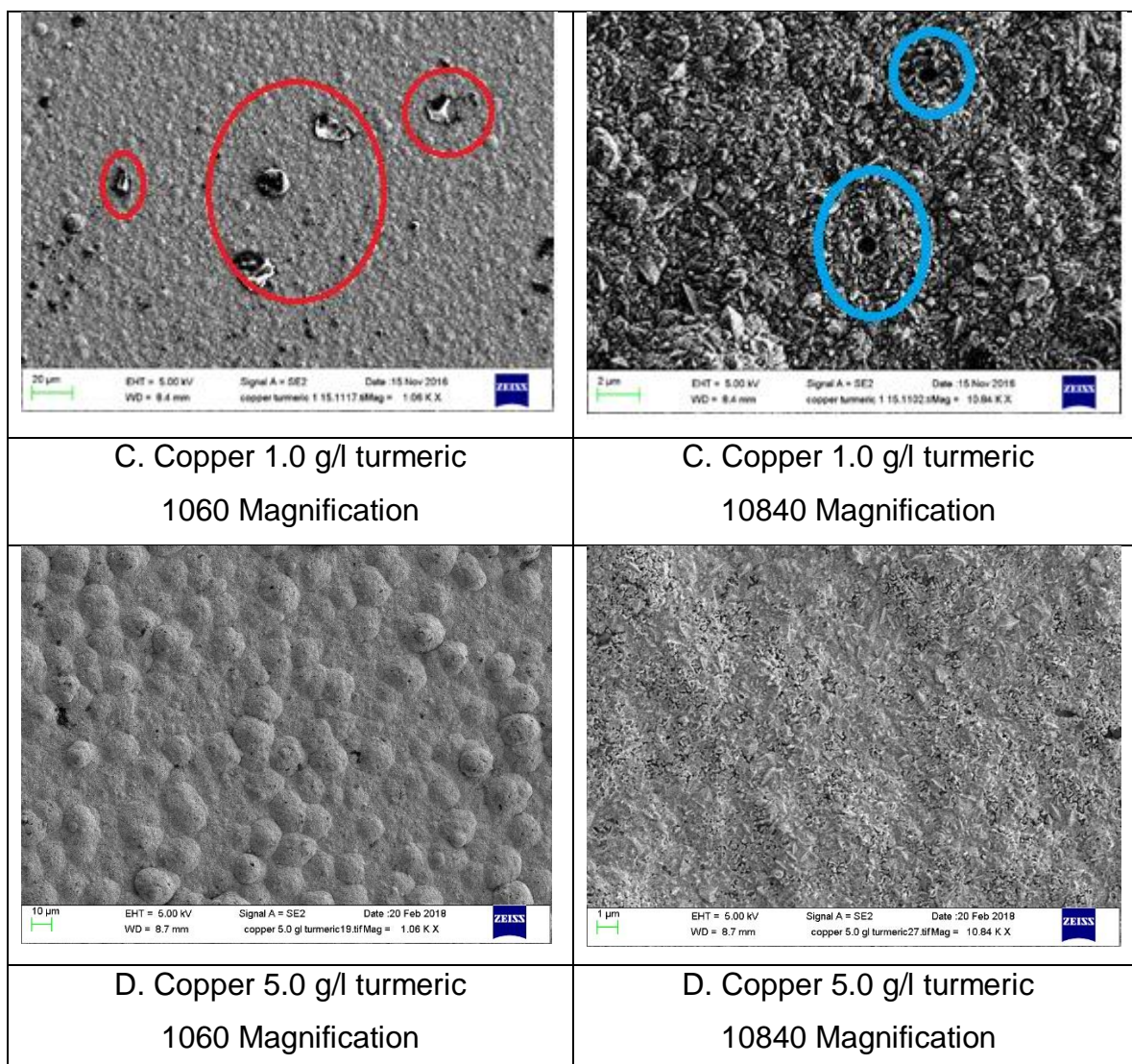


Figure 5.9. SEM Images of surface of copper coating samples. The red circles show turmeric particles on the surface of the coating which are not part of the structure of the deposit. The blue circles show cavity in the coating were turmeric particles have been dislodged.

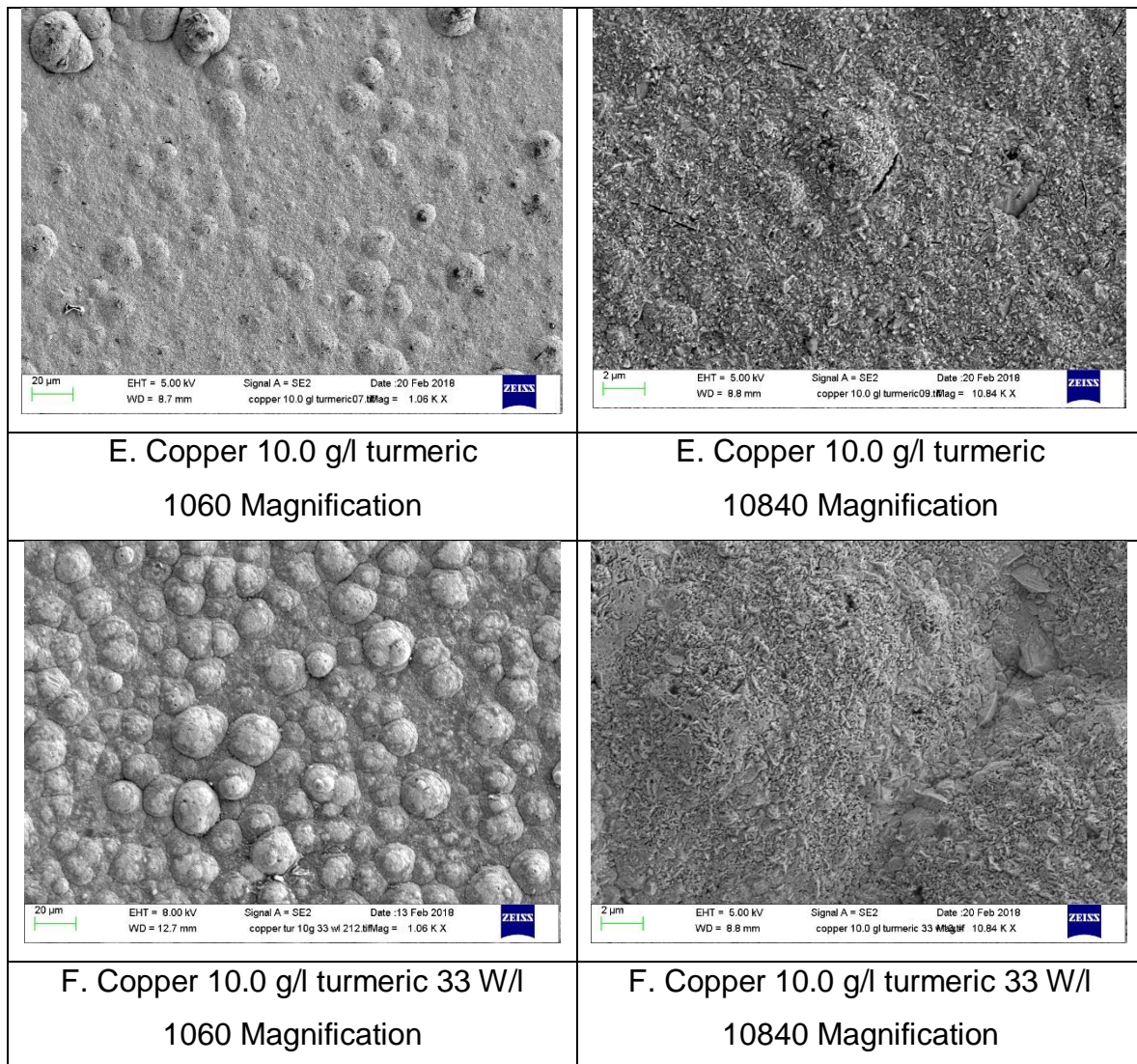


Figure 5.10. SEM Images of surface of copper coating samples.

At lower magnifications, sample (A) exhibited a smooth, uniform appearance. Nodules were observed at lower magnifications for samples (B) to (F). Although, in general a progressive increase in the size of nodules was observed from samples (C) to (F), sample (E) exhibited fewer nodules. At higher magnifications, sample (A) and (B) had a similar pyramidal type grain structure, whilst samples (C) to (F) appeared smoother and more porous.

The nodules present on the surface of the deposits is likely due to the presents of Tween 20 and turmeric in the electrolyte. Nodulation can be caused by an uneven current distribution on the cathode, which can be caused by the presence of surfactants and suspended particles in the electrolyte [8,9].

5.3.3. Grain structure

Ion beam images of the cross section of the deposits are presented in Figure 5.11. and Figure 5.12.

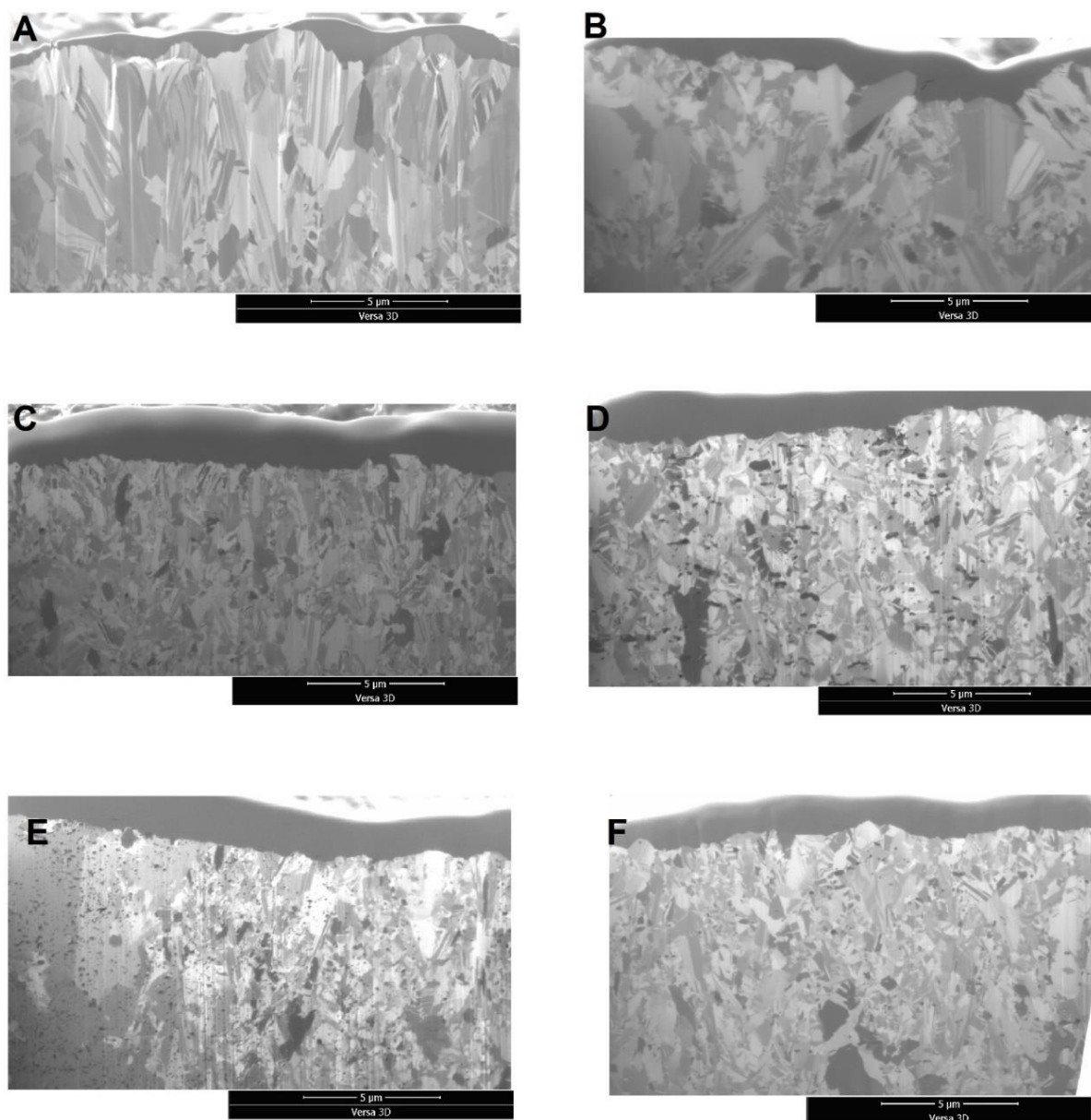


Figure 5.11. Ion beam images of cross section of copper turmeric coating samples. (A) pure copper. (B) copper with Tween 20. (C) copper with Tween 20 and 1.0 g/l of turmeric in the electrolyte. (D) copper with Tween 20 and 5.0 g/l of turmeric in the electrolyte. (E) copper with Tween 20 and 10.0 g/l of turmeric in the electrolyte. (F) copper with Tween 20 and 10.0 g/l of turmeric in the electrolyte sonicated at a power of 33 W/l before electrodeposition.

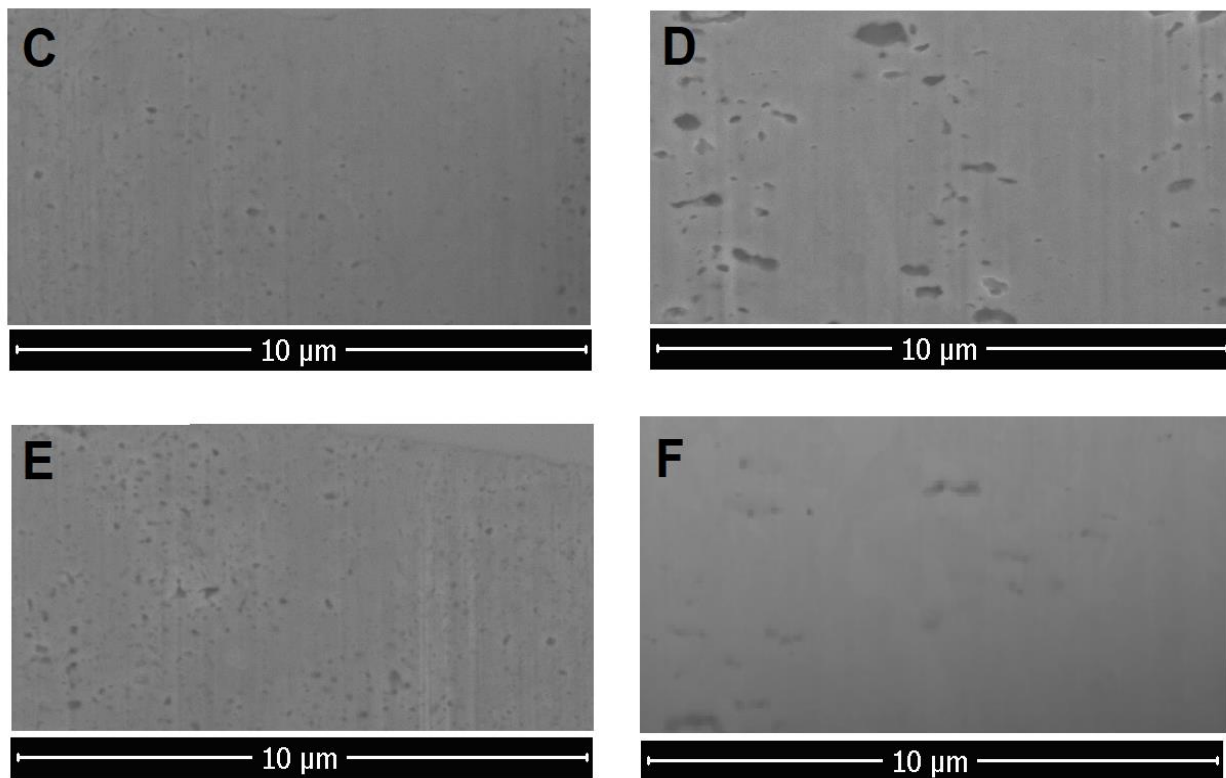


Figure 5.12. Ion beam images of cavities present in coatings. (C) copper with Tween 20 and 1.0 g/l of turmeric in the electrolyte. (D) copper with Tween 20 and 5.0 g/l of turmeric in the electrolyte. (E) copper with Tween 20 and 10.0 g/l of turmeric in the electrolyte. (F) copper with Tween 20 and 10.0 g/l of turmeric in the electrolyte sonicated at a power of 33 W/l before electrodeposition.

Samples (A) and (B) exhibited a mainly columnar structure of large crystals with high aspect ratios (the size of major axis divided by the size of minor axis), smaller more irregular shaped crystals were also present. A significant refinement of the grain structure was observed for sample (C), with a further refinement exhibited by sample (D). Sample (E) did exhibit some refinement in its grain structure compared to samples (A) and (B), however, much larger grains similar to those present in samples (A) and (B) were also observed. Sample (F) exhibited a grain structure similar in appearance to sample (D).

Further examination of the cross-section of deposits (C) to (F) revealed the presents of small cavities. Table 5.1. shows the mean size of the cavities present in the cross-section of the deposits.

Table 5.1. Mean size of cavities present in the cross-section of the deposits

Sample name	Mean cavity size / nm	Standard error / nm
Sample A	No cavities identified	NA
Sample B	No cavities identified	NA
Sample C	129.755	14.164
Sample D	316.083	127.744
Sample E	91.364	38.667
Sample F	292.609	35.451

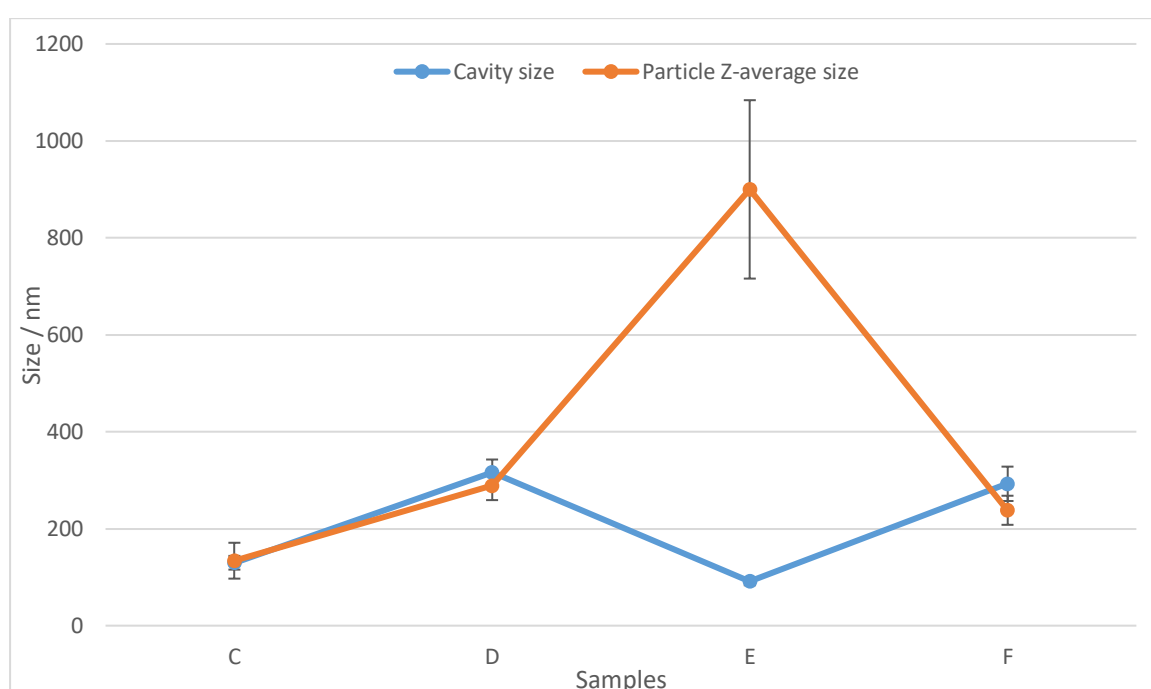


Figure 5.13. Comparison between the mean cavity size measured in the ion beam images by ImageJ to the Z-average size of turmeric particles in the electrolyte measured by DLS. (C) copper with Tween 20 and 1.0 g/l of turmeric in the electrolyte. (D) copper with Tween 20 and 5.0 g/l of turmeric in the electrolyte. (E) copper with Tween 20 and 10.0 g/l of turmeric in the electrolyte. (F) copper with Tween 20 and 10.0 g/l of turmeric in the electrolyte sonicated at a power of 33 W/l before electrodeposition.

A comparison of the mean cavity size and Z-average size of the turmeric particles in the electrolyte is presented in Figure 5.13. A strong correlation between the turmeric particles size and the cavity size can be seen for samples (C), (D) and (F), this suggests that the cavities present in the deposits were from turmeric particles that were incorporated. However, a large disparity was observed between mean cavity size

and Z-average size of turmeric in the electrolyte for sample (E). This may be due to the large Z-average size of turmeric particles in the electrolyte. Not all particles that reach the surface of the cathode are absorbed, and a certain residential time is needed for those that are [10,11]. The majority of particles in the electrolyte for sample (E), may be too large to be absorbed into the deposit, leaving only the smaller particles to be incorporated.

5.3.4. Grain size

5.3.4.1. Copper turmeric

Grain size data obtained from the copper deposits by the line intercept method is presented in Table 5.2. A progressive reduction in grain size was observed from samples (A) to (D). However, sample (E) showed a significant increase in grain size, exhibiting the largest grains of all deposits in the y-axis direction. Sample (F) exhibited a grain size close to that of samples (C) and (D).

It was not possible to obtain EBSD data on the copper turmeric deposits in this research. This could be due to several factors:

- 1) A grain size smaller than the stepping size of the EBSD (33 nm).
- 2) EBSD is extremely sensitive to surface roughness.
- 3) Amorphous sample or localised amorphous areas.
- 4) The sample containing materials not detectable by EBSD.

Data obtained from the line intercept method showed the deposits were not amorphous and have a grain size of greater than 33 nm. However, EBSD is unable to detect turmeric particles in the coatings, and the presence of filler particles in the samples can increase the surface roughness of the polished cross-section, leading to increased zero solutions for the copper turmeric composites. Copper is also an extremely soft metal and readily scratches, the polishing method used in this research may not be adequate for EBSD. This made the results of copper turmeric samples obtain by EBSD in this research unreliable, and therefore are not presented here.

Table 5.2. Table of grain sizes of copper turmeric samples obtained by the line intercept method of the FIB-SEM images. (A) pure copper. (B) copper with Tween 20. (C) copper with Tween 20 and 1.0 g/l of turmeric in the electrolyte. (D) copper with Tween 20 and 5.0 g/l of turmeric in the electrolyte. (E) copper with Tween 20 and 10.0 g/l of turmeric in the electrolyte. (F) copper with Tween 20 and 10.0 g/l of turmeric in the electrolyte sonicated at a power of 33 W/L before electrodeposition

Sample	Grain size in Y-axis direction /nm	Grain size in X-axis direction /nm
A	662 ± 77	437 ± 26
B	523 ± 55	395 ± 44
C	328 ± 27	234 ± 4
D	259 ± 23	233 ± 13
E	791 ± 300	348 ± 10
F	321 ± 18	283 ± 6

The results obtained for the grain size analysis on the copper turmeric deposits, suggest an optimal turmeric particle size of between 200 nm and 300 nm may exist for reducing the grain size of the deposit. The grain size of the deposit reduced from sample (C) to (D) with an increase in the Z-average size of turmeric particles in the electrolyte from 130 nm to 298 nm. The grain size of the deposit increase from sample (D) to (E) with an increase in the Z-average size of turmeric particles in the electrolyte from 298 nm to 900 nm. However, when the Z-average size of turmeric particles in the electrolyte was reduce from 900 nm to 238 nm from sample (E) to (F) a significant reduction in grain size was observed, with sample (F) exhibiting similar grain size to sample (D).

5.3.4.2. Copper nano-diamonds

To identify if the optimal particle size for grain refinement observed for turmeric was also exhibited for other particles, copper deposits containing nano-diamonds of a known size were produced and studied. The grain size of copper nano-diamond deposits obtained by EBSD is shown in Table 5.3. with the grain structure maps presented in Figure 5.14.

Table 5.3. Table of grain sizes of copper nano-diamond samples obtained by the EBSD. (A) Copper with Tween 20 and 1.0 g/l of 100 nm diamonds. (B) Copper with Tween 20 and 5.0 g/l of 100 nm diamonds. (C) Copper with Tween 20 and 10.0 g/l of 100 nm diamonds. (D) Copper with Tween 20 and 1.0 g/l of 250 nm diamonds. (E) Copper with Tween 20 and 5.0 g/l of 250 nm diamonds. (F) Copper with Tween 20 and 10.0 g/l of 250 nm diamonds. (G) Copper with Tween 20 and 1.0 g/l of 1000 nm diamonds. (H) Copper with Tween 20 and 5.0 g/l of 1000 nm diamonds. (I) Copper with Tween 20 and 10.0 g/l of 1000 nm diamonds.

Sample	Grain size in Y-axis direction /nm	Grain size in X-axis direction /nm
A	844 ± 27	779 ± 67
B	369 ± 53	321 ± 37
C	1311 ± 128	1030 ± 131
D	612 ± 12	608 ± 11
E	576 ± 126	594 ± 119
F	364 ± 64	439 ± 11
G	959 ± 29	1071 ± 50

All copper nano-diamond deposits exhibited a mixture of grain shapes and sizes, containing both finer and coarse grains, and grains with complex shapes. The mean grain size for composites containing 100 nm diamonds over the 3 concentrations was approximately 776 nm, with the smallest grain size of 320 nm in the Y-axis direction and 370 nm in the X-axis direction obtained at a concentration of 5.0 g/l. The mean grain size for composites containing 250 nm diamonds over the 3 concentrations was approximately 530 nm, with the smallest grain size of 360 nm in the Y-axis and 440 nm in the X-axis directions obtained at a concentration of 10.0 g/l. The mean grain size for composites containing 1000 nm diamonds over the 3 concentrations was approximately 1030 nm, with the smallest grain size of 440 nm in the Y-axis direction and 460 nm in the X-axis direction obtained at a concentration of 5.0 g/l.

Although the results show that the deposit with the smallest grain size was produced from an electrolyte containing 100 nm nano-diamonds, deposits produced from electrolytes containing 250 nm nano-diamonds exhibited grains close to that size, and in general, the deposits produced from electrolytes containing 250 nm had smaller grains than those produced from electrolytes containing 100 nm and 1000 nm.

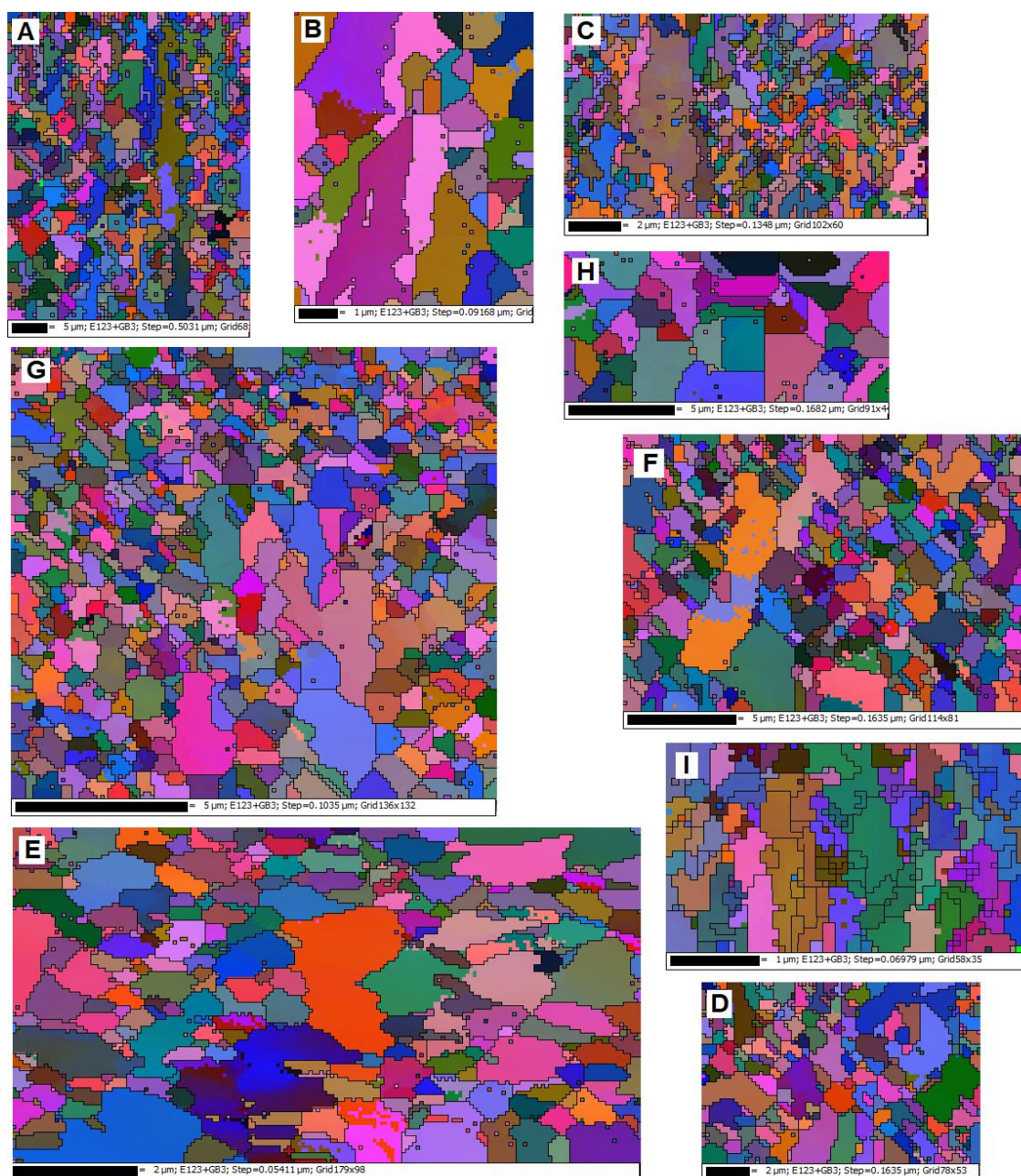


Figure 5.14. Images of grain structure of copper nano-diamond deposits obtain from EBSD. (A) Copper with Tween 20 and 1.0 g/l of 100 nm diamonds. (B) Copper with Tween 20 and 5.0 g/l of 100 nm diamonds. (C) Copper with Tween 20 and 10.0 g/l of 100 nm diamonds. (D) Copper with Tween 20 and 1.0 g/l of 250 nm diamonds. (E) Copper with Tween 20 and 5.0 g/l of 250 nm diamonds. (F) Copper with Tween 20 and 10.0 g/l of 250 nm diamonds. (G) Copper with Tween 20 and 1.0 g/l of 1000 nm diamonds. (H) Copper with Tween 20 and 5.0 g/l of 1000 nm diamonds. (I) Copper with Tween 20 and 10.0 g/l of 1000 nm diamonds.

5.4. Copper coating properties

5.4.1. Hardness

The hardness of the copper deposits with varying turmeric concentrations in the electrolyte is presented in Figure 5.15.

Sample (A) showed the lowest microhardness at approximately 135 ± 5 HV, which is within the range of values reported in the literature for pure copper [1,2,7,12-20]. A progressive increase in hardness was seen in the deposits from sample (A) to sample (D). Sample (E) exhibited a large reduction in hardness back to the level seen for sample (B). However, a large increase in hardness was observed for sample (F), back to the level of sample (D).

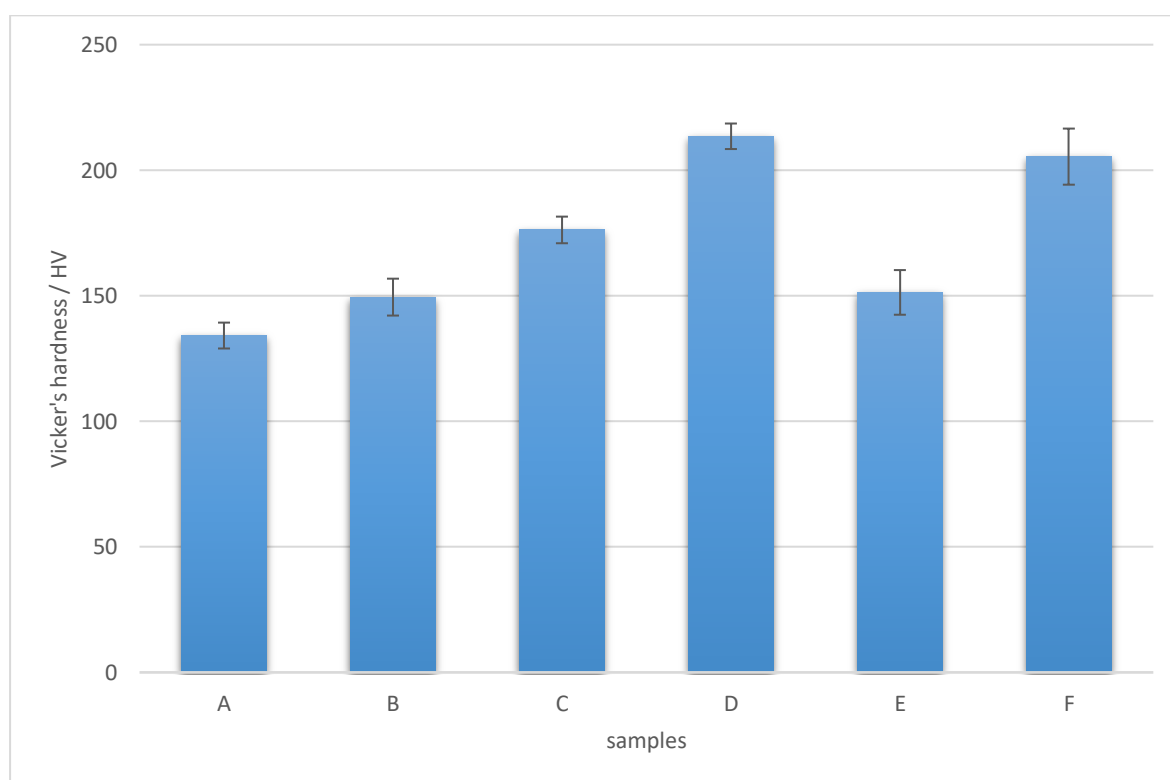


Figure 5.15. Hardness of copper coating obtained by Vicker's indenter. (A) pure copper (B) copper with Tween 20. (C) copper with Tween 20 and 1.0 g/l of turmeric in the electrolyte. (D) copper with Tween 20 and 5.0 g/l of turmeric in the electrolyte. (E) copper with Tween 20 and 10.0 g/l of turmeric in the electrolyte. (F) copper with Tween 20 and 10.0 g/l of turmeric in the electrolyte sonicated at a power of 33 W/l before electrodeposition.

The change in grain size of the deposits is likely responsible for the change in hardness observed. A comparison between hardness and grain size is shown in Figure 5.16.

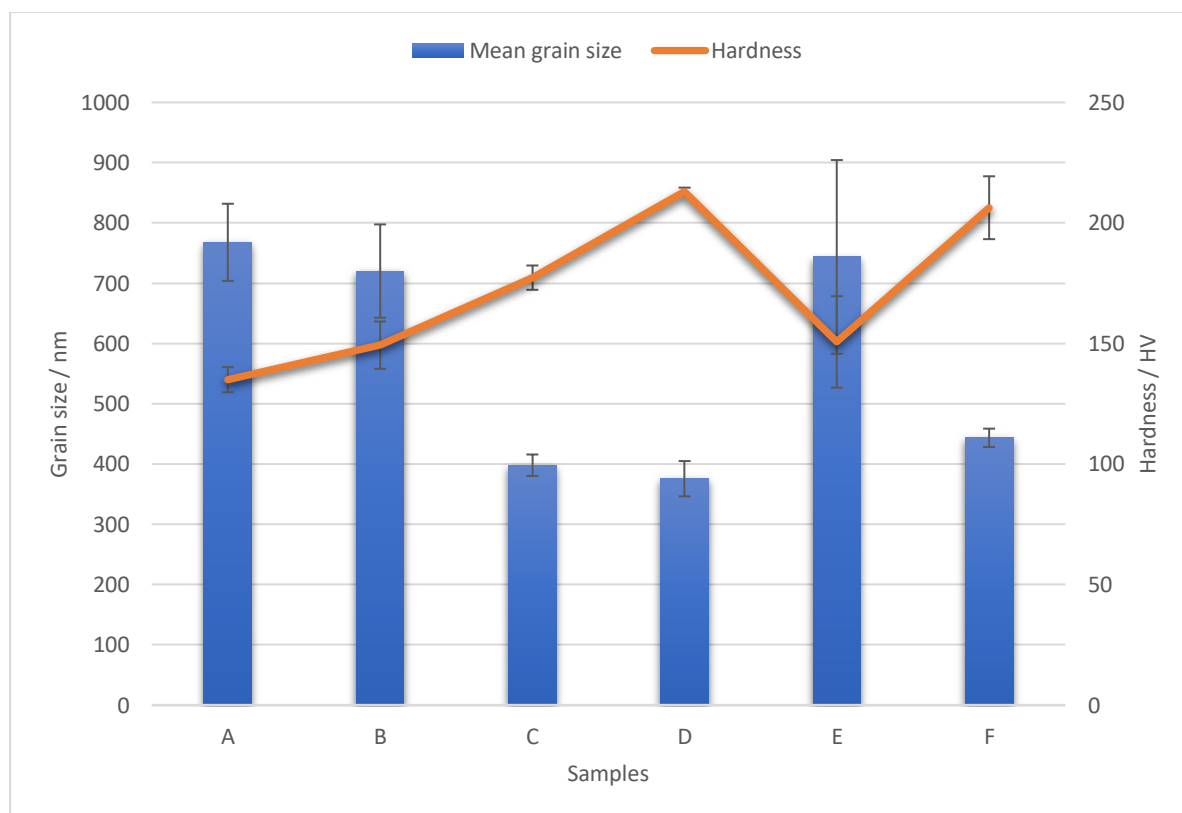


Figure 5.16. Hardness of copper deposits compared to their combined x-axis and y-axis mean grain size. (A) pure copper (B) copper with Tween 20. (C) copper with Tween 20 and 1.0 g/l of turmeric in the electrolyte. (D) copper with Tween 20 and 5.0 g/l of turmeric in the electrolyte. (E) copper with Tween 20 and 10.0 g/l of turmeric in the electrolyte. (F) copper with Tween 20 and 10.0 g/l of turmeric in the electrolyte sonicated at a power of 33 W/l before electrodeposition.

A strong reverse correlation can be seen between the hardness of the deposits and their mean grain size. As stated in Chapter 2, when sufficient force is applied to a metal, dislocations are forced to pile up at grain boundaries, either because a barrier to crossing over exists, or a source must be activated in the next grain boundary. A specific concentration for a given grain is required to initiate slip into its neighbouring grain boundary. This concentration is most likely achieved through a dislocation build-up. Stress is higher as the number of dislocations increases; the more substantial the grain size the quicker the stress is reached [21-24].

5.4.2. Surface roughness

The average surface roughness (Ra) and total surface roughness (Rt) are shown in Figures 5.17. and 5.18. Respectively.

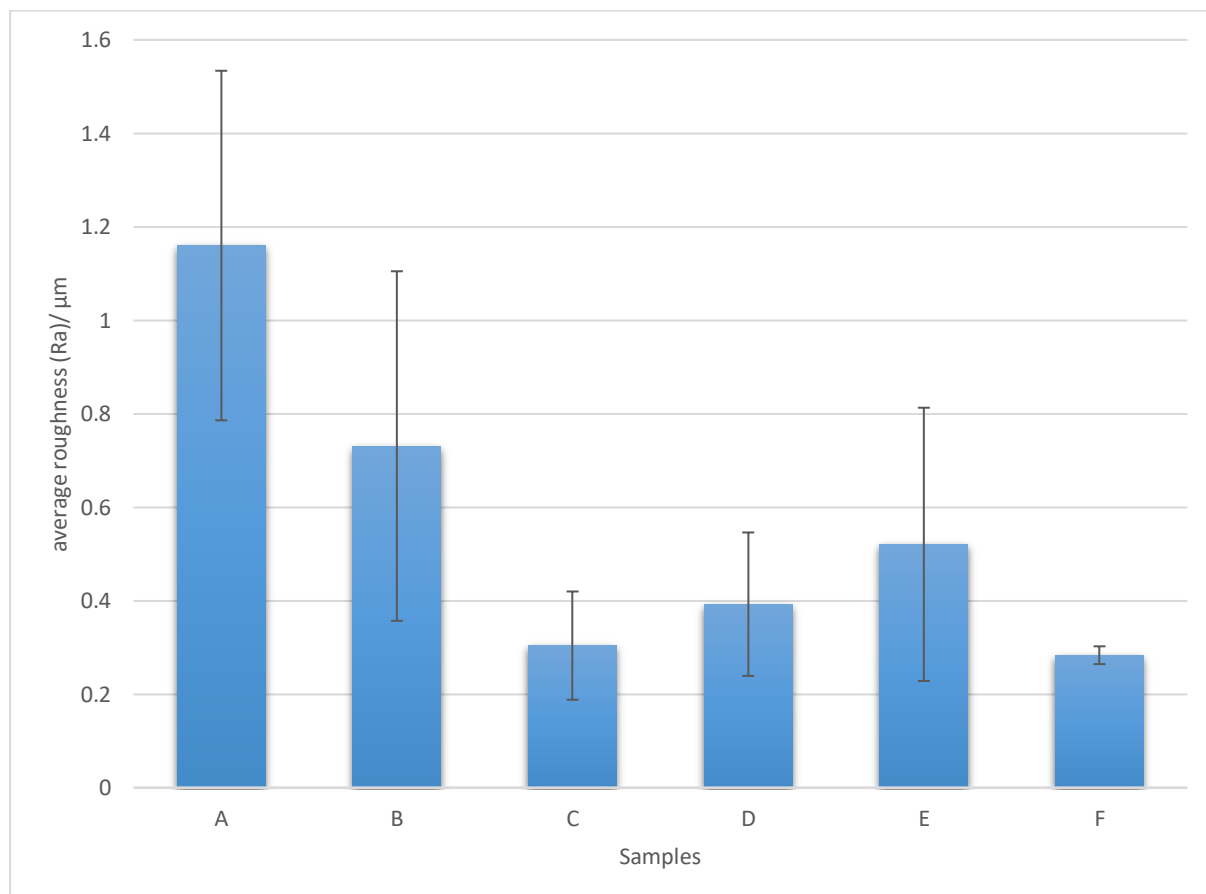


Figure 5.17. Average surface roughness (Ra) of copper deposits obtained by WLI. (A) pure copper. (B) copper with Tween 20. (C) copper with Tween 20 and 1.0 g/l of turmeric in the electrolyte. (D) copper with Tween 20 and 5.0 g/l of turmeric in the electrolyte. (E) copper with Tween 20 and 10.0 g/l of turmeric in the electrolyte. (F) copper with Tween 20 and 10.0 g/l of turmeric in the electrolyte sonicated at a power of 33 W/l before electrodeposition.

A progressive decrease in Ra value was observed from samples (A) to (C), with an increase from samples (C) to (E) before reducing again from samples (E) to (F). The Rt value increased from sample (A) to (B) then decrease to sample (C). After an increase in Rt from sample (C) to (D) a progressive decrease in Rt was observed from samples (D) to (F).

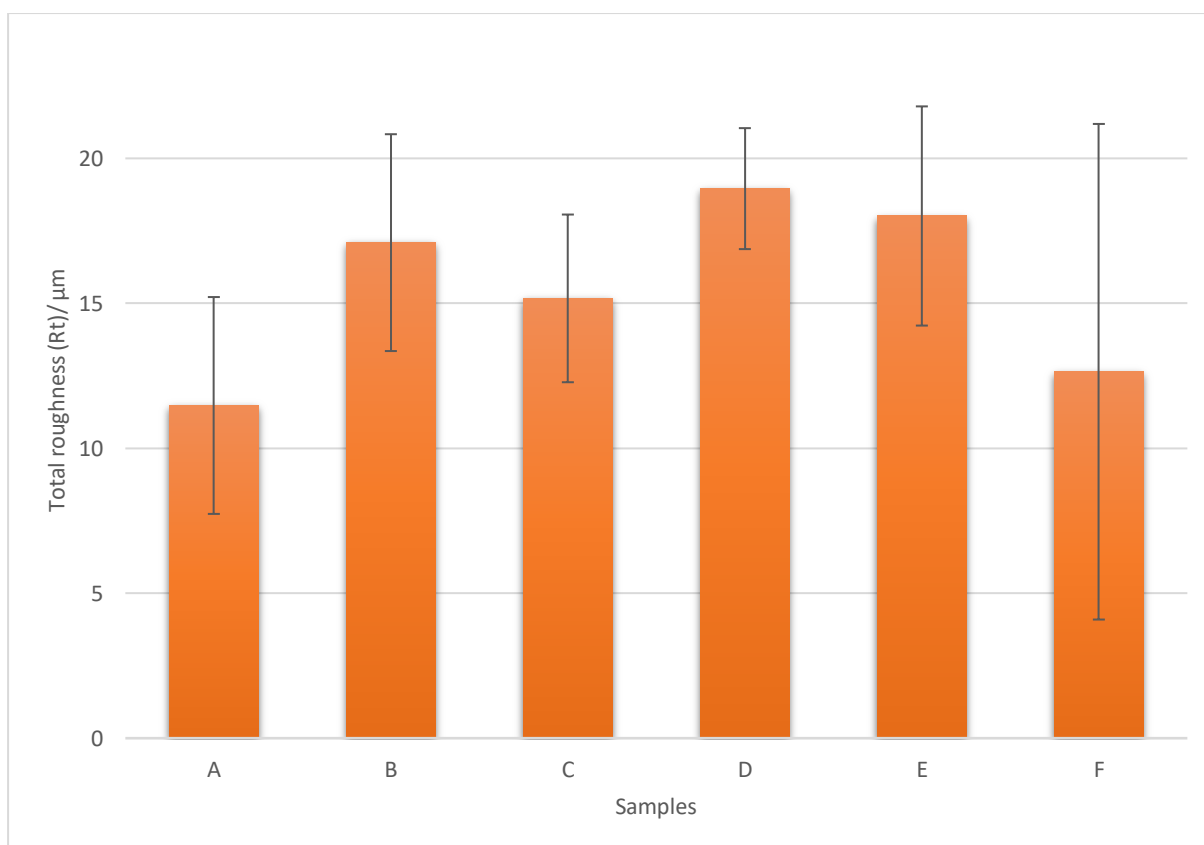


Figure 5.18. Total surface roughness (R_t) of copper deposits obtained by WLI. (A) pure copper. (B) copper with Tween 20. (C) copper with Tween 20 and 1.0 g/l of turmeric in the electrolyte. (D) copper with Tween 20 and 5.0 g/l of turmeric in the electrolyte. (E) copper with Tween 20 and 10.0 g/l of turmeric in the electrolyte. (F) copper with Tween 20 and 10.0 g/l of turmeric in the electrolyte sonicated at a power of 33 W/l before electrodeposition.

The variation in R_a value may be due to the change in grain structure exhibited by the deposits. R_a is a measurement of the average roughness across the whole sample area. A reduction in grain size would lead to a more refined grain structure, this could result in a smoother surface finish for the deposit and a reduction in R_a value. Although, there is a general correlation between the grain size of the deposits and their R_a , it is not perfect and the large error in the R_a values indicates a large degree of variation in surface roughness from sample to sample.

The variation in R_t values may be due to the change in nodulation of the deposits. R_t is a measurement of the change in height from the lowest point to the highest point. A change in nodule size could result in a change in R_t value. Sample (A) exhibited the lowest R_t value and had no visible surface nodules. There was a reduction in nodules size from sample (B) to sample (C) and a decrease in R_t , then an increase in nodule

size to sample (D) and an increase in R_t . However, this correlation is not complete as a reduction in R_t value was observed from sample (E) to (F) with an increase in nodulation, a large error in the R_t values also indicates a large degree of variation in surface roughness from sample to sample

5.4.3. Hydrophobic behaviour

The water contact angle (WCA) of copper deposits with varying turmeric concentrations is presented in Figure 5.19. Comparison of their WCA to R_a , R_t and grain size are presented in Figure 5.20. Figure 5.21. and Figure 5.22. respectively.

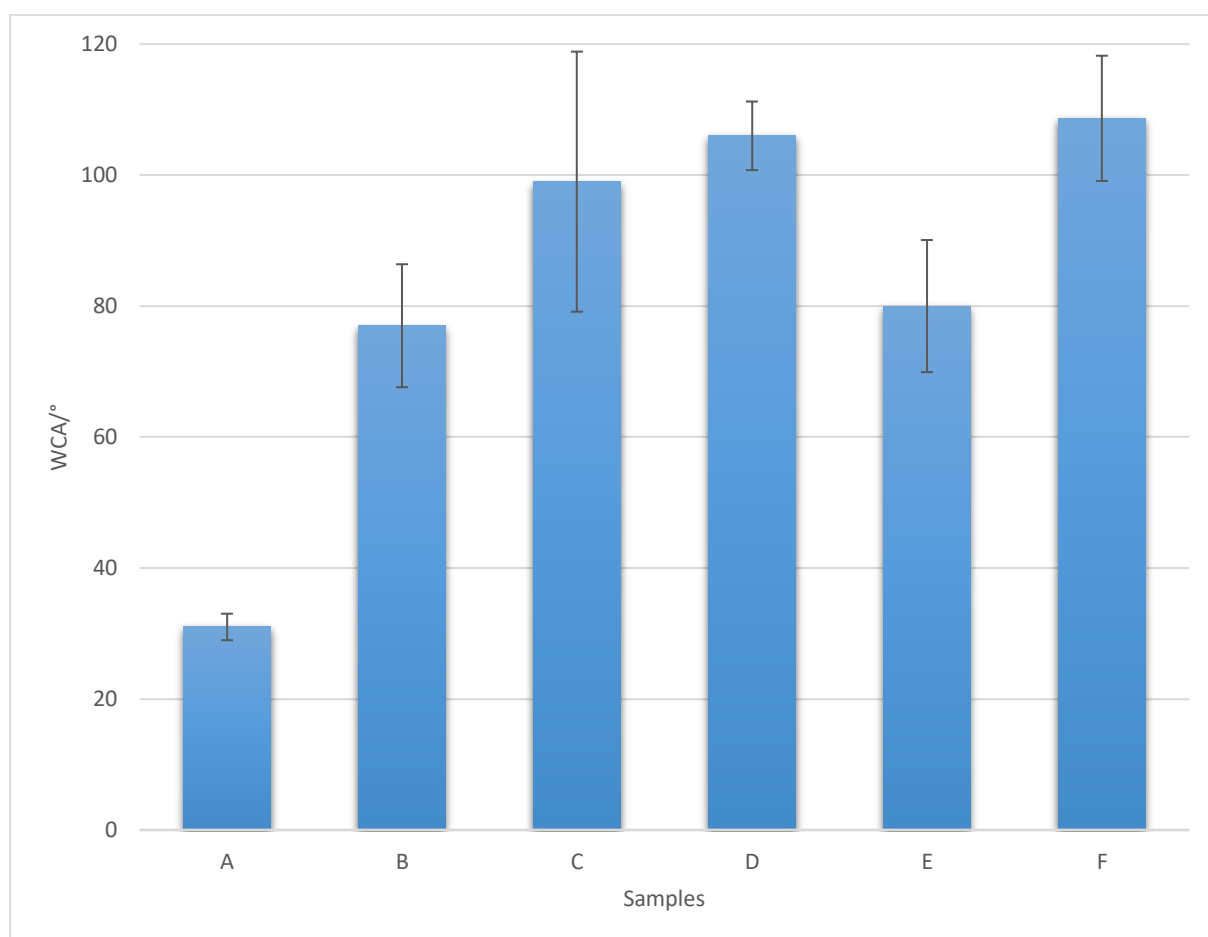


Figure 5.19. WCA of copper coatings obtained by drop shape analysis. (A) pure copper. (B) copper with Tween 20. (C) copper with Tween 20 and 1.0 g/l of turmeric in the electrolyte. (D) copper with Tween 20 and 5.0 g/l of turmeric in the electrolyte. (E) copper with Tween 20 and 10.0 g/l of turmeric in the electrolyte. (F) copper with Tween 20 and 10.0 g/l of turmeric in the electrolyte sonicated at a power of 33 W/l before electrodeposition.

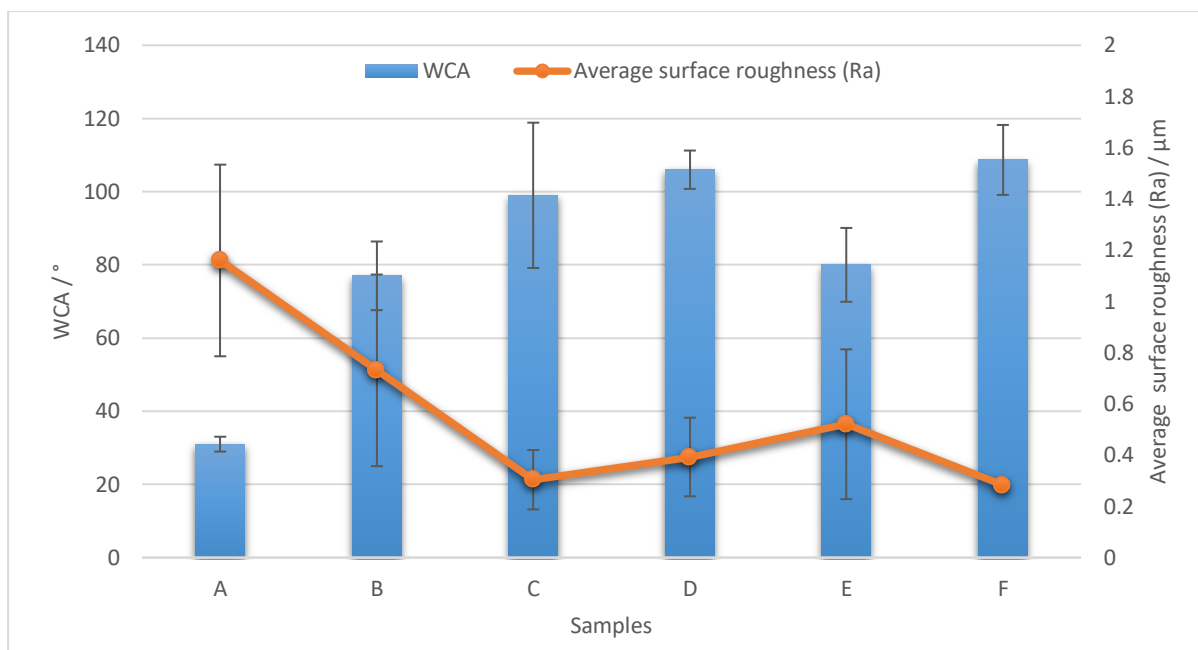


Figure 5.20. Comparison of Ra to WCA of copper coatings. (A) pure copper. (B) copper with Tween 20. (C) copper with Tween 20 and 1.0 g/l of turmeric in the electrolyte. (D) copper with Tween 20 and 5.0 g/l of turmeric in the electrolyte. (E) copper with Tween 20 and 10.0 g/l of turmeric in the electrolyte. (F) copper with Tween 20 and 10.0 g/l of turmeric in the electrolyte sonicated at a power of 33 W/l before electrodeposition.

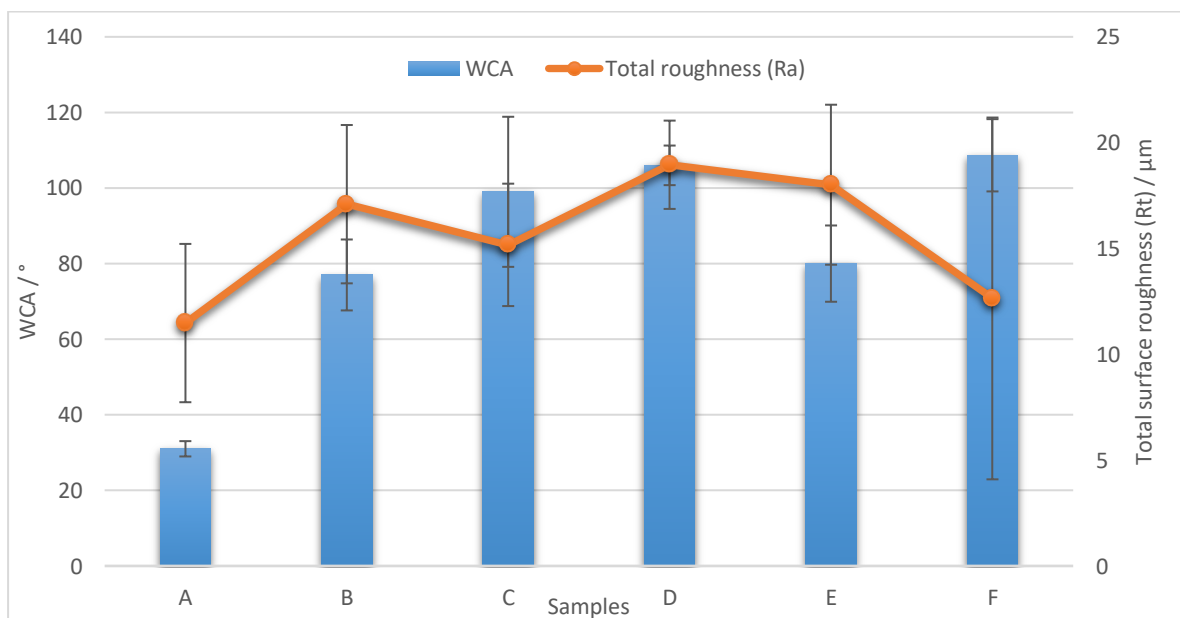


Figure 5.21. Comparison of Rt to WCA of copper coatings. (A) pure copper. (B) copper with Tween 20. (C) copper with Tween 20 and 1.0 g/l of turmeric in the electrolyte. (D) copper with Tween 20 and 5.0 g/l of turmeric in the electrolyte. (E) copper with Tween 20 and 10.0 g/l of turmeric in the electrolyte. (F) copper with Tween 20 and 10.0 g/l of turmeric in the electrolyte sonicated at a power of 33 W/l before electrodeposition.

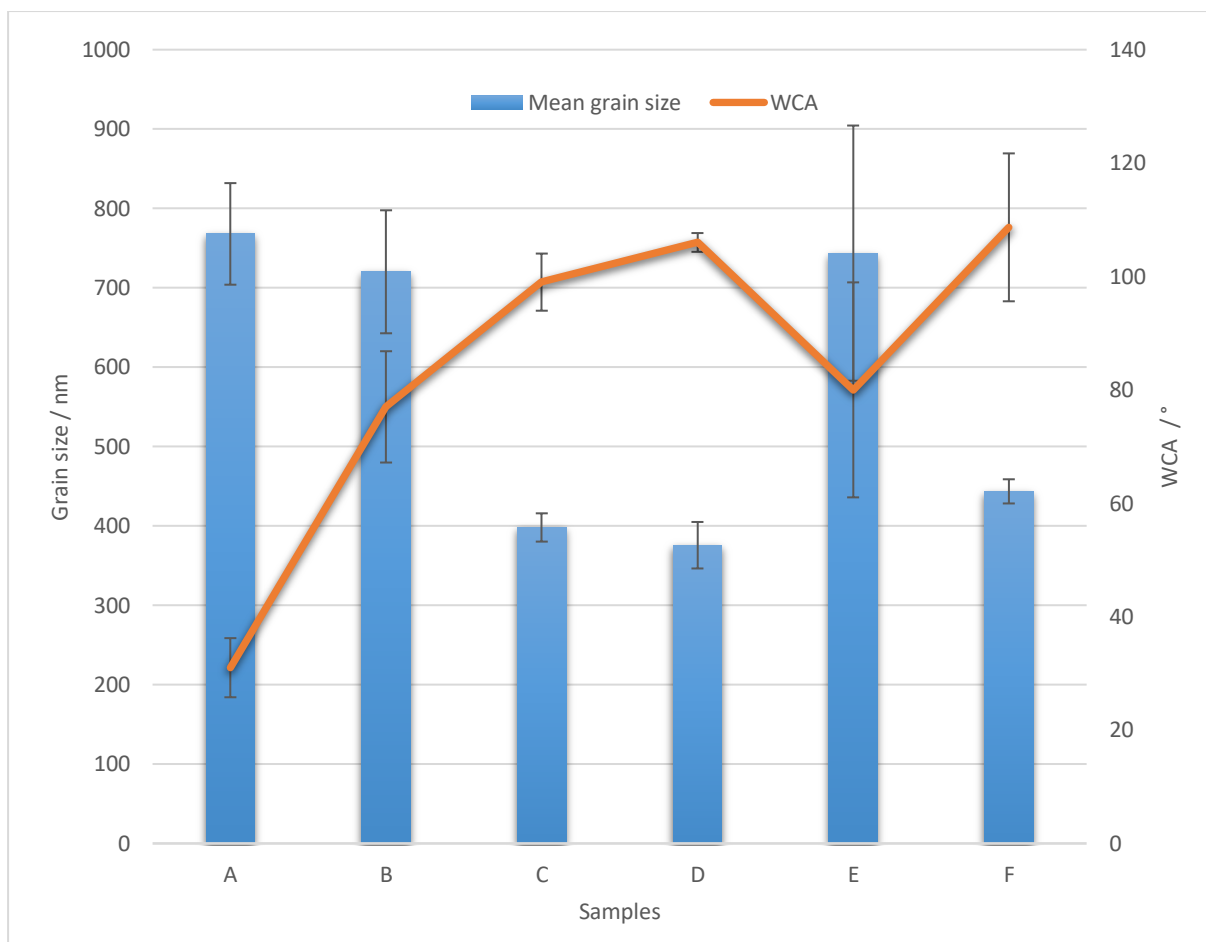


Figure 5.22. Comparison of WCA of the copper deposits to their combined x-axis and y-axis mean grain size. (A) pure copper (B) copper with Tween 20. (C) copper with Tween 20 and 1.0 g/l of turmeric in the electrolyte. (D) copper with Tween 20 and 5.0 g/l of turmeric in the electrolyte. (E) copper with Tween 20 and 10.0 g/l of turmeric in the electrolyte. (F) copper with Tween 20 and 10.0 g/l of turmeric in the electrolyte sonicated at a power of 33 W/l before electrodeposition.

Samples (A), (B) and (E) showed hydrophilic behaviour having a WCA of $<90^\circ$, with samples (C), (D) and (F) exhibiting hydrophobic behaviour. A progressive increase in WCA was observed from samples (A) to (D), with a significant reduction observed from samples (D) to (E). A further change in WCA was observed for sample (F), increasing its WCA back to the level of sample (D).

The surface free energy of a deposit is the primary factor influencing that deposits WCA [25-27]. Many factors can effect surface free energy including surface roughness and grain structure [28-30]. The Cassie Baxter model states, increasing the roughness of a hydrophobic surface can increase the WCA, and increasing the roughness of a hydrophilic surface can decrease the WCA [29,31].

Although the observed Ra values for samples (A) and (B), were consistent with surface roughness effects on their observed WCA values. Sample (E), had the highest Ra value of all the copper turmeric deposits and exhibited the lowest WCA, Samples (C) and (F) had similar Ra values and different WCA values. Although the observed Rt values for samples (C) and (D), were consistent with their surface roughness affecting the observed WCA values. Sample (E) had a higher Rt value than either sample (C) or (F) yet had a lower WCA.

A strong reverse correlation was observed between the WCA of the deposits and a reduction in their grain size. The grain structure of a deposit is known to influence that deposits surface free energy, a reduction in grain size would lead to a reduction in surface free energy and an increase in WCA [26,27]. Although, the surface roughness of the deposits would have influence the deposits WCA, the change in grain structure exhibited by the deposits is likely the dominant factor in this research.

5.4.4. Corrosion rate

5.4.4.1. Electrochemical corrosion tests

The corrosion rate calculated from I_{corr} value obtained by Tafel plots is shown in Figure 5.23. A comparison of electrochemical corrosion rate to Ra is presented in Figure 5.24.

Sample (A) exhibited the highest corrosion rate of all copper deposits at approximately 0.027 mm y^{-1} . A progressive decrease in corrosion rate was observed from samples (A) to (C), with an increase observed from samples (C) to (E) before decreasing again for sample (F). All samples containing turmeric exhibited a significant reduction in corrosion rate compared to the pure copper deposits.

The primary factor influencing the corrosion rate of a metal is the environment it is exposed to, but other factors such as grain structure also have an influence [32,33]. However, the change in surface roughness is likely responsible for the change in electrochemical corrosion rate observed in the copper deposits in this research. A comparison of the Ra value and electrochemical corrosion rate show a strong correlation. Most corrosion takes place electrochemically at the interface between the

metal and electrolyte [34]. Increasing surface roughness would lead to an increase in surface area, this would increase the area of interaction between the surface and electrolyte increasing the corrosion rate.

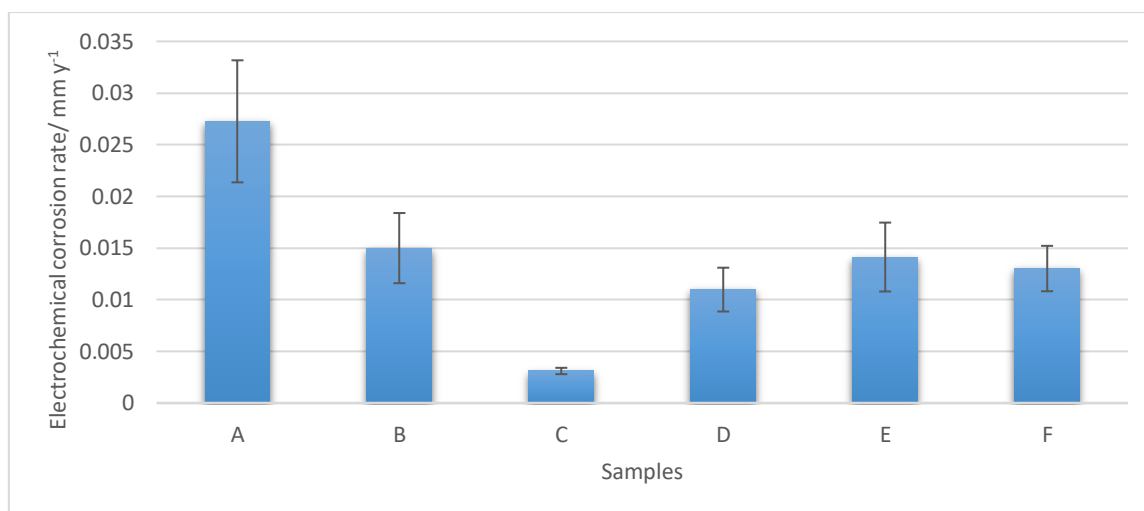


Figure 5.23. Mean corrosion rate estimated by the Tafel plot method. (A) pure copper. (B) copper with Tween 20. (C) copper with Tween 20 and 1.0 g/l of turmeric in the electrolyte. (D) copper with Tween 20 and 5.0 g/l of turmeric in the electrolyte. (E) copper with Tween 20 and 10.0 g/l of turmeric in the electrolyte. (F) copper with Tween 20 and 10.0 g/l of turmeric in the electrolyte sonicated at a power of 33 W/l before electrodeposition.

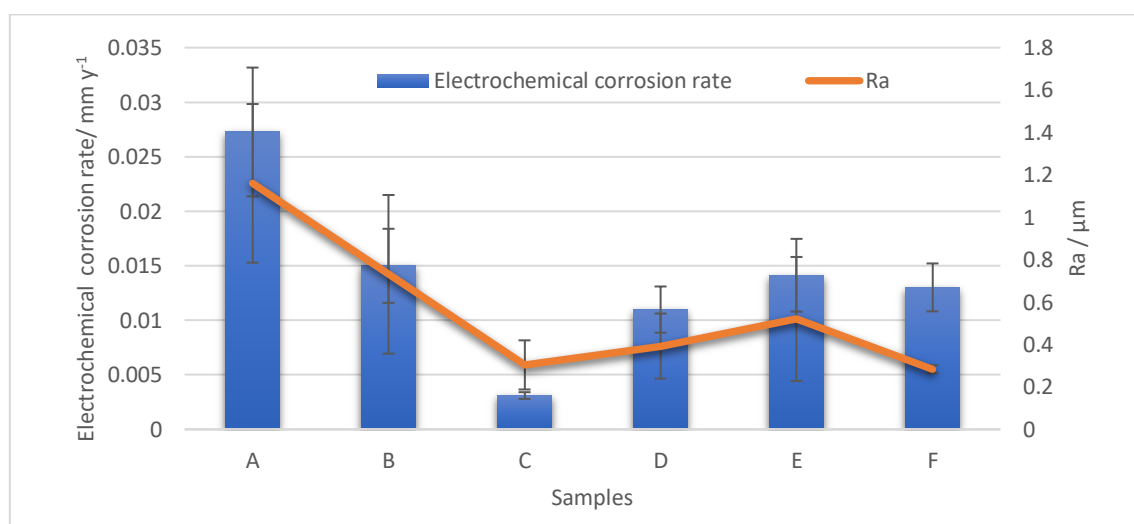


Figure 5.24. Comparison of electrochemical corrosion rate to Ra. (A) pure copper (B) copper with Tween 20. (C) copper with Tween 20 and 1.0 g/l of turmeric in the electrolyte. (D) copper with Tween 20 and 5.0 g/l of turmeric in the electrolyte. (E) copper with Tween 20 and 10.0 g/l of turmeric in the electrolyte. (F) copper with Tween 20 and 10.0 g/l of turmeric in the electrolyte sonicated at a power of 33 W/l before electrodeposition.

5.4.4.2. Salt spray analysis

Photographic images of copper samples before and after salt spray analysis, are presented in Figure 5.25. and their calculated corrosion rates shown in Figure 5.26.



















Samples	0 hours	24 hours	240 hours
A			
B			
C			
D			
E			
F			

Figure 5.25. Images of sample before and after spray analysis. (A) pure copper. (B) copper with Tween 20. (C) copper with Tween 20 and 1.0 g/l of turmeric in the electrolyte. (D) copper with Tween 20 and 5.0 g/l of turmeric in the electrolyte. (E) copper with Tween 20 and 10.0 g/l of turmeric in the electrolyte. (F) copper with Tween 20 and 10.0 g/l of turmeric in the electrolyte sonicated at a power of 33 W/l before electrodeposition.

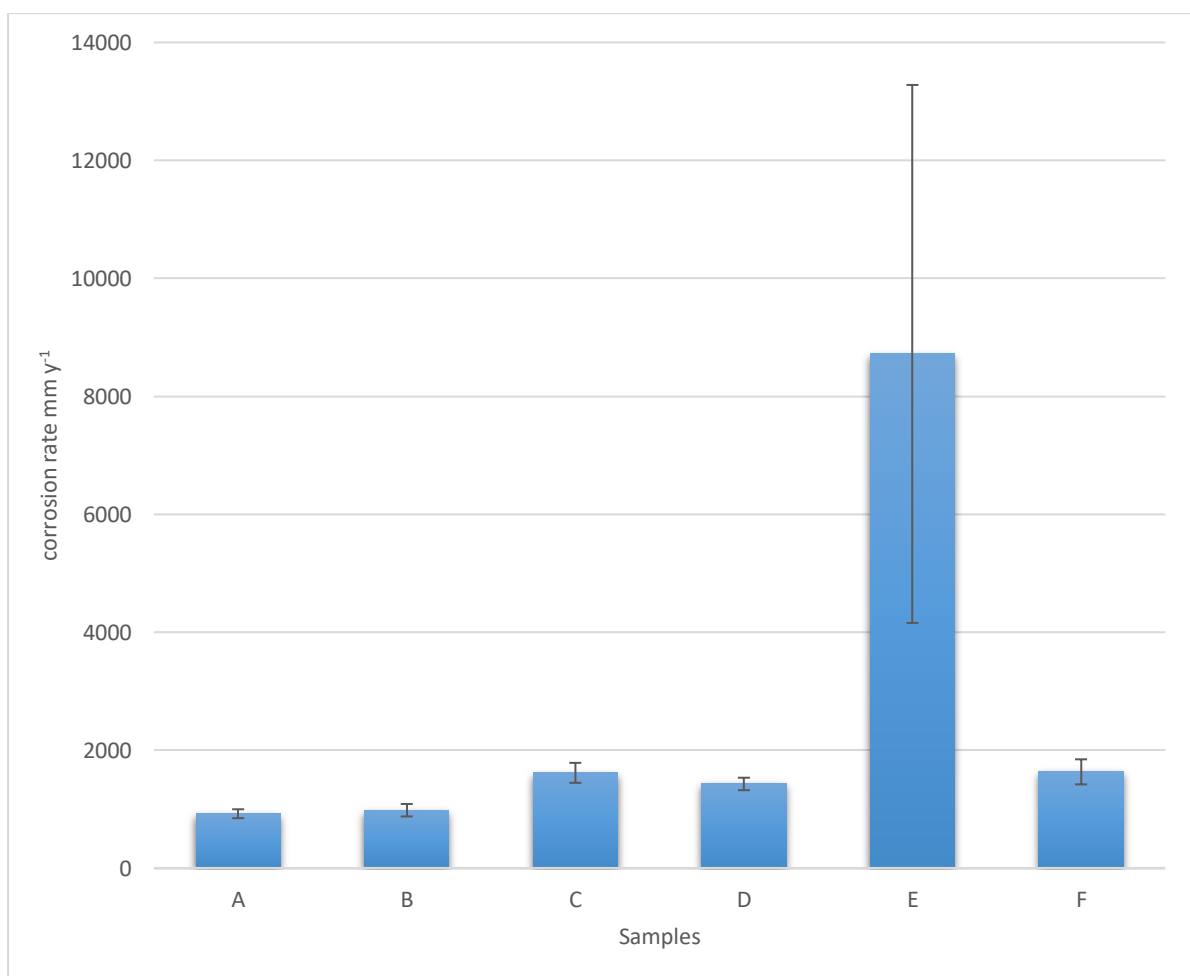


Figure 5.26. Bar chart of corrosion rate calculated from salt spray analysis. (A) pure copper. (B) copper with Tween 20. (C) copper with Tween 20 and 1.0 g/l of turmeric in the electrolyte. (D) copper with Tween 20 and 5.0 g/l of turmeric in the electrolyte. (E) copper with Tween 20 and 10.0 g/l of turmeric in the electrolyte. (F) copper with Tween 20 and 10.0 g/l of turmeric in the electrolyte sonicated at a power of 33 W/l before electrodeposition.

All samples exhibited corrosion after 240 hours, however sample (E) exhibited severe corrosion. The dark red areas of the deposits can be attributed to the copper (I) oxide (Cu_2O), the black areas can be attributed to the Copper (II) oxide (CuO), and the green areas can be attributed to localised corrosion caused by corrosive ions [35]. The white areas were likely due to the corrosion products of zinc (ZnO and Zn(OH)_2) from the brass substrate, caused by the failure of the copper coating allowing oxygen and moisture to reach the brass underneath [36]. Samples (A) and (B) exhibited similar corrosion rates, with a small increase observed for sample (C). Samples (C), (D) and (F) exhibited similar corrosion rates. A significant increase in corrosion rate was observed for sample (E).

All copper deposits exhibited a higher corrosion rate in salt spray analysis compared to the electrochemical analysis. In aqueous solutions the H_2O molecules dissociate to form H^+ and OH^- ions. Metals in aqueous solutions are corroded when H^+ ions transfer electrons from the metal to dissolved O_2 (forming H_2O). The rate of corrosion is dependent on the transfer of electrons to the H^+ ions, and thus dependent on H^+ interacting with the metal. However, the concentration of H^+ in pure water is relatively low. When NaCl is added to an aqueous solution NaCl dissociates to form ions (Na^+ and Cl^-), which increases the conductivity of the solution. This allows electrons to be transferred from the metal at an accelerated rate, increasing the corrosion rate [37].

5.5. Copper results discussion

The results from the electrodeposited copper turmeric composite coating analysis show not only is turmeric a viable sustainable alternative to some of the more commonly used filler particles, but the extent of the increase in hardness at such a low particle cost may make it superior to many.

The results obtained from the microstructural analysis showed that turmeric had a significant effect on the grain structure of the deposits. There was a reverse correlation between the concentration of turmeric in the electrolyte and the turmeric particle content of the deposits. The reduction in particle content with increasing particle electrolyte concentration may be due to an increase in turmeric particle aggregation in the electrolyte [5-7]. An increase in particle collision may also be responsible for the reduction in particle content. At high electrolyte particle concentrations, there would be an increase in the number of particles colliding with the deposit. This would result in an increasing chance of particles in the solution colliding with particles on the surface of the deposit. If energy is sufficient this may result in dislodging the particles from the growing matrix and decreasing the particle content of the deposit.

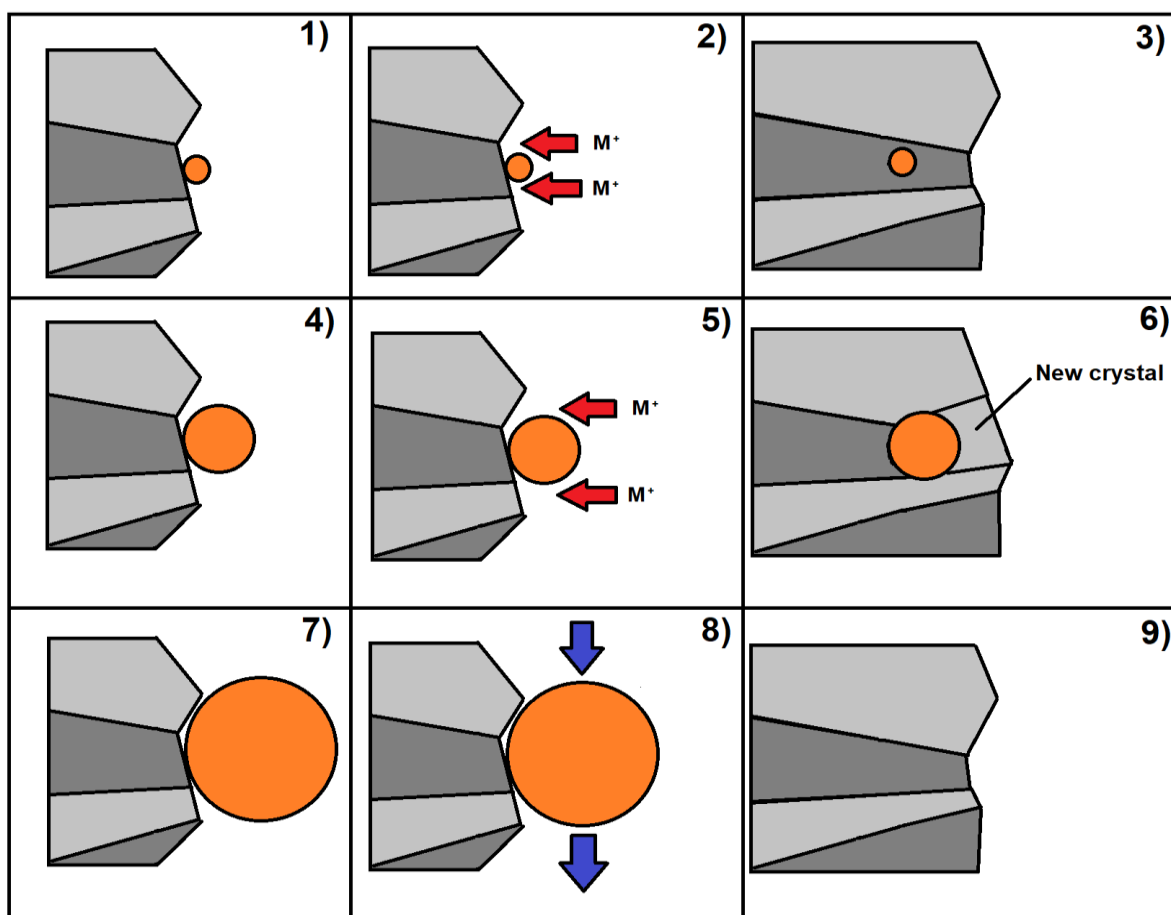


Figure 5.27. Diagram of the effects of turmeric Z-average size on grain disruption of an electrodeposited copper coating. (1) A small particle collides with the growing deposit. (2) The particle absorbed. (3) The particle is entrapped in the growing crystal. (4) An optimal size particle collides with the growing deposit. (5) The particle is absorbed disrupting the crystal growth. (6) The particle is then entrapped by a new crystal or an encroaching crystal. (7) A large particle collides with the growing deposit. (8) The particle is removed by flow of the electrolyte or collision of another particle before absorption. (9) The crystal continues to grow.

A strong correlation was observed between the grain structure of the deposit and the Z-average size of turmeric particles in the electrolyte. An optimal particle size of between 200 nm and 300 nm was observed for reducing the size of grains in the deposit. This was also confirmed by observation of the copper nano-diamond deposits. The optimal particle size observed may be due to the way in which the particles interact with the growing deposit (Figure 5.27.). If the particle is too small, when it is absorbed on to the deposit it will not prevent the deposition of metal ions on to the growing crystal underneath. The particle would be entrapped into the growing deposit but would not disrupt the crystals growth, and therefore no reduction in grain size would be observed.

Figure 5.28. shows an ion beam image of cavities in a crystal of sample (E) likely caused by the presents of turmeric. If the optimal size particle is absorbed on to the deposit, it will prevent the deposition of metal ions on to the growing crystal underneath. Crystal growth would be disrupted, and a reduction in grain size would be observed. If the particle is too big, it will be removed from the deposit by the flow of the bath or by collision with another particle before it is absorbed. This would not result in the disruption of the crystal growth or a reduction in grain size.

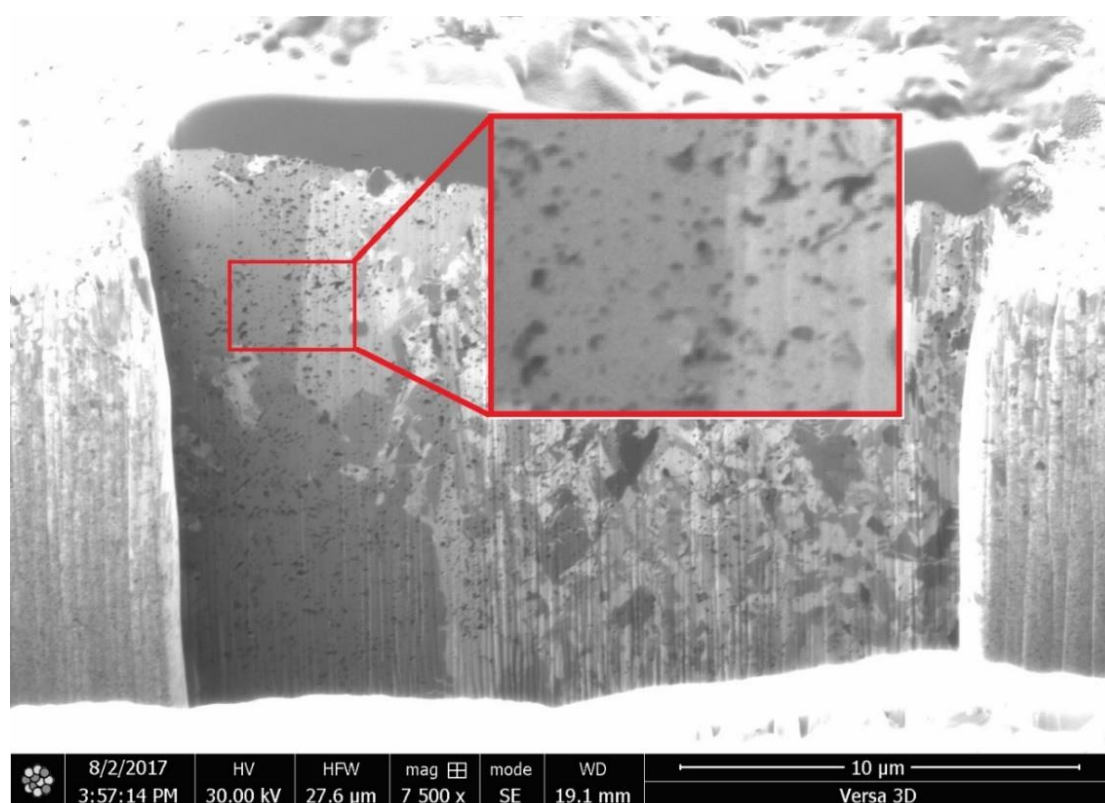


Figure 5.28. Ion beam image of sample (E) with cavity visible within a crystal.

The reduction in grain size caused by the incorporation of turmeric into the copper deposits, produced coatings with increased hardness when compared to the pure copper deposits. The hardness was also increased when compared to other more commonly used filler particles. Figure 5.29. shows the percentage increase in hardness of electrodeposited copper with the incorporation of turmeric and other more commonly used filler particles. Turmeric increased the hardness of the deposit to the same extent as nano-SiC (63 % and 61 % respectively), and to a greater extent than micro-SiC, (SWCNT) single-walled carbon nano-tubes and micro-WC (34 %, 36 %, and 16 % respectively) [14,38-41]. Although the plating parameters (such as pulse

current, current density, bath agitation, particle size and concentration) can also influence the hardness of a composite deposit, the result of the Vicker's hardness tests obtained in this research indicates that turmeric may not only be a suitable sustainable alternative to some of the commonly used filler particles, but may be superior to many for enhancing the hardness of a copper deposit.

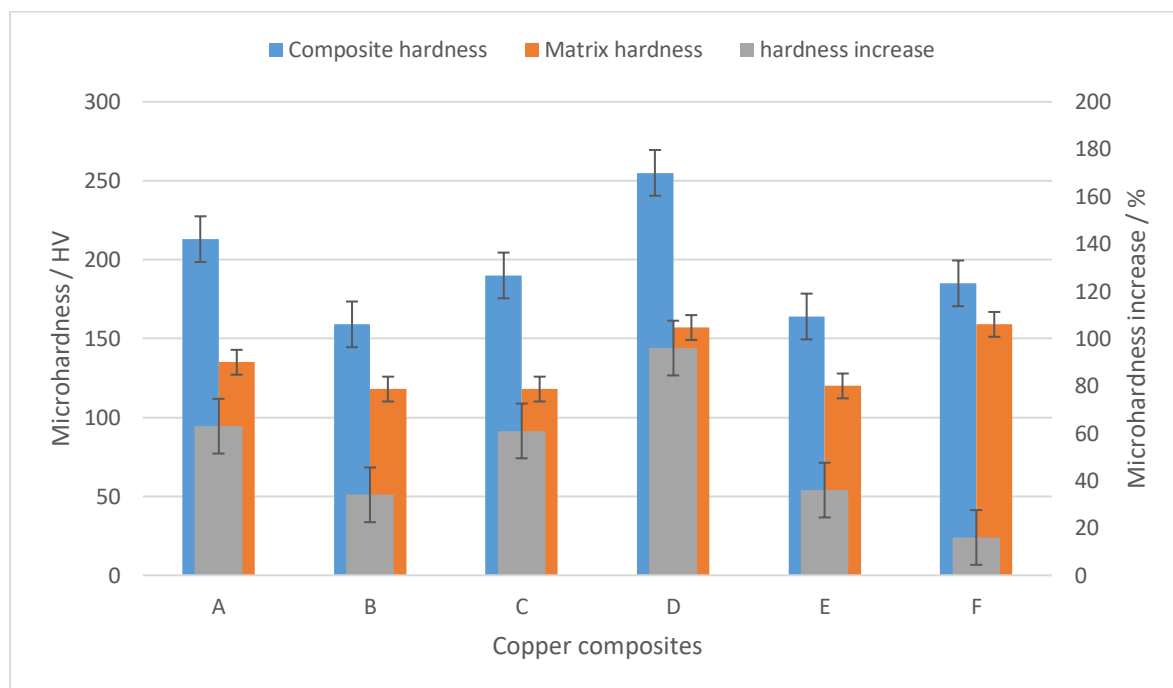


Figure 5.39. Increase in microhardness of copper deposits when various filler particles are added to the electrolyte. (A) Turmeric particles. (B) Micro SiC particles [14,41]. (C) Nano SiC particles [38,41]. (D) Graphene particles [38]. (E) Single walled carbon nano-tubes [39,42]. (F) Micro WC particles [40].

The WCA of the copper coating was also increased by the addition of Tween 20 and turmeric to the electrolyte, changing the behaviour of the coating from hydrophilic to hydrophobic. Hydrophobic surfaces have many potential industrial applications including water repellent coatings, self-cleaning surfaces, sensor applications and in microfluidics. Although the grain structure was the primary factor increasing the WCA, increasing the surface roughness may enhance WCA, further increasing the coatings hydrophobic properties [43-48].

The corrosion behaviour of the coatings incorporating turmeric was complex, showing an increase in electrochemical corrosion resistance in 0.1 M of Na_2SO_4 compared to pure copper, and a decrease in corrosion resistance when exposed to the salt spray test. The results of the corrosion analysis indicate that the incorporation of turmeric

into a copper deposit may be advantageous or detrimental for corrosion resistance depending on the environment the coatings are exposed to.

Reducing the grain size of a copper deposit can either decrease or increase the corrosion resistance depending on the electrolyte. When exposed to air the surface of a metal is covered by an oxide film, however once submerged in an aqueous solution the oxide film may start to dissolve exposing the bare metal surface. In acidic conditions, the oxide film may be completely dissolved, known as an active state. Oxide films tend to be thinner at grain boundaries and incursions (such as turmeric particles), thus initially the underlying metal will be exposed there first in localised areas. In active systems, a decrease in grain size and an increase in incursions lead to an increase in the corrosion rate. The solubility of the oxide film is less in near neutral solutions compared to acidic solutions. If a near neutral solvent contains inhibiting ions the solubility of the oxide film may be suppressed, the oxide film may stabilise to form a passive layer (which prevents corrosion), placing the metal in a passive state. In a passive environment, a reduction in grain size decreases the corrosion rate of the metal [33]. However, other factors can also influence the corrosion resistance of copper. The literature has shown that the incorporation of inert particles into a matrix can cause weak points between the embedded particles and the matrix. These weak points allow the electrolyte to enter the coating, allowing deeper penetration into the matrix and accelerated corrosion [49].

5.6. Conclusions

- The incorporation of turmeric particles into a copper matrix reduced the grain size of the deposit, enhancing physical properties such as hardness and WCA.
- The turmeric particle content in the deposit is a reverse correlation to the concentration of turmeric in the electrolyte, with increased bath concentration resulting in a decrease in particle content of the coating.
- The Z-average size of turmeric particle in the electrolyte has a greater influence on the grain structure of the deposit than either the concentration of turmeric in the electrolyte or the concentration of turmeric in the coating.

- There is an optimal size of particle for reducing the grain size of an electrodeposited copper turmeric coating of around 250 nm, which was confirmed by EBSD results of copper nano-diamond deposits.
- The reduction in grain structure seen with the incorporation of turmeric increases the microhardness and WCA of the copper deposit.
- The corrosion resistance of the copper turmeric showed an increase when estimated by Tafel plot and a decrease when measured by salt spray analysis.
- The increase in hardness seen with the incorporation of turmeric was greater than that reported for SWCNT, micro-WC, and micro-SiC and equal to that seen by nano-SiC, making turmeric a potential sustainable alternative to these filler particles.
- The addition of turmeric to the electrolyte increased the WCA of the deposit and changed the coating from hydrophilic to hydrophobic. The WCA of the coatings may be increased further by increasing the roughness of the surface.
- Hydrophobic coatings have many potential industrial applications including water repellent coatings, self-cleaning surfaces, sensor applications and in microfluidics.

5.7. Reference list

- [1] M.A. Malik, M.A. Hashim, F. Nabi, S.A. Al-Thabaiti, Z. Khan, Anti-corrosion ability of surfactants: a review, *International Journal of Electrochemical Science*. 6 (2011) 1927-1948.
- [2] R. Vittal, H. Gomathi, K. Kim, Beneficial role of surfactants in electrochemistry and in the modification of electrodes, *Advances in Colloid and Interface Science*. 119 (2006) 55-68.
- [3] I. Tudela, Y. Zhang, M. Pal, I. Kerr, T.J. Mason, A.J. Cobley, Ultrasound-assisted electrodeposition of nickel: Effect of ultrasonic power on the characteristics of thin coatings, *Surface and Coatings Technology*. 264 (2015) 49-59.
- [4] S. Ghosh, P. Limaye, B. Swain, N. Soni, R. Agrawal, R. Dusane, A. Grover, Tribological behaviour and residual stress of electrodeposited Ni/Cu multilayer films on stainless steel substrate, *Surface and Coatings Technology*. 201 (2007) 4609-4618.
- [5] H. Gül, F. Kılıç, M. Uysal, S. Aslan, A. Alp, H. Akbulut, Effect of particle concentration on the structure and tribological properties of submicron particle SiC

reinforced Ni metal matrix composite (MMC) coatings produced by electrodeposition, *Applied Surface Science*. 258 (2012) 4260-4267.

[6] M. Vaezi, S. Sadrnezhaad, L. Nikzad, Electrodeposition of Ni–SiC nano-composite coatings and evaluation of wear and corrosion resistance and electroplating characteristics, *Colloids and Surfaces A: Physicochemical and Engineering Aspects*. 315 (2008) 176-182.

[7] M. Eslami, H. Saghafian, F. Golestani-fard, A. Robin, Effect of electrodeposition conditions on the properties of Cu–Si₃N₄ composite coatings, *Applied Surface Science*. 300 (2014) 129-140.

[8] D. Suarez, F. Olson, Nodulation of electrodeposited copper in the presence of thiourea, *Journal of Applied Electrochemistry*. 22 (1992) 1002-1010.

[9] T. Andersen, C. Pitt, L. Livingston, Nodulation of electrodeposited copper due to suspended particulate, *Journal of Applied Electrochemistry*. 13 (1983) 429-438.

[10] F. C. Walsh* C. Ponce de Leon., A review of the electrodeposition of metal matrix composite coatings by inclusion of particles in a metal layer: an established and diversifying technology, *Transaction of the Institute of Metal Finishing*. 92 (2014) 83-98.

[11] R. Bazzard, P. Boden, Nickel-Chromium Alloys by Codeposition: Part II—Diffusion Heat Treatment of Codeposited Composites, *Transaction of the Institute of Metal Finishing*. 50 (1972) 207-210.

[12] A. Ashok, H. Maharana, A. Basu, Effect of electro-co-deposition parameters on surface mechanical properties of Cu–TiO₂ composite coating, *Bulletin of Materials Science*. 38 (2015) 335-342.

[13] C.G. Fink, J.D. Prince, The Codeposition of Copper and Graphite, *Transactions of the American Electrochemical Society*. 54 (1928) 315-321.

[14] M. Hakamada, Y. Nakamoto, H. Matsumoto, H. Iwasaki, Y. Chen, H. Kusuda, M. Mabuchi, Relationship between hardness and grain size in electrodeposited copper films, *Materials Science and Engineering: A*. 457 (2007) 120-126.

[15] A. Hovestad, L. Janssen, Electrochemical codeposition of inert particles in a metallic matrix, *Journal of Applied Electrochemistry*. 25 (1995) 519-527.

[16] H. Maharana, P. Rai, A. Basu, Surface-mechanical and electrical properties of pulse electrodeposited Cu–graphene oxide composite coating for electrical contacts, *Journal of Materials Science*. 52 (2017) 1089-1105.

[17] V. Medeliene, M. Kurtinaitienė, G. Bikulčius, V. Stankevič, A study of copper coatings electrodeposited in electrolyte with a metallic powder of chromium, *Surface and Coatings Technology*. 200 (2006) 6123-6129.

- [18] Y. Raghupathy, A. Kamboj, M. Rekha, N.N. Rao, C. Srivastava, Copper-graphene oxide composite coatings for corrosion protection of mild steel in 3.5% NaCl, *Thin Solid Films*. 636 (2017) 107-115.
- [19] V. Stankovic, M. Gojo, Electrodeposited composite coatings of copper with inert, semiconductive and conductive particles, *Surface and Coatings Technology*. 81 (1996) 225-232.
- [20] M. Zhou, Y. Mai, H. Ling, F. Chen, W. Lian, X. Jie, Electrodeposition of CNTs/copper composite coatings with enhanced tribological performance from a low concentration CNTs colloidal solution, *Materials Research Bulletin*. 97 (2018) 537-543.
- [21]] E.O. Hall, *Proceedings of the Physical Society London B*. 64 (1951).
- [22] N. Hansen, Hall–Petch relation and boundary strengthening, *Scripta Materialia*. 51 (2004) 801-806.
- [23] G. Hughes, S. Smith, C. Pande, H. Johnson, R. Armstrong, Hall-Petch strengthening for the microhardness of twelve nanometer grain diameter electrodeposited nickel, *Scripta Metallurgica*. 20 (1986) 93-97.
- [24] N.J. Petch, *The Journal of the Iron and Steel Institute*. 174 (1953).
- [25] D. Janssen, R. De Palma, S. Verlaak, P. Heremans, W. Dehaen, Static solvent contact angle measurements, surface free energy and wettability determination of various self-assembled monolayers on silicon dioxide, *Thin Solid Films*. 515 (2006) 1433-1438.
- [26] C. Herring, Some theorems on the free energies of crystal surfaces, *Physical review*. 82 (1951) 87.
- [27] L. Vitos, A. Ruban, H.L. Skriver, J. Kollar, The surface energy of metals, *Surface Science*. 411 (1998) 186-202.
- [28] R.N. Wenzel, Surface roughness and contact angle. *The Journal of Physical Chemistry*. 53 (1949) 1466-1467.
- [29] W. Choi, Tuteja. A, Mabry. J, R. Cohen, McKinley. G, A modified Cassie–Baxter relationship to explain contact angle hysteresis and anisotropy on non-wetting textured surfaces, *Journal of Colloid and Interface Science*. 339 (2009) 208-216.
- [30] A. Cassie, S. Baxter, Wettability of porous surfaces, *Transactions of the Faraday society*. 40 (1944) 546-551.
- [31] E. Bormashenko, Why does the Cassie–Baxter equation apply? *Colloids and Surfaces A: Physicochemical and Engineering Aspects*. (2008) 47-50.
- [32] W. Luo, Y. Xu, Q. Wang, P. Shi, M. Yan, Effect of grain size on corrosion of nanocrystalline copper in NaOH solution, *Corrosion Science*. 52 (2010) 3509-3513.

- [33] K. Ralston, N. Birbilis, Effect of grain size on corrosion: a review, *Corrosion*. 66 (2010) 075005-075005-13.
- [34] Gamry Instruments, Getting Started with Electrochemical Corrosion Measurement. Application note, Gamry instruments. (2011).
- [35] J. Wu, C. Cai, Z. Zhou, H. Qian, F. Zha, J. Guo, B. Feng, T. He, N. Zhao, J. Xu, Low-cost mussel inspired poly (catechol/polyamine) coating with superior anti-corrosion capability on copper, *Journal of Colloid and Interface Science*. 463 (2016) 214-221.
- [36] L. Sziráki, E. Szocs, Z. Pilbath, K. Papp, E. Kálmán, Study of the initial stage of white rust formation on zinc single crystal by EIS, STM/AFM and SEM/EDS techniques, *Electrochimica Acta*. 46 (2001) 3743-3754.
- [37] S. Hassani, K.P. Roberts, S.A. Shirazi, J.R. Shadley, E.F. Rybicki, C. Joia, Flow Loop Study of NaCl Concentration Effect on Erosion, Corrosion, and Erosion-Corrosion of Carbon Steel in CO₂-Saturated Systems, *Corrosion*. 68 (2012) G1-G9.
- [38] C.L. Pavithra, B.V. Sarada, K.V. Rajulapati, T.N. Rao, G. Sundararajan, A new electrochemical approach for the synthesis of copper-graphene nanocomposite foils with high hardness, *Scientific reports*. 4 (2014) 4049.
- [39] C. Guiderdoni, E. Pavlenko, V. Turq, A. Weibel, P. Puech, C. Estournès, A. Peigney, W. Bacsa, C. Laurent, The preparation of carbon nanotube (CNT)/copper composites and the effect of the number of CNT walls on their hardness, friction and wear properties, *Carbon*. 58 (2013) 185-197.
- [40] V. Medelienė, A. Kosenko, Structural and functional properties of electrodeposited copper metal matrix composite coating with inclusions of WC, *Materials Science*. 14 (2008) 29-33.
- [41] J. Zhu, L. Liu, H. Zhao, B. Shen, W. Hu, Microstructure and performance of electroformed Cu/nano-SiC composite, *Materials & Design*. 28 (2007) 1958-1962.
- [42] Z. Wang, X. Cai, C. Yang, L. Zhou, C. Hu, An electrodeposition approach to obtaining carbon nanotubes embedded copper powders for the synthesis of copper matrix composites, *Journal of Alloys and Compounds*. 735 (2018) 1357-1362.
- [43] M.H. Kwon, W.Y. Jee, C.N. Chu, Fabrication of hydrophobic surfaces using copper electrodeposition and oxidation, *International Journal of Precision Engineering and Manufacturing*. 16 (2015) 877-882.
- [44] Z. Chen, F. Li, L. Hao, A. Chen, Y. Kong, One-step electrodeposition process to fabricate cathodic superhydrophobic surface, *Applied Surface Science*. 258 (2011) 1395-1398.
- [45] Y. Huang, D. Sarkar, X. Chen, Fabrication of Superhydrophobic Surfaces on Aluminum Alloy Via Electrodeposition of Copper Followed by Electrochemical Modification, *Nano-Micro Letters*. 3 (2011) 160-165.

- [46] Y. Huang, D.K. Sarkar, X. Chen, A one-step process to engineer superhydrophobic copper surfaces, *Materials Letters*. 64 (2010) 2722-2724.
- [47] G. McHale, N. Shirtcliffe, M. Newton, Super-hydrophobic and super-wetting surfaces: analytical potential? *Analyst*. 129 (2004) 284-287.
- [48] A. Lafuma, D. Quéré, Superhydrophobic states, *Nature materials*. 2 (2003) 457.
- [49] M. Lekka, D. Koumoulis, N. Kouloumbi, P. Bonora, Mechanical and anticorrosive properties of copper matrix micro-and nano-composite coatings, *Electrochimica Acta*. 54 (2009) 2540-2546.

6. Nickel results

6.1. Overview

In order to understand the effect that the incorporation of turmeric particles has on the physical properties of the electrodeposited nickel coatings, pure nickel, nickel with Tween 20 and nickel with turmeric coatings were produced and characterised. This Chapter contains the results and discussion of the physical properties of the electrodeposited nickel coatings, and in an effort to understand these physical properties this Chapter also contains results and discussion of the microstructure of the nickel coatings. This Chapter has been divided into three sections:

- Electrodeposition: this section contains information on the Hull cell test, and the surface finish of the coatings.
- Microstructure: this section has results from surface morphology, grain structure, grain size, and particle content of the nickel turmeric samples.
- Coating properties: this section contains information on the hardness, water contact angle, surface roughness, and both electrochemical and salt spray corrosion analysis of the nickel turmeric samples.

6.2. Electrodeposition

6.2.1. Watts nickel deposition

A photographic image of the surface of the Watts turmeric electrolyte is presented in Figure 6.1. Images of the surface finish of nickel and nickel turmeric samples produced from a nickel Watts bath are presented in Figure 6.2.



Figure 6.1. Image of the surface of the nickel Watts electrolyte with 10.0 g/l of Tween 20 and 1.0 g/l of turmeric.

Initially, an even turmeric dispersion was achieved in the nickel Watts electrolyte by the application of ultrasound at a power of 11 W/L using a 20 kHz probe for 20 min prior to electrodeposition. Once ultrasound was stopped and stirring applied (during electrodeposition), the turmeric particles re-agglomerated and rose to the surface of the electrolyte forming large aggregates.

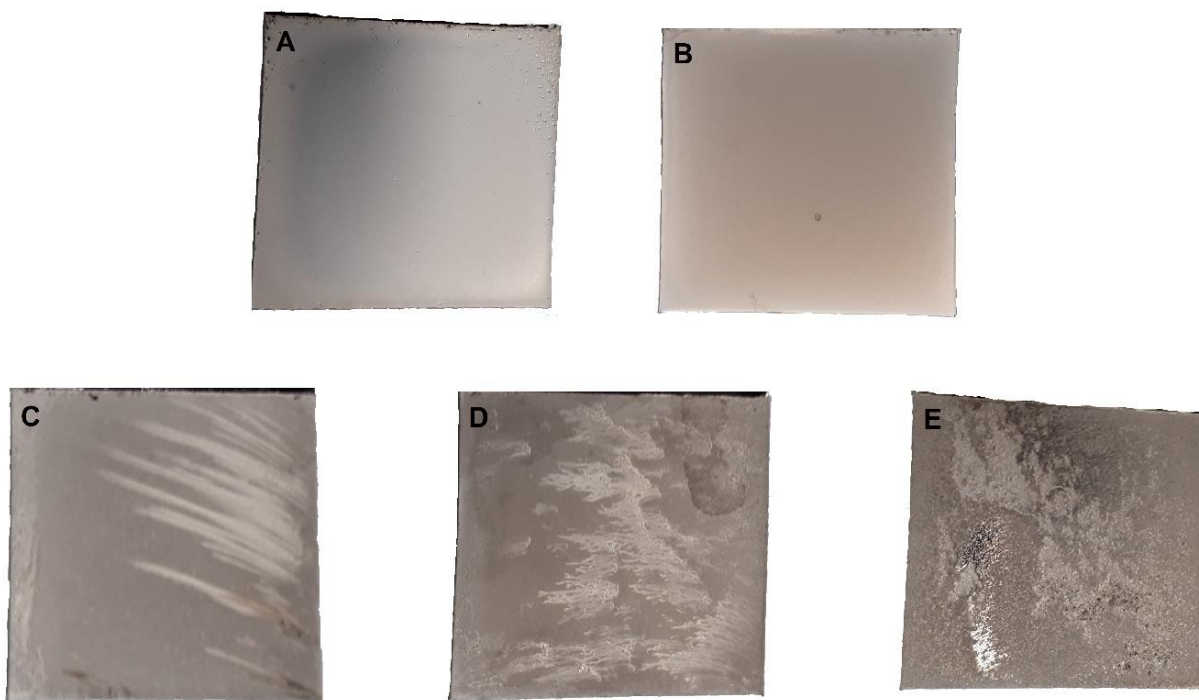


Figure 6.2. images of the surface of nickel coating samples produced from a Watts bath. (A) pure nickel. (B) nickel with Tween 20 (C) nickel with Tween 20 and 1.0 g/l of turmeric in the electrolyte. (D) nickel with Tween 20 and 5.0 g/l of turmeric in the electrolyte. (E) nickel with Tween 20 and 10.0 g/l of turmeric in the electrolyte.

Although the pure nickel coating showed a smooth finish (A), edge build up, and small pits (caused by gas bubbles on the surface of the cathode) were present at the edge of the sample. When 10.0 ml/l of Tween 20 was added (B) to the Watts bath, the deposit produced showed a smooth uniform finish of a lighter grey colour, although some edge build-up was displayed no pits were present. All samples containing turmeric (C, D and E) showed poor quality non-uniform finishes. The deposits showed features similar in appearance to scratch marks (from a right to left direction) and areas where the substrate was visible underneath the deposit.

The ionic strength of the Watts electrolyte was likely responsible for the large turmeric aggregates present on its surface. Turmeric particles are hydrophobic and require a surfactant to disperse them uniformly in an aqueous solution [1]. The ability of a surfactant to disperse a particle in an aqueous solution and the magnitude of the particle's interaction can be strongly affected by the ionic strength of the electrolyte. Both the charge density of the ions and their concentration in the electrolyte can increase the tendency of hydrophobic particles to aggregate in solution [1-4]. In most

cases, hydrophobic interactions are enhanced by the addition of a salt to a solution, this can result in salting out (reaggregation of the particles in solution). Salting out of the particles can increase as the charge density of the ions in solution increases, becoming significant at even moderate ion concentrations (0.1-1.0 M) [2]. When ultrasound was applied to the Watts turmeric solution, aggregates were broken up at a faster rate than their formation. Once ultrasound was stopped and stirring applied, large aggregates were formed which rose to the surface of the solution.

The presence of large aggregates in the solution resulted in the poor quality of the nickel Watts turmeric deposits. During electrodeposition, large turmeric aggregates collided with the cathode and prevented the reduction of Ni^{2+} at that point, until they were dislodged by the flow of the bath or the collision of another large aggregate. This led to the right to left (direction of bath flow) scratch like marks in the nickel Watts turmeric coatings.

The presence of bubbles on the surface of the pure nickel sample produced from a Watts bath can be attributed to the formation of hydrogen gas on the surface of the cathode. During electrodeposition if the pH is too low the reduction of H^+ can take place on the cathode, forming bubbles of gas (H_2) [5,6]. The current density is typically higher at the edges of the cathode than the centre, resulting in greater reduction of H^+ at the edges compared to the centre [5,7]. The gas bubbles on the cathode prevent the deposition of nickel at that area and pits are formed. When 10.0 g/l of Tween 20 was added to the electrolyte, no bubbles were formed on the cathode. As stated in Chapter 5 surfactants can modify the grain structure of a deposit and can also act as brighteners. Brighteners can work by increasing the nucleus density of newly formed nickel nucleus and increased rate of hydrogen desorption from the cathode. The desorption of hydrogen decreases or stops the formation of pits on the surface of the cathode [8-13].

6.2.2. Hull cell test

Photographic images of Hull cell panels after the electrodeposition of nickel from a low ion concentration electrolyte (LICE) are shown in Figure 6.3.

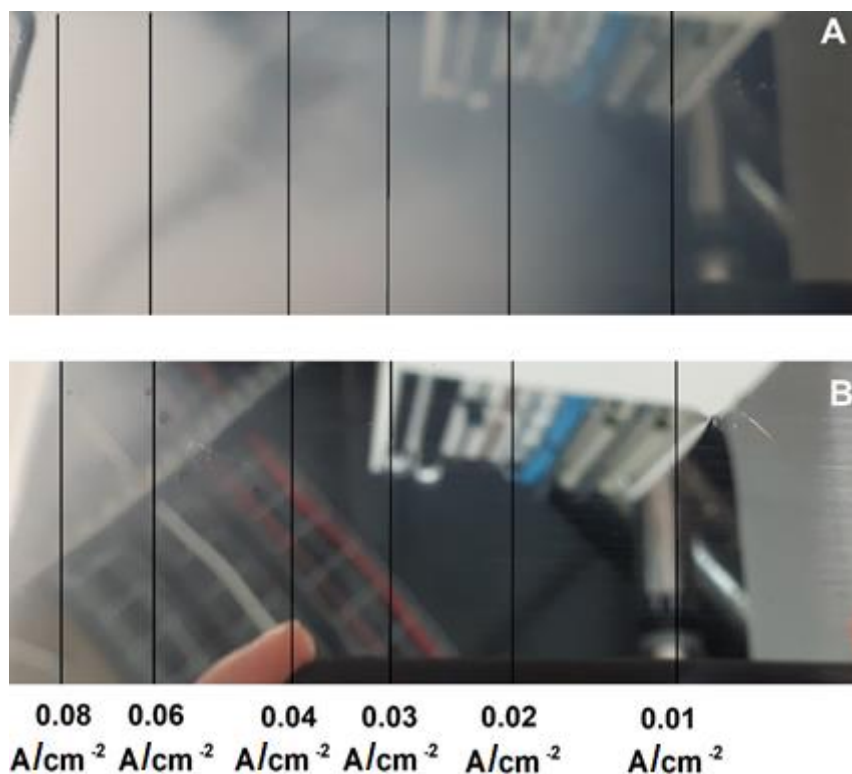


Figure 6.3. Image of Hull cell panels (A) electrodeposited LICE nickel. (B) electrodeposited LICE nickel with 10.0 ml/l of Tween 20.

Deposit A shows a bright finish until 0.01 A/cm^2 , after which the deposit became duller in appearance with a matte finish after 0.02 A/cm^2 . Deposit B has a mirror bright finish until 0.08 A/cm^2 , after which the deposit became duller in appearance. The brightness of an electrodeposited coating is often an indication of its smoothness. Additives such as brighteners can be utilised to increase the smoothness of the deposit and therefore its brightness [14,15]. The literature has shown that surfactants can act as brighteners modifying the grain structure and improving the smoothness and brightness of the finish [8-13].

6.2.3. Lower ion concentration electrolyte (LICE) nickel

A photographic image of the surface of the LICE turmeric electrolyte is presented in Figure 6.4. Images of nickel and nickel turmeric samples produced from a nickel LICE electrolyte is presented in Figure 6.5.



Figure 6.4. Image of the surface beaker containing LICE nickel electrolyte with 10.0 g/l of Tween 20 and 1.0 g/l of turmeric.

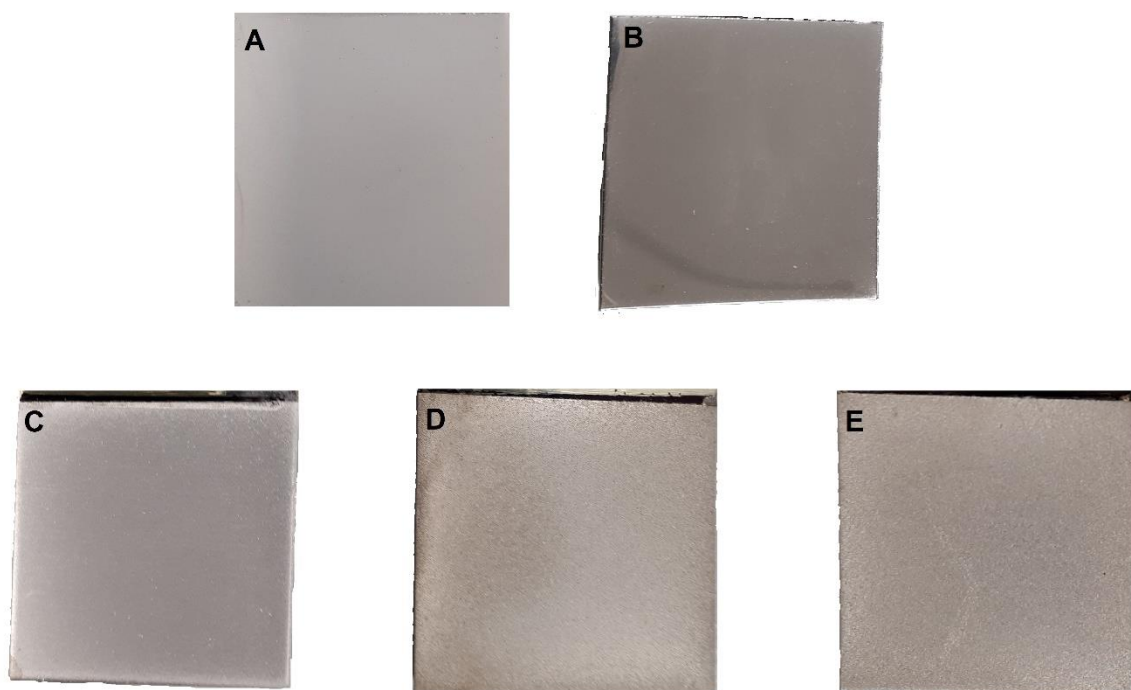


Figure 6.5. images of the surface of nickel coating samples produced from a LICE nickel electrolyte. (A) pure nickel. (B) nickel with Tween 20. (C) nickel with Tween 20 and 1.0 g/l of turmeric in the electrolyte. (D) nickel with Tween 20 and 5.0 g/l of turmeric in the electrolyte. (E) nickel with Tween 20 and 10.0 g/l of turmeric in the electrolyte.

Ultrasound generated from a 20 kHz probe at a power of 11 W/l applied to the LICE nickel turmeric solutions resulted in a uniform dispersion of turmeric throughout the electrolyte. Once ultrasound was stopped and stirring applied (during electrodeposition), the turmeric particles remained dispersed in the electrolyte with little aggregation visible on the surface of the solution (Figure 6.3.).

Although the pure nickel sample produced from the LICE nickel electrolyte (A) showed a similar colour and texture to the pure nickel produced from the Watts bath, the finish was more matte like in appearance. When 10.0 ml/l of Tween 20 was added to the LICE electrolyte, the deposit had a mirror bright finish, with no pits present. The LICE nickel turmeric coatings (C, D and E) showed a more uniform and higher quality finish when compared to their Watts counterparts. The samples showed a progressively darker grey colour and a reduction in brightness with increasing bath turmeric concentration. All LICE nickel deposits showed some edge build up.

The reduction in ion concentration in the LICE electrolyte allowed the turmeric to disperse uniformly and remained dispersed throughout the duration of the electrodeposition process. This resulted in nickel turmeric coatings of better quality and more uniform finish than those produced for the Watts electrolyte. Although both pure nickel samples produced from a Watts electrolyte and a LICE electrolyte were similar in appearance when Tween 20 was added to the LICE electrolyte a mirror like finish was produced which was not seen for the Watts electrolyte.

6.3. Microstructure

6.3.1. Particle content

The carbon content of individual LICE nickel deposits obtained by GDOES are presented in Figures 6.6. to 6.9. with their mean carbon content presented in Figure 6.10. A comparison between deposit carbon content and turmeric electrolyte concentration is presented in Figure 6.11.

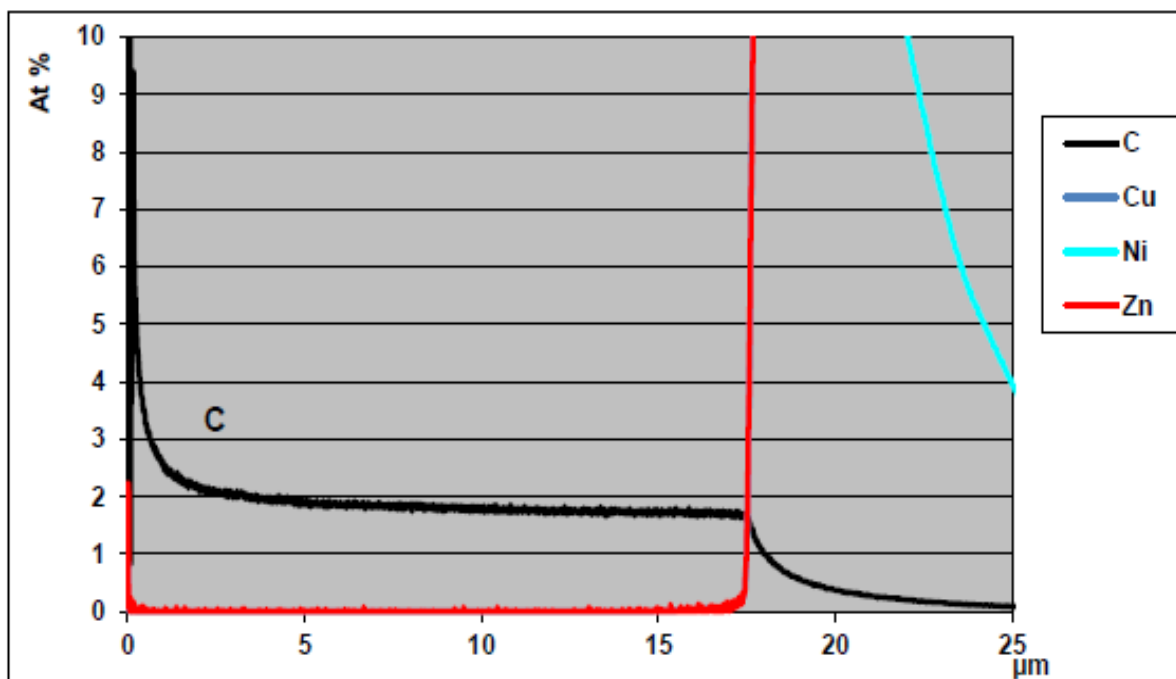


Figure 6.6. Coating composition of LICE nickel with 10.0 ml/l of Tween 20 in the electrolyte (sample (C)).

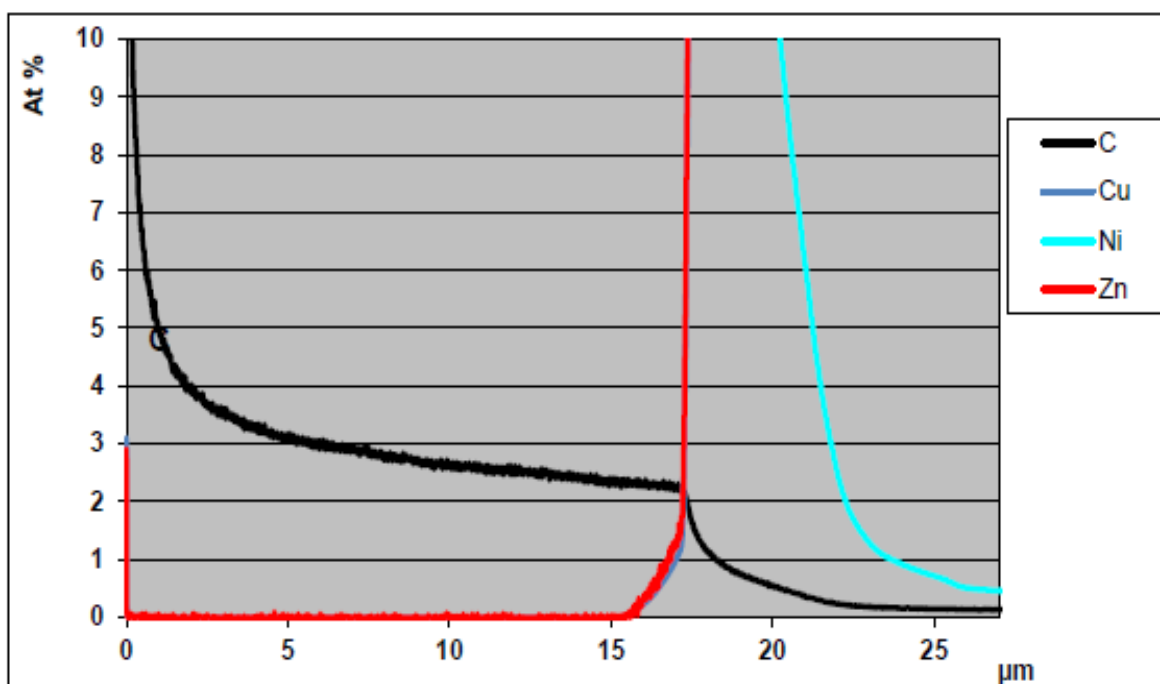


Figure 6.7. Coating composition of LICE nickel with 1.0 g/l of turmeric in the electrolyte (sample (D)).

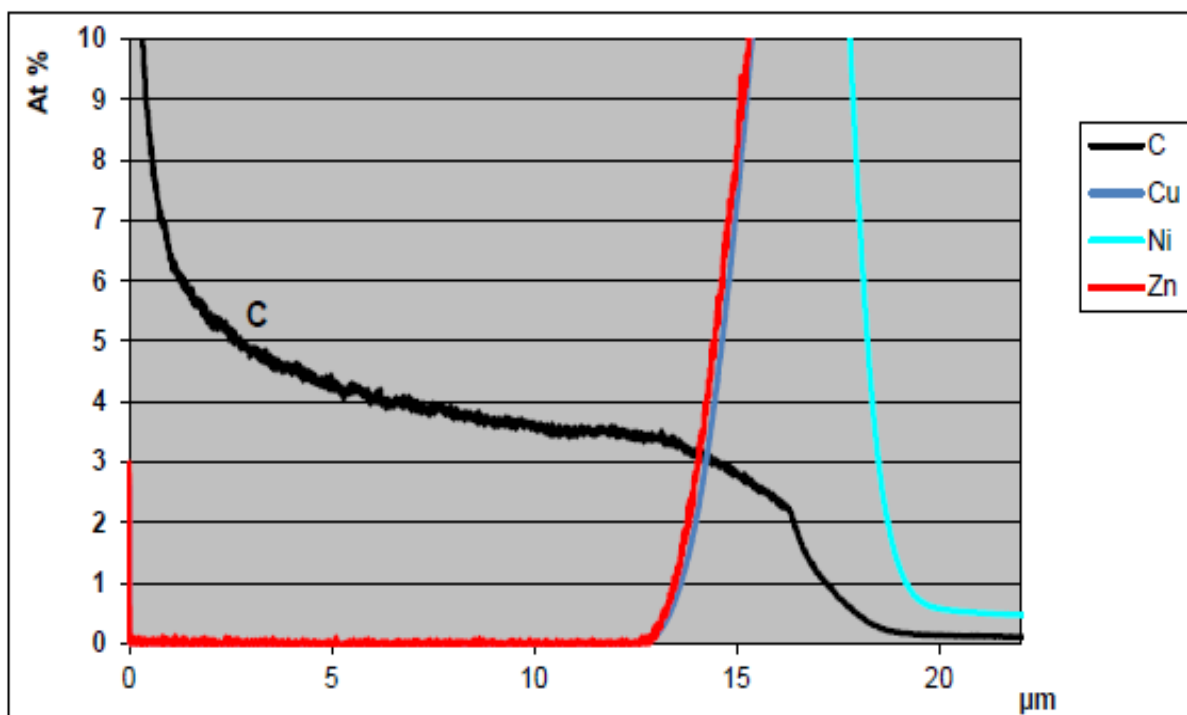


Figure 6.8. Coating composition of LICE nickel with 5.0 g/l of turmeric in the electrolyte (sample (E)).

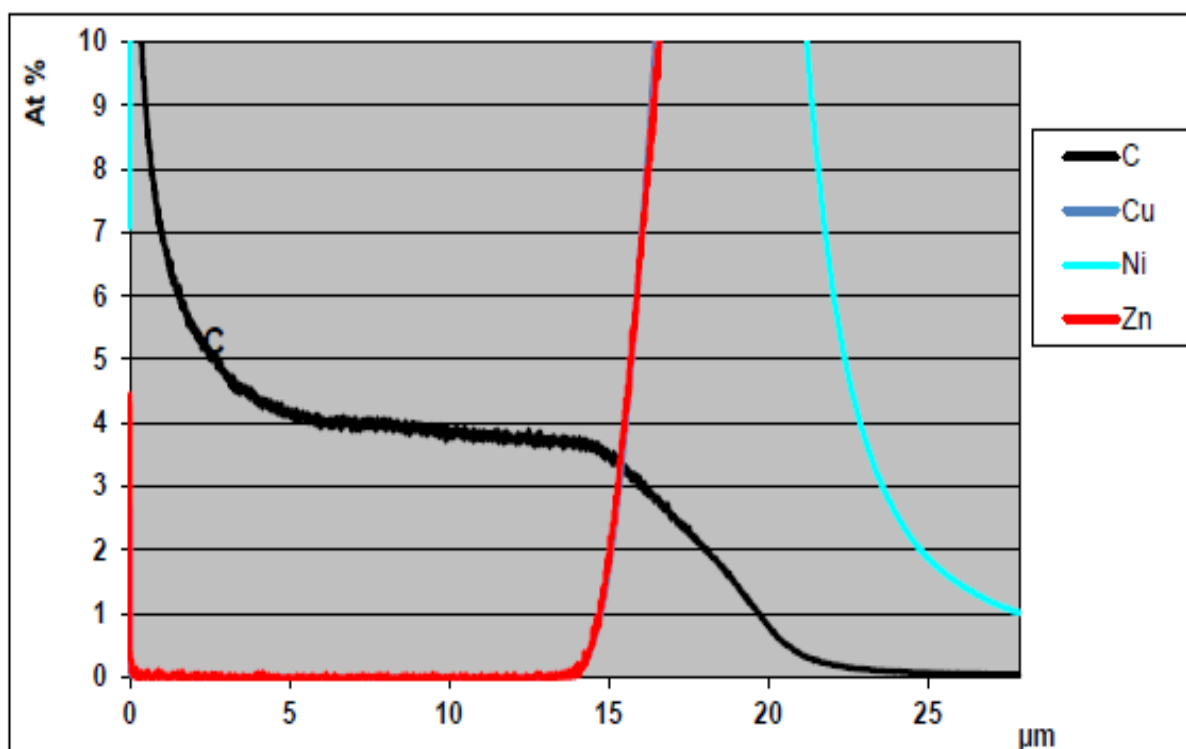


Figure 6.9. Coating composition of LICE nickel with 10.0 g/l of turmeric in the electrolyte (sample (F)).

The large spike in the carbon content near the surface of the deposits is likely due to organic contaminants on the surface of the coatings. All samples showed a slight reduction in carbon content with increasing depth of the deposit. The depth of deposit varied between approximately 20 and 25 μm from sample to sample. This could be due to variation in thickness of deposit across the surface of the sample. During electrodeposition a non-uniform distribution of current on the cathode (with the current at the edges being higher than at the centre) can cause variations in the thickness of deposit across the surface of the sample [5,7]. An non-uniform current distribution can also cause nodulation, which can cause high and low points on the surface of the sample leading to varying thickness of deposit [16-19].

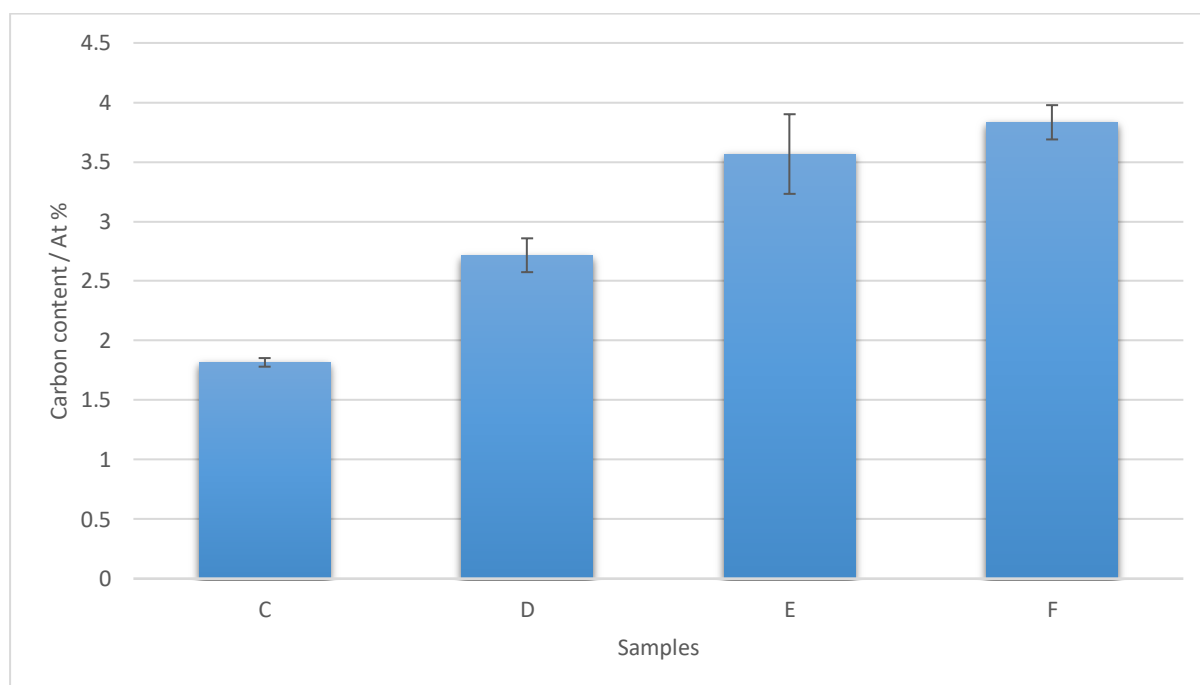


Figure 6.10. Carbon content in nickel deposits obtained by GDOES. (C) LICE nickel with 10.0 ml/l of Tween 20. (D) LICE nickel with 10.0 ml/l of Tween 20 and 1.0 g/l of turmeric. (E) LICE nickel with 10.0 ml/l of Tween 20 and 5.0 g/l of turmeric. (F) LICE nickel with 10.0 ml/l of Tween 20 and 10.0 g/l of turmeric.

A progressive increase in carbon content was observed from samples (C) to (F). The carbon content exhibited by sample (C), can be attributed to the incorporation of Tween 20 into the deposit. The literature has shown that carbon containing additive such as surfactants can be incorporated into electrodeposited nickel when present in the electrolyte [20,21]. The increase in carbon content thereafter can be attributed to the presence of both Tween 20 and turmeric in the electrolyte.

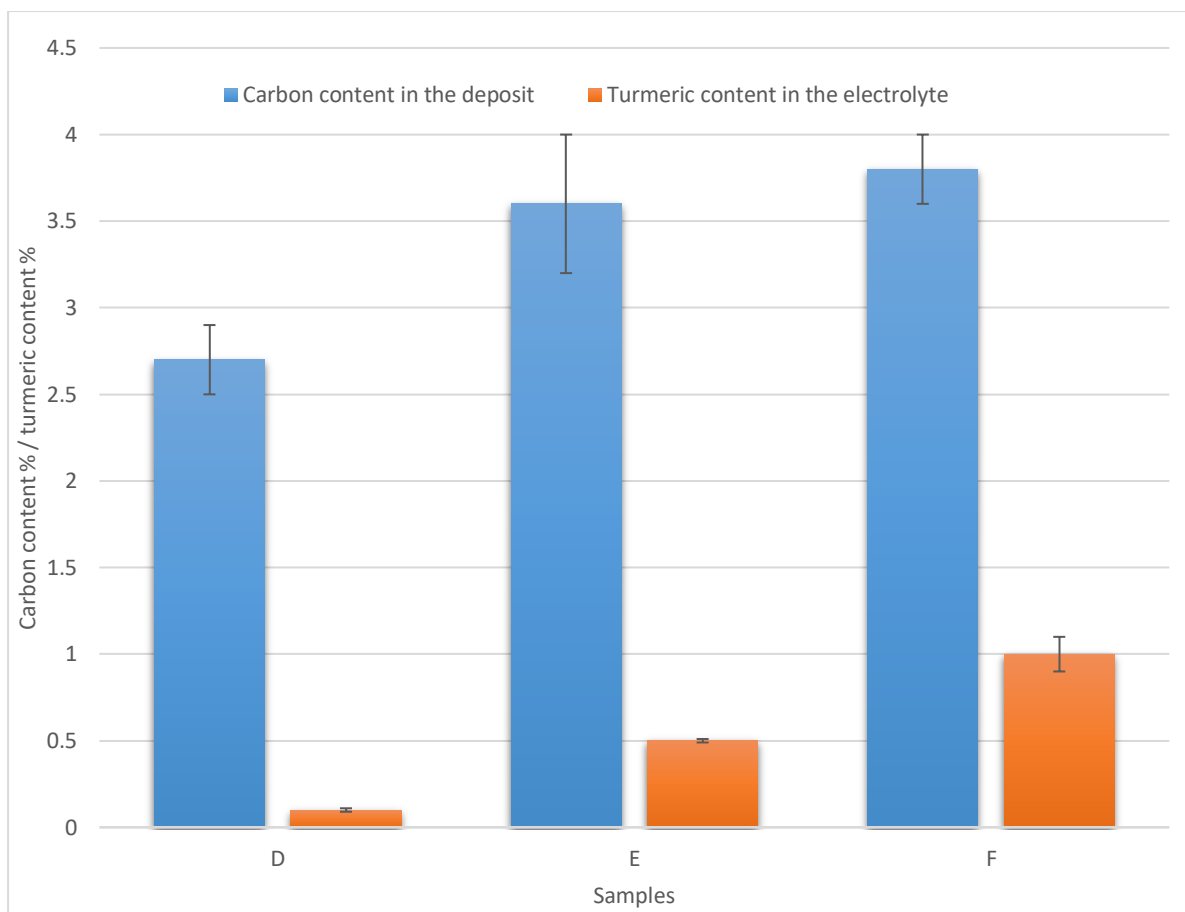


Figure 6.11. Comparison of carbon % in nickel deposits obtained by GDOES, against turmeric % in the electrolyte. (D) LICE nickel with 10.0 ml/l of Tween 20 and 1.0 g/l of turmeric. (E) LICE nickel with 10.0 ml/l of Tween 20 and 5.0 g/l of turmeric. (F) LICE nickel with 10.0 ml/l of Tween 20 and 10.0 g/l of turmeric.

There was also a strong correlation between turmeric concentration in the electrolyte and the carbon content in the nickel samples. Turmeric concentration in the electrolyte increased the carbon content in the coatings. When the concentration of turmeric is increased from 1.0 g/l to 10.0 g/l (0.1% and 1.0 % wt respectively) there is an increase in the carbon content of the coating. However, the increase in carbon content from 5.0 g/l to 10.0 g/l (0.5 % and 1.0 % wt), is small. The literature has shown that when producing an electrodeposited metallic coating, increasing the particle content in the electrolyte can increase the content of particles in the electrodeposited coating up until a saturation point is reached; if the concentration of particles in the electrolyte is increased after that, there is little increase in the particle content of the deposit or even a small decrease [22-24].

6.3.2. Surface morphology

SEM images of nickel coatings produced with varying concentrations of turmeric in the electrolyte are presented in Figure 6.12. to Figure 6.14.

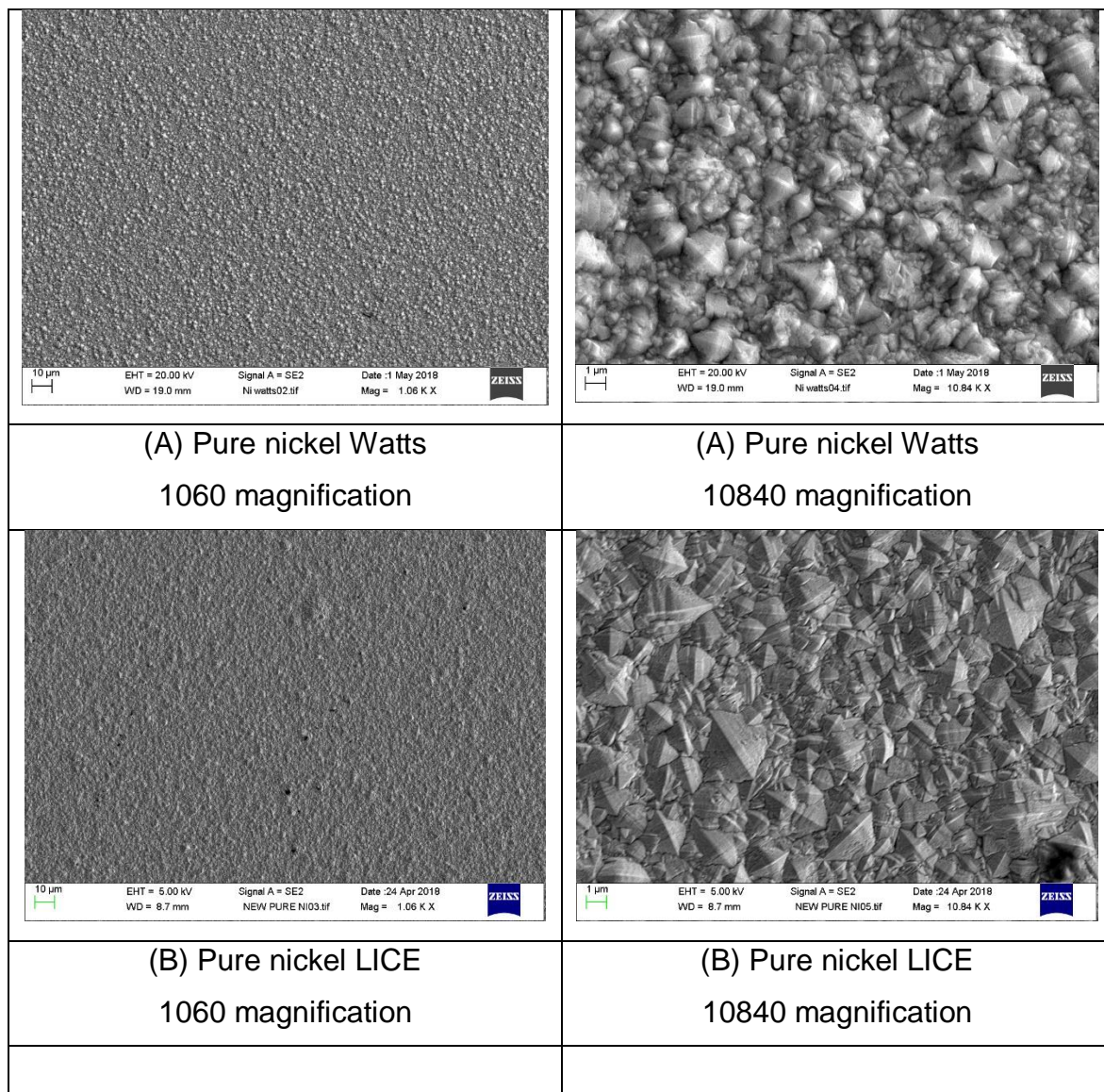


Figure 6.12. SEM Images of surface of nickel coating samples.

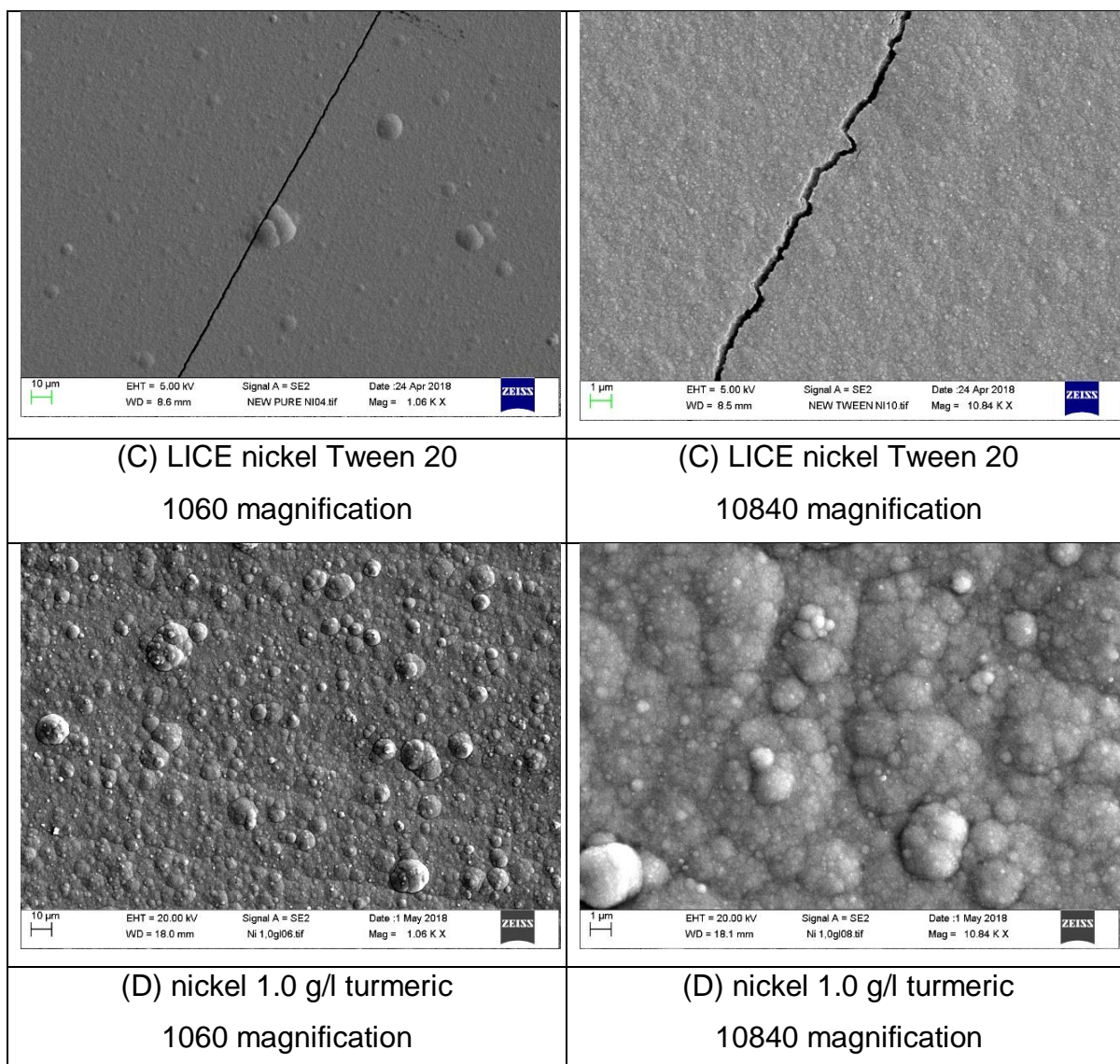


Figure 6.13. SEM Images of surface of nickel coating samples.

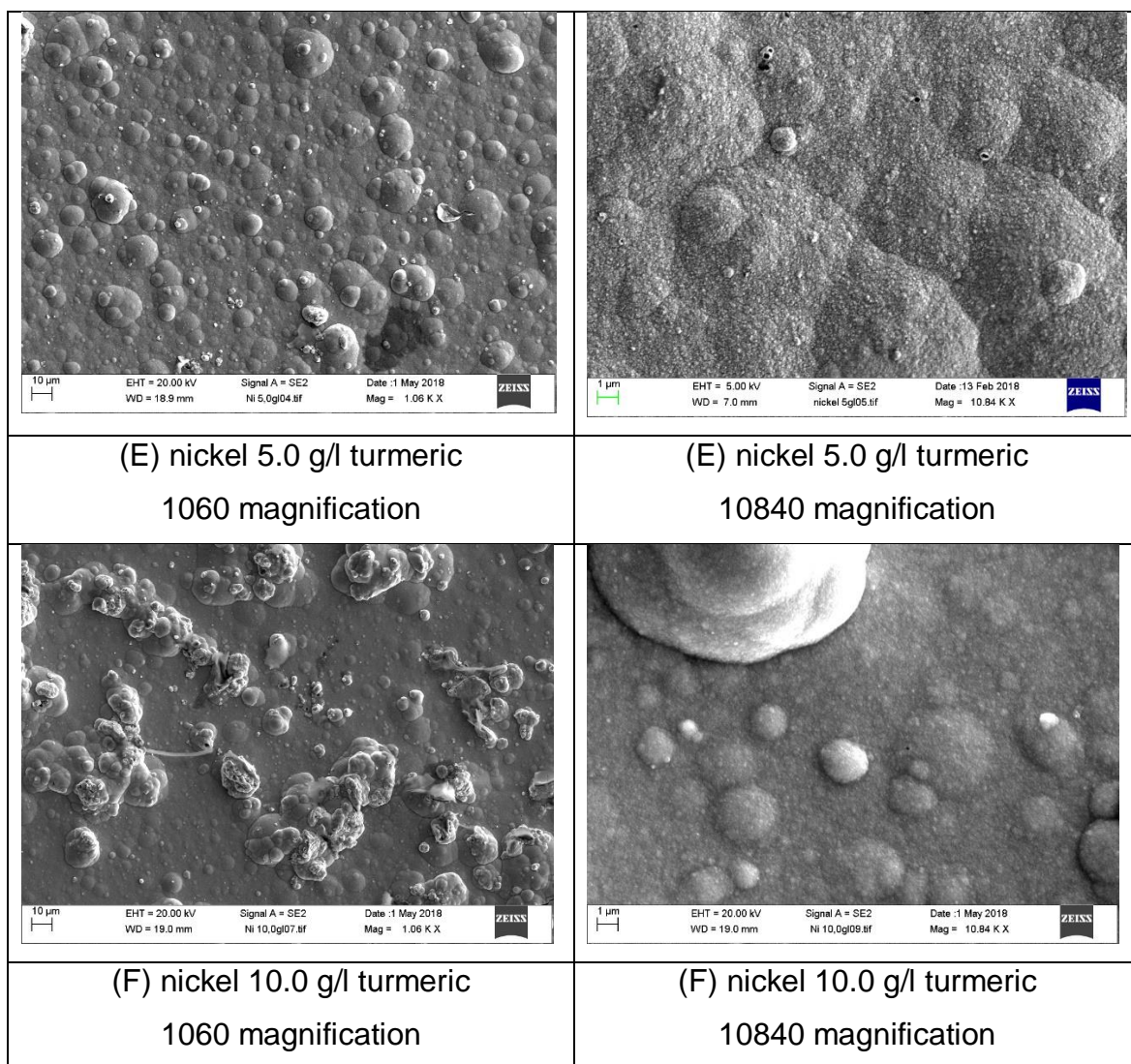


Figure 6.14. SEM Images of surface of nickel coating samples.

At lower magnifications samples (A) and (B) appeared very similar, however at higher magnifications, although both deposits displayed similar pyramidal type structure, clear differences could be seen. Sample (C) exhibited a significant refinement in grain structure, with the presence of microcracks observed. Nodules on the surface of the deposits was exhibited for samples (D) to (F), and at higher magnifications grooves were also observed. A progressive increase in nodulation and decrease in grooves was exhibited from samples (D) to (F), with the nodules becoming larger and more irregular in appearance.

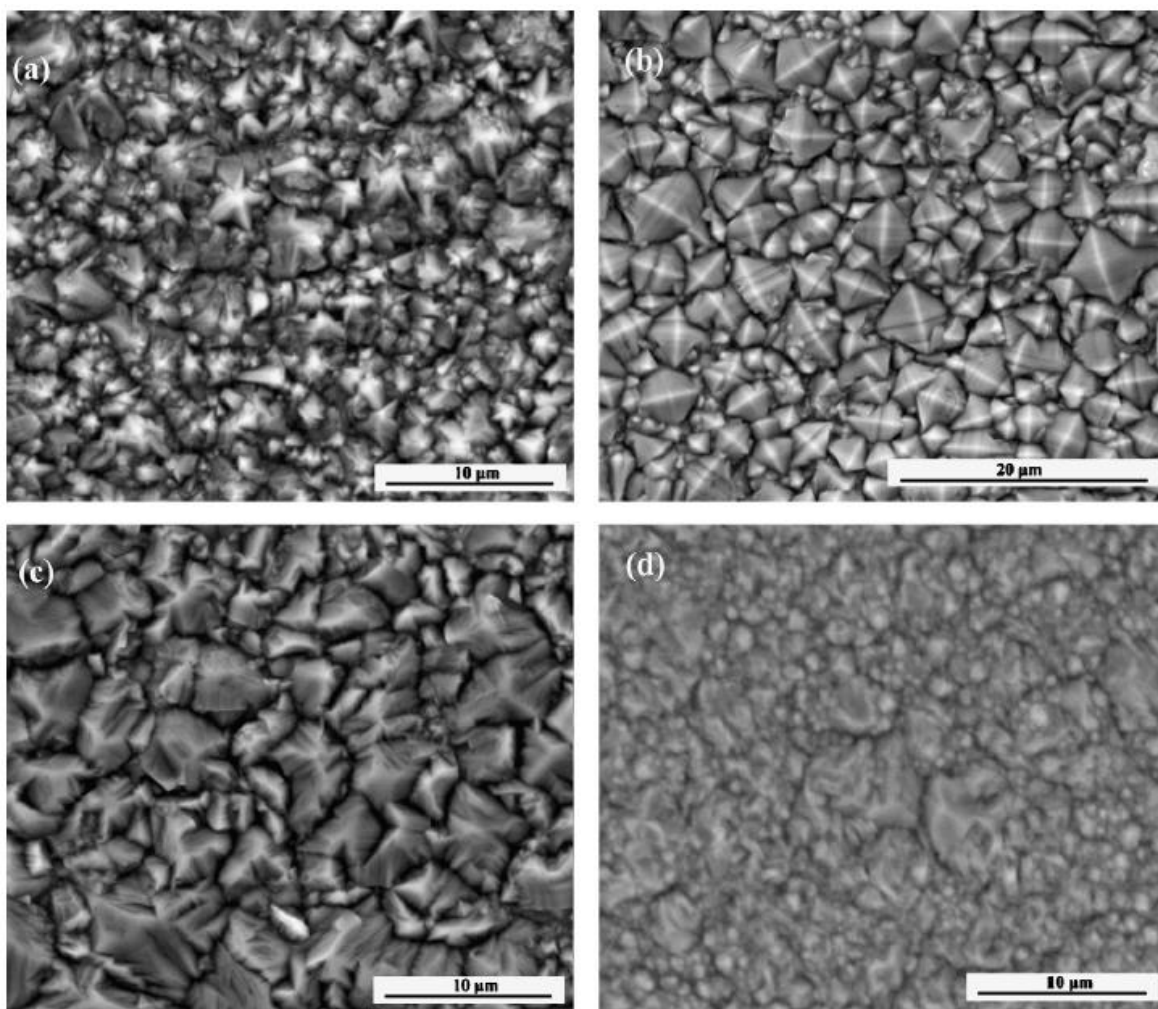


Figure 6.15. Show SEM images of the surface of pure nickel deposits (a) [110], (b) [211], (c) [100] and (d) [210] [25].

It has been shown in the literature that high magnification SEM images can be used to identify different crystal orientations by comparing their structure to surfaces with known crystal orientations [25]. Electrocrystallisation of nickel has been shown to be a highly inhibited process due to hydrogen codeposition (which is dependent on plating conditions such as current density and bath pH). The literature shows that nickel deposits produced from a Watts type electrolyte display 3 inhibited textures ([110], [210] and [211]) due to the presence of both atomic and molecular forms of absorbed and colloidal hydrogen in the cathodic interface [25-27]. SEM images of the surface of deposits produced from additive free Watts baths are presented in Figure 6.15. The surface structure of the pure nickel produced from the Watts electrolyte (A) in this research closely resembled that of Figure 6.15. (a) (the preferred [110] crystal orientation), and that of the pure nickel deposit produced from the LICE electrolyte (B)

closely resembled that of Figure 6.15. (b) (the preferred [211] crystal orientation). The literature has also shown that increasing the Cl^- ion concentration in a Watts type electrolyte changes the preferred crystal orientation from [110] to [211], and increasing the SO_4^{2-} ion concentration changes the preferred crystal orientation from [110] to [210], then back again to [110] with further increases [28]. This suggests that the pure nickel sample produced from the Watts electrolyte in this research (A) has a [110] preferred crystal orientation and the pure nickel sample produced from the LICE electrolyte (B) has a [211] preferred crystal orientation.

Additives such as surfactants can be incorporated into nickel deposits, often inducing excessive brittleness and stresses [14,29,30]. Intrinsic stress occurs at the triple junction of grain boundaries between crystallites. Tensile stress is caused by grains coalescing at the triple grain boundary, while compressive stress is caused by the insertion of atoms at the triple grain boundary mediated by the diffusion of atoms across the surface [31]. Stress can also be induced after deposition by thermal expansion, mismatch between substrate and coating or grain growth in coating if it possesses sufficient atomic mobility. Microcracks can occur as a result of the release of the built up intrinsic stress in the coating [30,31]. The microcracks present in sample (C) are likely due to the release of intrinsic stresses caused by the incorporation of Tween 20 into the coating.

Nodules are quite common in nickel deposits and are caused by uneven current distribution on the cathode, which can be caused by the incorporation of inert particles into the matrix (such as turmeric) [16-19]. The incorporation of inert particles into a nickel matrix can also refine the grain structure of the deposit with less intrinsic stress than surfactants alone.

6.3.3. Grain structure

EBSD maps (with associated colour key) generated from the cross section of the nickel deposits are presented in Figure 6.16. Ion beam images of the cross section of the deposits are presented in Figure 6.17.

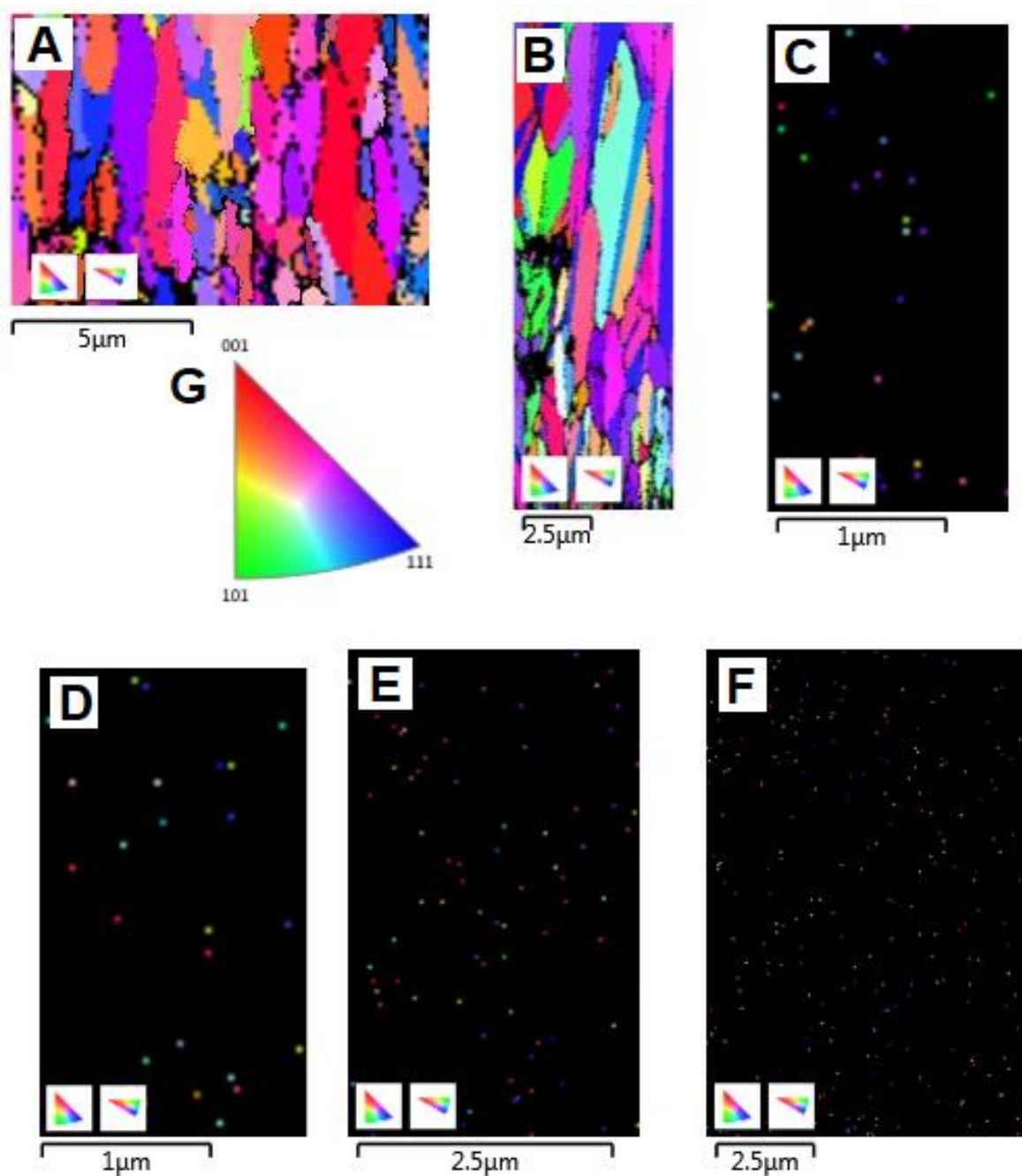


Figure 6.16. EBSD images of the grain structure of nickel deposits. (A) Pure nickel electrodeposited from a Watts bath. (B) Pure nickel electrodeposited from a LICE bath. (C) LICE nickel with 10.0 ml/l of Tween 20. (D) LICE nickel with 10.0 ml/l of Tween 20 and 1.0 g/l of turmeric. (E) LICE nickel with 10.0 ml/l of Tween 20 and 5.0 g/l of turmeric. (F) LICE nickel with 10.0 ml/l of Tween 20 and 10.0 g/l of turmeric. (G) crystal orientation colour key.

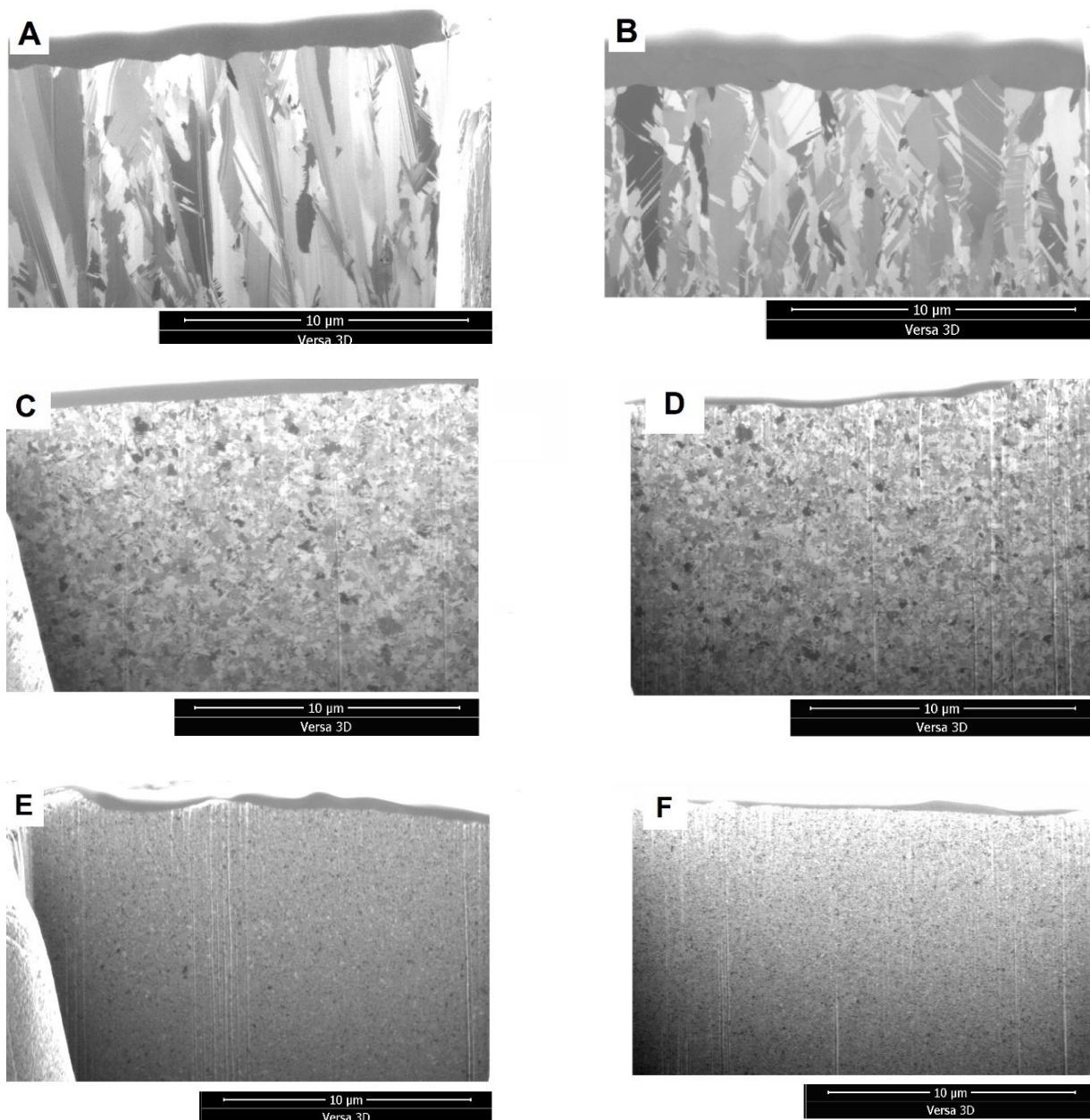


Figure 6.17. Ion beam images of cross-section of nickel turmeric coating samples. (A) Pure nickel electrodeposited from a Watts bath. (B) Pure nickel electrodeposited from a LICE bath. (C) LICE nickel with 10.0 ml/l of Tween 20. (D) LICE nickel with 10.0 ml/l of Tween 20 and 1.0 g/l of turmeric. (E) LICE nickel with 10.0 ml/l of Tween 20 and 5.0 g/l of turmeric. (F) LICE nickel with 10.0 ml/l of Tween 20 and 10.0 g/l of turmeric.

Both the EBSD maps and the ion beam images showed samples A and B had analogous grain structure, with both samples exhibiting similar size grains of mainly columnar crystals with high aspect ratios, however, smaller more irregular shaped crystals were also present. The crystal orientation colour key showed clear differences in the preferred crystal orientation between samples (A) and (B). No EBSD maps could

be generated for samples (C) to (F). Ion beam images for samples (C) and (D) show a significant refinement in the grain structure of the deposits, with both deposits exhibiting similar grains of low aspect ratio. Ion beam images of samples (E) and (F) showed that no clear grain structure was identifiable, with both deposits exhibiting an amorphous like appearance.

As stated in Chapter 5. The inability to generate EBSD data may be due to several factors:

- 1) A grain size smaller than the stepping size of the EBSD (33 nm).
- 2) EBSD is extremely sensitive to surface roughness.
- 3) Amorphous sample or localised amorphous areas.
- 4) The sample containing materials not detectable by EBSD.

The presence of such a small amount of turmeric is unlikely to result in such large zero solutions. Although, turmeric may make the polishing of the cross-section problematic, again it is unlikely to result in such large zero solutions. However, the absence of EBSD data for samples (E) and (F) is likely due to their amorphous like appearance.

6.3.4. Grain Size

A table of the mean grain size of nickel deposits calculated from the line intercept method and EBSD data are presented in Table 6.1.

Samples (A) and (B) exhibited similar grain size in both the y-axis and x-axis directions. A significant reduction in grain size was observed for samples (C) and (D), with both samples exhibiting similar grain size. Individual grains could not be identified in samples (E) and (F), therefore no grain size could be calculated.

The absence of EBSD data for samples (C) and (D) is likely due to the small grain size exhibited by the deposits. Both samples (C) and (D) exhibited a mean grain size within error of 33 nm. The minimum stepping size of the EBSD detector was 33 nm, and grains smaller than this were undetectable.

Table 6.1. Table of grain sizes of nickel and nickel turmeric samples (A) Pure nickel electrodeposited from a Watts bath. (B) Pure nickel electrodeposited from a LICE bath. (C) LICE nickel with 10.0 ml/l of Tween 20. (D) LICE nickel with 10.0 ml/l of Tween 20 and 1.0 g/l of turmeric. (E) LICE nickel with 10.0 ml/l of Tween 20 and 5.0 g/l of turmeric. (F) LICE nickel with 10.0 ml/l of Tween 20 and 10.0 g/l of turmeric.

Sample	EBSD data		Line intercept data	
	Grain size y-axis nm	Grain size x-axis nm	Grain size y-axis nm	Grain size x-axis nm
A	748 ± 56	473 ± 5	887 ± 47	456 ± 23
B	811 ± 6	305 ± 68	742 ± 47	378 ± 43
C	Not detected	Not detected	66 ± 50	92 ± 50
D	Not detected	Not detected	58 ± 50	72 ± 50
E	Not detected	Not detected	Not detected	Not detected
F	Not detected	Not detected	Not detected	Not detected

6.4. Nickel coating properties

6.4.1. Hardness

The variation in hardness of the nickel and nickel composite deposits electrodeposited from both a Watts and LICE electrolyte is shown in Figure 6.18.

Samples (A) and (B) exhibited significantly similar hardness of 277 ± 5.0 HV and 260 ± 10.0 HV respectively, this was within the range of values reported for Watts nickel in the literature [5,32-35]. A significant increase was observed for samples (C) and (D), with both samples exhibiting significantly similar hardness. A further significant increase in hardness was observed for samples (E) and (F), with again both samples again exhibiting significantly similar hardness.

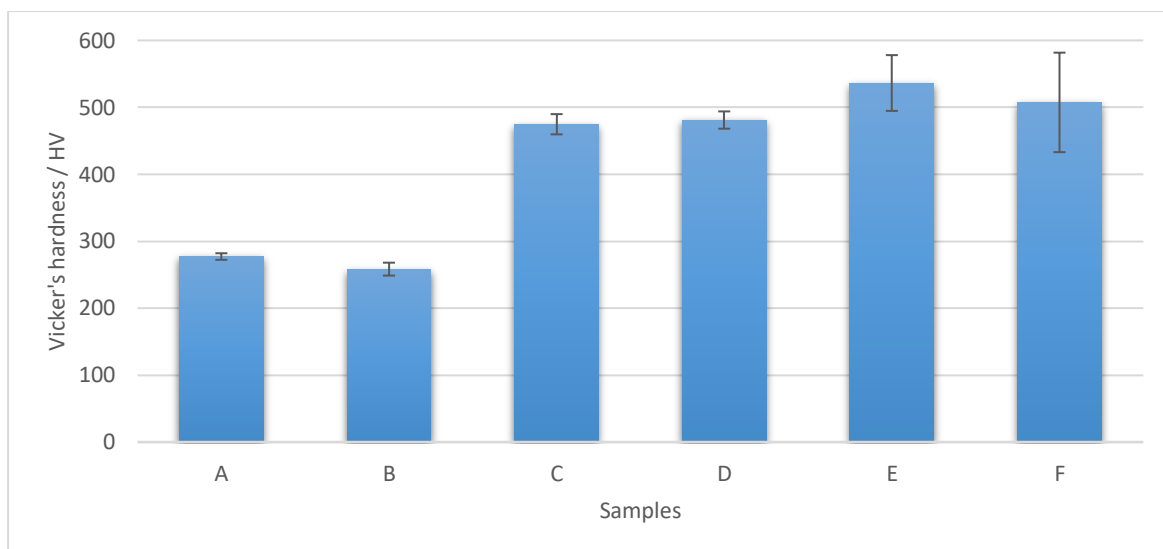


Figure 6.18. Hardness of nickel coating measured with a Vicker's indenter, with varying concentrations of turmeric in the electrolyte. (A) Pure nickel electrodeposited from a Watts bath. (B) Pure nickel electrodeposited from a LICE bath. (C) LICE nickel with 10.0 ml/l of Tween 20. (D) LICE nickel with 10.0 ml/l of Tween 20 and 1.0 g/l of turmeric. (E) LICE nickel with 10.0 ml/l of Tween 20 and 5.0 g/l of turmeric. (F) LICE nickel with 10.0 ml/l of Tween 20 and 10.0 g/l of turmeric.

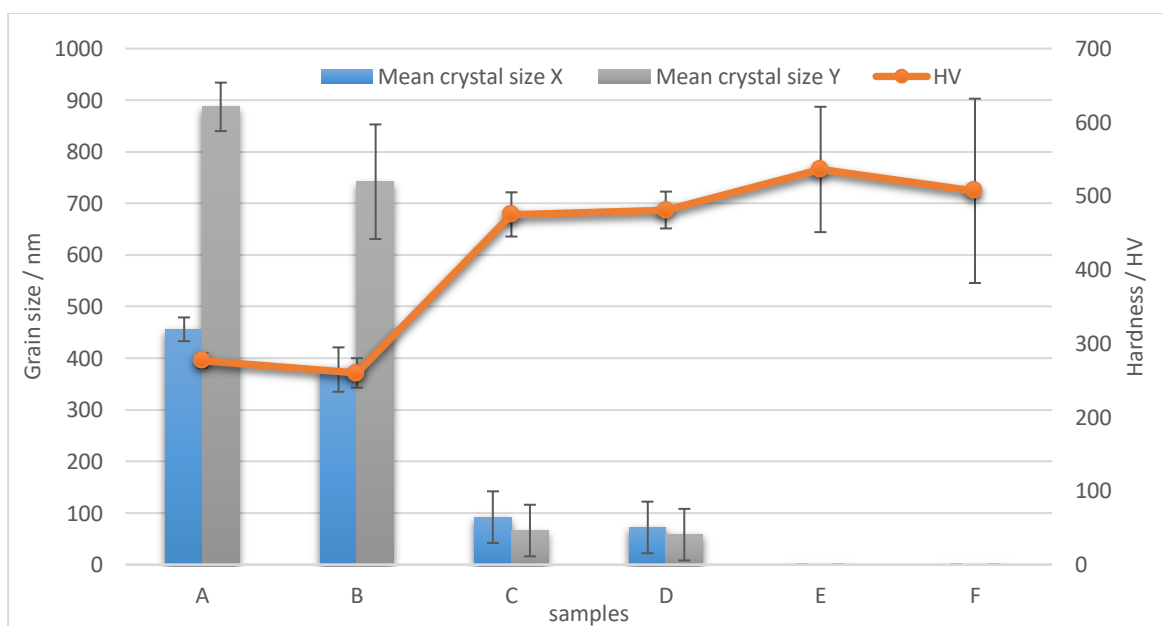


Figure 6.19. Comparison between the mean grain size in the X and Y axis against the microhardness of the deposit. (A) Pure nickel electrodeposited from a Watts bath. (B) Pure nickel electrodeposited from a LICE bath. (C) LICE nickel with 10.0 ml/l of Tween 20. (D) LICE nickel with 10.0 ml/l of Tween 20 and 1.0 g/l of turmeric. (E) LICE nickel with 10.0 ml/l of Tween 20 and 5.0 g/l of turmeric. (F) LICE nickel with 10.0 ml/l of Tween 20 and 10.0 g/l of turmeric.

The increase in hardness with the addition of both Tween 20 and turmeric to the electrolyte can be attributed to their effect on the grain structure of the deposits. Figure 6.19 shows a strong reverse correlation between the grain size and the hardness of the deposits. The literature shows that grain size is the primary factor affecting the hardness of an electrodeposit [9,36-46].

As the grain size in an electrodeposit is reduced the number of grain boundaries increase. When sufficient force is applied to the deposit, dislocations build-up at grain boundaries, either because a barrier to crossing over exists, or a source must be activated in the next grain boundary. A specific concentration for a given grain is required to initiate slip into the neighbouring grain boundary. This concentration is most likely achieved through a dislocation build-up. Stress is higher as the number of dislocations increases; the more substantial the grain size the quicker the stress is reached.

However, this is only true at low temperatures where creep due to plastic deformation is irrelevant [42,45,46].

6.4.2. Surface roughness

The average surface roughness (R_a) and total surface roughness (R_t) are shown in Figures 6.20. and 6.21. Respectively.

Both samples (A) and (B) exhibited similar R_a value. A small reduction in R_a was observed from sample (C), with a progressive increase observed thereafter from sample (D) to (F). Sample (A) exhibited the lowest R_t with a significant increase in R_t observed for sample (B). A reduction in R_t was observed from sample (B) to (C), with a progressive increase observed thereafter from sample (D) to (F).

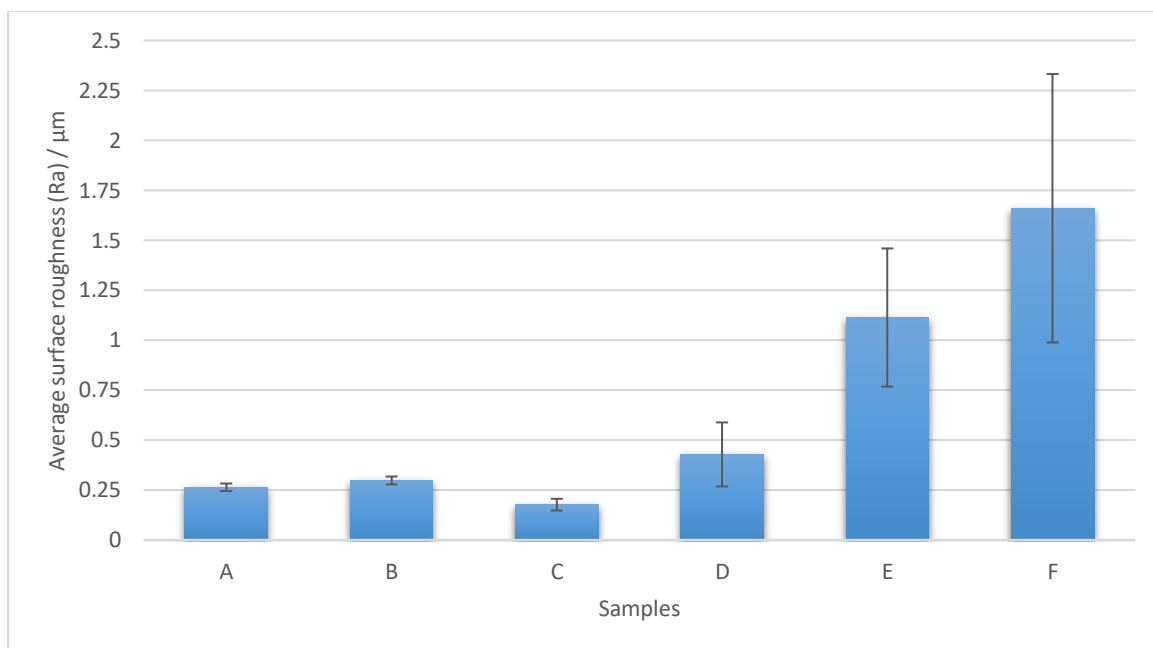


Figure 6.20. Average surface roughness (Ra) of nickel coatings measured with varying concentrations of turmeric in the electrolyte. (A) Pure nickel electrodeposited from a Watts bath. (B) Pure nickel electrodeposited from a LICE bath. (C) LICE nickel with 10.0 ml/l of Tween 20. (D) LICE nickel with 10.0 ml/l of Tween 20 and 1.0 g/l of turmeric. (E) LICE nickel with 10.0 ml/l of Tween 20 and 5.0 g/l of turmeric. (F) LICE nickel with 10.0 ml/l of Tween 20 and 10.0 g/l of turmeric.

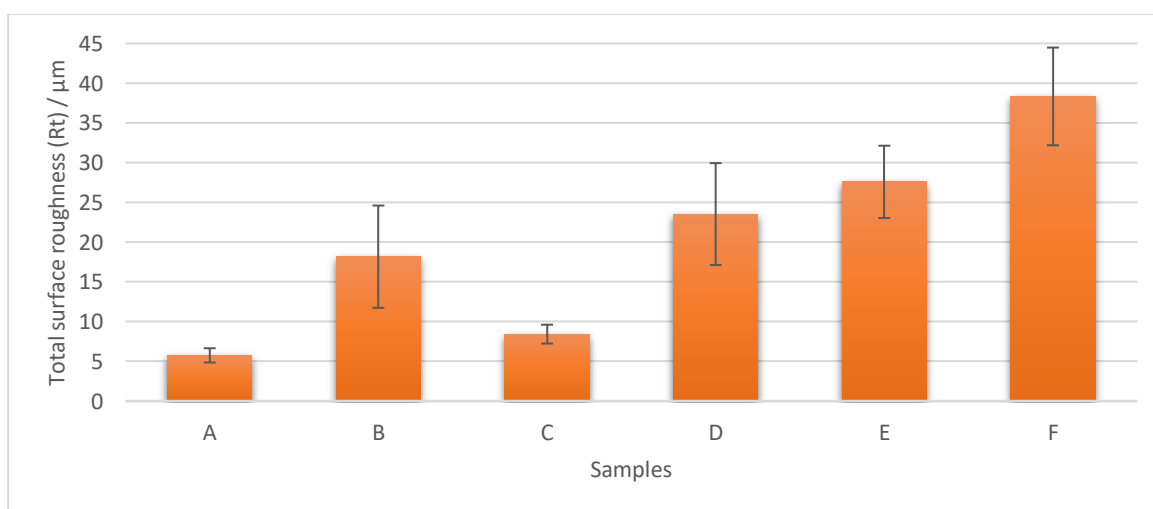


Figure 6.21. Total surface roughness (Rt) of nickel coatings measured with varying concentrations of turmeric in the electrolyte. (A) Pure nickel electrodeposited from a Watts bath. (B) Pure nickel electrodeposited from a LICE bath. (C) LICE nickel with 10.0 ml/l of Tween 20. (D) LICE nickel with 10.0 ml/l of Tween 20 and 1.0 g/l of turmeric. (E) LICE nickel with 10.0 ml/l of Tween 20 and 5.0 g/l of turmeric. (F) LICE nickel with 10.0 ml/l of Tween 20 and 10.0 g/l of turmeric.

The results obtained from the surface roughness analysis are consistent with observations made from both the deposits surface morphology and surface finish.

Sample (C) showed the lowest Ra value, yet sample (A) showed the lowest Rt value. As stated in Chapter 5. Ra is the average surface roughness across the whole sample area, whereas Rt is the change in height from lowest to highest point across the sample area. Therefore, the smaller grain size of sample (C) would be consistent with the smaller Ra value. However, the presence of microcracks and some nodules would be consistent with a higher Rt value. The progressive increase in both Ra and Rt values from samples (D) to (F) can be attributed to the increase in nodulation in the deposits. Although samples (A) and (B) had similar Ra values and grain structure, their Rt values were different, this is likely due to random variation in the height and/or depth across the surface of deposit (B).

Sample (C) displayed the brightest finish of all nickel deposits, the brightness of an electrodeposited coating can be attributed to an increase in the deposits surface smoothness [14,15]. A progressive reduction in the surface brightness was exhibited from deposit (D) to (F), this is consistent with the observed increase in Ra value. Both deposits (A) and (B) exhibited similar surface brightness and similar Ra.

6.4.3. Hydrophobic behaviour

The variation in WCA of the nickel and nickel composite coatings electrodeposited from Watts and LICE electrolytes is shown in Figure 6.22. Comparison of the WCA to deposit grain size is presented in Figure 6.23. With comparison between WCA and Ra and Rt presented in Figure 6.24. and Figure 6.25. respectively.

A reduction in WCA was observed from sample (A) to (B). A progressive increase in WCA was observed from sample (B) to (D), thereafter a reduction was observed with samples (E) and (F) which had similar WCA.

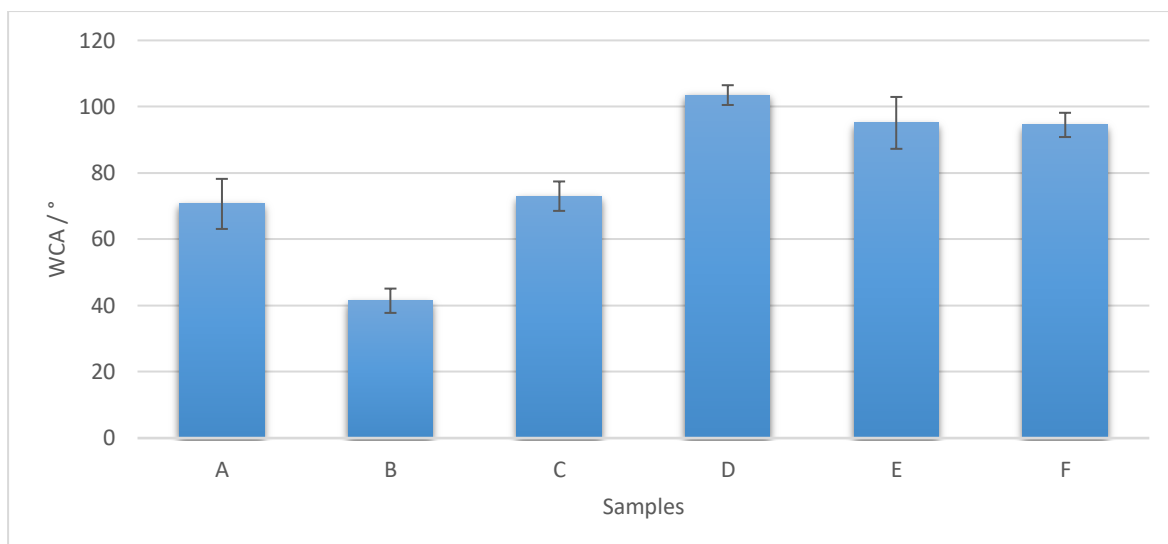


Figure 6.22. WCA of nickel coatings measured with varying concentrations of turmeric in the electrolyte. (A) Pure nickel electrodeposited from a Watts bath. (B) Pure nickel electrodeposited from a LICE bath. (C) LICE nickel with 10.0 ml/l of Tween 20. (D) LICE nickel with 10.0 ml/l of Tween 20 and 1.0 g/l of turmeric. (E) LICE nickel with 10.0 ml/l of Tween 20 and 5.0 g/l of turmeric. (F) LICE nickel with 10.0 ml/l of Tween 20 and 10.0 g/l of turmeric.

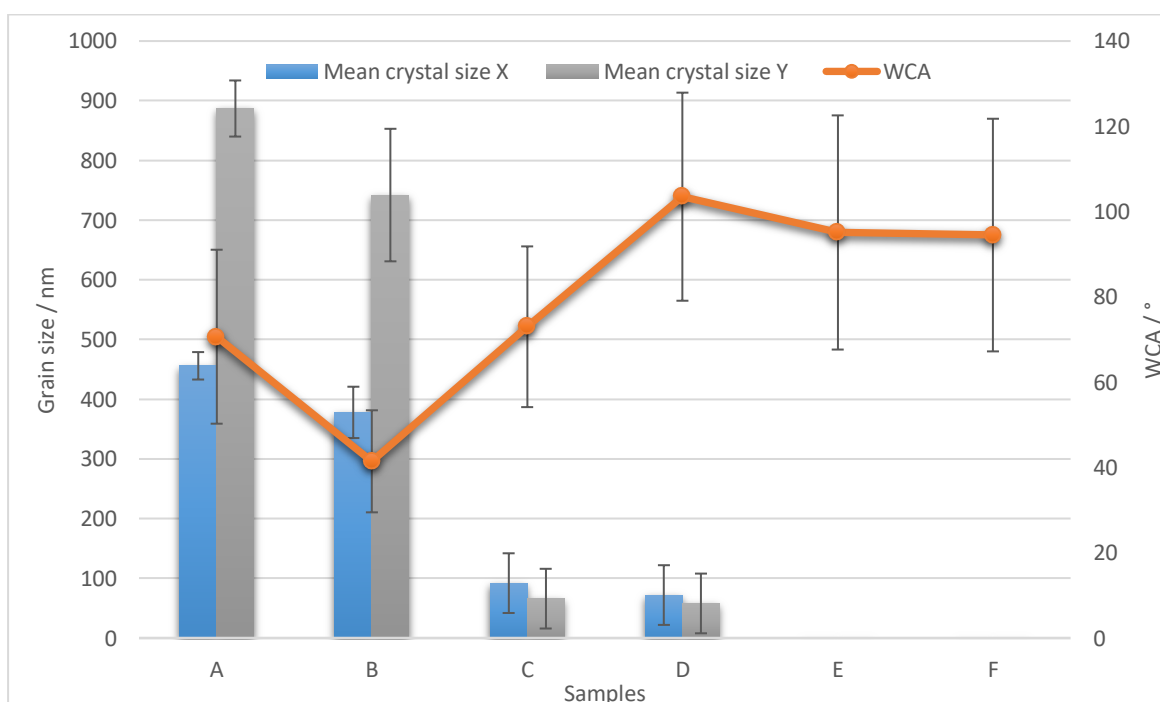


Figure 6.23. Comparison between the mean grain size of the nickel deposits and their WCA. (A) Pure nickel electrodeposited from a Watts bath. (B) Pure nickel electrodeposited from a LICE bath. (C) LICE nickel with 10.0 ml/l of Tween 20. (D) LICE nickel with 10.0 ml/l of Tween 20 and 1.0 g/l of turmeric. (E) LICE nickel with 10.0 ml/l of Tween 20 and 5.0 g/l of turmeric. (F) LICE nickel with 10.0 ml/l of Tween 20 and 10.0 g/l of turmeric.

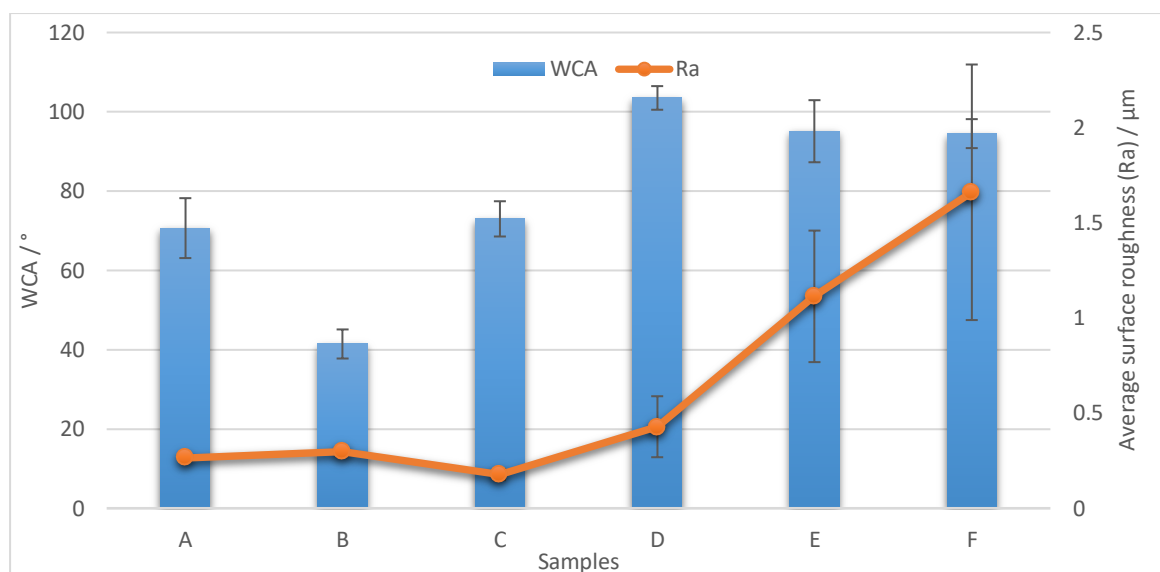


Figure 6.24. Average surface roughness (Ra) of nickel coating compared to their WCA. (A) Pure nickel electrodeposited from a Watts bath. (B) Pure nickel electrodeposited from a LICE bath. (C) LICE nickel with 10.0 ml/l of Tween 20. (D) LICE nickel with 10.0 ml/l of Tween 20 and 1.0 g/l of turmeric. (E) LICE nickel with 10.0 ml/l of Tween 20 and 5.0 g/l of turmeric. (F) LICE nickel with 10.0 ml/l of Tween 20 and 10.0 g/l of turmeric.

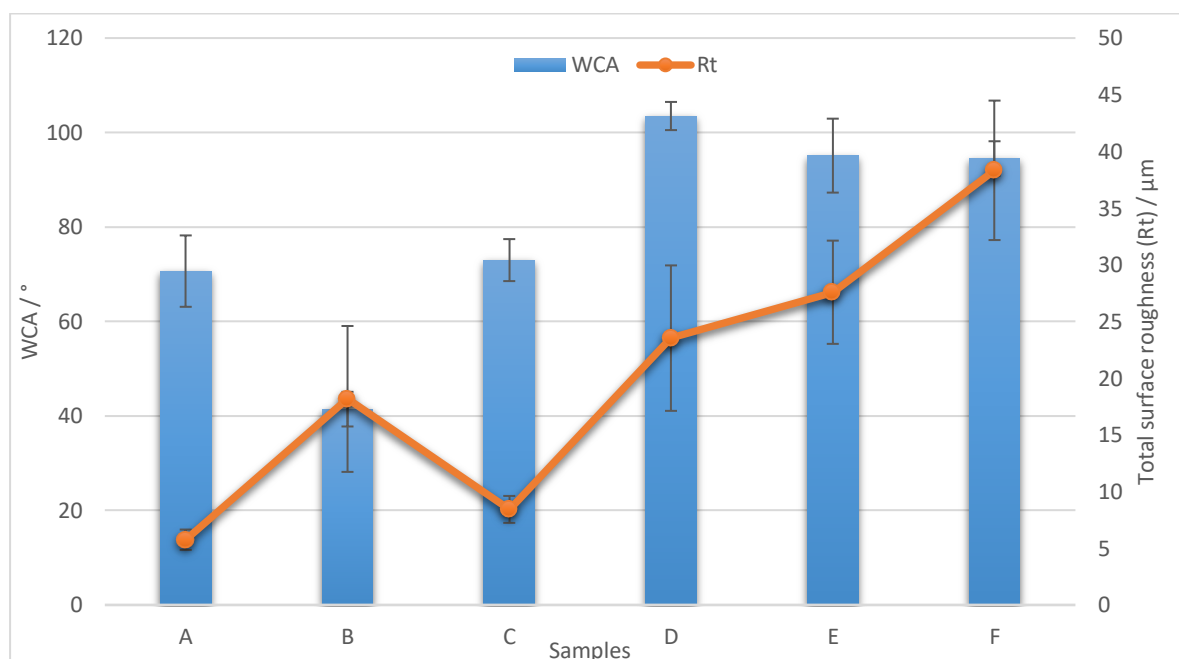


Figure 6.25. Total surface roughness (Rt) of nickel coatings compared to their WCA. (A) Pure nickel electrodeposited from a Watts bath. (B) Pure nickel electrodeposited from a LICE bath. (C) LICE nickel with 10.0 ml/l of Tween 20. (D) LICE nickel with 10.0 ml/l of Tween 20 and 1.0 g/l of turmeric. (E) LICE nickel with 10.0 ml/l of Tween 20 and 5.0 g/l of turmeric. (F) LICE nickel with 10.0 ml/l of Tween 20 and 10.0 g/l of turmeric.

Surface free energy has a major influence on the WCA of a deposit [47-49]. Many factors can influence the surface free energy of a deposit such as, grain structure, surface roughness and surface composition [50-54].

Observations of change in the deposits WCA did not show a strong correlation to any one single factor, instead exhibiting complexed mixed behaviour where a combination of changes to the grain structure, surface roughness and surface composition all impacted the overall WCA. Samples (A) and (B) exhibited similar grain size and Ra values yet showed very different preferred crystal orientation and Rt. Both the change in preferred crystal orientation and Rt could be responsible for the change in WCA observed. A change in preferred crystal orientation would lead to a change in the surface free energy, which could change the WCA [50,51]. An increase in the surface roughness of the hydrophilic surface would also be consistent with a decrease in the WCA of the deposit [52-54]. An increase in WCA and Rt was observed from samples (B) to (C), yet a reduction in grain size and Ra was also observed. A reduction in both grain size and Ra is consistent with an increase in WCA. As reducing Ra would increase WCA and a reduction in grain size would lead to a reduction in surface free energy and increase WCA [52-55]. The incorporation of carbon from Tween 20 into the deposit would have also changed the surface composition, this is likely to have changed the surface free energy and impacted the WCA. An increase in WCA, Ra and Rt was observed from samples (C) to (D), yet the deposits exhibited a similar grain size. A reduction in surface roughness is consistent with an increase in WCA [52-54]. However, the incorporation of turmeric into the deposit is likely to have also changed the surface free energy impacting the WCA.

The WCA of the samples (D) to (F) was very similar, however a progressive increase in surface roughness was observed from samples (D) to (F), the grain structure of sample (D) was also different to that of samples (E) and (F). The increase in surface roughness would normally be consistent with an increase in WCA, however, the incorporation of turmeric into the deposit is likely to have impacted the surface free energy of the samples. The change in surface free energy from the incorporation of turmeric, may have had a greater influence on the WCA than the increase in surface roughness. The change in hydrophobic behaviour of the nickel deposits was due to a combination of surface roughness, grain structure and surface composition.

6.4.4. Corrosion rate

6.4.4.1. Electrochemical corrosion tests

The approximated corrosion rate calculated by the Tafel plots is shown in Figure 6.26.

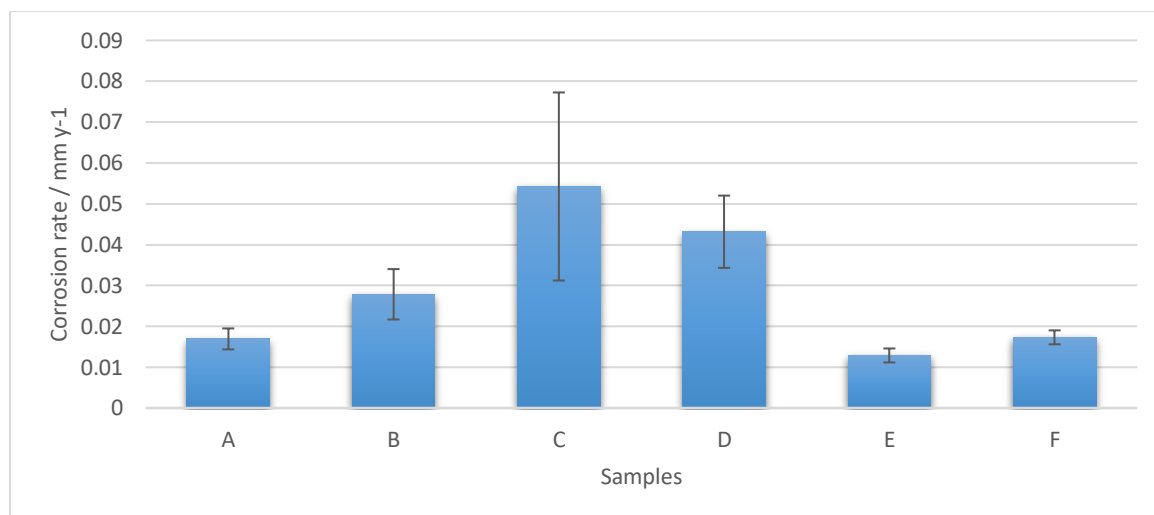


Figure 6.26. Bar chart of corrosion rate estimated by the Tafel plot method. (A) Pure nickel electrodeposited from a Watts bath. (B) Pure nickel electrodeposited from a LICE bath. (C) LICE nickel with 10.0 ml/l of Tween 20. (D) LICE nickel with 10.0 ml/l of Tween 20 and 1.0 g/l of turmeric. (E) LICE nickel with 10.0 ml/l of Tween 20 and 5.0 g/l of turmeric. (F) LICE nickel with 10.0 ml/l of Tween 20 and 10.0 g/l of turmeric.

A progressive increase in corrosion rate was observed from sample (A) to (C), with sample (C) exhibiting the highest corrosion rate of all the deposits. A progressive decrease in corrosion rate was observed thereafter from samples (C) to (E), before a small increase again from sample (E) to (F). Sample (E) exhibited the lowest corrosion rate of all the nickel deposits.

A large variation in the corrosion rate with overlaying error was observed in samples (B) to (D), indicating a large degree of variation in the corrosion properties between individual deposits within the same set of samples. The electrolyte is the primary factor influencing the corrosion rate of a material. However, other factors such as surface morphology, grain size and porosity can also influence the corrosion rate [12,58-61]. The increase in corrosion rate from sample (A) to (B) may be due to the change in surface morphology, with the increase in corrosion rate from sample (B) to (C) likely due to the presence of microcracks in the surface of the deposit. The reduction in corrosion rate from sample (C) to (D) may be due to the absence of those microcracks

in the deposit. The further reduction in corrosion rate from samples (D) to (E) was likely due to the reduction in grain size.

6.4.4.2. Salt spray

Photographic images of the nickel deposits before and after salt spray analysis are presented in Figure 6.27. With the corrosion rate calculated by weight loss after salt spray analysis presented in Figure 6.28.








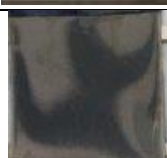










Samples	0 hours	24 hours	240 hours
A			
B			
C			
D			
E			
F			

Figure 6.27. Images of nickel coatings before and after salt spray analysis. (A) Pure nickel electrodeposited from a Watts bath. (B) Pure nickel electrodeposited from a LICE bath. (C) LICE nickel with 10.0 ml/l of Tween 20. (D) LICE nickel with 10.0 ml/l of Tween 20 and 1.0 g/l of turmeric. (E) LICE nickel with 10.0 ml/l of Tween 20 and 5.0 g/l of turmeric. (F) LICE nickel with 10.0 ml/l of Tween 20 and 10.0 g/l of turmeric.

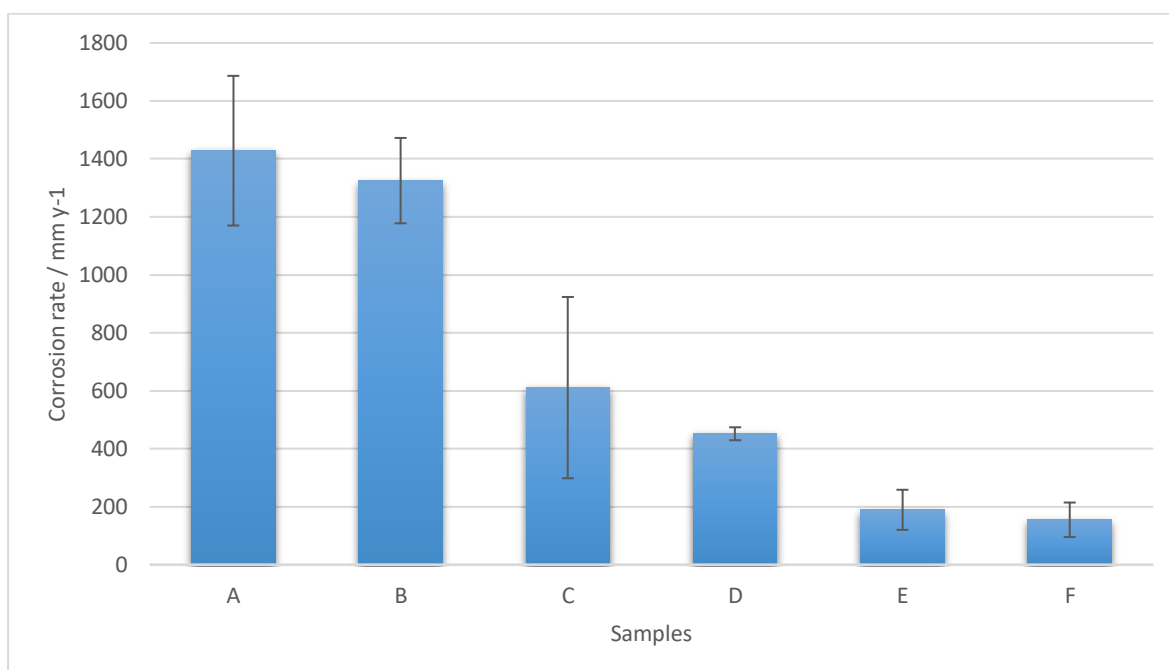


Figure 6.28. Bar chart of corrosion rate calculated by weight loss after salt spray analysis. (A) Pure nickel electrodeposited from a Watts bath. (B) Pure nickel electrodeposited from a LICE bath. (C) LICE nickel with 10.0 ml/l of Tween 20. (D) LICE nickel with 10.0 ml/l of Tween 20 and 1.0 g/l of turmeric. (E) LICE nickel with 10.0 ml/l of Tween 20 and 5.0 g/l of turmeric. (F) LICE nickel with 10.0 ml/l of Tween 20 and 10.0 g/l of turmeric.

Visual inspection of the nickel deposits after salt spray analysis appeared to show only low levels of corrosion. Samples (A) and (B) exhibited the most corrosion after 240 hours, with calculations of their mass loss showing both samples exhibited significantly similar corrosion rates. Sample (C) dulled in appearance after 24 hours with a pattern appearing on the surface of the deposit. Although deposits (D), (E) and (F) exhibited less visible signs of corrosion after 240 hours (compared to sample (A) and (B)), sample (E) appeared to have a brighter surface finish after 240 hours than after 24 hours. Mass loss calculations showed that samples (C) and (D) exhibited significantly similar corrosion rates, as did samples (E) and (F).

All nickel samples showed a significantly higher corrosion rate in the salt spray test compared to the electrochemical corrosion test. The addition of NaCl to an aqueous solution can increase the conductivity of the solution increasing the corrosion rate. The presence of Na⁺ ions also acts as a catalyst increasing the rate of electron transfer from the metal increasing the rate of corrosion [56].

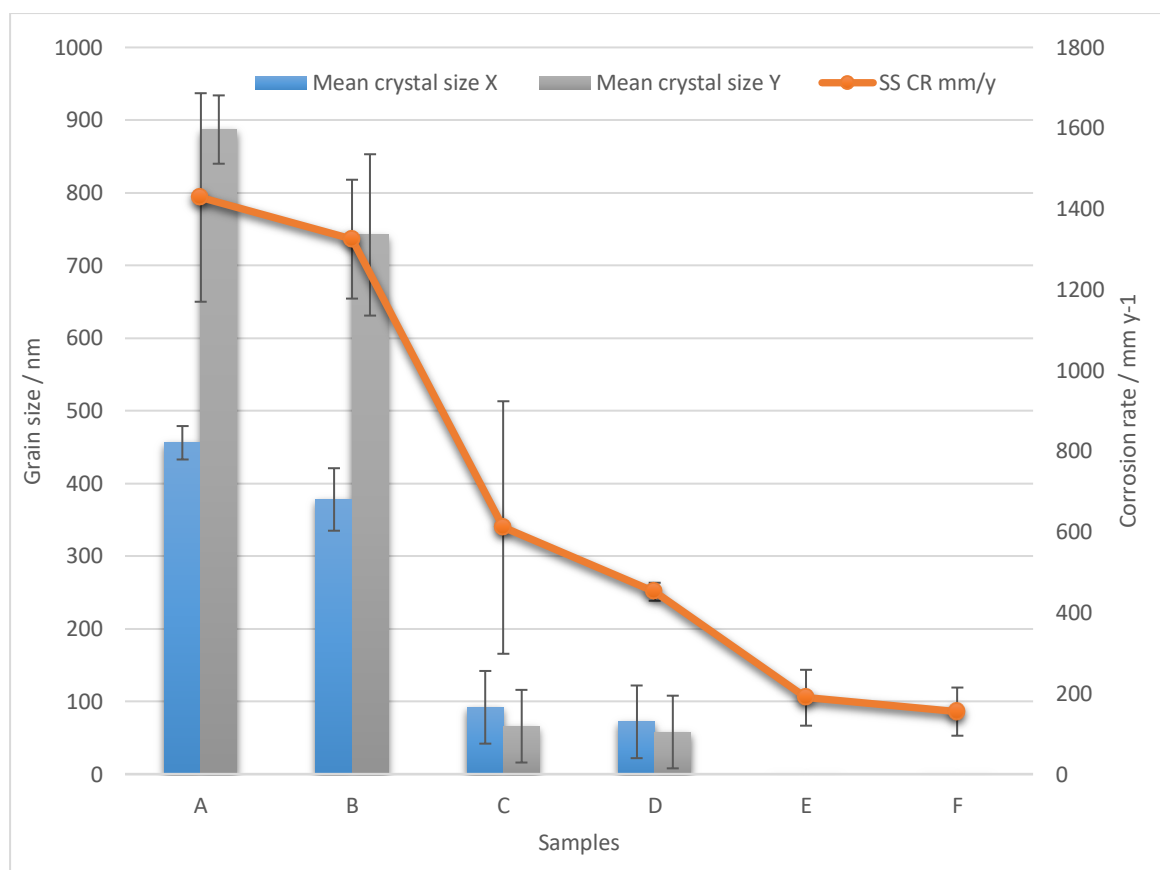


Figure 6.29. Comparison between the mean grain size and the corrosion rate of the deposit measured by salt spray analysis (SS CR mm y⁻¹). (A) Pure nickel electrodeposited from a Watts bath. (B) Pure nickel electrodeposited from a LICE bath. (C) LICE nickel with 10.0 ml/l of Tween 20. (D) LICE nickel with 10.0 ml/l of Tween 20 and 1.0 g/l of turmeric. (E) LICE nickel with 10.0 ml/l of Tween 20 and 5.0 g/l of turmeric. (F) LICE nickel with 10.0 ml/l of Tween 20 and 10.0 g/l of turmeric

The reduction in grain size exhibited by the deposits is responsible for their increased resistance to salt spray corrosion. A comparison of corrosion rate to grain size is presented in Figure 6.29. A strong reverse correlation between grain size and salt spray corrosion rate can be seen. As stated in Chapter 5, the electrolyte is the primary factor influencing corrosion. The surface of a metal is covered by an oxide film when exposed to air. However, the bare metal surface may be exposed by the oxide film starting to dissolve when the metal is submerged in an aqueous solution, which is known as an active state. At grain boundaries and incursions (such as turmeric particles) oxide films tend to be thinner, and thus initially the underlying metal will be exposed there first. The corrosion rate is increased by a reduction in grain size and an increase in incursions in active systems. However, in near neutral solutions the oxide

film is less soluble, and if inhibiting ions are present the solubility may be suppressed, stabilising the oxide film to form a passive layer. Oxide films form more rapidly on surfaces with smaller grain size, yet oxide films are more stable on surfaces with larger grain size. Therefore, in a passive environment, a reduction in grain size decreases the corrosion rate of the metal and in an active environment increases it [57].

The pattern seen on the surface of sample (C) in the salt spray corrosion test, was likely due to the position of the sample in the salt spray chamber causing the solution to run off the surface at the corner of the sample.

The increase in brightness of deposit (E) after 240 hours in the salt spray chamber, may have been due to the preferential corrosion of protrusions on the surface of the sample increasing the smoothness and brightness of the deposit.

6.5. Nickel results discussion

The results from the electrodeposited nickel turmeric composite coating analysis show not only is turmeric a viable sustainable alternative to some of the more commonly used filler particles, but the extent of the increase in hardness and corrosion resistance at such a low particle cost may make it superior to many.

Although, the ionic strength of the Watts electrolyte resulted in the presence of large aggregates in the solution, which produced very poor-quality nickel turmeric deposits. The lower ionic strength of the LICE nickel electrolyte resulted in a uniform dispersion of turmeric in the solution, and the production of higher quality nickel turmeric deposits.

The results obtained from the microstructural analysis of the LICE nickel deposits showed that both Tween 20 and turmeric had a significant influence on the grain structure of the deposits. These results were consistent with the literature. Studies have shown that the incorporation of surfactants and inert particles into an electrodeposited coating can change the grain structure of an electrodeposit [10,62-66]. Both pure nickel samples produced from Watts and LICE electrolyte had similar grain structure and size. The addition of 10.0 ml/l of Tween 20 to the LICE electrolyte (C), saw the incorporation of carbon into the deposit, which resulted in a substantial reduction in grain size. However, this also led to microcracks in the surface of the

deposit caused by the build-up of intrinsic stresses [66,67]. The further addition of 1.0 g/l of turmeric to the electrolyte (D) led to an increase in the carbon content but did not significantly change the grain structure of the deposit. The lack of observed change in grain structure can be attributed to the significant effect of Tween 20. The grain structure of the deposit was so significantly changed by the addition of Tween 20, that a small amount of turmeric was unable to change it any further. Increasing the turmeric concentration in the electrolyte to 5.0 g/l (E) increased the carbon content of the deposit and changed the grain structure further giving the deposit an amorphous like appearance. further increasing the turmeric electrolyte concentration thereafter to 10.0 g/l (F), resulted in a small increase in the carbon content of the coating, but no change in grain structure. This was because at a carbon content of 3.6%, the peak grain structure modification had been achieved, and increasing the carbon content of the deposits thereafter could not change the grain structure any further. The particle size dependency seen in the copper samples (Chapter 5.) was not observed in the nickel deposits, with the deposit's particle content having a greater influence on the grain structure of the coating than the turmeric particle size.

The reduction in grain size caused by the incorporation of turmeric into the deposit had a significant effect on the hardness of the nickel deposits. The hardness was also increased when compared to other more commonly used filler particles. It can be seen from Figure 6.30. that the percentage increase in the deposit hardness with the incorporation of the optimal turmeric particle content is greater than that seen for WC, SiC, MWCNT, graphene and alumina. However, it should be noted this is not a direct comparison as the electrodeposition conditions (such as current density, pH, particle content and electrolyte composition) can all influence the hardness of the deposit. However, the result of the Vicker's hardness tests obtained in this research indicates that turmeric may not only be a suitable sustainable alternative to some of the commonly used filler particles but may be superior to many for enhancing the hardness of a copper deposit.

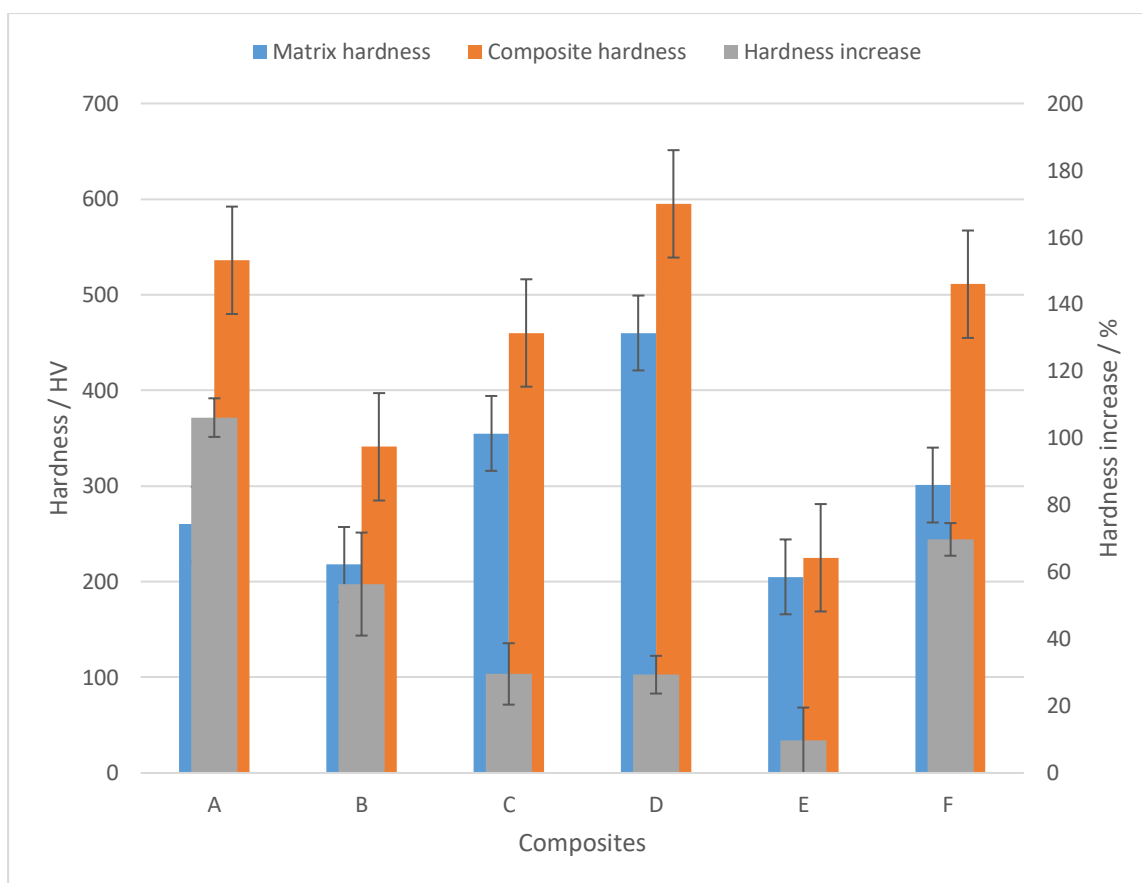


Figure 6.30. The effects on hardness of the incorporation of various particle into electrodeposited nickel composites. (A) turmeric. (B). WC [66,68]. (C) SiC [23,69]. (D) MWCNT [70]. (E) Graphene [65]. (F) Alumina [71,72].

The incorporation of turmeric into the deposit also resulted in a significant increase in the WCA of the deposits, changing the behaviour of the coating from hydrophilic to hydrophobic. Hydrophobic surfaces have many potential industrial applications including water repellent coatings, self-cleaning surfaces, sensor applications and in microfluidics. A further increase in WCA of the deposits may be observed by further increasing the surface roughness of the coating [53,54].

The corrosion resistance of the deposits in both the electrolytes tested was also significantly improved by the incorporation of turmeric into the deposits. Although only a small reduction in corrosion rate was seen for the Na_2SO_4 electrolyte, the deposits resistance to salt spray corrosion was substantial, with approximately a 700 % reduction in mass loss due to corrosion at optimal turmeric content.

The electrolyte is the primary factor influencing the corrosion rate of a metal, in active environments the corrosion rate is increased by a reduction in grain size and in a

passive environment a reduction in grain size decreases the corrosion rate of the metal [57]. However, the method used to calculate the corrosion rate can also influence the results obtained. In the Tafel plot method, the corrosion rate is an approximation calculated from the corrosion current of the metal. Most corrosion takes place electrochemically at the interface between two dissimilar metals or a metal and an electrolyte. Corrosion occurs at a rate determined by the equilibrium between the oxidation and reduction reactions, However, at the equilibrium, there is no net current flow, so the corrosion current cannot be measured directly. Therefore, the equilibrium must be approximated from the potential of the metal. Thus, the electrochemical corrosion rate in this research was approximated from the potential of the metal [73]. Whereas, the corrosion rate calculated from the salt spray analysis was a measurement of actual corrosion, determined from the weight loss.

The significant enhancement of the nickel deposits resistance to salt spray corrosion gives the coating many potential corrosion protective applications, particularly in salt water environment such as desalination plants and marine and petrochemical industries [74,75].

6.6. Conclusions

- The incorporation of Tween 20 and turmeric particles into the LICE nickel matrix reduced the grain size of the deposit, enhancing physical properties such as microhardness, WCA and resistance to salt spray corrosion.
- When 5.0 g/l and 10.0 g/l of turmeric was added to the LICE electrolyte the deposits produced appeared to be either amorphous or had a grain size smaller than the stepping size of the EBSD (33 nm), and too small to be seen in the FIB-SEM images.
- The turmeric particle content in the deposit is correlated to the concentration of turmeric in the electrolyte.
- The increase in microhardness seen with the incorporation of turmeric was greater than that reported for MWCNT, WC, SiC, graphene, and alumina particles. making turmeric a potential sustainable alternative to these filler particles for increasing hardness.

- The addition of turmeric to the electrolyte increased the WCA of the deposit and changed the coating from hydrophilic to hydrophobic.
- Hydrophobic coatings have many potential industrial applications including water repellent coatings, self-cleaning surfaces, sensor applications and in microfluidics.
- The high salt spray corrosion resistance of the nickel turmeric deposits may make them suitable for applications in salt water environments.

6.7. Reference list

[1] M.A. Euterpio, C. Cavaliere, A.L. Capriotti, C. Crescenzi, Extending the applicability of pressurized hot water extraction to compounds exhibiting limited water solubility by pH control: curcumin from the turmeric rhizome, *Analytical and bioanalytical chemistry*. 401 (2011) 2977.

[2] R. Zangi, B. Berne, Aggregation and dispersion of small hydrophobic particles in aqueous electrolyte solutions, *The Journal of Physical Chemistry B*. 110 (2006) 22736-22741.

[3] R.A. French, A.R. Jacobson, B. Kim, S.L. Isley, R.L. Penn, P.C. Baveye, Influence of ionic strength, pH, and cation valence on aggregation kinetics of titanium dioxide nanoparticles, *Environmental Science & Technology*. 43 (2009) 1354-1359.

[4] D.J. McClements, S.R. Dungan, Factors that affect the rate of oil exchange between oil-in-water emulsion droplets stabilized by a nonionic surfactant: droplet size, surfactant concentration, and ionic strength, *The Journal of Physical Chemistry*. 97 (1993) 7304-7308.

[5] I. Tudela, Y. Zhang, M. Pal, I. Kerr, T.J. Mason, A.J. Cobley, Ultrasound-assisted electrodeposition of nickel: Effect of ultrasonic power on the characteristics of thin coatings, *Surface and Coatings Technology*. 264 (2015) 49-59.

[6] S.U. Khan, M. Al-Shahry, W.B. Ingler Jr, Efficient photochemical water splitting by a chemically modified n-TiO₂, *Science*. 297 (2002) 2243-2245.

[7] S. Ghosh, P. Limaye, B. Swain, N. Soni, R. Agrawal, R. Dusane, A. Grover, Tribological behaviour and residual stress of electrodeposited Ni/Cu multilayer films on stainless steel substrate, *Surface and Coatings Technology*. 201 (2007) 4609-4618.

- [8] T.M. Chang, M. Sone, A. Shibata, C. Ishiyama, Y. Higo, Bright nickel film deposited by supercritical carbon dioxide emulsion using additive-free Watts bath, *Electrochimica Acta*. 55 (2010) 6469-6475.
- [9] A. Rashidi, A. Amadeh, The effect of saccharin addition and bath temperature on the grain size of nanocrystalline nickel coatings, *Surface and Coatings Technology*. 204 (2009) 353-358.
- [10] A. Fahami, B. Nasiri-Tabrizi, M. Rostami, R. Ebrahimi-Kahrizsangi, Influence of surfactants on the Characteristics of Nickel Matrix Nanocomposite Coatings, *ISRN Electrochemistry*. (2013) 1-8.
- [11] A. Wang, B. Chen, L. Fang, J. Yu, L. Wang, Influence of branched quaternary ammonium surfactant molecules as levelers for copper electroplating from acidic sulfate bath, *Electrochimica Acta*. 108 (2013) 698-706.
- [12] M.A. Malik, M.A. Hashim, F. Nabi, S.A. Al-Thabaiti, Z. Khan, Anti-corrosion ability of surfactants: a review, *International Journal of Electrochemical Science*. 6 (2011) 1927-1948.
- [13] R. Vittal, H. Gomathi, K. Kim, Beneficial role of surfactants in electrochemistry and in the modification of electrodes, *Advances in Colloid and Interface Science*. 119 (2006) 55-68.
- [14] V. Darrort, M. Troyon, J. Ebothé, C. Bissieux, C. Nicollin, Quantitative study by atomic force microscopy and spectrophotometry of the roughness and brightness of electrodeposited nickel in the presence of additives, *Thin Solid Films*. 265 (1995) 52-57.
- [15] R. Weil, R. Paquin, The relationship between brightness and structure in electroplated nickel, *Journal of the Electrochemical Society*. 107 (1960) 87-91.
- [16] Y. Song, D. Shan, R. Chen, E. Han, A novel dual nickel coating on AZ91D magnesium alloy, *Transactions of Nonferrous Metals Society of China*. 18 (2008) s339-s343.
- [17] D. Suarez, F. Olson, Nodulation of electrodeposited copper in the presence of thiourea, *Journal of Applied Electrochemistry*. 22 (1992) 1002-1010.
- [18] T. Andersen, C. Pitt, L. Livingston, Nodulation of electrodeposited copper due to suspended particulate, *Journal of Applied Electrochemistry*. 13 (1983) 429-438.
- [19] J. Kubisztal, A. Budniok, A. Lasia, Study of the hydrogen evolution reaction on nickel-based composite coatings containing molybdenum powder, *International Journal of Hydrogen Energy*. 32 (2007) 1211-1218.
- [20] A. El-Sherik, U. Erb, J. Page, Microstructural evolution in pulse plated nickel electrodeposits, *Surface and Coatings Technology*. 88 (1997) 70-78.

- [21] F. Ebrahimi, G. Bourne, M.S. Kelly, T. Matthews, Mechanical properties of nanocrystalline nickel produced by electrodeposition, *Nanostructured materials*. 11 (1999) 343-350.
- [22] M. Eslami, H. Saghafian, F. Golestani-fard, A. Robin, Effect of electrodeposition conditions on the properties of Cu–Si₃N₄ composite coatings, *Applied Surface Science*. 300 (2014) 129-140.
- [23] H. Gül, F. Kılıç, M. Uysal, S. Aslan, A. Alp, H. Akbulut, Effect of particle concentration on the structure and tribological properties of submicron particle SiC reinforced Ni metal matrix composite (MMC) coatings produced by electrodeposition, *Applied Surface Science*. 258 (2012) 4260-4267.
- [24] M. Vaezi, S. Sadrnezhaad, L. Nikzad, Electrodeposition of Ni–SiC nano-composite coatings and evaluation of wear and corrosion resistance and electroplating characteristics, *Colloids and Surfaces A: Physicochemical and Engineering Aspects*. 315 (2008) 176-182.
- [25] S. Spanou, E. Pavlatou, N. Spyrellis, Ni/nano-TiO₂ composite electrodeposits: Textural and structural modifications, *Electrochimica Acta*. 54 (2009) 2547-2555.
- [26] J. Amblard, M. Froment, G. Maurin, N. Spyrellis, A method of preparing cross sectioned vertically thin foils-description of the various types of fibers in nickel electrodeposits, *Journal de microscopie et de spectroscopie électroniques*. 6 (1981) 311.
- [27] J. Amblard, M. Froment, N. Spyrellis, Origine des textures dans les depots electrolytiques de nickel, *Surface Technology*. 5 (1977) 205-234.
- [28] H. Karayannis, G. Paternarakis, Effect of the Cl⁻ and SO₄²⁻ ions on the selective orientation and structure of Ni electrodeposits, *Electrochimica Acta*. 40 (1995) 1079-1092.
- [29] E. Saubestre, The Chemistry of bright Nickel plating solutions, *Plating*. 45 (1958) 1219-1227.
- [30] H. Alimadadi, M. Ahmadi, M. Aliofkhazraei, S.R. Younesi, Corrosion properties of electrodeposited nanocrystalline and amorphous patterned Ni–W alloy, *Materials & Design*. 30 (2009) 1356-1361.
- [31] A. Engwall, Z. Rao, E. Chason, Origins of residual stress in thin films: Interaction between microstructure and growth kinetics, *Materials & Design*. 110 (2016) 616-623.
- [32] I. Tudela, Y. Zhang, M. Pal, I. Kerr, A.J. Cobley, Ultrasound-assisted electrodeposition of thin nickel-based composite coatings with lubricant particles, *Surface and Coatings Technology*. 276 (2015) 89.
- [33] N.P. Wasekar, P. Haridoss, S. Seshadri, G. Sundararajan, Influence of mode of electrodeposition, current density and saccharin on the microstructure and hardness of electrodeposited nanocrystalline nickel coatings, *Surface and Coatings Technology*. 291 (2016) 130-140.

- [34] B. Lv, Z. Hu, X. Wang, B. Xu, Electrodeposition of nanocrystalline nickel assisted by flexible friction from an additive-free Watts bath, *Surface and Coatings Technology*. 270 (2015) 123-131.
- [35] C.K. Lee, Wear and corrosion behavior of electrodeposited nickel-carbon nanotube composite coatings on Ti-6Al-4V alloy in Hanks' solution, *Tribology International*. 55 (2012) 7.
- [36] Q. Zhang, Y. Liu, Y. Liu, Y. Ren, Y. Wu, Z. Gao, X. Wu, P. Han, Enhanced tensile ductility and strength of electrodeposited ultrafine-grained nickel with a desired bimodal microstructure, *Materials Science & Engineering A; Materials Science & Engineering A*. 701 (2017) 196-202.
- [37] J. Lohmiller, M. Greuer, C. Braun, A. Kobler, C. Kübel, K. Schüller, V. Honkimäki, H. Hahn, O. Kraft, R. Birringer, P.A. Gruber, Untangling dislocation and grain boundary mediated plasticity in nanocrystalline nickel, *Acta Materialia*. 65 (2014) 295-307.
- [38] K. Schüller, B. Philippi, M. Weinmann, V.M. Marx, H. Vehoff, Effects of processing on texture, internal stresses and mechanical properties during the pulsed electrodeposition of nanocrystalline and ultrafine-grained nickel, *Acta Materialia*. 61 (2013) 3945-3955.
- [39] R. Mishra, B. Basu, R. Balasubramaniam, Effect of grain size on the tribological behavior of nanocrystalline nickel, *Materials Science and Engineering: A*. 373 (2004) 370-373.
- [40] J. Schiøtz, F.D. Di Tolla, K.W. Jacobsen, Softening of nanocrystalline metals at very small grain sizes, *Nature*. 391 (1998) 561.
- [41] N. Krasilnikov, W. Lojkowski, Z. Pakiela, R. Valiev, Tensile strength and ductility of ultra-fine-grained nickel processed by severe plastic deformation, *Materials Science and Engineering: A*. 397 (2005) 330-337.
- [42] G. Hughes, S. Smith, C. Pande, H. Johnson, R. Armstrong, Hall-Petch strengthening for the microhardness of twelve nanometer grain diameter electrodeposited nickel, *Scripta Metallurgica*. 20 (1986) 93-97.
- [43] Z. Ren, N. Meng, K. Shehzad, Y. Xu, S. Qu, B. Yu, J. Luo, Mechanical properties of nickel-graphene composites synthesized by electrochemical deposition, *Nanotechnology*. 26 (2015) 065706.
- [44] N. Hansen, Hall-Petch relation and boundary strengthening, *Scripta Materialia*. 51 (2004) 801-806.
- [45] E.O. Hall, *Proceedings of the Physical Society London B*. 64 (1951).
- [46] N.J. Petch, *The Journal of the Iron and Steel Institute*. 174 (1953).
- [47] S. Wang, Y. Zhang, N. Abidi, L. Cabrales, Wettability and surface free energy of graphene films, *Langmuir*. 25 (2009) 11078-11081.

- [48] E. Chibowski, Surface free energy of a solid from contact angle hysteresis, *Adv. Journal of Colloid and Interface Science*. 103 (2003) 149-172.
- [49] D. Janssen, R. De Palma, S. Verlaak, P. Heremans, W. Dehaen, Static solvent contact angle measurements, surface free energy and wettability determination of various self-assembled monolayers on silicon dioxide, *Thin Solid Films*. 515 (2006) 1433-1438.
- [50] L. Vitos, A. Ruban, H.L. Skriver, J. Kollar, The surface energy of metals, *Surface Science*. 411 (1998) 186-202.
- [51] M. McLean, Determination of the surface energy of copper as a function of crystallographic orientation and temperature, *Acta Metallurgica*. 19 (1971) 387-393.
- [52] A. Cassie, S. Baxter, Wettability of porous surfaces, *Transactions of the Faraday society*. 40 (1944) 546-551.
- [53] E. Bormashenko, Why does the Cassie–Baxter equation apply? *Colloids and Surfaces A: Physicochemical and Engineering Aspects*. 324 (2008) 47-50.
- [54] R.N. Wenzel, Surface roughness and contact angle. *The Journal of Physical Chemistry*. 53 (1949) 1466-1467.
- [55] W. Choi, Tuteja. A, Mabry. J, R. Cohen, McKinley. G, A modified Cassie–Baxter relationship to explain contact angle hysteresis and anisotropy on non-wetting textured surfaces, *Journal of Colloid and Interface Science*. 339 (2009) 208-216.
- [56] S. Hassani, K.P. Roberts, S.A. Shirazi, J.R. Shadley, E.F. Rybicki, C. Joia, Flow Loop Study of NaCl Concentration Effect on Erosion, Corrosion, and Erosion-Corrosion of Carbon Steel in CO₂-Saturated Systems, *Corrosion*. 68 (2012) G1-G9.
- [57] K. Ralston, N. Birbilis, Effect of grain size on corrosion: a review, *Corrosion*. 66 (2010) 075005-075005-13.
- [58] F. Nasirpour, M.R. Sanaeian, A.S. Samardak, E.V. Sukovatitsina, A.V. Ognev, L.A. Chebotkevich, M.-. Hosseini, M. Abdolmaleki, An investigation on the effect of surface morphology and crystalline texture on corrosion behavior, structural and magnetic properties of electrodeposited nanocrystalline nickel films, *Applied Surface Science*. 292 (2014) 795-805.
- [59] A. El-Sayed, H. Mohran, H. Abd El-Lateef, Corrosion Study of Zinc, Nickel, and Zinc-Nickel Alloys in Alkaline Solutions by Tafel Plot and Impedance Techniques, *Metallurgical and Materials Transactions*. 43 (2012) 619-632.
- [60] K.D. Ralston, N. Birbilis, Effect of Grain Size on Corrosion: A Review, *Corrosion*. 66 (2010) 1D.
- [61] C.P. Kumar, T. Venkatesha, R. Shabadi, Preparation and corrosion behavior of Ni and Ni–graphene composite coatings, *Materials Research Bulletin*. 48 (2013) 1477-1483.

- [62] O.S.A. Rahman, N.P. Wasekar, G. Sundararajan, A.K. Keshri, Experimental investigation of grain boundaries misorientations and nano twinning induced strengthening on addition of silicon carbide in pulse electrodeposited nickel tungsten composite coating, *Materials Characterization*. 116 (2016) 1-7.
- [63] E. García-Lecina, I. García-Urrutia, J.A. Díez, J. Fornell, E. Pellicer, J. Sort, Codeposition of inorganic fullerene- like WS₂nanoparticles in an electrodeposited nickel matrix under the influence of ultrasonic agitation, *Electrochimica Acta*. 114 (2013) 859-867.
- [64] E. Rudnik, L. Burzyńska, A.U. Dolasiński, M. Misiak, Electrodeposition of nickel/SiC composites in the presence of cetyltrimethylammonium bromide, *Applied Surface Science*. 256 (2010) 7414.
- [65] A. Gajewska-Midziulek, Composite coatings with nickel matrix and graphene as dispersed phase, *Polish Journal of Chemical Technology*. 20 (2018) 54-59.
- [66] N. Elkhoshkhany, A. Hafnawy, A. Khaled, Electrodeposition and corrosion behavior of nano-structured Ni-WC and Ni-Co-WC composite coating, *Journal of Alloys and Compounds*. 695 (2017) 1505-1514.
- [67] T. Yamasaki, P. Schloßmacher, K. Ehrlich, Y. Ogino, Formation of amorphous electrodeposited Ni-W alloys and their nanocrystallization, *Nanostructured Materials*. 10 (1998) 375-388.
- [68] M. Surender, B. Basu, R. Balasubramaniam, Wear characterization of electrodeposited Ni-WC composite coatings, *Tribology International*. 37 (2004) 743-749.
- [69] C. Zanella, M. Lekka, P. Bonora, Effect of ultrasound vibration during electrodeposition of Ni-SiC nanocomposite coatings, *Surface Engineering*. 26 (2010) 511-518.
- [70] S. Khabazian, S. Sanjabi, The effect of multi-walled carbon nanotube pretreatments on the electrodeposition of Ni-MWCNTs coatings, *Applied Surface Science*. 257 (2011) 5850-5856.
- [71] S. Mirzamohammadi, H. Khorsand, M. Aliofkhazraei, Effect of different organic solvents on electrodeposition and wear behavior of Ni-alumina nanocomposite coatings, *Surface and Coatings Technology*. 313 (2017) 202-213.
- [72] E. Beltowska-Lehman, P. Indyka, A. Bigos, M. Kot, L. Tarkowski, Electrodeposition of nanocrystalline Ni-W coatings strengthened by ultrafine alumina particles, *Surface and Coatings Technology*. 211 (2012) 62-66.
- [73] Gamry Instruments, Getting Started with Electrochemical Corrosion Measurement. Application note, Gamry instruments. (2011).
- [74] AZoM, Nickel (Ni) - Properties, Applications, 2018 (2001).

[75] J. Sudagar, J. Lian, W. Sha, Electroless nickel, alloy, composite and nano coatings—A critical review, *Journal of Alloys and Compounds*. 571 (2013) 183-204.

7. Conclusions

7.1. Research conclusions

During this research project, it was demonstrated that turmeric particles (with the aid of the surfactant Tween 20) could be uniformly dispersed in both acid copper and LICE nickel electrolytes using ultrasound from a 20 kHz horn before electrodeposition. It was also demonstrated that turmeric particles could be successfully electrocodeposited into both nickel and copper matrices. The incorporation of turmeric into both the nickel and copper matrices had a significant effect on the surface morphology and grain structure of the deposit, changing both the surface texture and reducing the grain size. The reduction of the grain size resulted in a substantial increase in the microhardness of both copper and nickel deposits, and an increase in resistance to salt spray corrosion in the nickel deposits. The reduction in grain size also resulted in an increase in WCA for the copper deposits. The nickel deposit also showed an increase in WCA with the incorporation of turmeric, however it was due to a combination of grain structure, surface roughness and surface composition. These findings showed that turmeric is a viable, sustainable alternative to some of the more commonly used filler particles currently utilised in composite electrodeposition.

An additional unexpected finding was that there was an optimal particle size for reducing the grain size of the copper deposit, which was not the case for the nickel deposit. This could be due to the difference in the growth mechanism between the nickel and copper deposits. Assuming that the nucleation of the deposits follows a hemispherical growth mode, the formation of the deposits consists of four stages [1-3]:

- 1) Nucleation.
- 2) Nucleus growth.
- 3) Coalescence.
- 4) Film formation.

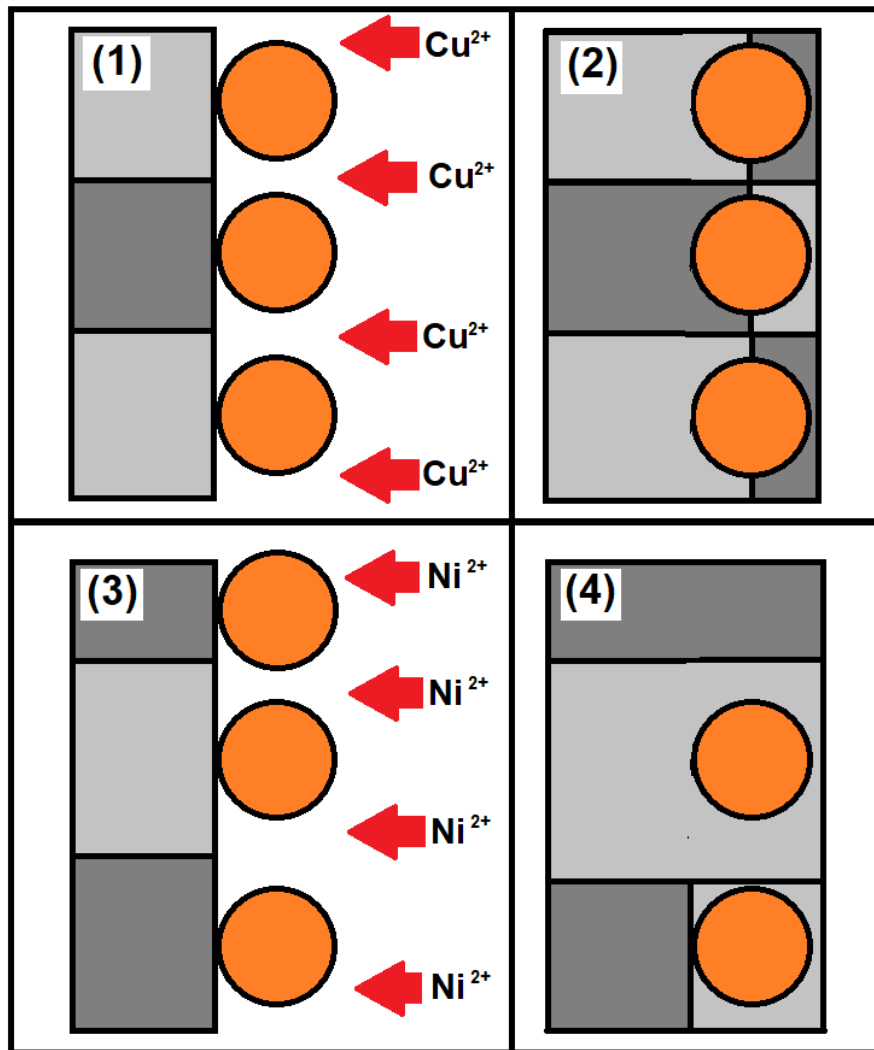


Figure 7.1. Diagram of codeposition of particles into matrices with different growth mechanisms. (1) Shows a deposit with low variation in the crystal size, metal ions are prevented from reaching the growing crystal (2) The crystal growth is disrupted, and grain size reduced. (3) Shows a deposit with high variation in the crystal size, metal ions are prevented from reaching the growing crystal in some cases and in others are not. (4) The crystal growth is disrupted for some crystals and for others it is not.

In copper electrolytes with pH 3 or lower, crystal growth proceeds by the instantaneous nucleation of islands of copper onto the cathode [2,4]. The nucleation of copper is fast compared to the crystal growth in instantaneous nucleation, forming the nuclei at all possible growth sites in a very short time. As copper ions in the electrolyte reach the nuclei, the nuclei grow and start to coalesce forming crystals.

Nickel crystal growth proceeds by progressive nucleation. Nucleation is slow and continuous compared to crystal growth in progressive nucleation. Nuclei are formed at the surface of the cathode while other clusters are still growing. Progressive nucleation could lead to crystals of more varying size compared to instantaneous nucleation. A higher variation in crystal size of the deposits would lead to no optimal particle size for reducing the grain size of the deposit (Figure 7.1.).

For the growth of a crystal to be disrupted (decreasing grain size) the metal ions in the electrolyte must be prevented from reaching that growing crystal. The optimal particle size for that crystal is one that is large enough to prevent the metal ions from reaching the growing crystal but not too large that it cannot be absorbed. If the crystal size of the deposit has high variation than there is not a single (optimal) particle size most suitable for reducing the grain size of the deposit. In this case, a high degree of variation of particle size in the electrolyte would likely be the most suitable for decreasing the grain size of the deposit.

7.2. Future Recommendation

As the spice turmeric as shown its viability as a potential sustainable filler particle for enhancing the properties of both copper and nickel matrices, other spices and herbs (not used in this research) may have potential as sustainable filler particles. Possible future research could be to produce composite copper and nickel coatings containing other spice filler particles or incorporate turmeric into other metal matrices.

As mentioned in earlier Chapters, the surface roughness of a coating can affect the WCA of that coating [5-7]. Possible further research could be to increase the surface roughness of the copper and nickel turmeric composites in an attempt to produce super hydrophobic surfaces ($>150^\circ$).

Another possible further research project could be to test if instantaneous nucleation is responsible for the optimal particle size seen in the copper deposit. The literature has shown that nucleation and growth is strongly dependent on the pH of the electrolyte, and at pH 3 or higher the nucleation mechanism for electrodeposited copper changes from instantaneous to progressive [4]. The pH of the copper electrolyte could be increased to pH 3, then composite deposits produced. The grain size of the deposits could then be analysed to see if the optimal particle size for decreasing the grain size of the deposit still exists.

7.3. Reference list

- [1] D. Grujicic, B. Pesic, Electrochemical and AFM study of nickel nucleation mechanisms on vitreous carbon from ammonium sulfate solutions, *Electrochimica Acta*. 51 (2006) 2678-2690.
- [2] A. Radisic, P. Vereecken, P. Searson, F. Ross, The morphology and nucleation kinetics of copper islands during electrodeposition, *Surface Science*. 600 (2006) 1817-1826.
- [3] M.E. Hyde, R.G. Compton, A review of the analysis of multiple nucleation with diffusion controlled growth, *Journal of Electroanalytical Chemistry*. 549 (2003) 1-12.
- [4] D. Grujicic, B. Pesic, Electrodeposition of copper: the nucleation mechanisms, *Electrochimica Acta*. 47 (2002) 2901-2912.
- [5] W. Choi, Tuteja. A, Mabry. J, R. Cohen, McKinley. G, A modified Cassie–Baxter relationship to explain contact angle hysteresis and anisotropy on non-wetting textured surfaces, *Journal of Colloid and Interface Science*. 339 (2009) 208-216.
- [6] E. Bormashenko, Why does the Cassie–Baxter equation apply? *Colloids and Surfaces A: Physicochemical and Engineering Aspects*. 324 (2008) 47-50.
- [7] A. Cassie, S. Baxter, Wettability of porous surfaces, *Transactions of the Faraday society*. 40 (1944) 546-551.

Appendix A Spice selection

A.1. Overview

This Appendix describes the experimental procedures undertaken to assess the suitability of 6 spice for incorporation into the composite coatings.

A.2. Methods

The successful incorporation of spice particles into a composite coating by electrodeposition depends on many factors, including how the spice particles behave in the electrolyte. The spices must survive the harsh acidic environment of the electrolyte, they must disperse uniformly throughout the electrolyte and large agglomeration of the spice particles must be minimised [1,2].

A.2.1. Spice preparation

Six spices were purchased from the online retailer Healthy Supplies (Table A.1.). Most of the spices arrived as whole leaf's (or buds in the case of cloves) making them too large for incorporation into the composite coating. The spices were first ground to facilitate their incorporation into the coating and increase their surface area, however, this could also increase the solubility of the spices which was undesired in this research project. Two methods of grinding were used, pestle and mortar and an Andrew James electric coffee grinder model AJ000026. The spices were ground for between 30 s and 5 min, depending on their hardness. After each spice was ground, the spices were examined under a Nikon fluorescence microscope at x20 magnification.

Table A.1. *Spices purchased from Healthy Supplies*

Spice/Herb	Supplier	Code	Quantity / g	Price / £
Oregano leaves (organic)	Sussex Wholefoods	7ORE1	90	4.26
Cloves whole (organic)	Sussex Wholefoods	7CLO1	100	3.99
Marjoram leaves (organic)	Sussex Wholefoods	7MAR1	90	4.26
Thyme leaves (organic)	Sussex Wholefoods	7TYM1	100	5.50
Rosemary leaf (organic)	Sussex Wholefoods	7ROS1	100	8.52
Turmeric powder	Hampshire Foods	ZTRM5	100	1.52

A.2.2. The solubility of the spices

The spices solubility was examined, to assess the chemical resistance of the spice particles to the electrolyte. The dark colours of the electrolytes made it difficult to visually identify the spice particles in solution and so for this reason, electrolyte mimics were produced. The electrolyte mimics simulated the acidic conditions of the electrolyte but had no metal ions, allowing visual identification of the spices in solution.

The electrolyte mimics were produced by preparing a solution of the same pH as the complete electrolyte. The copper electrolyte mimic solution of (pH 0.5 – 1.0) was a 3.7 M solution prepared from concentrated H₂SO₄ (S.G 1.83 >95%) supplied by Fisher Scientific UK Ltd in DI water. The Nickel electrolyte mimic solution (pH 2.5 - 3.5) was a 1.05 M solution prepared from H₃BO₃ (ACS reagent 99.5%) supplied by Sigma Aldrich Ltd UK.

The spice particles must not dissolve in the harsh acidic environment of the electrolyte, if they are to be successfully incorporated into the composite coating. For this reason, the solubility of the spice particles in the electrolytes was assessed.

A mass of 0.1 ± 0.02 g of each ground spice and 80 ml of each electrolyte mimic was added to 100 ml beakers and heated for 30 min at 50 °C on an IKA RCT Basic hot plate. The resulting solutions were then left at room temperature overnight. The following day the solutions were filtered under suction (the nickel electrolyte mimic solutions required reheating beforehand to dissolve recrystallized H_3BO_3) through pre-weighed hardened ash less filter papers supplied by Whatman International Ltd UK. After thoroughly rinsing through with RO water, the filter papers were placed in a drying oven for 6 hours at 90°C, the filter papers were then re-weighed, and the mass of the remaining spice calculated.

A.2.3. Ultrasonic equipment used for dispersion

Both an ultrasonic horn (20 kHz Sonic systems sonic processor P100/3-20 with horn model GA99893) and an ultrasonic bath (Ultrawave QS12 cleaning bath, 32-38 kHz operating frequency, 300 W heating power 12.5 L capacity) were used to disperse the particles throughout the project. The power of each system was first estimated using calorimetry [3]. All powers detailed in this research project (table A.2.) were calculated by this method.

Only water was used for the calorimetry experiments as it was the main constituent of the electrolyte, and both cheaper and safer than using the electrolyte. A volumetric flask was used to measure out 500 ml of reverse osmosis water (RO), which was then added to a 600 ml beaker. The beaker was then placed in the bath where the effect of the ultrasound was most prominent (or the horn placed in the beaker in the case of the ultrasonic horn), the beaker, position of the beaker, and water level remained constant throughout the course of the experiment (Figure A.1.). The bath was then switched on at 100% power for 5 min. An Extech Instruments Easyview 15 data logger was used to measure the temperature change every 3 s for the 5 min duration. This was then repeated for the ultrasonic horn at an estimated power of 15 W/l and 47 W/l.

The Data was collected and plotted on polynomial graphs, and the power of each system calculated (A.1.) a presented in table A.2.

$$P = \frac{dT}{dt} cp M \quad (A.1.)$$

Where P is the power of the system at that setting, dT is the change in temperature, dt is the change in time, M is the mass of the water in the beaker, and cp is the heat capacity of water.

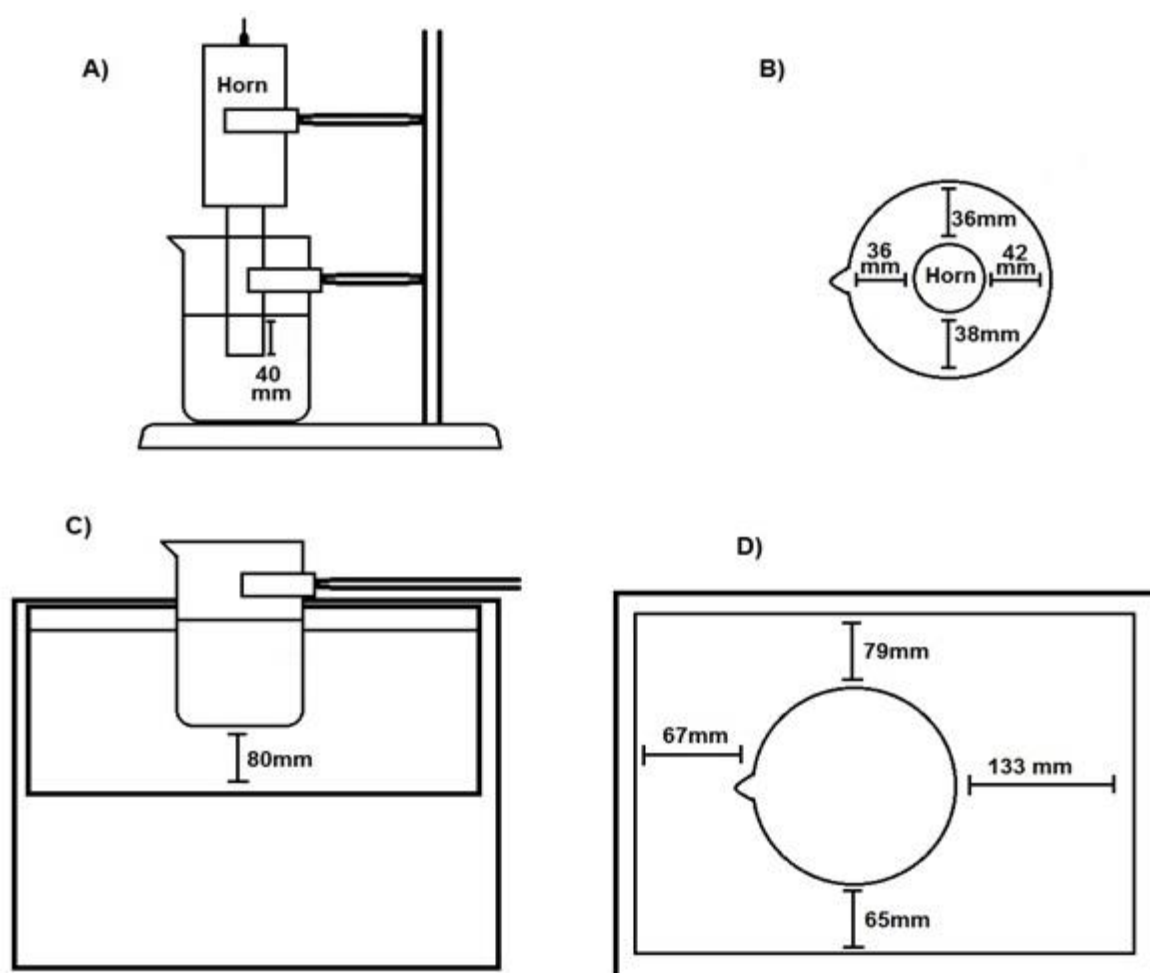


Figure A.1. Diagram of beaker position while sonication was taking place. (A) Side view of horn. (B) Overhead view of horn. (C) Side view of bath. (D) Overhead view of bath.

Table A.2. Power outputs of ultrasound systems measured by calorimetry.

Ultrasound System	Power setting on the system	Measured power output / w/l
32-38 kHz Bath	100%	11
20 kHz Horn	15 w/l	11
20 kHz Horn	47 w/l	33

A.2.4. Spice particle dispersion and suspension

A dispersion experiment was conducted, to assess how the spice particles dispersed and stayed suspended in the electrolyte. The study used two non-ionic surfactants, Tween 20 and Tween 80 (Figure A.2.). Due to the problems of the recrystallization of H_3BO_3 in the nickel electrolyte mimic as it cooled over time, only the copper electrolyte mimic was used.

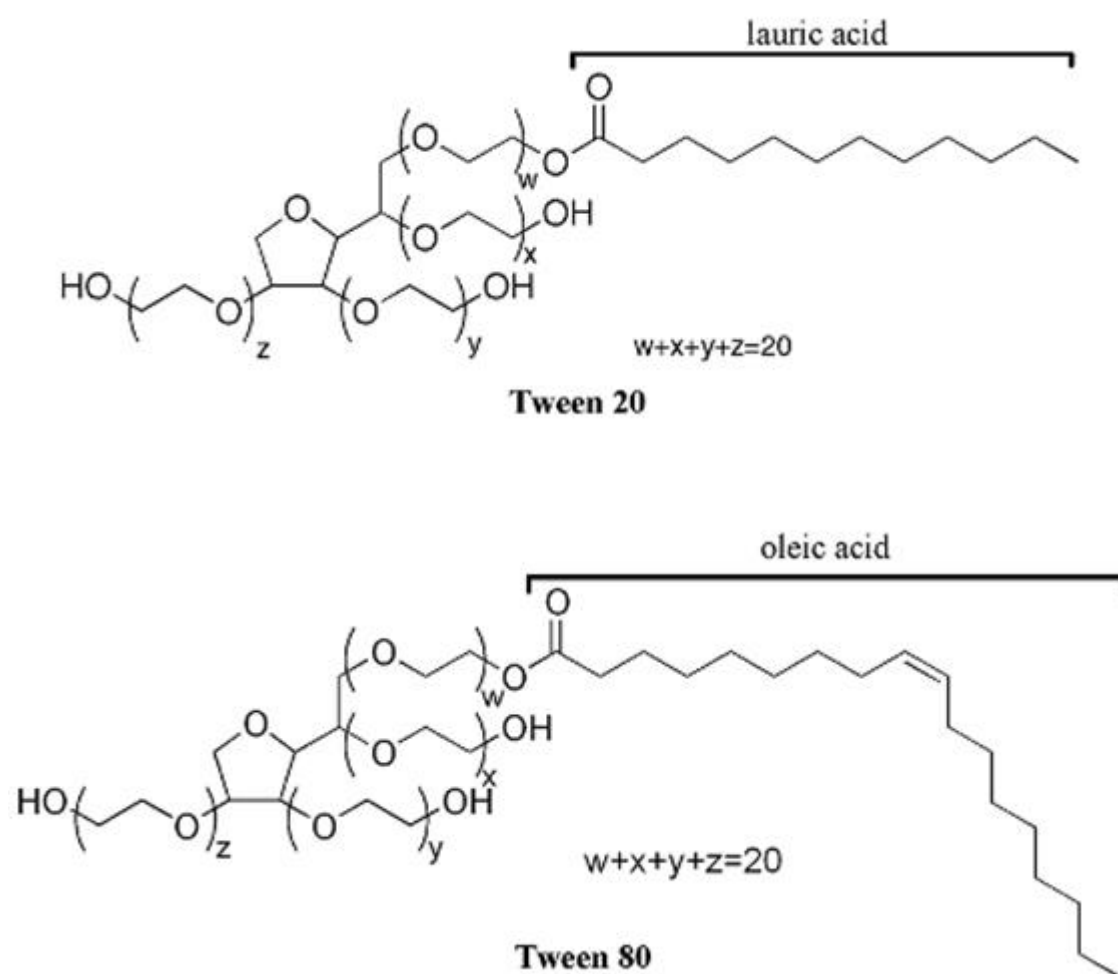


Figure A.2. Chemical structures of Tween 20 and Tween 80 [4].

A known amount of each ground spice (0.3 ± 0.02 g) with 100 ml of the copper electrolyte mimic was placed in a 150 ml beaker (no surfactant was added). The solution was then placed in the 32 – 38 kHz ultrasonic bath at a power of 11 W/l for 5 min. The solutions were then transferred to glass vials and monitored for 1 hour.

The spice solutions were then remade with the addition of 1.0 ± 0.1 ml of Tween 20 and 1.0 ± 0.1 ml of Tween 80 both supplied by Sigma Aldrich UK Ltd, and left to stand overnight. The following day the experiment was repeated on the spice solution with Tween 20 and Tween 80.

A.3. Results

A.3.2. Spice grinding

Figure A.3. and Figure A.4. Show images of spices before and after grinding with a pestle and mortar.

For oregano and marjoram, 90 s of grinding in the pestle and mortar was sufficient to produce fine pea green and greyish-green powders respectively. The clove buds remained almost completely intact after 5 min of grinding in the pestle and mortar. For both thyme and rosemary, the size of the leaves was reduced after 5 min, however grinding in the pestle and mortar was insufficient to produce fine powders.

Figure A.5. and Figure A.6. Show images of spices before and after grinding in an electric coffee grinder. Fine powders were produced for both oregano and marjoram after 30 s of grinding in the electric coffee grinder. For Thyme and Rosemary leaves 60 s of grinding was required to produce a brownish-green powder and olive-green powder respectively, however, large fibres were still present, increasing the grinding time to 5 min did not remove the fibres (Figure A.7.). Clove buds required 2 min to produce a coarse, moist chocolate brown powder, increasing the grinding time up to 5 min did not produce a fine powder.







Before Grinding	After Grinding
	
Oregano	
	
Clove	
	
Marjoram	

Figure A.3. Images of spices before and after grinding in a pestle and mortar.



Before Grinding	After Grinding
	
Thyme	
	
Rosemary	

Figure A.4. Images of spices before and after grinding in a pestle mortar







Before Grinding	After Grinding
	
Oregano	
	
Clove	
	
Marjoram	

Figure A.5. Images of spices before and after grinding in an electric coffee grinder.

Before Grinding	After Grinding
	
Thyme	
	
Rosemary	

Figure A.6. Images of spices before and after grinding in an electric coffee grinder.

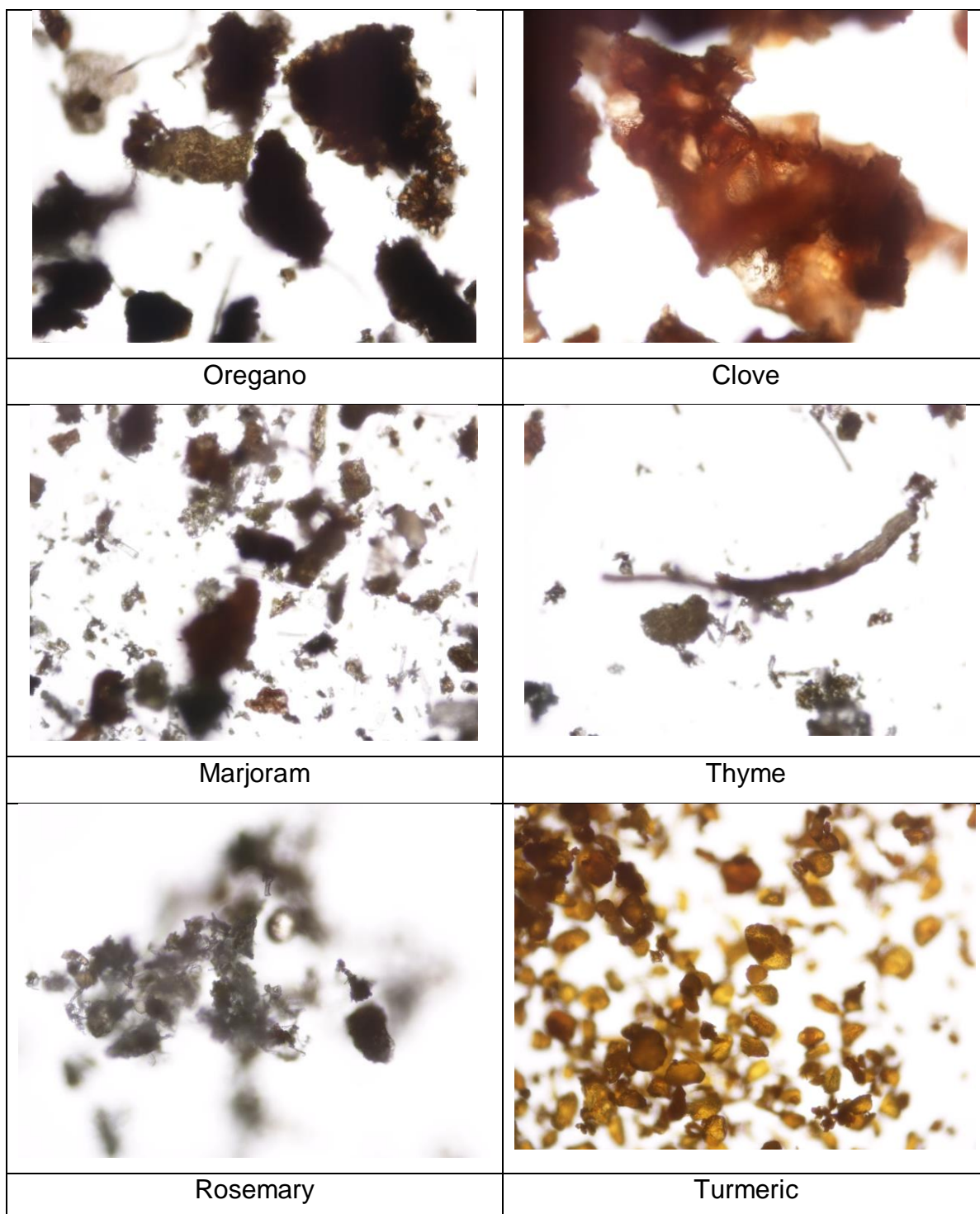


Figure A.7. Images of the spices after grinding in an electric coffee grinder (except for turmeric which was purchased pre-ground) under Nikon fluorescence microscope at x20 magnification.

A.3.3. Spice solubility test

The solubility of the spices in the copper and nickel electrolyte mimic was assessed by mass differential of before and after experiment (Figure A.8. and Figure A.9. respectively).

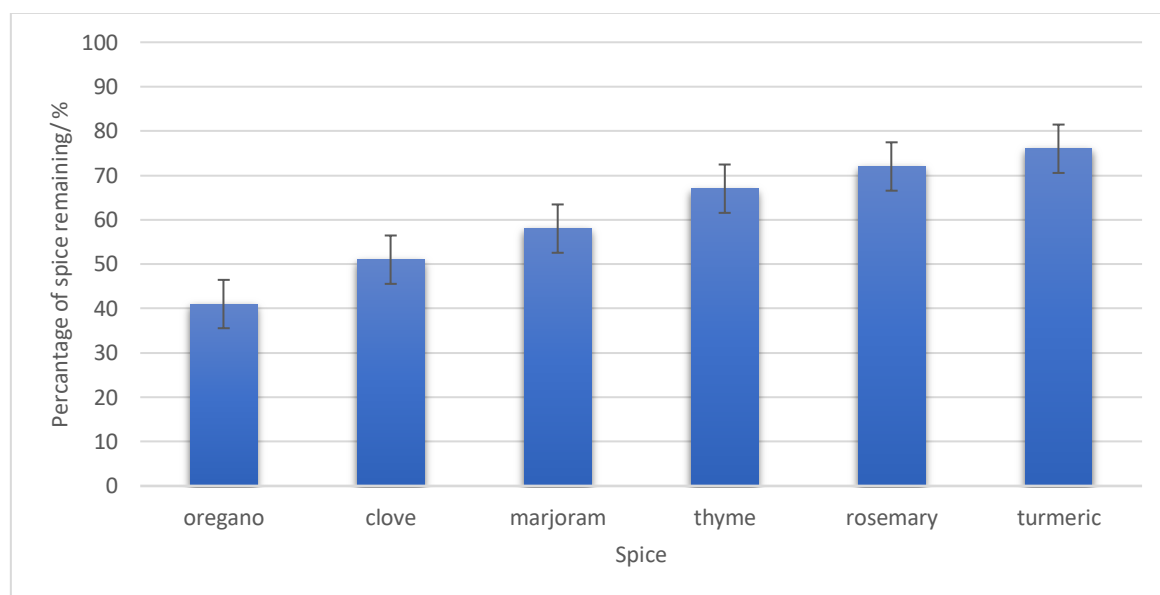


Figure A.8. The percentage of mass remaining in copper electrolyte mimic after solubility test for various spices.

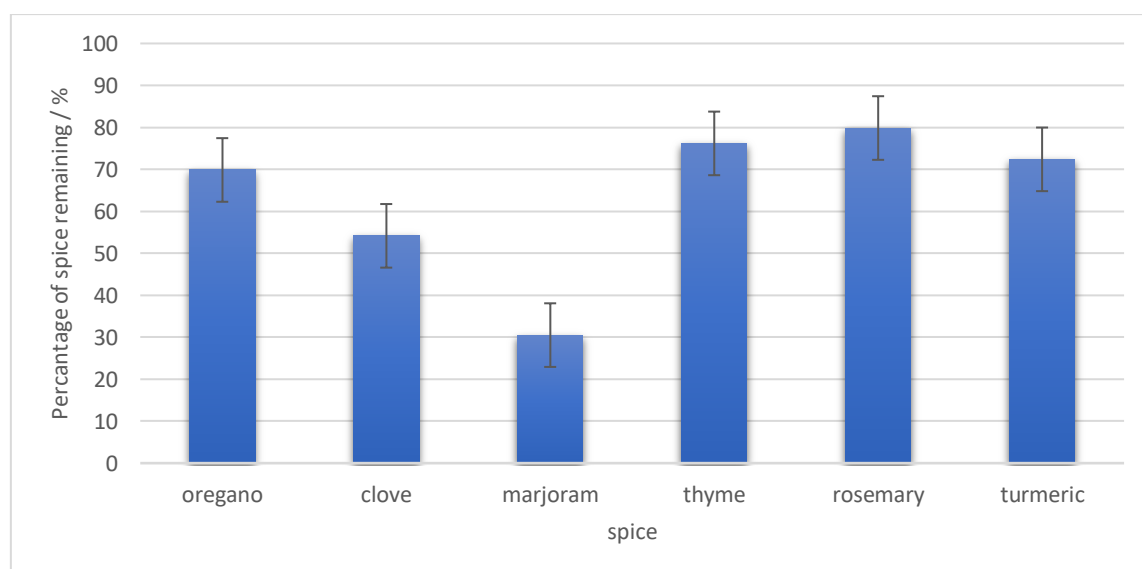


Figure A.9. Bar chart of the percentage of mass remaining in nickel electrolyte mimic after solubility test for various spices.

All the samples tested showed some spice remaining in the copper electrolyte mimic after the solubility test. Turmeric had the highest percentage of spice remaining in solution indicating the lowest solubility. Rosemary and thyme also showed low solubility, with marjoram and cloves exhibiting moderate solubility, whilst oregano showed the lowest percentage of spice in solution after the solubility test indicating the highest solubility.

From Figure A.9. It can be seen that again, all samples showed some spice remaining in the nickel electrolyte mimic after the solubility test. Rosemary had the highest percentage of spice remaining in solution indicating the lowest solubility. Turmeric and thyme also showed low solubility, oregano and cloves showed moderate solubility, whilst marjoram showed the lowest percentage of spice in solution after the solubility test indicating the highest solubility.

A.3.4. Spice particle dispersion and suspension

Figure A.10. and Figure A.11. Shows the dispersion of the spices in the copper electrolyte mimic with and without surfactant. Results from the dispersion experiment with nickel electrolyte mimic were not obtained, due to the recrystallisation of boric acid in solution as the temperature cooled below 35 °C.

The spices that were dispersed in solution without a surfactant rapidly re-agglomerated and either settled to the bottom or rose to the surface of the solutions. With thyme and turmeric, the solutions at 1 hour after agitation were more transparent than the solutions at 5 min after agitation. However, for oregano, cloves, marjoram, and rosemary no clear visual difference between the samples at 5 min after agitation and 1 hour after agitation could be identified.

For spices dispersed in solution with Tween 80, re-agglomeration was slower than that of the spices dispersed without surfactant. However, in marjoram and rosemary samples large agglomerates were visible on the surface of the solutions. With oregano and thyme samples, at 1 hour after agitation, the spice particles had started to re-

agglomerate and rise to the surface, and with turmeric, after 1 hour particles had begun to settle at the bottom of the sample.

For spices dispersed in solution with Tween 20, re-agglomeration was slower than both that of the spices dispersed without surfactant and with Tween 80. There was no visual difference between samples 5 min after agitation and samples 1 hour after agitation for oregano, cloves, thyme, rosemary, and turmeric. However, for marjoram, the sample at 1 hour after agitation was more transparent than the sample after 5 min after agitation, and particles were present on the bottom of the solution.



















Spice	No surfactant		Tween 80		Tween 20	
	5 min after agitation	1 hour after agitation	5 min after agitation	1 hour after agitation	5 min after agitation	1 hour after agitation
Oregano						
Clove						
Marjoram						

Figure A.10. Spices dispersed in copper electrolyte mimic with and without surfactant



















Spice	No surfactant		Tween 80		Tween 20	
	5 min after agitation	1 hour after agitation	5 min after agitation	1 hour after agitation	5 min after agitation	1 hour after agitation
Thyme						
Rosemary						
Turmeric						

Figure A.11. Spices dispersed in copper electrolyte mimic with and without surfactant.

A.4. Discussion

The ability of a spice to remain dispersed and survive the harsh environments of the electrolytes is essential for its uniform incorporation into the electrodeposits. These results show that of the six spices tested turmeric offers the best chance of successful incorporation.

Grinding with either the pestle and mortar or the electric coffee grinder was unable to produce fine powders free of large fibres for both thyme and rosemary. These fibres may be too large to be physically incorporated into the electrodeposited coatings, or if

incorporated protrude from the surface of the deposit [5]. Therefore, without additional pre-treatment or filtering, thyme and rosemary were not suitable for electrocodeposition into the coatings produced in this research project.

The codeposition of a particle into an electrodeposited coating is dependent on the presence of the particle in the electrolyte. If the particle has high solubility in the electrolyte the particles incorporation into the coating could be adversely affected. The higher solubility of the spices oregano and cloves in the copper electrolyte mimic made them less suitable for incorporation into the copper electrodeposited coating. The higher solubility of the spice marjoram in the nickel electrolyte mimic made it less suitable for incorporation into the nickel electrodeposited coating. Therefore, the spices oregano, marjoram, and cloves were not suitable for electrocodeposition in this research project.

Although the 2 electrolyte mimics had different pH's the spices turmeric, rosemary, thyme, and clove showed similar solubility in both, whilst oregano and marjoram showed difference solubility. The difference in solubility of oregano and marjoram in the 2 electrolyte mimics could be due to a counterion effect. The counterion for H_2SO_4 is SO_4^{2-} (the sulphate ion), and BO_3^{3-} (the borate ion) for H_3BO_3 . Both the sulphate and borate ions can act as ligands and form complexes, which can increase the solubility of a compound [6-8]. The compounds/oils in marjoram may form complexes more readily with borate ions than with sulphate ions, which would result in increased solubility in the nickel electrolyte mimic compared to the copper electrolyte mimic. The compounds/oils in oregano may complex with sulphate ions more readily than with borate, which would result in increased solubility in the copper electrolyte mimic compared to the nickel electrolyte mimic.

A uniform dispersion of particles in the electrolyte is essential to obtain a coating with uniform particle content (and properties) throughout; therefore the dispersion of particles in the electrolyte is of great importance [5,9,10]. These results show that to prevent the particles from re-agglomerating after dispersion; it is essential to use a surfactant. Although both Tween 80 and Tween 20 improved the dispersion and helped prevent re-agglomeration of all the spices tested, marjoram and rosemary did not disperse as evenly in Tween 80 as in Tween 20, and turmeric stayed dispersed for longer in Tween 20 than Tween 80. Therefore, in this research project, Tween 20 was a more suitable surfactant to use for dispersing the spices in the electrolyte.

The inability to obtain fine powders for thyme and rosemary by either pestle and mortar or electric coffee grinder eliminated them from this research project. The higher solubility of clove, oregano, and marjoram in the electrolyte mimics also excluded them from the research. Therefore, the only spice used in this research was turmeric, with the surfactant Tween 20 used to assist its dispersion.

A.5. Conclusions

- Results from the spice preparation experiments show using the grinding methods in this research, it is not possible to produce powders suitable for incorporation into the electrodeposited coatings, for thyme and rosemary. The results also show that the solubility of oregano, marjoram, and clove in the electrolyte mimics made them less suitable for incorporation into the electrodeposited coatings than turmeric, thyme, and rosemary. Therefore, in this research project, the most suitable spice for incorporation into the electrodeposited coating was turmeric.
- A surfactant is needed to disperse the spices in copper electrolyte mimic, and of the 2 tested Tween 20 produced better results. Therefore, for this research project, Tween 20 was used to help disperse turmeric.

A.6. Reference list

[1] R. Zangi, B. Berne, Aggregation and dispersion of small hydrophobic particles in aqueous electrolyte solutions, *The Journal of Physical Chemistry B*. 110 (2006) 22736-22741.

[2] G. Schwarz, A theory of the low-frequency dielectric dispersion of colloidal particles in electrolyte solution, *The Journal of Physical Chemistry*. 66 (1962) 2636-2642.

[3] T.J. Mason, D. Peters, *Practical Sonochemistry: Power Ultrasound Uses and Applications*, Woodhead Publishing, 2002.

[4] Johnson. Mary, *Detergents: Triton X-100, Tween-20, and More*, 2017 (2016).

- [5] F. C. Walsh* C. Ponce de Leon., A review of the electrodeposition of metal matrix composite coatings by inclusion of particles in a metal layer: an established and diversifying technology, Transactions of the Institute of Metal Finishing. 92 (2014) 83-98.
- [6] S. Trofimenko, Coordination chemistry of pyrazole-derived ligands, Chemical Reviews. 72 (1972) 497-509.
- [7] R. Pizer, P. Ricatto, Thermodynamics of Several 1: 1 and 1: 2 Complexation Reactions of the Borate Ion with Bidentate Ligands. 11B NMR Spectroscopic Studies¹, Inorganic Chemistry. 33 (1994) 2402-2406.
- [8] L. Fransson, L. Cöster, Interaction between dermatan sulphate chains II. Structural studies on aggregating glycan chains and oligosaccharides with affinity for dermatan sulphate-substituted agarose, Biochimica et Biophysica Acta (BBA)-General Subjects. 582 (1979) 132-144.
- [9] I. Tudela, Y. Zhang, M. Pal, I. Kerr, A.J. Cobley, Ultrasound- assisted electrodeposition of composite coatings with particles, Surface and Coatings Technology. 259 (2014) 363-373.
- [10] E. García-Lecina, I. García-Urrutia, J.A. Díez, J. Morgiel, P. Indyka, A comparative study of the effect of mechanical and ultrasound agitation on the properties of electrodeposited Ni/ Al₂O₃ nanocomposite coatings, Surface and Coatings Technology. 206 (2012) 2998-3005.